

TEXTILE MATERIALS

Edited by

Fernando B.N. Ferreira

Ana Maria Rocha

Andrea Zille

António Dinis Marques

Raul Fangueiro



TRANS TECH PUBLICATIONS

Textile Materials

Edited by
Fernando B.N. Ferreira
Ana Maria Rocha
Andrea Zille
António Dinis Marques
Raul Fangueiro

Textile Materials

Special topic volume with invited peer-reviewed papers only

Edited by

**Fernando B.N. Ferreira, Ana Maria Rocha, Andrea Zille,
António Dinis Marques and Raul Figueiro**

■
■ *Scientific.Net* ■

Copyright © 2022 Trans Tech Publications Ltd, Switzerland

All rights reserved. No part of the contents of this publication may be reproduced or transmitted in any form or by any means without the written permission of the publisher.

Trans Tech Publications Ltd
Kapellweg 8
CH-8806 Baech
Switzerland
<https://www.scientific.net>

Volume 333 of
Solid State Phenomena
ISSN print 1012-0394
ISSN web 1662-9779

(Pt. B of Diffusion and Defect Data - Solid State Data (ISSN 0377-6883))

Full text available online at <https://www.scientific.net>

Distributed worldwide by

Trans Tech Publications Ltd
Kapellweg 8
CH-8806 Baech
Switzerland

Phone: +41 (44) 922 10 22
e-mail: sales@scientific.net

Preface

In this specialised publication, the reader will find research results and real engineering developments in the field of modern technical textiles.

Modern technical textile materials, ranging from ordinary reinforcing fabrics in the construction and production of modern composite materials to specialised textile materials in the composition of electronics, sensors and other intelligent devices, play an important role in many areas of human technical activity. The use of specialized textiles, for example, in medicine makes it possible to achieve important results in diagnostics, prosthetics, surgical practice and the practice of using specialized fabrics at the health recovery stage.

The use of reinforcing fabrics in construction can significantly improve the mechanical properties of concrete and various plaster mixtures, which increases the reliability and durability of various structures and buildings in general.

In mechanical engineering, the use of composite materials reinforced with special textiles can simultaneously reduce weight and improve the mechanical properties of machine parts. Fabric-reinforced composites occupy a significant place in the automotive industry, aerospace engineering, and shipbuilding. Here, the mechanical reliability and thermal resistance of the body material of the product, along with its low weight, are very relevant.

The presented edition will be useful and interesting for engineers and researchers whose activities are related to the design, production and application of various technical textile materials.

Table of Contents

Preface

Chapter 1: Smart Textiles and Functional Fabrics

Development of a Testing Protocol to Assess the Washability of E-Textiles S. Rotzler and M. Schneider-Ramelow	3
Protective Coating for Electrically Conductive Yarns for the Implementation in Smart Textiles P.R.C. Böhnke, H. Winger, F. Wieczorek, M. Warncke, L.M. Lüneburg, I. Kruppke, A. Nocke, E. Häntzsche and C. Cherif	11
Development of Filled Immiscible Polymers Blend Monofilaments for Water Detection in Composite J. Regnier, C. Campagne, É. Devaux and A. Cayla	21
Dispenser Printing with Electrically Conductive Microparticles E. Lempa, M. Rabe and L. Van Langenhove	31
Novel Knitting Vision - Modern Ways for Integral Knitting of Intelligent Gloves for Tactile Internet Applications F. Wieczorek, H. Winger, P.R.C. Böhnke, J. Wagner, E. Häntzsche, A. Nocke, I. Kruppke and C. Cherif	39
Development of Actuator Networks by Means of Diagonal Arrangements of Shape Memory Alloys in Adaptive Fiber-Reinforced Plastics M. Ashir, A. Nocke and C. Cherif	47
Effects of Stitch Density, Thread Tension and Using Conductive Yarn as Upper or Lower Thread on Reading Performance of Embroidered RFID Tag Antennas M.N. Duman, I. Usta and G.B. Esmer	55
Development and Durability Analysis of the Functionalized Fabric E. Mohsenzadeh, H. Gidik, D. Dupont, A. Hemberg and D. Lahem	63
Heating filament with Self-Regulation Temperature by Coating a Metallic Yarn with a Conductive Polymer Composite L. Marischal, A. Cayla, G. Lemort, V. Laurent, C. Campagne and É. Devaux	69
Melt Spinning of Elastic and Electrically Conductive Filament Yarns and their Usage as Strain Sensors H. Probst, J. Wollmann, J. Mersch, A. Nocke and C. Cherif	81
Polymer/CNT Composites and Filaments for Smart Textiles: Melt Mixing of Composites M. Kaplan, B. Krause and P. Pötschke	91
Dynamic Qualities of Smart Textiles: Study of Stimuli Magnitude with Chromic Pigments I. Cabral and A.P. Souto	97
Study on Electrical Characteristics of Flexible Textile Aluminium-Air Battery/Wetness Sensor and their Applications U. Briedis, A. Vališevskis and M.A. Carvalho	107
Improving Adhesion of Graphene Nanoplatelets to Cotton-Based Knitted Fabrics Using Plasma Treatment L.M. Arruda, I.P. Moreira, I. Boticas, J. Bessa and R. Figueiro	117
Curing Adhesives with Woven Fabrics Made of Polymer Optical Fibre and PET Yarn J. Kallweit, R. Seewald, M. Pätzelt, A. Schiebahn, U. Reisgen and T. Gries	129
EMI Shielding of the Copper/Nickel-Coated Polyester Nonwoven S. Palanisamy, V. Tunakova, Y.F. Wang, D. Karthik and J. Militký	137
Flexible Textile Printed Piezoresistive Pressure Sensors E. Osswald, H. Carvalho, I. Cabral, A.P. Souto and A. Cunha	143
Textile Heat Flux Sensor Used in Stress Detection of Children with CP F.Z. Tlemsani, H. Gidik, E. Mohsenzadeh and D. Dupont	153

Scalable Flexible Electromagnetic Interference Shielding Textiles Based on MWCNTs and PEDOT:PSS

A.R. Sousa, R. Matos, J.R.M. Barbosa, O.S.G.P. Soares, J. Ferreira, G. Santos, A. Silva, J. Morgado, P. Soares, S.A. Bunyaev, G.N. Kakazei, C. Freire, M.F.R. Pereira, A.M. Pereira and C. Pereira

161

Chapter 2: Technical Textiles and Fibers for Reinforcing Composite Materials**Tetrahedral Profiled Carbon Rovings for Concrete Reinforcements**

P. Penzel, M. May, L. Hahn, C. Cherif, M. Curbach and V. Mechtcherine

173

Spherically Curved Woven Fabrics - Shaping on the Loom

D. Nuss, M.Q. Pham, C. Sennewald, G. Hoffmann and C. Cherif

183

The Evaluation of Thermal Insulation Performances of 100% Recycled Thermoplastic Composites

M. Kucukali-Ozturk, I. Yalcin-Enis and H. Sezgin

197

Chapter 3: Modelling of Yarn Interaction and Textile Mechanical Behaviour**Mechanical Properties of Carbon Fiber Reinforced Composites Filled with Carbon Microparticles**

J. Novotná, B. Tomková and L. Výborný

205

An Alpha Finite Element Method for Linear Static and Buckling Analysis of Textile-Like Sheet Materials

N.T. Quyen, N.T. Quoc, N.D. Tru, A.J.P. Gomes and F.B.N. Ferreira

211

A Node-Based Strain Smoothing Technique for Free Vibration Analysis of Textile-Like Sheet Materials

N.T. Quyen, N.T. Quoc, N.D. Tru, A.J.P. Gomes and F.B.N. Ferreira

219

Simulation of Mechanical Behaviour of Woven Fabrics at the Scale of Yarns under Multi-Loading

N. Ogreni, G. Zavalani, L. Nikolla and A. Sinoimeri

227

CHAPTER 1:

Smart Textiles and Functional Fabrics

Development of a Testing Protocol to Assess the Washability of E-Textiles

Sigrid Rotzler^{1,a*} and Martin Schneider-Ramelow^{1,b}

¹Technical University Berlin, Microperipheric Center, Gustav-Meyer-Allee 25, 13355 Berlin, Germany

^arotzler@tu-berlin.de, ^bmartin.schneider-ramelow@tu-berlin.de

*corresponding author

Keywords: E-Textiles; electronic textiles, wash testing, test methods, standardization

Abstract. Most e-textiles are developed for wearable use and thus need to be washable to guarantee a textile typical usability. Yet, there are no e-textile specific wash testing standards and as a result, employed testing protocols vary greatly, resulting in a lack of comparability. To address this issue, an e-textile wash testing protocol modelled after testing methods provided by the standard ISO 6330 (the standard currently most often used as a basis for e-textile wash testing) as well as gentle household washing methods was developed and verified regarding its cleaning capability.

Introduction

A growing number of products incorporate electronic functionality into textiles. Many of these hybrid e-textiles are conceived as garments, intended to be worn on or near the body, and thus need to be washable to guarantee a textile typical usability [1]. To ensure such washability, e-textiles need to undergo wash testing during their development phase. To date, there is no e-textile wash testing standard. In the absence of such standards, testing is either done according to other standards, predominantly *ISO 6330 Textiles – Domestic washing and drying procedures for textile testing* [2], but also other textile standards (e.g. for colorfastness testing), under household washing conditions or with alternative methods (placing the samples in water with or without agitation) [3]. This variation in testing procedures limits comparability between tested e-textiles. The employed procedures are often not a good equivalent of actual washing procedures, and thus not necessarily suited for the assessment of washability under household washing conditions. The washing procedures in the most widely used standard *ISO 6330* differ from common household washing programs in length and structure [2, 4]. The applicability of the programs provided by the standard for e-textile wash testing has not yet been researched.

E-Textile Wash Testing Program

To test e-textiles for their washability in the absence of specific standards, a wash testing program that more closely resembles actual gentle household washing procedures was compiled. The testing program is based on a *delicates* household program – in line with a general consensus among experts that e-textiles should be washed gently [5]. This call for gentle washing conditions is further emphasized by results from previous wash testing – revealing mechanical action during washing to be the overall most damaging of the four *Sinner's washing factors* (duration, chemistry/biology, temperature, mechanical action) [1]. Other studies reach a similar conclusion [6, 7]. Thus, a suitable testing program is as gentle as possible while still offering a satisfactory cleaning capability.

A low washing temperature of 30°C is chosen for the test program, because some e-textiles are prone to damages after cyclical exposure to higher washing temperatures of 40°C and above. This is caused by a mismatch of the coefficient of thermal expansion between the involved materials (polymers, metallization layers, textile elements) [1]. Lower washing temperatures of 30°C and below are also generally advised for delicate laundry items [3] – among which e-textiles can be counted. The structure of the proposed testing program (modeled after a *silk/delicates* household washing program)

is the following: main wash cycle, followed by an intermediate spinning cycle (500 rpm), two rinsing cycles and a final spinning cycle (800 rpm). The total duration of the program is 40 min, with a washing temperature of 30°C and a water volume of 12l and on-time of the motor of 40% (both during main wash and rinsing).

As different types of e-textiles exhibit different vulnerabilities and requirements, one single washing program will not be enough for comprehensive e-textile wash testing. Especially for e-textiles with a medical or PPE application, industrial washing might be advised due to procedural and hygienic concerns. This research focuses on household wash testing for e-textiles. A single washing program is chosen that should be suitable for both e-textiles vulnerable to increased mechanical strain and those vulnerable to increased temperatures. For future standards, a range of different washing programs for different areas of applications for e-textiles will be advisable, though.

Cleaning Capability of Test Program

As the main aim of washing is the cleanliness of the laundry, a suitable testing program needs to exhibit sufficient cleaning capabilities for expectable soiling occurring during the use phase of e-textiles. The testing of cleaning capabilities of a washing program is done following *IEC 60456:2010 Clothes washing machines for household use – Methods for measuring the performance* [8]. According to this standard – used to assess washing machines – a given washing program has to be run with added stain stripes featuring five different stain types: *red wine, cocoa, blood, soot & mineral oil* as well as *sebum*. After one wash cycle, the cleaning capability of the reviewed washing machine is evaluated by comparing the remission value of each of the five stain swatches of the stain stripe with the results of a reference machine. The brighter the swatch, the cleaner. To adjust the standard's methods for the purpose of evaluating the cleaning capabilities of the compiled e-textiles testing program, a reference program from the range of household washing programs, *Easy Care*, was chosen instead of a reference washing machine. The choice of this reference program reflects the consensus of experts that e-textiles should be washed gently [1], with *Easy Care* being at the least gentle end of gentle household washing programs [4]. For greater comparison, *SportivePlus*, another household washing program potentially used by consumers to launder e-textiles – with many e-textiles being developed for sports applications – was tested against the compiled test washing program. To evaluate detergent suitability not only from the viewpoint of washing damage but also from a cleanliness angle, both detergents used in the following section (ECE (A) powder detergent without bleach and *Perwoll* liquid detergent) are tested with the test washing program.

Table 1: Washing programs for the assessment of cleaning capabilities

program	device	duration	mechanical action	chemistry
test program	Electrolux Wascator	40 min	800 rpm spin cycle 40% on-time	60 ml <i>Perwoll</i> liquid detergent
test program	Electrolux Wascator	40 min	800 rpm spin cycle 40% on-time	60 g ECE
<i>SportivePlus</i>	Siemens IQ 700	47 min	800 rpm spin cycle 60% on-time [4]	60 g ECE
reference program				
<i>Easy Care</i>	Siemens IQ 700	59 min	1200 rpm spin cycle 90% on-time [4]	60 g ECE

Table 1 gives an overview of the three different washing programs and the amount and type of detergent used. Although the IEC standard only covers *Cotton, Easy Care* and *Wool* washing programs, the applicability of the provided testing method for programs other than those mentioned in the standard – among them programs with the aim of gentle laundry treatment – has been previously

verified [4]. IEC 60456 was used as a basis, but changes were made to the provided test method due to available resources and infrastructure.

The following parameters were the same for all conducted tests:

- washing temperature: 30°C
- load: 2kg, consisting of 9 100% CO pillow cases (CO-base load items according to IEC 60456)
- supplier of stain strips: WFK Testgewebe GmbH
- number of stain strips per test cycle: 3
- number of wash cycles per program: 1
- water: tap water with hardness of 2,4 - 2,9 mmol/l [9]

After wash testing, the stain strips were air-dried and ironed according to standard protocols. Color evaluation was done using a *CM 3700 (Konica-Minolta)*. The remission values for each of the stain swatches from the compiled test washing program for both detergents as well as the *SportivePlus* program were compared to those of the *Easy Care* program used as a reference. If the color results sufficiently match those of the reference program, the cleaning capability for the respective stain type is comparable to the reference program. The tolerance formula employed by the software of the *CM 3700* is CMC 2:1 (Lab*/Distance/CMC 2:1/dE:1,00). If the color distance between a stain swatch and the corresponding reference swatch is within the tolerance, the result is registered as *pass*, otherwise as *fail*. Table 3 gives the results of the color comparison. The test program with the commercial liquid wool detergent exhibits reduced cleaning capabilities for all stain types compared to the reference program with the ECE standard detergent. Even the unstained swatch shows worse results, indicating that some of the soil from the stained swatches lead to discoloration of the clean swatch.

All except the *red wine* swatch for both the test program with ECE detergent and *SportivePlus* with ECE detergent show comparable values to *Easy Care*. The *blood* stain shows especially good results for both programs. *Cocoa* is cleaned slightly better by the *SportivePlus* program. These results indicate an almost identical cleaning capability for both the test program and *SportivePlus* compared to *Easy Care* – when using the same detergent. If possible use cases and the corresponding projected typical staining for e-textiles are taken into account (mainly medical, sports or PPE), the slightly lower cleaning capability for the *red wine* stain does not render the test program unsuitable. For sports, PPE and medical use cases, the stain swatches *sebum*, *soot & mineral oil* as well as *blood* are much more representative.

Table 2: Results of the cleaning capability test

program	detergent	stain type					
		unstained	sebum	soot & mineral oil	blood	cocoa	red wine
test program	<i>Perwoll</i>	fail	fail	fail	fail	fail	fail
test program	ECE	pass	pass	pass	pass	pass	fail
<i>SportivePlus</i>	ECE	pass	pass	pass	pass	pass	fail

The results of the stain stripe analysis indicate a sufficient cleaning capability of the compiled test program for e-textile specific use cases. The test program can thus be deemed suitable for washability testing for e-textiles. The liquid *Perwoll* detergent is inferior in its cleaning ability to the standard ECE powder detergent.

Evaluation of Suitable Detergent for E-Textile Wash Testing

Not only the washing program has to be suitable for e-textile testing, a fitting detergent has to be selected as well. The influence of different detergents on the washing reliability of e-textiles has not been researched to great extent. Gaubert et al. wash knitted conductive fabrics in four different ways:

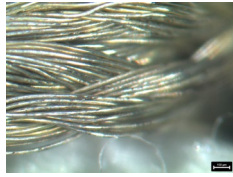
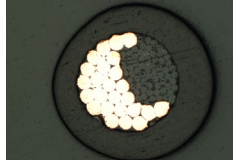
without detergent, with a household powder detergent (containing bleach), with a liquid household detergent (containing no bleach) and using only sodium percarbonate (a bleaching agent). With the sheet resistance as an indicator, the results are worst for the textiles washed with sodium percarbonate and the powder detergent, and best for the samples washed without any detergent. Those results indicate the damaging influence of bleaching components in the detergents for metallized textiles [10]. No conclusions can be drawn about the difference in suitability between powder and liquid detergents with similar ingredients. Other sources look into the difference of washing e-textiles with and without detergent, but don't compare different types of detergent [11, 12].



Figure 1: Types of conductive tracks used in detergent evaluation. Top: direct embroidery (DIR), middle: direct embroidery with non-conductive overlay (OVR), bottom: TFP embroidered sample (TFP).

As mentioned, for many e-textile washing tests, the standard *ISO 6330* is used as a basis. The standard includes three types of powder detergent of different composition for front loading, horizontal axis washing machines (the predominant type in Europe). Of those, reference detergent 3 (ECE (A)) resembles household (bleach free) color detergents if the separately packed bleaching agent and activator are not mixed in [2]. ECE (A) without bleach is the most commonly used detergent among researchers conducting e-textile washing tests according to *ISO 6330* [3]. To validate this detergent's suitability for e-textile testing, we compared washing results with the results of a common liquid, bleach-free household detergent for delicate laundry (*Perwoll* liquid wool detergent).

Table 3: Properties of conductive yarns

yarn	used in samples	construction	R [Ω/m]	yarn count/ diameter	picture
<i>Madeira HC 40</i>	DIR, OVR	silver coated nylon multifilament	< 300	290 dtex	
<i>Elektrisola</i> (custom made)	TFP	silver coated copper litz wires, aramid multifilament core, thermoplastic insulation	< 1	0,45 mm	

The detergents were tested with three different types of embroidered conductive tracks on plain woven cotton/linen substrate: direct embroidered tracks (DIR), direct embroidered tracks with protective, non-conductive embroidery overlay (OVR) and insulated litz wire embroidered using tailored fiber placement (TFP) (see Fig. 1). All embroidery was performed on a ZSK industrial embroidery machine. Both DIR and OVR samples were embroidered with *Madeira HC40* conductive embroidery thread. For increased reliability and conductivity [13], the embroidery for each track did not consist of a single line but three narrow zig-zag lines on top of each other. In the OVR samples, the tracks were covered with a second embroidered layer, non-conductive thread in a broad, tight zig-zag pattern. Results from Ankhili et al. suggest that this type of embroidered overlay leads to better protection from washing damage than a laminated polyurethane foil coating [14]. The TFP samples were made with litz wire from *Elektrisola*, consisting of 25 silver-coated copper micro-wires wrapped around an aramid fiber core and coated with an insulating thermoplastic extrusion. All samples were contacted using snap buttons. For the TFP samples, the end of the litz wires were stripped of their insulation prior to contacting. Table 3 gives the properties of both conductive yarns used. Initial fabric size for each sample was 40 x 20 cm², embroidery was done only on one half of the fabric. After embroidering, the fabric was folded into a size of 20 x 20 cm² and serged around the edges.

Table 4: Mean values for relative change in resistance after washing for liquid detergent (L) and powder detergent (P)

cycle	R _{rel}					
	DIR-L	DIR-P	OVR-L	OVR-P*	TFP-L	TFP-P
1	1,14	1,30	1,12	(1,13) 1,79	1,25	1,00
5	2,42	2,50	1,51	(1,44) 2,33	1,33	1,08
10	5,37	4,35	1,91	(1,81) 3,00	1,25	1,03

* with and (without) third sample

For each type of conductive track, a total of 6 samples were produced, three for each type of detergent. Apart from the self-compiled washing program, the wash testing was done using *ISO 6330* as a basis. To achieve a total load of 2 kg, PES and CO base load items were added to the samples. According to the standard, 20g of detergent should be used for each cycle. As the standard also calls for water of an unavailable low hardness of 0,7 mmol/l, the amount of detergent was adjusted to 30g to factor in the higher local water hardness [4,9]. For each the ECE powder detergent (P) and the liquid *Perwoll* (L), 10 wash cycles were run. After each cycle, the samples were air dried overnight. To assess the damage after washing, the resistance of each conductive track was measured before the first washing cycle (R_0) and again after each of the ten washing cycles (R_n). The relative change in resistance $R_{rel,n}$ was used as an indicator of washing damage, with

$$R_{rel,n} = R_n/R_0. \quad (1)$$

Table 4 gives the mean values for R_{rel} for all six tracks of each embroidery type and detergent combination after 1, 5 and 10 cycles. Compared to the direct embroidery samples (DIR and OVR), the resistance increase of the TFP samples is much lower. Due to the protective thermoplastic insulation of the Elektrisola thread used in the TFP samples, abrasion and other mechanical wear during washing is reduced, leading to fewer damages. In line with the results from Ankhili et al. [14], the non-conductive overlay in the OVR samples also has a protective quality, leading to a slower resistance increase in the OVR samples compared to the unprotected DIR samples. For all three sample types, the values for the standard powder detergent show slightly better results than the liquid detergent. One of the OVR-P samples exhibited significantly worse results than the other samples, possibly a result from damages during sample production. If the results of this sample are included, the OVR-P results are slightly worse than the OVR-L results. Omitting the sample leads to similar results for both detergents, slightly better for ECE. A failure analysis using SEM imagery shows that both detergents lead to a comparable amount of loss of silver coating in the DIR samples (see figure 2).

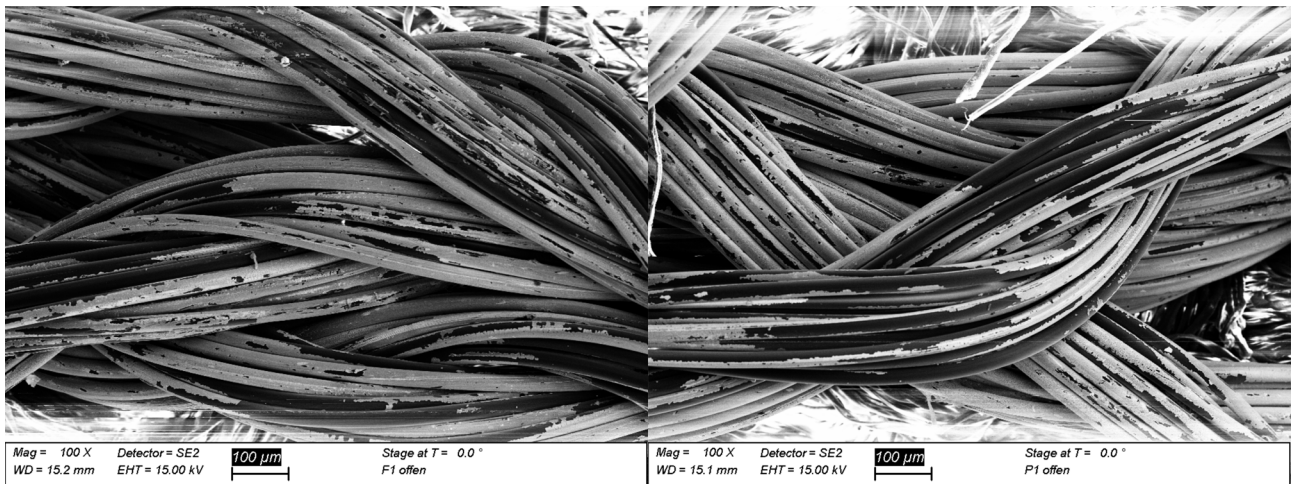


Figure 2: SEM-image of loss of silver coating after 10 wash cycles in DIR test sample. Left: liquid Perwoll detergent, right: ISO 6330 standard powder detergent.

Overall, this indicates a good suitability of the ECE (A) detergent from *ISO 6330* for e-textiles wash testing: the use of this detergent does not lead to an increased washing damage compared to a household detergent for gentle laundry care. Considering also the significantly worse results for *Perwoll* in terms of cleaning capability, the ECE detergent is the preferable testing detergent of the two. Another reason to choose the standard detergent over the commercial one is the unchanging ratio and type of ingredients, as the exact detergent composition is specified in the standard. This guarantees a better replicability of washing results than for commercial detergents whose ingredients can be changed at will by the manufacturer.

Testing Protocol for E-Textiles

Based on the results of the washing capability testing and the research into the detergent influence, the following wash testing protocol is proposed for e-textile washing reliability testing:

- washing program: main wash, intermediate spinning (500 rpm), two rinsing cycles, spinning (800 rpm). Duration: 40 min; temperature: 30 C; on-time: 40%; water volume: 12l.
- load*¹: additional PES base load items for a total of 2 kg, test samples should not account for more than half of the total load.

¹ * indicates testing procedures in accordance with the standard *ISO 6330*

- drying*: air drying.
- detergent*: 20 g of ECE-2 standard powder detergent (if necessary due to higher water hardness, adjust amount accordingly)
- number of cycles: according to application scenario of tested e-textiles.

To assess the washability of the tested e-textiles, a suitable parameter (e.g. change in resistance, change in function ...) has to be determined before testing. The most suitable parameter or parameters will depend on the application and composition of the tested e-textile. Depending on the total number of cycles, the test for a change in the chosen parameter can be done after each washing cycle or only after specified cycles.

Summary

The presented research provides a wash testing method for e-textiles that considers both the susceptibility of many e-textile systems to high mechanical wear and washing temperatures as well as the requirement for a suitable test method to show a sufficient cleaning capability. The study shows that (with similar ingredients), ISO 6330 powder detergent will not lead to more damages than liquid household detergent, making it the preferable testing detergent of the two, due to its superior cleaning capability and standardized composition. Creating a suitable e-textile wash testing protocol can alleviate the current very high variation in testing practices and can enable comparable washability assessments for different e-textiles.

References

- [1] S. Rotzler, C. Kallmayer, C. Dils, M. von Krshiwoblozki, U. Bauer, and M. Schneider-Ramelow, Improving the washability of smart textiles: influence of different washing conditions on textile integrated conductor tracks, *J Tex Inst* 111.12 (2020) 1766–1777. Doi: 10.1080/00405000.2020.1729056.
- [2] ISO 6330:2012 Textiles – Domestic washing and drying procedures for textile testing, International Organization for Standardization, Geneva, 2012.
- [3] S. Rotzler, M. von Krshiwoblozki, and M. Schneider-Ramelow, Washability of e-textiles: current testing practices and the need for standardization, *Text Res J* (2021), pp. 1-17. Doi: 10.1177/0040517521996727
- [4] S. Rotzler, Evaluierung bestehender Prüfmethode zur Wäscheschonung & deren Anwendbarkeit auf Sonderprogramme, Bachelorthesis, Hochschule für Technik und Wirtschaft Berlin, Berlin, 2017.
- [5] S. Rotzler, Einfluss der Sinnerschen Faktoren sowie der textilen Substrate auf die Waschbarkeit textilintegrierter Leiterbahnen, Masterthesis, Hochschule für Technik und Wirtschaft Berlin, Berlin, 2018.
- [6] Q. Li and X. M. Tao, Three-dimensionally deformable, highly stretchable, permeable, durable and washable fabric circuit boards, *Proc R Soc A* 470 (2014) 20140472. Doi: 10.1098/rspa.2014.0472.
- [7] S. uz Zaman, X. Tao, C. Cochrane, and V. Koncar, Understanding the Washing Damage to Textile ECG Dry Skin Electrodes, Embroidered and Fabric-Based; set up of Equivalent Laboratory Tests, *Sensors* 20(5) (2020) 1272. Doi: 10.3390/s20051272.
- [8] IEC 60456:2010 Clothes washing machines for household use - Methods for measuring the performance, International Electrotechnical Commission, 2010.
- [9] Berliner Wasserbetriebe, Water Hardness Information, <https://www.bwb.de/de/analysedaten-nachpostleitzahlen.php> (2020).

- [10] V. Gaubert, H. Gidik, N. Bodart, and V. Koncar, Investigating the Impact of Washing Cycles on Silver-Plated Textile Electrodes: A Complete Study, *Sensors* 20 (2020) 1739. doi: 10.3390/s20061739.
- [11] H. Gui, S. Tan, Q. Wang, Y. Yu, F. Liu, J. Lin, and J. Liu, Spraying printing of liquid metal electronics on various clothes to compose wearable functional device, *Sci China Technol Sci* 60(2) (2017) 306–316. doi: 10.1007/s11431-016-0657-5.
- [12] J. Virkki, T. Björninen, T. Kellomäki, S. Merilampi, I. Shafiq, L. Ukkonen, L. Sydänheimo, and Y. Chan, Reliability of washable wearable screen printed UHF RFID tags, *Microelectron Reliab* 54 (2014) 840–846. doi: 10.1016/j.microrel.2013.12.011.
- [13] S. uz Zaman, X. Tao, C. Cochrane, and V. Koncar, Launderability of Conductive Polymer Yarns Used for Connections of E-textile Modules: Mechanical Stresses, *Fibers Polym* 20(11) (2019) 2355–2366. doi: 10.1007/s12221-019-9325-x.
- [14] A. Ankhili, S. uz Zaman, X. Tao, C. Cochrane, V. Koncar, and D. Coulon, Washable embroidered textile electrodes for long-term electrocardiography monitoring, *Text Leather Rev*, 2(3) (2019) 126–135. doi: 10.31881/TLR.2019.27.

Protective Coating for Electrically Conductive Yarns for the Implementation in Smart Textiles

Philippa Ruth Christine Böhnke^{1,3,a*}, Hans Winger^{1,3,b},
Florian Wiczorek^{1,3,c}, Mareen Warncke^{1,d}, Lisa-Marie Lüneburg^{2,3,e},
Iris Kruppke^{1,3,f}, Andreas Nocke^{1,3,g}, Eric Häntzsche^{1,3,h},
and Chokri Cherif^{1,3,i}

¹Institute of Textile Machinery and High Performance Materials,
Technische Universität Dresden, 01069 Dresden

²Institute of Machine Elements and Machine Design,
Technische Universität Dresden, 01069 Dresden

³Centre for Tactile Internet with Human-in-the-Loop (CeTI),
Technische Universität Dresden, 01069 Dresden

^aphilippa.boehnke@tu-dresden.de, ^bhans.winger@tu-dresden.de,

^cflorian.wiczorek@tu-dresden.de, ^dmareen.warncke@tu-dresden.de,

^elisa.lüneburg@tu-dresden.de, ^firis.kruppke@tu-dresden.de, ^gandreas.nocke@tu-dresden.de,

^heric.haentzsche@tu-dresden.de, ⁱchokri.cherif@tu-dresden.de

Keywords: silver plated, polyamide yarn, embroidery, resistance, mechanical impact, textile sensor

Abstract. The Cluster of Excellence “Centre for Tactile Internet with Human-in-the-Loop (CeTI)” [1] deals with developments and inventions concerning smart devices used in many fields, e.g. industry 4.0, medicine and skill learning. These kind of applications require smart devices, sensors, actors and conductive structures. Textile structures address these applications by meeting requirements such of being flexible, adaptable and wearable.

Within this paper, the development of a protective coating for electrically conductive (EC) yarns is captured. These EC yarns are nowadays often used for smart textile applications. One challenge in their application is the integration into textile structures. Often, the handling and usage of EC yarns leads on the one hand to damages on the surface of the yarn and on the other hand to reduced electromechanically characteristics. This paper aims to characterize these EC yarns in regard to develop a suitable protective coating based on polypropylene (PP). To achieve this development, an extensive characterization of the EC yarns as well as the protective coating itself is important. The surface free energy (SFE), the topographical and the chemical characteristics are necessary for developing a suitable protective coating. However, the yarns are characterized before and after implementation into the textile structure and furthermore after the coating respectively with the developed finish.

Introduction

Smart textiles gain more and more interest and applications in our society. By implementing electronic components into textile garments and technical textiles, these products are created. One application of sensor yarns is the implementation in smart textiles i.e. in sportswear, health care and work safety [2]. Here, they can be used as elastic or stretchable sensors [3]. To make these electrical components combinable with our everyday live and with the handling in production is a big challenge [2]. The electronic components implemented in textiles have different functions and forms. Moreover, they can be classified into sensing and actuating units. Electrically conductive (EC) materials in yarn shape dominate the first group. Here, different materials like stainless steel, core-sheath yarns and wrapped metal yarns are first thought products [2, 4, 5]. These yarn shaped sensors can be implemented via knitting, weaving or embroidery [2, 6]. Another method to create EC components in or on textiles is a functionalized surface. Methods are e.g. chemical metallization or etching. Further methods are printing [6], coating and lamination of electrical conductive materials [2, 4, 5].

EC materials are metals, polymers (intrinsic or extrinsic) [5], filaments and fibers e. g. carbon fibre and stainless steel yarn [2]. Additionally, the attention of this paper lies on polymeric metal-plated yarns. Despite the following section deals with state of the research of EC materials shaped like yarn or even beeing yarn. Beside silver-plated EC yarns, there are also other yarn-shaped EC structures. Uzun *et al.* developed a cellulose yarn coated with MXene. MXene are two-dimensional transition metal carbides and nitrides, they are highly electronically conductive [7]. Furthermore, Islam *et al.* developed flexible melt spun thermoplastic EC yarns based on polypropylene (PP) and polylactid acid (PLA), coated with polydopamine (PDA) and poly(3,4-ethylenedioxy thiophene): poly(styrenesulfonate) (PEDOT:PSS) [4].

Metallized yarn offer currently the smallest and most flexible EC structures on textile basis. Because of their textile basis they can be more easily integrated by typical textile technologies i.e. knitting, weaving or embroidery. Nevertheless, the protection of the EC yarn or textile structure is challenging. Through the sizing/avivage of the producer and the surrounding textile, the EC yarn has a minimum of protection. However, the used textile technologies and the daily usage of the smart textiles gives high mechanical impact on the EC yarn. The impact causes abrasion and the resistance of the EC yarn increases and electrical conductivity decreases.

To analyse the origin of these damages various research projects have been done. Ismar *et al.* analysed the effect of water and chemical stresses on silver-plated polyamide (PA) yarns. They state that washing of *e*-textiles is one of the major hurdles that have to be faced nowadays. Additionally, it is proven by FTIR-ATR, UV-Vis spectroscopy and electrical resistance measurement that water damages the yarn more than the washing detergent does. The damage is originated in the removal of the silver layer in water and washing detergent solution [8]. Conductive structures, which are available on the market such as silver-coated yarns, do not have enough abrasion resistance for the implementation via knitting in an industrial scale. Furthermore, they are damaged via the usage in smart textiles by wearing, washing and drying [2]. To protect these yarns against the mechanical impact arose by these scenarios a protective coating should be developed. Next to this, research has been done concerning the protection of metal-plated EC yarns. Baribina *et al.* examined a water-repellent coating for PA yarn plated with silver. The analyses are fulfilled with textured and non-textured yarn and the coating should improve the conductive behaviour after several washing cycles to further improve the lifetime of the product. To achieve this, a silicone and nano-coating are used and applicated with a brush directly and discontinuous on the fiber [9]. Within another project a protective coating out of PP for PA yarns plated with silver is developed. Alagirusamy *et al.* used PP staple fibers to wrap around silver-coated yarns. Afterwards the yarns is put in the oven and the PP is melted to an homogenous sheath [10]. Further, Raja *et al.* used poly vinyl pyrrolidone (PVP) for stabilization of silver nanoparticles in watery solutions as well as for the application on textiles. Within this work the used substrates are wool and cotton based and the application is microbial resistance [11]. On the market exists one yarn produced by Statex, which is covered in thermoplastic polyurethane (TPU). However, this protection is made in shape of a loose shell with no mounting on the EC yarn. To increase the protection against mechanical impact via implementation, wearing, washing and drying this paper claims that a direct coating has to be brought onto the fiber. So within this paper a development or rather application of suitable coating should be made, that has good adhesion to TPU or better is directly applicated onto the silver-coated PA and would lead to higher abrasion resistance and with that better processability.

A protective coating has to meet some requirements besides the later on application of the conductive yarn concerning the implementation and usage. The coating should not obstruct the EC characteristics. Moreover, the coating should be temperature stable and glideable or should show less frictional resistance to guarantee good processability in textile processes. Furthermore, the coating should have sufficient elasticity but at the same time sufficient adhesion to the silver layer on the PA yarn. Finally, the coating should be isolating or electrical conductive depending on the use case.

For usage with the silver-coated polymeric yarns, the coating should be non-abrasive, strong but also flexible. For the appliance, the process temperatures for the coating should not be higher than

the glass temperature of the polymeric material of the yarn. Therefore, the coating materials have to be melted underneath this temperature or should be applicable as a solution.

In preliminary studies, various polymeric materials are tested as coating for EC yarns. During these tests, waxes became of major interest in particular as watery emulsions. At first, PP is chosen as basis for the coating due to their excellent characteristics concerning temperature resistance, strength and availability. However, PP does not fulfil all set requirements for the coating. The most disadvantageous characteristic of PP is its inelasticity. To weaken this characteristic in the final coating and to ensure the usability especially in smart textiles a further polymer (polyethylene (PE)) and an additive (glycerine) are added.

To determine the impact of the coating the optical analysis (light and scanning electron microscopy) and resistance measurement are used to analyse the reference yarns in comparison to the coated yarns. Furthermore, the reference yarns are characterized concerning their surface energy with tensiometric analysis and their chemical composition is analysed with Fourier-transformed infrared spectroscopy. In addition, the coating is analysed with these two methods but also with thermogravimetric analysis.

Methods and Materials

Silver-plated yarns. In Table 1 the yarn materials are shortly presented due to their characteristics given by producer. All yarns are PA 6.6 based and plated with silver.

Table 1. Electrically conductive yarns used as basis material

Producer	Name	Abbreviation	Composition	Titer [dtex]	Resistance [$\Omega \cdot m^{-1}$]
Madeira	HC40	HC40	PA 6.6	117x2	< 300
Statex	Shieldex 117/17 dtex 2PLY HC+B	S HC+B	PA 6.6	117/17 x2	< 300
Statex	Shieldex 117/17 dtex 2PLY	S	PA 6.6	117/17 x2	< 1500

Coating materials. The following table shows the used components for the coating.

Table 2. Components used for the coating

Producer	Name	Material composition
Deurex AG	P 3601 W	Water-based emulsion of PP wax
	EO 4001 W	Water-based emulsion of oxidized wax
Carl Roth GmbH + Co KG	Solvagreen	Glycerine, $\geq 98\%$ water free

Coating process. The coating has a basis of PP wax solved in a watery emulsion combined with a watery emulsion of PE and as slip additive glycerine. The two wax emulsions are each added with an amount of 49 vol.-% while the glycerol is added with 2 vol.-%. The coating is stirred with a magnetic stirrer for 30 minutes at room temperature with a stirring rate of 180 rpm.

With the Lab Foulard HVF from Mathis AG (Oberhasli, Swiss) the yarns are coated with a barrel speed of $2 \text{ m} \cdot \text{min}^{-1}$ and a barrel pressure of 1 bar. For leading the yarns through the coater, a yarn tube is placed above the barrels. After the yarns went through the barrels, they are wound on cardboard tubes for drying under constant conditions in a drying cabinet at $30 \text{ }^\circ\text{C}$ for about 30 minutes.

Contact angle measurement. With the contact angle measurement, the surface free energy (SFE) of the reference yarns is calculated and assessed. Later, also the coatings SFE is determined and theoretical compatibility of both, yarn and coating is compared.

The EC yarns are measured using Washburn method also known as capillary method. Here, the yarn is cut into small pieces with a length of about 5 mm. Afterwards these short fibers are filled into a glass and metal sample holder with a filter paper at the bottom. The sample holder then is put into n-hexane ($>99\%$, Carl Roth GmbH + Co KG (Karlsruhe, Germany), surface tension at $23 \text{ }^\circ\text{C}$, $18.40 \text{ mN} \cdot \text{m}^{-1}$) to determine the capillary constant. Afterwards, the measurement is performed with a minimum two different test liquids. These test fluids are deionized water (surface tension at $23 \text{ }^\circ\text{C}$, $72.8 \text{ mN} \cdot \text{m}^{-1}$) and diiodomethane ($>99\%$, Sigma-Aldrich Chemie GmbH (Darmstadt, Germany),

surface tension at 23 °C, 50.8 mN·m⁻¹). The performed measurement is static and takes 120 s. Per sample five measurements are performed. As mentioned before the coating is also characterized via tensiometric analysis. The measurement is static and sessile drop method is used. For this, the coating is prepared as a film on a glass objective. The film is dried for 24 hours at room temperature.

The measurement is performed following DIN 55660-2 with a minimum of two test fluids (deionized water and diiodomethane). The method of Owens, Wendt, Rabel and Kaeble (OWRK) is used to determine the polar and disperse part of SFE of the specimen [12,13]. Eq. 1 describes the relation of the contact angle and polar and disperse surface tensions:

$$\frac{(1 + \cos \theta) \cdot \sigma_l}{2 \cdot \sqrt{\sigma_l^D}} = \sqrt{\sigma_s^P} \cdot \sqrt{\frac{\sigma_l^P}{\sigma_l^D}} \quad (1)$$

The contact angles (θ) are used to calculate the SFE. Furthermore, the polar (σ_P) and disperse (σ_D) parts of the SFE are determined with this formula. The indices l and s are describing the liquid and solid states, from i.e. the test liquid and the filament surface. Krüss Force Tensiometer K100 (Hamburg, Germany) is used to determine the contact angles between the test liquids and the yarns and Drop Shape Analyzer (DSA) 100 from Krüss is used for the SFE measurement of the coating. The Software Advance from Krüss GmbH (Hamburg, Germany) is used to perform the measurement and to calculate the SFE from the contact angles.

Resistance measurement. The determination of the electrical resistance is used to quantify and assess the conductive behavior of the yarns before and after being coated and as well after being mechanically demanded. The measurement is performed with a self-constructed four-terminal sensing measuring station with a specimen length of 500 mm ten times per specimen. To define the values of the measurements a voltmeter (2) and a constant current source (1) are used. The specimen (3) is contacted via four Kelvin clamps (4). Fig. 1 below shows the circuit diagram of the measuring station.

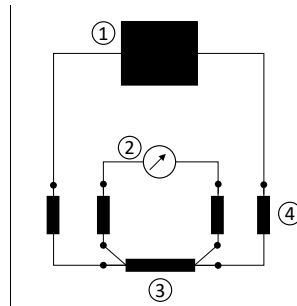


Fig. 1. Four-terminal sensing measuring station

Optical analysis. The evaluation of the yarns surface is determined with the light microscope (LM) Scope A.1 Axio from Carl Zeiss Microscopy Deutschland GmbH (Oberkochen, Germany) with incident light. The measurement of the diameters is performed with the software Zen2Core from Zeiss and five measurements per sample are made. Further, a scanning electron microscope (SEM) Quanta 250 FEG SEM from FEI (Hillsboro Oregon, United States of America) with the magnitudes 500 and 1000 is used.

Fourier-transformed infrared spectroscopy. Fourier-transformed infrared attenuated total reflection (FTIR-ATR) spectroscope Nicolet 6700 from Thermo Fisher Scientific GmbH (Waltham, Massachusetts, United States of America) with a diamond is used for the determination of the yarns composition.

Thermogravimetric Analysis. Thermogravimetric analysis (TGA) is performed with TGA Q500 from TA Instruments (New Castle, Delaware, United States of America). Measurements are done in nitrogen atmosphere from 30 °C to 350 °C in high-resolution mode.

Proof of concept – embroidery. To examine the developed coating a proof of concept was performed. Within this investigation the silver-plated and coated yarn was threaded through all guiding elements of the embroidery plant F-Kopf from ZSK Stickmaschinen GmbH (Krefeld,

Germany). Part of the guiding elements are the preload clamp, main road roller, thread take-up lever, fabric pusher and needle.

Results

Composition. Fig. 2 shows the FTIR-ATR spectra of the yarns references. At approximately 3300 cm^{-1} and 3100 cm^{-1} , the samples of HC40 and Statex show stretching vibration of N-H group. The band round 3000 cm^{-1} hints towards stretching vibrations of C-H groups as well as the band at 2850 cm^{-1} . At approximately 1700 cm^{-1} , the stretching vibration of C=O bond can be found. The bands at 1500 cm^{-1} and 1600 cm^{-1} hint towards C=C bonds. These, in turn, are hinting towards the amide groups of the PA. The band at approximately 1250 cm^{-1} is suggesting again a C-N stretching vibration hinting towards amide groups.

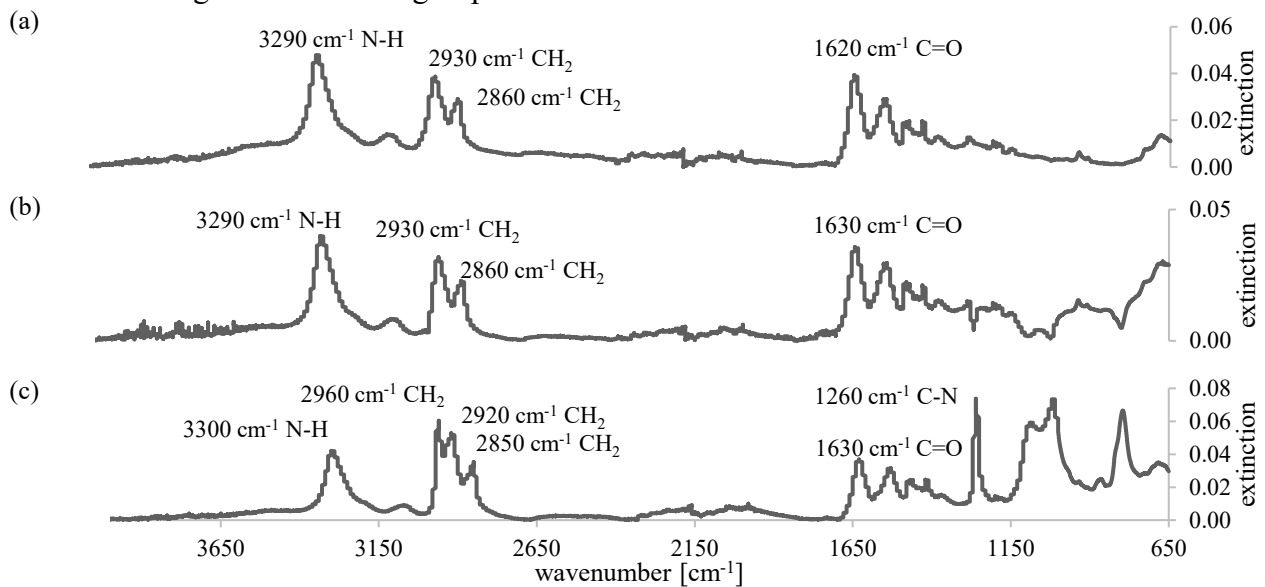


Fig. 2. FTIR-ATR spectroscopy of reference yarns (a) S, (b) S HC+B and (c) HC40

Surface characteristics. Table 3 shows the values determined with the Washburn method via tensiometric analysis for the yarns reference. On the first sight, it is obvious that the SFE of all reference yarns have similar values of about 21 to $23\text{ mN}\cdot\text{m}^{-1}$. Furthermore, all samples show small deviations and even polar and disperse parts of the yarns have similar values. Overall, the polar part of the yarns is smaller than the disperse ones.

Table 3. Surface free energy of yarns reference determined with WASHBURN method

	S	S HC+B	HC 40
SFE, total [$\text{mN}\cdot\text{m}^{-1}$]	21.96 ± 0.22	22.99 ± 0.68	20.98 ± 0.50
SFE, disperse [$\text{mN}\cdot\text{m}^{-1}$]	15.58 ± 0.16	16.82 ± 0.45	13.83 ± 0.50
SFE, polar [$\text{mN}\cdot\text{m}^{-1}$]	6.37 ± 0.07	6.17 ± 0.23	7.15 ± 0.03

Table 4 shows the measured contact angles from the reference yarns to the test liquids (diiodomethane and water). Here, the yarns show similar values concerning the contact angle to water. The contact angles to diiodomethane are slightly smaller than the ones to water. Looking at Table 3 with increasing contact angle to diiodomethane the disperse part of the SFE decreases.

Table 4. Contact angles of yarns reference determined with WASHBURN method

	S	S HC+B	HC 40
water [$^{\circ}$]	89.91 ± 0.03	89.23 ± 0.31	89.92 ± 0.03
diiodomethane [$^{\circ}$]	83.82 ± 0.32	81.32 ± 0.90	87.50 ± 0.77

Further, the references are characterized optically with LM and SEM. The following images in Fig. 3 are taken with a magnitude of 500. On each of the yarns surfaces particles, small abrasions and damages can be seen. S yarn (Fig. 3 (a)) shows the smoothest surface compared to the other yarns.

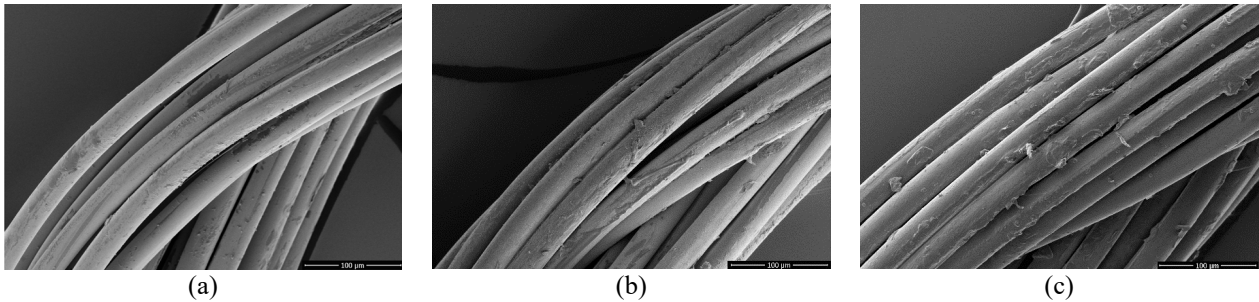


Fig. 3. Scanning electron microscopy images of (a) S, (b) S HC+B and (c) M HC40

The images are showing no obvious difference concerning the diameter of the filaments comprised in the yarns. Table 5 shows the diameters of the yarns.

Table 5. Filament diameter of reference yarns

Yarn	Diameter of filament [μm]
HC40	28.53 ± 0.82
S HC+B	27.64 ± 0.78
S	28.18 ± 0.73

The surface of the coated yarns is analysed with the LM. The following images (Fig. 4 (a) to (c)) show the coated yarns surface. Because the coating has no opaque colour, the yarns look similar to the reference. Furthermore, the coating is very thin, so the silver-plating is still visible.

Moreover, SEM images with a magnitude of 1000 of the coated yarns are shown in Fig 4 (d) to (f). Here, S yarn shows the smoothest surface with fewest deposits. S HC+B shows some small deposits on the surface but simultaneous the coating builds a closed surface around the filaments of the yarn. In contrast, the coating seems very brittle on the HC40 yarn. It is visible that the yarn is coated but there are gaps between the single filaments of the yarn and deposits on the filaments surface.

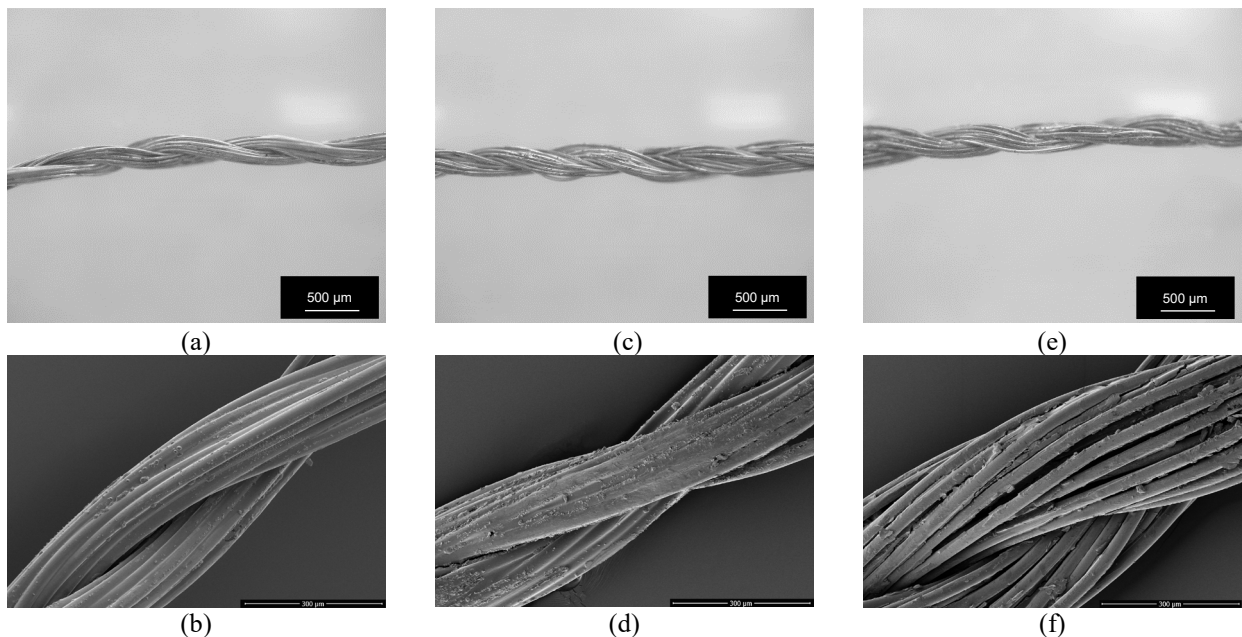


Fig. 4. LM and SEM images of coated yarns: (a) and (b) S, (c) and (d) S HC+B and (e) and (f) HC40

Furthermore, the coated and embroidered yarns are also characterized using LM. Fig. 5 shows the images of all three yarns. Both Statex yarns show almost smooth surface while HC40 shows a damaged surface.

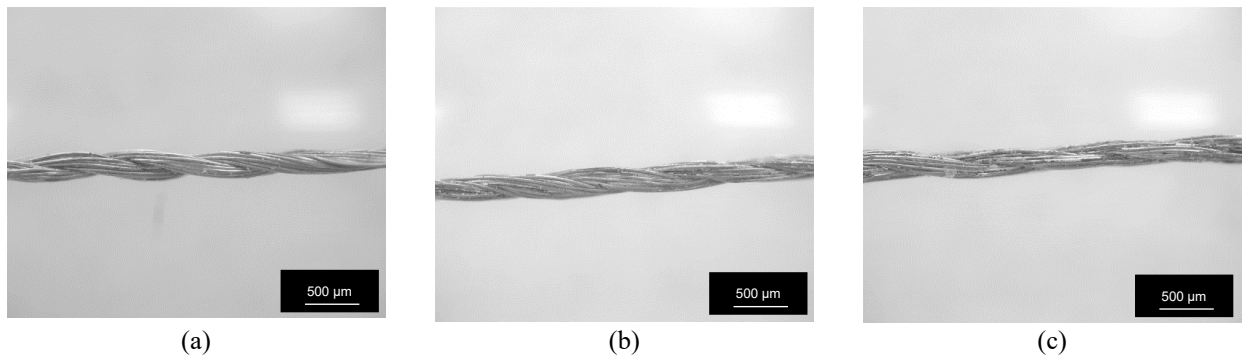


Fig. 5. LM images of coated and embroidered yarns: (a) S, (b) S HC+B and (c) HC40

Electrical characteristics. Table 6 shows the electrical resistance values of the reference, embroidered, coated and embroidered and coated yarns. The second column constitutes the results of the reference yarns. S yarn from Statex shows the highest resistance with a value of $293.20 \pm 13.07 \Omega \cdot \text{m}^{-1}$. The lowest value is represented by S HC+B with a value of $143.98 \pm 3.83 \Omega \cdot \text{m}^{-1}$. HC40 occurs with a resistance of $163.98 \pm 1.96 \Omega \cdot \text{m}^{-1}$. While the two last named yarns show very small deviation the deviation of S yarn is higher, but within the confidence interval with 4.67%.

S yarn after being embroidered exhibits a resistance of $833.00 \pm 237.04 \Omega \cdot \text{m}^{-1}$, which leads to an increase of 284% compared to the reference. S HC+B has a resistance of $215.40 \pm 14.62 \Omega \cdot \text{m}^{-1}$ which is about 150% of the reference. Finally, HC40 has a value of $210.40 \pm 4.80 \Omega \cdot \text{m}^{-1}$ which is about 128% of the reference value (Table).

The resistance of the coated yarns is also determined with the four-terminal sensing measurement set-up (Table 6). S yarn increased about 2.17% to a value of $299.57 \pm 8.52 \Omega \cdot \text{m}^{-1}$ while S HC+B decreased about 20.68% to a value of $114.21 \pm 20.61 \Omega \cdot \text{m}^{-1}$. HC40 increased about 24.36% to a value of $203.79 \pm 20.07 \Omega \cdot \text{m}^{-1}$. In contrast to the values of the reference, the coated yarns show a higher deviation. Just S yarn shows smaller deviation than the reference.

Finally, the resistance of the coated and embroidered yarns is measured with the four-terminal sensing measurement set-up. HC40 shows the lowest resistance with an increase compared to the embroidered reference of about 133%. After S HC+B firstly decreased the resistance now increases compared to the embroidered reference of about 160%. S yarn shows also embroidered the highest value but compared to the embroidered reference it is 56% lower.

Summed up S yarn shows within the references the highest resistance value while S H+B and HC40 are similar in resistance. Furthermore, the resistance of all reference yarns increases after embroidery, headed from S yarn. The coating has little impact on S yarn, decreases the resistance of S HC+B while the resistance of HC40 increases. After being embroidered S yarn shows the lowest increase of resistance followed by HC40 and S HC+B.

Table 6. Resistance of reference, coated yarns and embroidered yarns

Yarn	Resistance [$\Omega \cdot \text{m}^{-1}$]			
	Reference	Embroidered	Coated	Coated and Embroidered
S	293.20 ± 13.70	833.00 ± 237.04	299.57 ± 8.52	467.79 ± 79.09
S HC+B	143.98 ± 3.83	215.40 ± 14.62	114.21 ± 20.61	344.94 ± 50.57
HC40	163.87 ± 1.96	$210.40 \pm 4,80$	203.79 ± 20.07	280.77 ± 39.09

Coating – composition. To characterize the chemical composition of the final polyolefin based coating it is analysed with FTIR-ATR spectroscopy. Fig. 6 shows the spectrum of a dried sample of (a) the coating, (b) the PE wax and (c) the PP wax. The band at 2950 cm^{-1} gives a hint on asymmetrical stretching of CH_3 and occurs in Fig. 6 (a) and (c) as the methyl group of PP. Furthermore, the band at approximately 2920 cm^{-1} depicts asymmetric stretching of CH_2 and is part as well in PE and PP. Next to this distinctive peak at 2850 cm^{-1} hints towards symmetric stretching of CH_2 and furthermore towards the methylene group of PE. The band at 1460 cm^{-1} depicts bending deformation caused from the PE and the band at 1380 cm^{-1} depicts symmetrical deformation bending of CH_3 caused by PP

parts. A further band within the finger print area at 837 cm^{-1} points on rocking of C-C bonds evoked by PP.

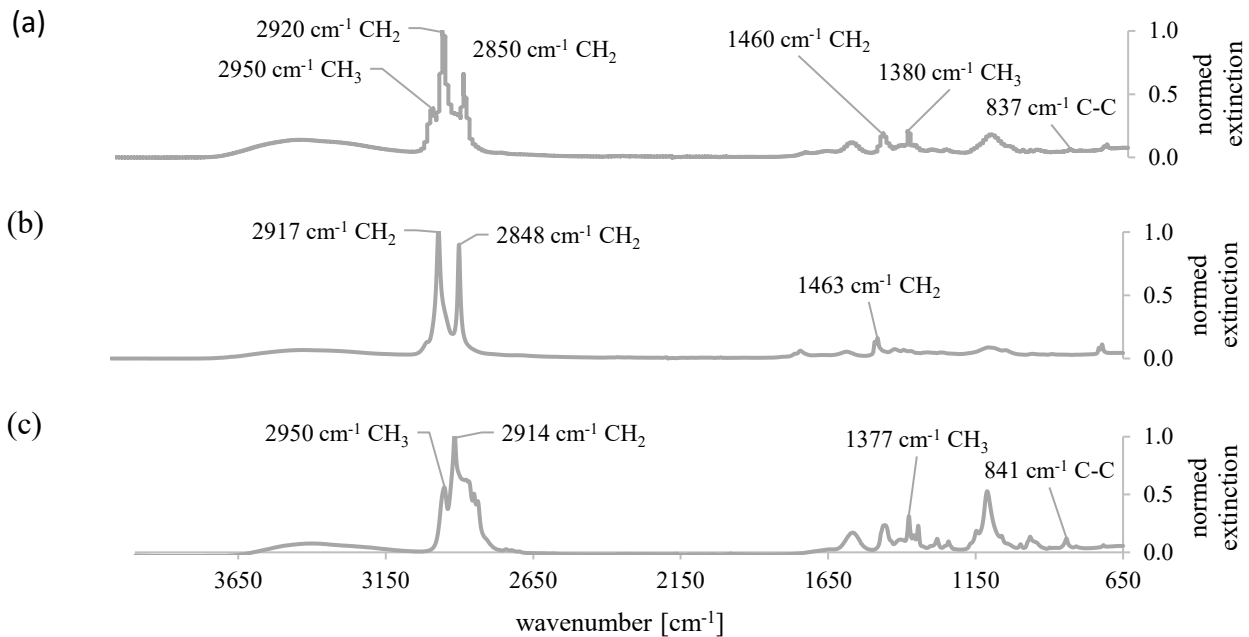


Fig. 6. FTIR-ATR spectrum of the (a) developed coating. (b) *E 4001 W* and (c) *P 3601 W*

Coating. Fig. 7 shows the result of a TGA made of the developed dried coating. At a temperature of $330\text{ }^{\circ}\text{C}$, there is a residue of 87.08% . The first mass loss emerges with 1.41% ending at $109.99\text{ }^{\circ}\text{C}$. Further mass loss of 1.38% ends at $159.90\text{ }^{\circ}\text{C}$. The biggest mass loss occurs with 6.82% ending at $289.97\text{ }^{\circ}\text{C}$. The last loss of 2.81% ends at $334.39\text{ }^{\circ}\text{C}$.

To evaluate the results of the TGA the following data concerning the decomposition temperature of the individual components is given. Glycerines decomposition begins at $290\text{ }^{\circ}\text{C}$, PE decomposition begins at $300\text{ }^{\circ}\text{C}$ and PP decomposition begins at $330\text{ }^{\circ}\text{C}$. Originated in these values the first mass loss points on the vaporization of water bonded to the coating. This water is a residue from the wax emulsions used as basis for the developed coating.

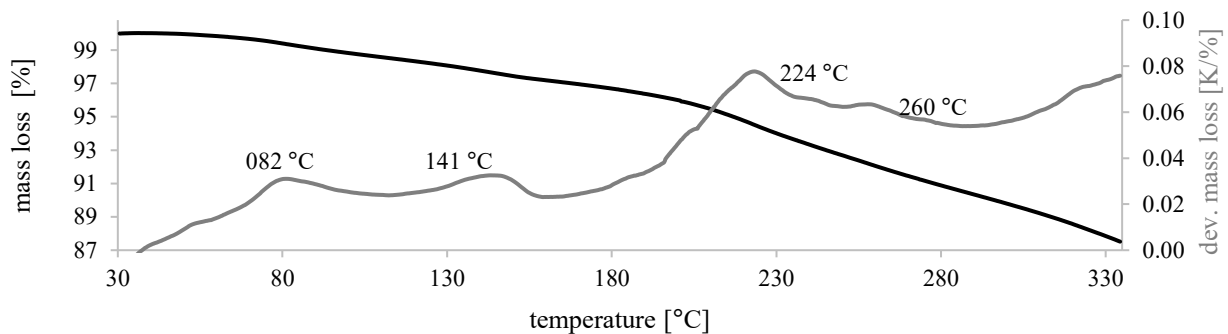


Fig. 7. TGA of coating

Fig. 8 shows the results from sessile drop measurement and the results determined with the Washburn method for the reference yarns. In contrast to the yarns the coating shows a very high SFE with a value of $52.79 \pm 4.10\text{ mN}\cdot\text{m}^{-1}$. The polar part occurs with $32.88 \pm 3.13\text{ mN}\cdot\text{m}^{-1}$ what is about two thirds of the whole value. Rather, the polar part of the yarns is one third of the whole value. Furthermore, the contact angle to water is smaller with a value of $45.78 \pm 4.13\text{ mN}\cdot\text{m}^{-1}$. The contact angle to diiodomethane is similar to the ones of the yarn with $75.40 \pm 1.81\text{ mN}\cdot\text{m}^{-1}$. Moreover, the deviation of the SFE of the coating are higher with a maximum of 9.02% concerning the contact angle of water.

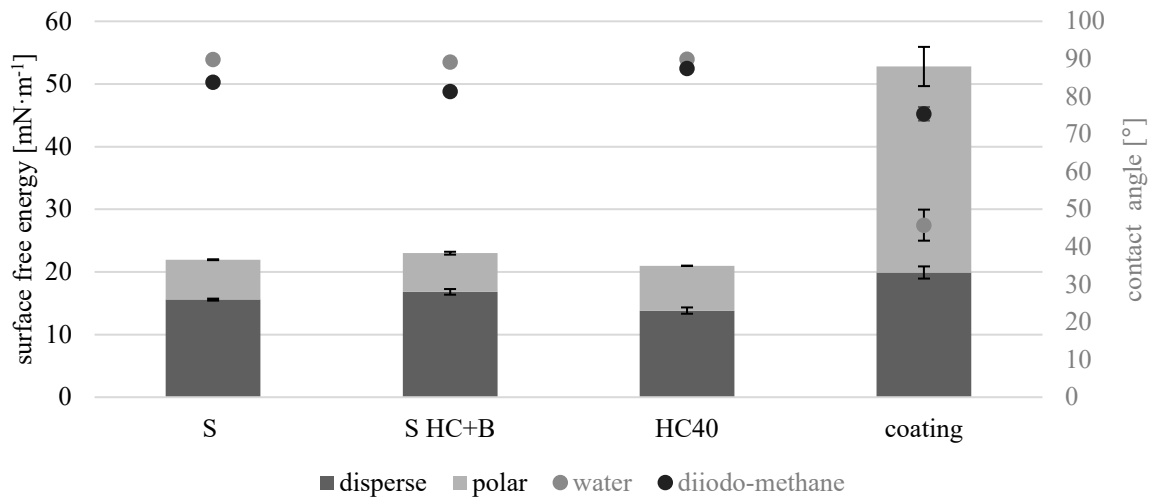


Fig. 8. Surface free energy and contact angle of coating and reference yarns

Discussion

The results of the performed studies state that the coating process itself does not have a negative effect of the characteristics of the yarn. Shieldex Yarn 117/17 dtex 2PLY HC+B (S HC+B) even shows a decrease in electrical resistance after being coated. Further, the developed coating shows better optical results on Statex yarns than on HC40. Nevertheless, HC40 shows the best electrical resistance after being coated and embroidered even if it shows the most damages compared to the other two yarns. The cause of these damages could be the non-sufficient adhesion between HC40 and the developed coating. An adaption of the composition of the coating is desirable for HC40 also regarding the electrical resistance. Shieldex 117/17 dtex 2PLY (S) shows the effect of the protective coating. Compared to the embroidered reference it shows half of the resistance. In consideration of the SEM images of the coated yarns the Statex yarns are covered fully without gaps while the HC40 is not completely covered with the coating and gaps are depicted between the filaments of the yarn. This leads to the need of a thicker coating concerning the HC40.

Summary

Summed up the coating protects the one out of three EC yarn against mechanical stress implemented via textile processing with an embroidery plant. The Shieldex 117/17 dtex 2PLY (S) could be protected while the effect of the coating is not detectable concerning Shieldex 117/17 dtex 2PLY C+B (S HC+B) and HC40. This can be remedied with the adjustment of coatings composition to increase the adhesion between the protective coating and EC yarn. Furthermore, the thickness of the coating should be increased to create further protecting potential. The thickness can be increased by using other coating processes and parameters. Additionally, the coating could be applied on other EC yarn-shaped structures to analyze the adhesion and protective effect on them. Also the implementation with other textile processing methods like knitting could be performed to detect differences or similarities in the protective behavior of the coating. Finally further characterization of the coated yarns could be performed, e.g. washing stability and temperature stability.

Acknowledgement

Funded by the German Research Foundation (DFG, Deutsche Forschungsgemeinschaft) as part of Germany's Excellence Strategy – EXC 2050/1 – Project ID 390696704 – Cluster of Excellence “Centre for Tactile Internet with Human-in-the-Loop” (CeTI) of Technische Universität Dresden

References

- [1] Technische Universität Dresden, Centre for Tectile Internet with Human-in the-loop: Deutsche Telekom Professur für Kommunikationsnetze. <https://www.ceti.one/>, 2021.
- [2] E. Ismar, S. Kurşun Bahadır, F. Kalaoglu, V. Koncar, Futuristic Clothes: Electronic Textiles and Wearable Technologies, *Global Challenges* 4 (2020) 1900092. <https://doi.org/10.1002/gch2.201900092>.
- [3] A. Vogl, P. Parzer, T. Babic, J. Leong, A. Olwal, M. Haller, StretchEBand: Enabling Fabric-Based Interactions through Rapid Fabrication of Textile Stretch Sensors, in: G. Mark, S. Fussell, C. Lampe, m.c. schraefel, J.P. Hourcade, C. Appert, D. Wigdor (Eds.), *Explore, innovate, inspire: CHI 2017 May 6-11, Denver, CO, USA*, Association for Computing Machinery Inc. (ACM), New York, NY, 2017, pp. 2617–2627.
- [4] G.M.N. Islam, S. Collie, M. Qasim, M.A. Ali, Highly Stretchable and Flexible Melt Spun Thermoplastic Conductive Yarns for Smart Textiles, *Nanomaterials* (Basel, Switzerland) 10 (2020). <https://doi.org/10.3390/nano10122324>.
- [5] T. Onggar, I. Kruppke, C. Cherif, Techniques and Processes for the Realization of Electrically Conducting Textile Materials from Intrinsically Conducting Polymers and Their Application Potential, *Polymers* 12 (2020) 2867. <https://doi.org/10.3390/polym12122867>.
- [6] I. Kim, H. Shahariar, W.F. Ingram, Y. Zhou, J.S. Jur, Inkjet Process for Conductive Patterning on Textiles: Maintaining Inherent Stretchability and Breathability in Knit Structures, *Adv. Funct. Mater.* 29 (2019) 1807573. <https://doi.org/10.1002/adfm.201807573>.
- [7] S. Uzun, S. Seyedin, A.L. Stoltzfus, A.S. Levitt, M. Alhabeab, M. Anayee, C.J. Strobel, J.M. Razal, G. Dion, Y. Gogotsi, Knittable and Washable Multifunctional MXene-Coated Cellulose Yarns, *Adv. Funct. Mater.* 29 (2019) 1905015. <https://doi.org/10.1002/adfm.201905015>.
- [8] E. Ismar, S.u. Zaman, X. Tao, C. Cochrane, V. Koncar, Effect of Water and Chemical Stresses on the Silver Coated Polyamide Yarns, *Fibers Polym* 20 (2019) 2604–2610. <https://doi.org/10.1007/s12221-019-9266-4>.
- [9] N. Baribina, I. Baltina, A. Oks, Application of Additional Coating for Conductive Yarns Protection against Washing, *Key Engineering Materials* 762 (2018) 396–401. <https://doi.org/10.4028/www.scientific.net/kem.762.396>.
- [10] R. Alagirusamy, J. Eichhoff, T. Gries, S. Jockenhoewel, Coating of conductive yarns for electro-textile applications, *The Journal of The Textile Institute* 104 (2013) 270–277. <https://doi.org/10.1080/00405000.2012.719295>.
- [11] A. Raja, G. Thilagavathi, Kannaian T., Synthesis of spray dried polyvinyl pyrrolidone coated silver nanopowder and its application on wool and cotton for microbial resistance, *Indian Journal of Fibre & Textile Resear* (2010) 59–64.
- [12] D.H. Kaelble, K.C. Uy, A Reinterpretation of Organic Liquid-Polytetrafluoroethylene Surface Interactions, *The Journal of Adhesion* 2 (1970) 50–60. <https://doi.org/10.1080/0021846708544579>.
- [13] D.K. Owens, R.C. Wendt, Estimation of the surface free energy of polymers, *J. Appl. Polym. Sci.* 13 (1969) 1741–1747. <https://doi.org/10.1002/app.1969.070130815>.

Development of Filled Immiscible Polymers Blend Monofilaments for Water Detection in Composite

Julie Regnier^{1,a}, Christine Campagne^{1,b} Éric Devaux^{1,c} and Aurélie Cayla^{1,d*}

¹Univ.Lille, ENSAIT, GEMTEX–Laboratoire de Génie et Matériaux Textiles, F-59000 Lille, France

^ajulie.regnier@ensait.fr, ^bchristine.campagne@ensait.fr, ^ceric.devaux@ensait.fr,
^daurelie.cayla@ensait.fr

Keywords: Water leak detection, conductive polymer composite, immiscible thermoplastic/elastomer blend, monofilament

Abstract. In order to avoid environmental pollution by effluents, the incorporation of electrical conductive yarns in a waterproof membrane allows detecting a leak or crack on industrial concrete structure. The membrane is made of composite materials: a glass textile structure equipped with the detector yarns and molded in an epoxy resin. The liquid's detection and the data's transmission depend on the yarn's conductivity variation and its chemical and physical properties.

This study aims to develop a water detector monofilament from conductive polymer composites (CPC): an immiscible polymers blend (polyamide 6.6/elastomer) filled with carbon nanotubes (CNT). The addition of elastomer in the CPC yarn is important to withstand the mechanical deformation of the resin structure without breaking. The morphology of the immiscible polymers blend and the localization of the CNT influence the electrical conductivity of the yarn and thus, its property of water detection. Two principles of water detection are investigated with this blend: the short circuit and the absorption. For the short circuit, the presence of liquid is detected when the liquid creates a conductive path between two yarns in parallel. While, the absorption principle is based on the conductivity variation with the yarn's swelling in contact with water.

Introduction

Concrete is a fragile material which can cause fluids leakages and which are sometimes dangerous for the environment (pollutant). For instance, the hydrocarbons contained in the retention tanks or the sulfuric acid in the wastewater treatment plants can represent a danger for soil pollution in the case of leaks. That is why, in the environmental field, liquids or gas detectors are more and more developed to monitor these industrial structures. Nowadays, conductive cables are used to detect a liquid leak on pipeline thanks to the electrical conductivity variation [1]. To monitor an industrial wall and detect a leak, more and more researches develop intelligent composite membranes [2,3]. They are made of resin or concrete and a reinforced textile which is equipped with smart filaments to detect the stress and deformation of the structure or a fluid leakage in case of damage.

Different concepts are established to detect fluid with smart textiles. For the water detection, the most commonly used is the short circuit principle with metallic yarns [4]. This technique uses two conductive yarns in parallel without initial contact. To detect and transmit the signal, the liquid has to create an electrical conductive connexion between the two conductive yarns. The signal depends on a lot of parameters : the distance between the two conductive yarns, their chemical and physical properties [5], the textile structure [6] and the liquid properties like its ionic conductivity and its surface tension [7,8].

In the literature, more and more researches are carried out to detect fluid leak with the Conductive Polymer Composites (CPC). The CPC yarns are made of a matrix of polymers blended with sufficient quantity of electrical conductive fillers to make the yarn conductive. This material transition: from the insulating state to the semiconductor state, is called the electrical percolation threshold. Thanks to the affinity of the polymer with the solvent to detect and its property of absorption [9–12], the solvent diffuses inside the yarn causing the matrix swelling. This phenomenon leads the variation of the interparticle distance inducing the electrical conductivity variation of the yarn. The advantage to use the CPC is the possibility to blend polymers to combine their different properties [13] or to

improve the compounds preparation. To optimize the fluid detector yarn with an immiscible polymers blend, the continuity of the fillers in one phase and the continuity of this phase is important. This phenomenon is called the double percolation [14]. This last one can be obtained by different parameters: the proportion of the blend's components [15], the extrusion parameters such as the shear conditions [16], the viscosity and the elasticity of the blend [17,18].

This study focuses on the formulation influence of an immiscible polymers blend on two water detection principles: a filled thermoplastic polymer and an elastomer providing yarn's flexibility. Regarding the thermoplastic polymer, the polyamide 6.6 (PA6.6) filled with carbon nanotubes is usually used in the literature for piezoresistive sensors monofilaments [19] or thermal detector [20]. Determined by Javadi Toghchi et al., the proportion by weight of carbon nanotubes in the PA6.6 at the electrical percolation threshold is of 2 wt.% [21]. Regarding the elastomer, it is more studied as monofilament for strain sensors [22] or to improve the mechanical or rheological properties of immiscible polymers blends [23–25].

In this study, the two principles of water detection are: the short circuit and the absorption. The short circuit is based on the creation of an electrical conductive path thanks to the water between to parallel conductive yarns. The absorption principle is based on the variation of the yarn's electrical conductivity in presence of liquid. First, this study concentrates on the development of a polyamide 6.6 (PA6.6) filled with 3 wt.% of carbon nanotubes (CNT) and a polypropylene based elastomer (PBE). The elastomer is used to prevent from the yarn break during the resin cracking and thus to not loss the electrical conductivity signal. As the PA6.6 and the PBE are immiscible, the elastomer allows also to locate the fillers in one phase (the PA6.6) and thus to decrease the percolation threshold with a low amount of fillers in the blend. The influence of the elastomer proportion is investigated on the morphology and the mechanical and electrical properties. Then, its electrical conductivity variation is investigated in an epoxy resin.

Experimental

Materials and process. The CPC is used for the detection of water infiltration in cracked zone in a composite membrane. Before testing the water detection in the membrane, the detector yarns are developed, characterized and tested without resin matrix for the two principles of detection. These detections are tested with demineralized water at room temperature. The water's measured conductivity is 0.1 $\mu\text{S}/\text{cm}$ and its surface tension is about 71.8 mN/m. These parameters are controlled before each tests to ensure their repeatability.

Conductive yarns. The detector yarns are composed of a blend of a thermoplastic polymer with fillers and a propylene-based elastomer (PBE). First the thermoplastic polymer: the polyamide 6.6 (PA6.6) is filled with 3 wt.% of carbon nanotubes (CNT).

The PA6.6 which is referenced TORZEN U4803 NC01 is provided by Invista (Wichita, KS, USA) and has a melting point of 263 °C.

The multiwalled carbon nanotubes NC 7000 (MWCNT) are supplied by Nanocyl (Sambreville, Belgium). These MWCNTs have an average length of approximately 1.5 μm , a diameter of 9.5 nm, and a specific area of 250-300 m^2/g .

Then, the elastomer is added to ensure the flexibility of the detector yarn and to support the mechanical deformation of the resin. The employed elastomer is the PBE VISTAMAXX 3000 which is supplied by ExxonMobil Chemical (Houston, Texas, USA). It is composed of isotactic polypropylene repeat units with random ethylene distribution.

Compounds preparation. The compounds preparation was carried out by a first extrusion to fill the PA6.6 with the CNT in order to disperse the fillers well. It is processed by a co-rotating intermeshing twin-screw extruder from Thermo-Haake PTW 16/25p (barrel length = 25:1 L/D). The temperature profile is: 260 °C – 270 °C – 275 °C – 275 °C – 280 °C with a rotating speed of 100 RPM.

Then a second extrusion step is performed to incorporate the elastomer inside the first blend in different proportions by weight: from 0 wt.% to 50 wt.% (Table 1). The second extrusion is achieved with the Process 11 Parallel Twin-Screw Extruder from Thermofischer (Waltham, Massachusetts, USA) with a barrel length of 40:1 L/D. The rotating speed of this extruder is 100 RPM, and the temperatures profiles is : 215 °C – 275 °C – 285 °C – 285 °C – 278 °C – 275 °C – 270 °C – 270 °C. Before each extrusions, the granulated polymers are dried at 80 °C for 16 h. The monofilaments have a diameter of approximately 1.5 mm \pm 0.07 mm.

Table 1. Summary of the different extruded monofilaments

Sample reference	Blend Proportion		Total fillers content in the blend
	wt.% PA6.6 _{3CNT}	wt.% PBE	wt.% CNT
PA6.6 _{3CNT}	100	0	3
PA6.6 _{3CNT} 90/PBE10	90	10	2.7
PA6.6 _{3CNT} 80/PBE20	80	20	2.4
PA6.6 _{3CNT} 70/PBE30	70	30	2.1
PA6.6 _{3CNT} 60/PBE40	60	40	1.8
PA6.6 _{3CNT} 50/PBE50	50	50	1.5

Implementation in the resin. The resin used in this study is made of an epoxy base and a curing agent amine. They are mixed in a glass beaker at a room temperature in proportion by weight base 1 / hardener 3. The resin dries out in eight hours at room temperature. To implement the monofilaments in the resin, a mold allows to cast the resin with the electrical conductive yarns (Fig. 1). The mold is composed of two parts: inferior and superior, to place the yarns in the middle of the resin plate.

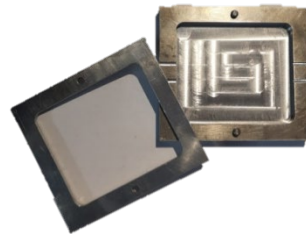


Figure 1. Mold used to form the composite.

The plates have a length of 7 mm, a larger of 6 mm and a thickness of 2 mm (Fig. 2). The mold allows the repeatability of the tests and the production of samples.

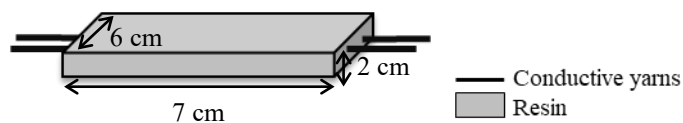


Figure 2. Implementation of the resin on the electrical conductive yarns.

Methods of characterization. To investigate the influence of the elastomer on the water detection properties, two principles of detection are established: the absorption principle and the short circuit. They both are based on the electrical conductivity variation of the monofilament in contact with water. Ten tests conditioned at 20 °C and a humidity of 35 % for each yarns and principles, are necessary to validate the results and the reproduction of these protocols.

Morphology. The Scanning Electron Microscope (SEM) images allows to observe the morphology of the different blends. First, the samples are prepared by cryofracture: frozen under nitrogen and then broken. They are observed by a Schottky Field Emission Scanning Electron Microscope SU5000 at 5 kV and different magnifications.

Mechanical properties. The elongation at break and the tenacity are measured by an MTS Criterion tensile bench from MTS (Minnesota, USA). The parameters fixed for the tests are: an initial length of 150 mm, an initial speed of 500 mm/min and a pre-loaded of 5 N. They are performed under a controlled and conditioned atmosphere of 65 % of humidity and a temperature of 20°C. Ten measurements for each blend are necessary to accept the results with a standard deviation of about 20 %.

Electrical and detection properties. To measure the electrical conductivity of the different blends, the monofilaments are connected to a Keithley 2461 SourceMeter (Beaverton, OR, USA). The current intensity is measured for a voltage applied which ranges from -0.5 V to 15 V with an increment of 0.1 V. The data of the current as a function of the voltage sent allows to determine the electrical conductivity (Eq. 1) :

$$\sigma = \frac{L}{RS} \quad (1)$$

where σ is the electrical conductivity of the system (S/m), L is the yarn's length ($L = 0,1$ m), S is the yarn's area (m^2) and R is the resistance measured (Ω).

The principle of detection by absorption (Fig. 3a) is based on the electrical conductivity variation of the monofilament in contact with water. The conductivities of the monofilament before and after 24 h soaked in water are calculated (Eq. 1). To observe the influence of the PBE percentage on the detection, the rate of change in the electrical conductivity between the dry and the wetted monofilament is calculated and called the water detector sensitivity (S_w) (Eq. 2):

$$S_w = \frac{\sigma_f - \sigma_i}{\sigma_i} \times 100 \quad (2)$$

where S_w is the water detector sensitivity (%), σ_i is the initial electrical conductivity (S/m) and σ_f the final electrical conductivity (S/m).

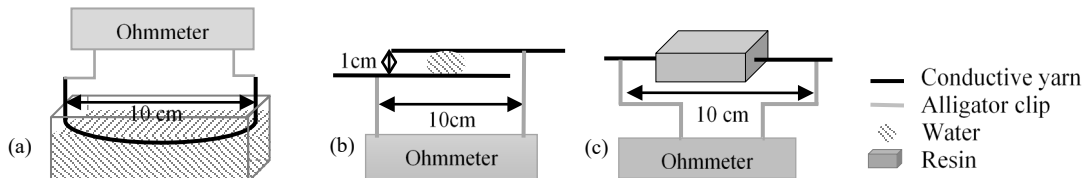


Figure 3. Principle of absorption (a), short circuit (b) and the electrical conductivity variation after the implementation (c).

The short circuit uses a drop of water to create a conductive path between two parallel yarns (Fig. 3b). The water closes the circuit between the two electrical conductive yarns and triggers the electrical signal. To compare the signal of the different PBE proportions, the conductance is calculated (Eq. 3). To make the test repeatable, the water is deposited on a square of 3×3 cm of absorbent paper which links the parallel yarns. It allows to overcome the shape of the drop and the problems of absorption that can vary the conductance of the circuit:

$$G = \frac{1}{R} \quad (3)$$

where G is the conductance of the circuit (S) and R the resistance of the circuit (Ω).

The monofilament implementation in the resin is then observed (Fig. 3c). The electrical conductivity before and after the monofilament implementation in the resin are calculated (Eq. 1). It allows to observe variation of the conductivity and the influence of the PBE percentage in the membrane creation process.

Results and Discussions

Influence of the morphology on the mechanical properties.

Morphology. The hypothesis of the behavior of the different blends' properties can be validated with the SEM images. The PA6.6_{3CNT}90/PBE10 SEM images (Fig. 4a) allows to reveal a nodular morphology of the PBE in the PA6.6_{3CNT}. While, a phase inversion is observed with the PA6.6_{3CNT}60/PBE40 SEM images (Fig. 4b). The 60/40 had a fibrillar morphology of the PA6.6_{3CNT} in the PBE.

In this study, the carbon nanotubes are first blended with the PA6.6 polymer. Therefore, the localization and the well dispersion of the CNT in the PA6.6 is conditioned by the extrusion sequence. No CNT's delocalization is observed after the addition of the PBE by the second extrusion. This localization of CNT and the formation of nodules with a small PBE contents are confirmed in other studies [26,25].

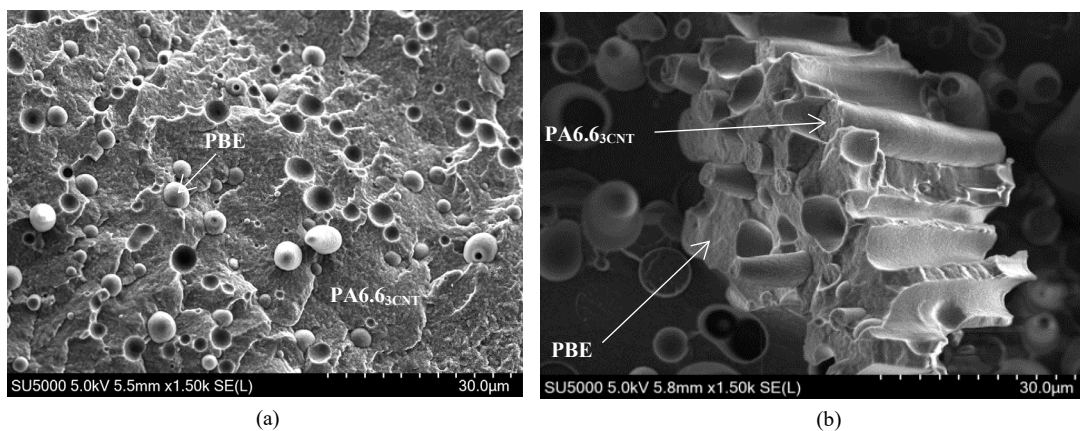


Figure 4. SEM images: Morphology of the monofilament PA6.6_{3CNT} /PBE in proportion by weight: (a) 90/10, (b) 60/40.

Mechanical properties. The influence of the PBE proportions in the blend is investigated on the mechanical properties. The elongation at break and the tenacity are measured (Fig. 5). The addition of a very low proportion of elastomer does not improve the mechanical properties of the blends. The elongation at break increases from 16.5 % without PBE to about 20 % for the blend with 30 wt.% of PBE. The tenacity is constant at about 3 cN/Tex for all the blends with a proportion below 30 wt.%. However, these properties drop sharply for proportions above 30 wt.% : to 5 % for the elongation at break and 1 cN/Tex for the tenacity.

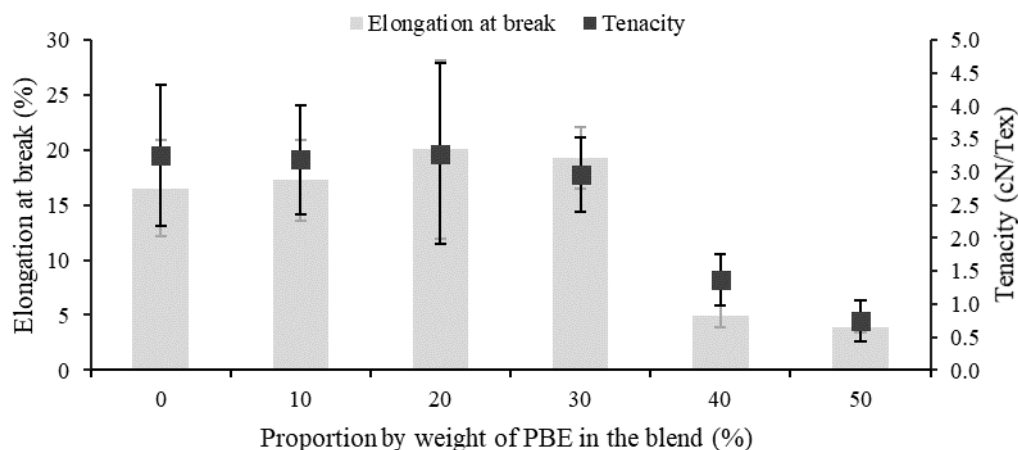


Figure 5. Elongation at break and tenacity of the monofilaments in different blend proportions.

These phenomena can be explained by the phase inversion. With a small proportion of elastomer, there is an elongation of the PBE nodules. While, the proportions above 30 wt.% have a larger interface between the PBE and the PA6.6_{3CNT} fibrils. This poor interface causes the premature rupture of the monofilaments. In conclusion, a small proportion of elastomer is sufficient to increase slightly the elongation of the blend.

Influence of the morphology on the electrical and detection properties.

Short circuit principle. The short circuit's signal depends on several parameters. The configuration of the circuit and the water properties are both fixed whereas the yarn's properties vary with the proportions of the blend and its morphology.

The first step of characterization was to measure the initial electrical conductivity of the different blends (Fig. 6). The initial electrical conductivity decreases with the addition of PBE in the blend. With more than 40 wt.% of PBE, the fillers content in the blend becomes lower than the one of the electrical percolation threshold founded by Javadi Toghchi et al. [21]: respectively 1.8 wt.% for the 60/40 against 2 wt.% for the percolation threshold. Therefore, a sharp drop in conductivity can be observed after 30 wt.% of PBE in the blend.

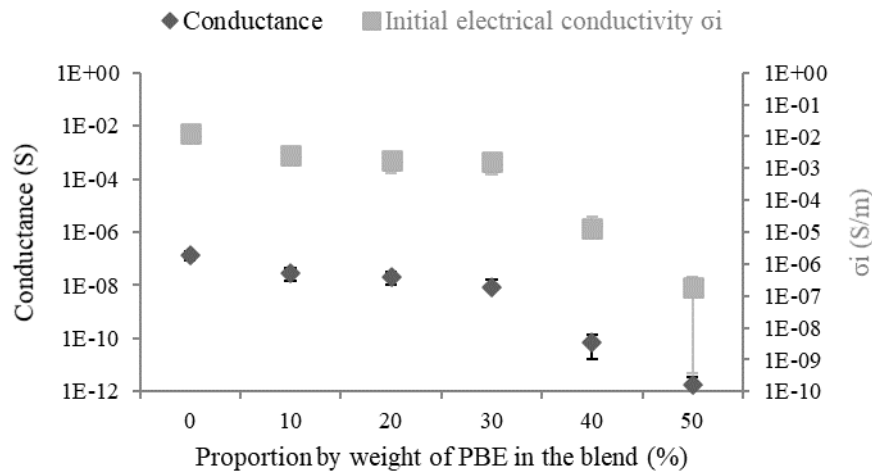


Figure 6. Short circuit principle: Conductance and initial electrical conductivity of the blends.

Regarding the short circuit principle, the same trend is observed as the initial conductivity. The conductance signal is from about 1.4×10^{-7} S without elastomer to 8.3×10^{-9} S with 30 wt.% of PBE in the blend. Then, it decreases to 1.7×10^{-12} S for PA6.6_{3CNT}50/PBE50. The electrical conductivity of a semiconducting polymer is between 10^{-7} and 10^4 S/m thus the short circuit with the PA6.6_{3CNT}50/PBE50 can be considered as a no longer conductive. By hypothesis, the creation of more contact points between the water and the CNT can be improved with a majority phase of PA6.6_{3CNT} and thus with a nodular morphology. The PA6.6 have a moisture regain of about 4.5 % which makes it more hydrophilic than PBE which is composed of polypropylene and ethylene with a moisture regain of about 0 % [27]. Therefore, the water accessibility can be limited with the fibrillar morphology which has a majority phase of PBE.

Absorption principle. For the absorption principle, the sensitivity to water calculated is the variation of conductivity of the monofilaments before and after soaked in water. Two behaviors are detected. The blends with less than 30 wt.% of PBE have a positive sensitivity: from 43 % to 28 % for the PA6.6_{3CNT}70/PBE30. It is due to an increase in conductivity whereas beyond 30 wt.%, a negative sensitivity is observed: from -26 % to -52 % for respectively 60/40 and 50/50.

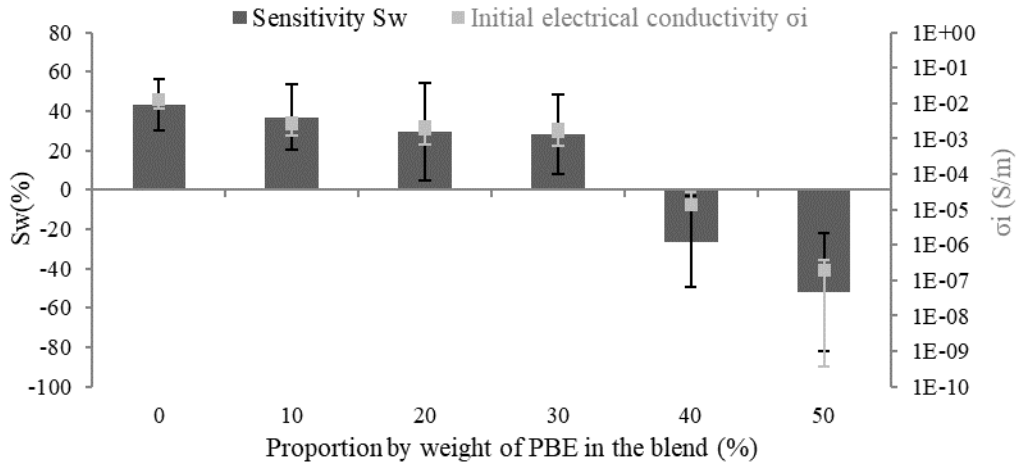


Figure 7. Principle of absorption: Water sensitivity and the initial conductivity of the monofilaments in different blend proportions.

This behavior variation is due to the phase inversion. For the positive sensitivities, the blends have a majority phase of the PA6.6_{3CNT} which promotes the conductive paths creation between absorbed water and fillers. Their water absorption property allows to increase the final conductivity of the monofilament. However, for the blends with majority phase of PBE, the swelling of the PA6.6_{3CNT} fibrils results in the increase in the interparticular distance which can explained the decrease of the electrical conductivity and thus the negative sensitivity.

Implementation in the resin. After characterizations of the blends for the water detection, the electrical properties variations after their implementation in the resin are determined (Fig.8). Without PBE in the blend, the electrical conductivity of the monofilament varies from 1×10^{-2} S/m at its initial state to 6.7×10^{-3} S/m after its implementation in the resin. While, adding small proportion of PBE in the blend stabilizes the conductivity of the monofilament after implementation in the resin about 2×10^{-3} S/m for 10 and 30 wt.% and 3.4×10^{-3} S/m for 20 wt.%. Therefore, the process of the yarn implementation in the resin have small influence on the yarn electrical conductivity which is important to develop and the install the waterproof membrane on the industrial structure.

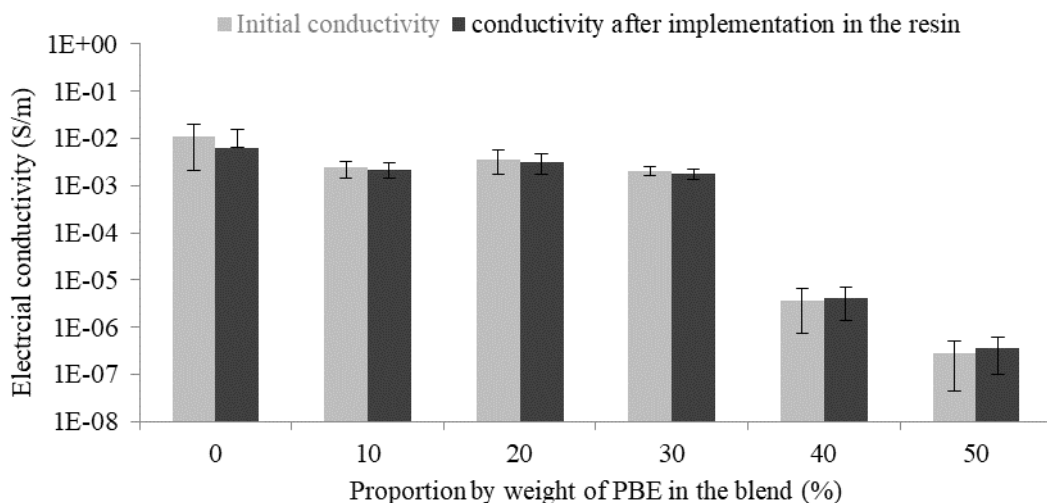


Figure 8. Electrical conductivity of the monofilament before and after its implementation in the resin

Summary

In conclusion, to develop a water detector yarn in a waterproof membrane, an immiscible polymers blend filled with carbon nanotubes : PA6.6_{3CNT}/PBE, is developed and characterized. The PA6.6_{3CNT} is employed for its good water detection property. The addition of PBE allows to decrease the total amount of fillers to make the yarn conductive. It allows also the yarn flexibility to mechanical stresses due in particular to the deformation of the epoxy resin membrane.

The monofilaments with a elastomer proportions less than 30 wt.% contain nodules of PBE in the PA6.6_{3CNT}. Above 30 wt.%, they have a fibrillar morphology of the PA6.6_{3CNT} in the PBE. The nodular morphology does not improve significantly the mechanical properties. Moreover, the blends with a high proportion of PBE have weaker mechanical properties due to the poor interfacial quality between the PBE and the PA6.6_{3CNT}. Regarding the blends with small PBE percentages, they have good electrical and water detection properties. No electrical conductivity variations is noticed after their implementation in the resin.

To improve the resin cracking resistance, a PBE monofilament filled with carbon nanotubes is investigated without the PA6.6. Their detection properties and their electrical conductivity variation after its implementation in the resin are studied.

Acknowledgment

This work falls within the project FUI 25 MONI2TEX, financed by the Région Haut-de-France and BPI France.

References

- [1] J. A. Sahakian, U. S. Patent 5177996A. (1993)
- [2] Y. Goldfeld, T. Quadflieg, T. Gries, and O. Rabinovitch, Smart textile reinforcement with embedded stainless steel yarns for the detection of wetting and infiltration in TRC structures, *Sensors and Actuators A: Physical*, vol. 243, 2016, pp. 139–150.
- [3] Y. Goldfeld, O. Rabinovitch, B. Fishbain, T. Quadflieg, and T. Gries, Sensory carbon fiber based textile-reinforced concrete for smart structures, *Journal of Intelligent Material Systems and Structures*, vol. 27, 2016, pp. 469–489.
- [4] Shuai Xu, Qian Ma, Xiao-Fang Yang, and Shu-Dong Wang, Design and fabrication of a flexible woven smart fabric based highly sensitive sensor for conductive liquid leakage detection, *RSC Advances (RSC Publishing)* vol. 7, 2017.
- [5] L. M. Castano and A. B. Flatau, Smart fabric sensors and e-textile technologies: a review, *Smart Mater. Struct.* vol. 23, 2014.
- [6] T. Pereira, P. Silva, H. Carvalho, and M. Carvalho, Textile moisture sensor matrix for monitoring of disabled and bed-rest patients, *IEEE EUROCON - International Conference on Computer as a Tool*, Lisbon, 2011, pp. 1–4.
- [7] I. Parkova, I. Ziemele, and A. Vi, Fabric Selection for Textile Moisture Sensor Design, *Material Science. Textile and Clothing Technology*, 2012, pp. 6.
- [8] V. Gaubert, H. Gidik, and V. Koncar, Boxer Underwear Incorporating Textile Moisture Sensor to Prevent Nocturnal Enuresis, *Sensors*, vol. 20, no. 12, 2020.
- [9] M. Castro, B. Kumar, J. F. Feller, Z. Haddi, A. Amari, and B. Bouchikhi, Novel e-nose for the discrimination of volatile organic biomarkers with an array of carbon nanotubes (CNT) conductive polymer nanocomposites (CPC) sensors, *Sensors and Actuators B: Chemical*, vol. 159, 2011, pp. 213–219.
- [10] M. Narkis, S. Srivastava, R. Tchoudakov, and O. Breuer, Sensors for liquids based on conductive immiscible polymer blends, *Synthetic Metals*, vol. 113, 2000, pp. 29–34.

-
- [11] T. Villmow, S. Pegel, A. John, R. Rentenberger, and P. Pötschke, Liquid sensing: smart polymer/CNT composites, *Materials Today*, vol. 14, 2011, pp. 340–345.
- [12] T. Villmow, A. John, P. Pötschke, and G. Heinrich, Polymer/carbon nanotube composites for liquid sensing: Selectivity against different solvents, *Polymer*, vol. 53, 2012, pp. 2908–2918.
- [13] P. A. Eutionnat-Diffo, A. Cayla, Y. Chen, J. Guan, V. Nierstrasz, and C. Campagne, Development of Flexible and Conductive Immiscible Thermoplastic/Elastomer Monofilament for Smart Textiles Applications Using 3D Printing, *Polymers*, vol. 12, 2020.
- [14] M. Sumita, K. Sakata, S. Asai, K. Miyasaka, and H. Nakagawa, ‘Dispersion of fillers and the electrical conductivity of polymer blends filled with carbon black’, *Polymer Bulletin*, vol. 25, 1991, pp. 265–271.
- [15] M. H. Al-Saleh and U. Sundararaj, An innovative method to reduce percolation threshold of carbon black filled immiscible polymer blends, *Composites Part A: Applied Science and Manufacturing*, vol. 39, 2008, pp. 284–293.
- [16] T. Villmow, B. Kretzschmar, and P. Pötschke, Influence of screw configuration, residence time, and specific mechanical energy in twin-screw extrusion of polycaprolactone/multi-walled carbon nanotube composites, *Composites Science and Technology*, vol. 70, 2010, pp. 2045–2055.
- [17] C. F. Antunes, M. van Duin, and A. V. Machado, Morphology and phase inversion of EPDM/PP blends – Effect of viscosity and elasticity, *Polymer Testing*, vol. 30, 2011, pp. 907–915.
- [18] D. Bourry and B. D. Favis, Cocontinuity and phase inversion in HDPE/PS blends: Influence of interfacial modification and elasticity, *Journal of Polymer Science Part B: Polymer Physics*, vol. 36, 1998, pp. 1889–1899.
- [19] L. Arboleda, A. Ares, M. J. Abad, A. Ferreira, P. Costa, and S. Lanceros-Mendez, Piezoresistive response of carbon nanotubes-polyamides composites processed by extrusion, *J Polym Res*, vol. 20, 2013, p. 326.
- [20] X. Guan et al., Carbon Nanotubes-Adsorbed Electrospun PA66 Nanofiber Bundles with Improved Conductivity and Robust Flexibility, *ACS Appl. Mater. Interfaces*, vol. 8, 2016, pp. 14150–14159.
- [21] M. Javadi Toghchi et al., Electrical conductivity enhancement of hybrid PA6,6 composite containing multiwall carbon nanotube and carbon black for shielding effectiveness application in textiles, *Synthetic Metals*, vol. 251, 2018, pp. 75–84.
- [22] P. A. Eutionnat-Diffo, A. Cayla, Y. Chen, J. Guan, V. Nierstrasz, and C. Campagne, Development of Flexible and Conductive Immiscible Thermoplastic/Elastomer Monofilament for Smart Textiles Applications Using 3D Printing, *Polymers*, vol. 12, 2020, p. 2300.
- [23] A. L. N. Da Silva, M. I. B. Tavares, D. P. Politano, F. M. B. Coutinho, and M. C. G. Rocha, Polymer blends based on polyolefin elastomer and polypropylene, *Journal of Applied Polymer Science*, vol. 66, 1997, pp. 2005–2014.
- [24] Y. Xu et al., Reactive Compatibilization of Polylactide/Polypropylene Blends, *Ind. Eng. Chem. Res.*, vol. 54, 2015, pp. 6108–6114.
- [25] I. Taraghi, A. Fereidoon, S. Paszkiewicz, and Z. Roslaniec, Nanocomposites based on polymer blends: enhanced interfacial interactions in polycarbonate/ethylene-propylene copolymer blends with multi-walled carbon nanotubes, *Composite Interfaces*, vol. 25, 2018, pp. 275–286.
- [26] P. J. Brigandi, J. M. Cogen, and R. A. Pearson, Electrically conductive multiphase polymer blend carbon-based composites, *Polymer Engineering & Science*, vol. 54, 2014, pp. 1–16.
- [27] M. Azeem, A. Boughattas, J. Wiener, and A. Havelka, Mechanism of liquid water transport in fabrics; a review, 2017, p. 9.

Dispenser Printing with Electrically Conductive Microparticles

E. Lempa^{1,a*}, M. Rabe^{1,b}, L. van Langenhove^{2,c}

¹Niederrhein University, 41065 Moenchengladbach, Germany

²Ghent University, 9052 Gent, Belgium

^{a,*}evelyn.lempa@hs-niederrhein.de, ^bmaike.rabe@hs-niederrhein.de,
^cLieva.VanLangenhove@UGent.be

Keywords: Conductive textiles, percolation threshold, filler particles, dispenser printing, 3D printing

Abstract. Electrically conductive textiles for wearable smart devices are in increasing demand [1]. The advantages of flexible fabric structures are combined with electronic functions, such as sensing or actuating, energy harvesting or illuminating, for the design of a multitude of smart textiles. Those functions are often created by applying conductive layers or patterns onto the textile surface with two-phase systems based on conductive filler particles in polymeric binders. However, those systems alter the textile-typical properties regarding haptic, drape, flexibility or weight, depending on the type of conductive particle used, i.e., metal- or carbon-based ones. Generally, electrical conductivity increases with the increase of conductive filler concentration. The relation between the various factors determining the electrical behavior as well as the percolation threshold for some dispersions and in particular the size and shape of the filler particles were previously assessed for planar coatings [2].

For that reason, in this research work electrically, conductive patterns were printed with dispenser printing technology using such two-phase dispersions based on polyurethane and polyacrylate binders and various metal microparticle flakes. With this application method linear resistance of approx. 25 to 100 Ohm per 100 cm depending on the textile structure could be realized, which was not even significantly reduced by household washing at 40°C or abrasion by Martindale.

Introduction

In order to apply conductive dispersions to textile surfaces in patterns, one cannot use coating methods but has to switch to printing techniques. Screen printing is widely used for printing electrodes or circuits, but one faces numerous limitations and disadvantages. The minimum line width as well as the maximum particle size depend on the mesh of the screens, which is greatly limited. Furthermore, as screens are in contact with the textile substrate, printing on highly three-dimensional surfaces is difficult and inaccurate. Additionally, the required fabrication of screens is not only costly but also time consuming. Finally, always a certain volume of print paste remains on the screen and squeegee and is wasted, which is a major disadvantage with respect to the high cost in additively manufactured circuits, but also from an ecological aspect.

Digital printing offers many advantages over screen printing. Inkjet printing is a contact free printing technology using inks specifically developed for those printheads. Print dispersions based on polymeric binders and metal or carbon microparticles are not suitable for the fine nozzle dimensions. Conductive inks are rather based on conductive polymers or/and metal or carbon nanoparticles.

In recent years, dispenser printing was investigated by numerous research teams as an alternative digital printing technique. It is a thick-film deposition technique used in fabricating smart textile devices such as sensors and energy harvesters. With dispenser printing circuits can be created in resolutions down to millimeter-sized features [3]. With a dispenser printer the dispersion in a pressurized syringe is deposited onto the textile material. The desired pattern is controlled in three dimensions using an XYZ stage-system. The resolution is dependent on the size of the syringe nozzle and the rheological behavior of the dispersion [4]. Dispenser printing is a digital drop-on-demand technique using a robotic actuator to precisely deposit print pastes in a manner similar to a 3D printer [5]. The technique is very versatile, suitable for a wide variety of dispersions and textile substrates, even delicate or adhesive materials. The vertical, non-contact position of the nozzle allows changes

dynamically while printing and printing on uneven substrates as well as over seams or on medical dressings [6]. Even skin-mountable stretch sensors can be manufactured cost-effectively by direct printing onto woven elastic fabrics in various patterns [7].

Electrically conductive patterns on textile surfaces can be realized with intrinsic conductive polymer dispersions based on polyethylenedioxythiophene (PEDOT), polyaniline (PANi), polypyrrole (PPy) or polyacetylene for coating and printing [8] or alternatively, with non-conductive polymeric dispersions such as aqueous polyurethane (PU), polyacrylate (PAC) or many others, filled with conductive particles based on metal or carbon as two-phase systems. In this case the transition between conductive and non-conductive states takes place at percolation threshold [9], which – to a great extent – is related to factors inherent with the fillers, such as basic conductivity, filler volume fraction, distribution and packing factor as well as general characteristics of the fillers like size, shape, surface area, morphology, orientation [10]. Carbon holds a specific resistance of $10^{-3} \Omega \text{ cm}$ while copper or silver exhibit $10^{-6} \Omega \text{ cm}$ [11]. Coatings on Polyester fabrics with dispersion filled with carbon black or carbon nanotubes reached sheet resistivities between 10^1 and $10^2 \Omega \text{ sq}$, while dispersions filled with copper and silver microparticles achieved results around $10^{-1} \Omega \text{ sq}$ [12].

For the packing factor, statistically, the maximum filler volume can be calculated to 64% for monodispersed spherical particles and can be increased above 64%, when blending different sized particles or reduced below 64%, when using skeleton forming or anisotropic longitudinal fillers [13]. Microparticles seem a superior choice for highly conductive structures, but the increase in cost and weight as well as the decrease in flexibility and bendability of the textile materials must be considered [14]. Furthermore, the binder polymer has a major influence on the conductivity of two-phase systems with particles, especially the interparticle filler spacing, the configuration and the crystallinity of the polymer [15]. Percolation threshold is depending on the configuration of the polymer chains as branches hinder the electron flow as well as highly amorphous regions, where filler particles are distributed homogeneously instead of forming conductive paths as happens in highly crystalline regions [16]. High temperature increases polymer diffusion and entanglement, thus blocks the formation of conductive particle paths and increases resistivity [17].

In this research work electrically, conductive patterns were printed with a dispenser printer using two phase dispersions based on different polymeric binders and metal microparticle flakes. With this application method linear resistance of approx. 25 to 100 Ohm per 100 cm depending on the textile structure could be realized, which was not even significantly reduced by household washing at 40°C or abrasion by Martindale.

Materials and Methods

The conductive patterns were printed on different textile materials with different dispersions blended with metal-based particles.

Textile materials: 100% polyester (PES) warp-knit, 125 g/m², washed, optical brightened, thermofixed and 100% PES ripstop woven, 105 g/m² washed, optical brightened, thermofixed and polyurethane (PUR)-coated.

Polymer materials: Commercially available binder dispersions, obtained from CHT R. Beitlich, Tübingen, Germany, were prepared for the digital printing process using a polyacrylate (PAC) binder, Tubicoat A22 (solid content 60%, density 1,0000 g/cm³ and pH 7,5-9,0) and a PUR binder, Tubicoat PU60 (solid content 60%, density 1,1000 g/cm³ and pH 8,0-9,0). For viscosity adjustments Tubicoat Thickener LP was added to the blends.

Filler materials: Two metallized micro-particles were obtained from Eckart GmbH. The two different types of metal particles were silver-coated copper particles with D50 specification of 11,6 µm (eConduct Copper 122000), named Copper 12 µm, and silver-coated glass particles with D50 specification of 30,4 µm (eConduct Glass 352000), named Glass 30 µm. Both microparticles are flakes with undefined edges, the glass particle is particularly flat and rather longitudinal.

Preparation of dispersions: The percolation threshold of metal particles was determined in previous work of the authors between 15 and 20 wt.-% metal particle in a polymeric binder with 12

to 15 % solid content [18]. For this reason, the printing dispersions for this research work were prepared by mixing the basic polymers with distilled water for a solid content 15,0%. The viscosity was adjusted to 60 dPas with 1-2% Tubicoat Thickener LP. The metal pigments were blended in with a VMA-Getzmann Dispermat LC30. Both metal particles were blended with the polymeric dispersions at 20% as is shown in table 1.

Table 1: Polymeric blends with metal particles

	A	B	C	D
PUR	80%	80%	-	-
PAC	-	-	80%	80%
Copper 12 μ m	20%	-	20%	-
Glass 30 μ m	-	20%	-	20%

Printing on textile: For printing the meander pattern, the 3D-digital food printer Procusini 3.0 was used with a 60 ml dispenser syringe and 0,8 mm nozzles, as shown in Fig.1. The overall length of the meander measured 100 cm and there were eight lines of 10 cm each between the turns. Within the Procusini software program the following settings were applied: line width 0,5 mm, speed 50%, flow rate 60%, thickness 0,55 mm, infill 25%, retracting 75%. After printing, the samples were dried in a Mathis Lab Dryer at 80°C, 180 s and subsequently annealed at 150°C, 60 s. Each dispersion was printed 10 times on both textile base materials.

Analytical methods: The viscosity was determined with the Haake Viscotester, Spindel 2. The evaluation of the printed pattern included linear resistance measured with a Voltcraft LCR-300 multimeter 2-point probe after drying and after annealing, each after conditioning at 20°C, 65% rel. hum. for 24 h. In addition, the abrasion resistance of the conductive circuits was determined with the Martindale Abrasion tester according to DIN EN ISO 12947 and furthermore the wash fastness of the conductive pattern on the basis of DIN EN ISO 105-C06. The patterns were also analyzed microscopically with a Keyence Microscope VH-Z20R regarding even depositing, line width and fabric penetration (images x50). With the Hitachi TM 3000 Tabletop microscope SEM images were obtained at an acceleration voltage of 15 kV to identify the distribution of the coating dispersion and in particular the metal particles (images x1,000). With the Keyence Laser Microscope further images of the different prints and the resulting topography were obtained (images x100).

Results and Discussion

The two-phase systems of polymer binder and metal microparticles were repeatably printable as shown in Fig. 1. The print results were identical even after 10 and more prints realized with one dispenser filling and without any blocking of the nozzle. Approximately 60 g of dispersion was used for 10 prints.

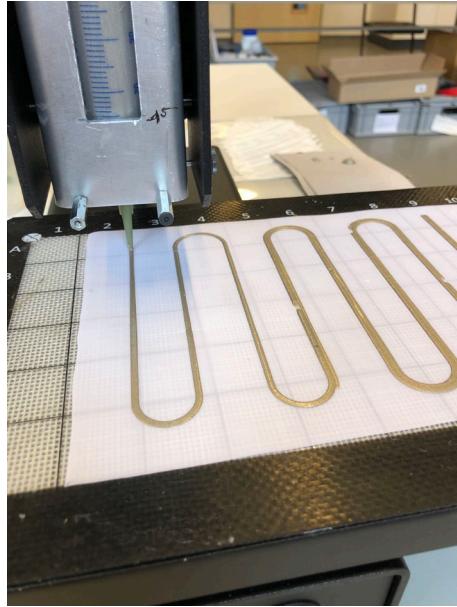
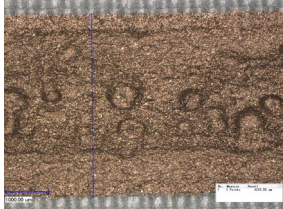
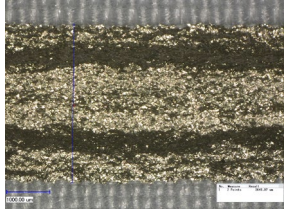
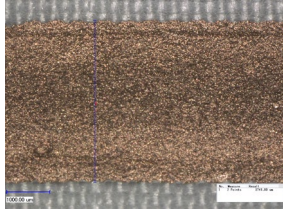
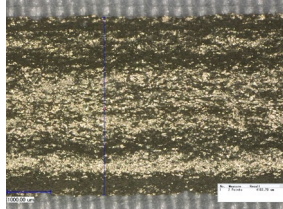
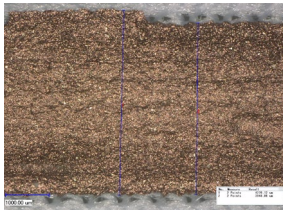
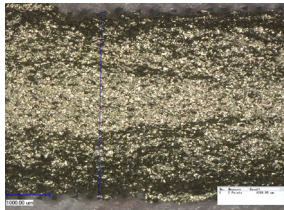
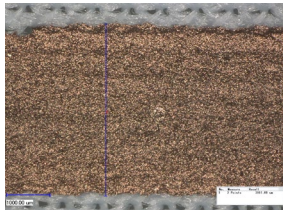
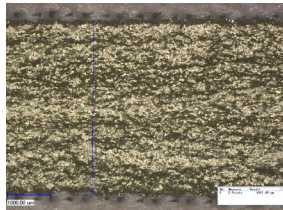


Fig. 1: Printed pattern on Procusini printer [Lempa, 22.02.2021]

The prints on the two different types of fabric with the four different dispersions were analysed under the microscope with images including the determination of the line width (table 2) and of the cross-section including the determination of the coating thickness (table 3).

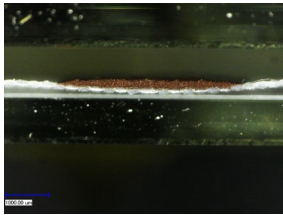
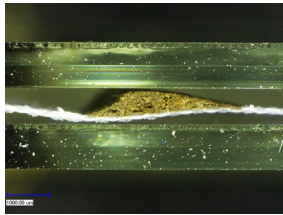
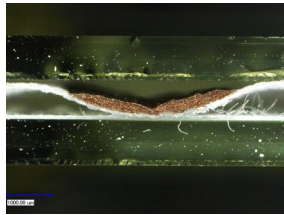
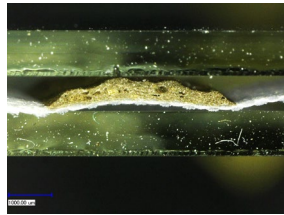
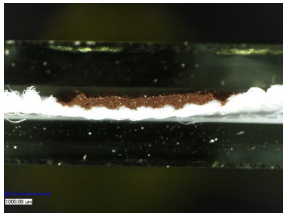
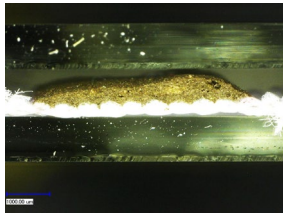
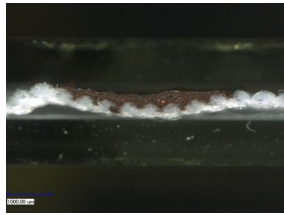
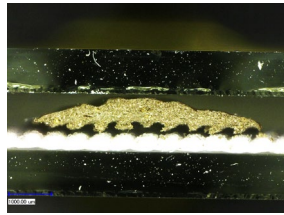
With the 0,8 mm syringe nozzle the line width of the prints was determined between 3,659 and 4,309 μm . No significant differences were detected between printing on warp-knit or ripstop fabric. However, as ripstop is a more three-dimensional structure, the distinct upper lines are visible in some of the microscopic images, such as B and D, when the silver-coated glass particle was used.

Table 2: Microscope images and line width of prints after annealing (50x enlarged)

	A	B	C	D
PES Ripstop woven	 Line width 4,220 μm	 Line width 3,659 μm	 Line width 3,742 μm	 Line width 4,109 μm
PES Warp-knit	 Line width 4,270 μm	 Line width 4,309 μm	 Line width 3,981 μm	 Line width 4,001 μm

The thickness of the prints measured from the cross-section averaged to approx. 250 to 400 μm on the warp-knit material and approx. 400 to 600 μm on the ripstop woven fabric.

Table 3: Microscopic images of the cross-section of prints after annealing (50x enlarged)

	A	B	C	D
PES Ripstop woven				
PES Warp-knit				

The prints with silver-coated copper particles led to less thickness, as the particles are much smaller. Average size D50 of the copper particles is specified with 11,6 μm . It is a flake of rather thick appearance. In contrast to this, the silver-coated glass particles resulted in a thicker build-up, as the average size D50 was specified at 30,4 μm , albeit that the flake is quite flat.

The images with the Laser microscope confirm the shape and size of the respective metal particles. The topography does not vary substantially between all prints. The measurements also verify the slightly higher build-up of prints with the larger glass particle. The images of both particles are shown in figure 2.

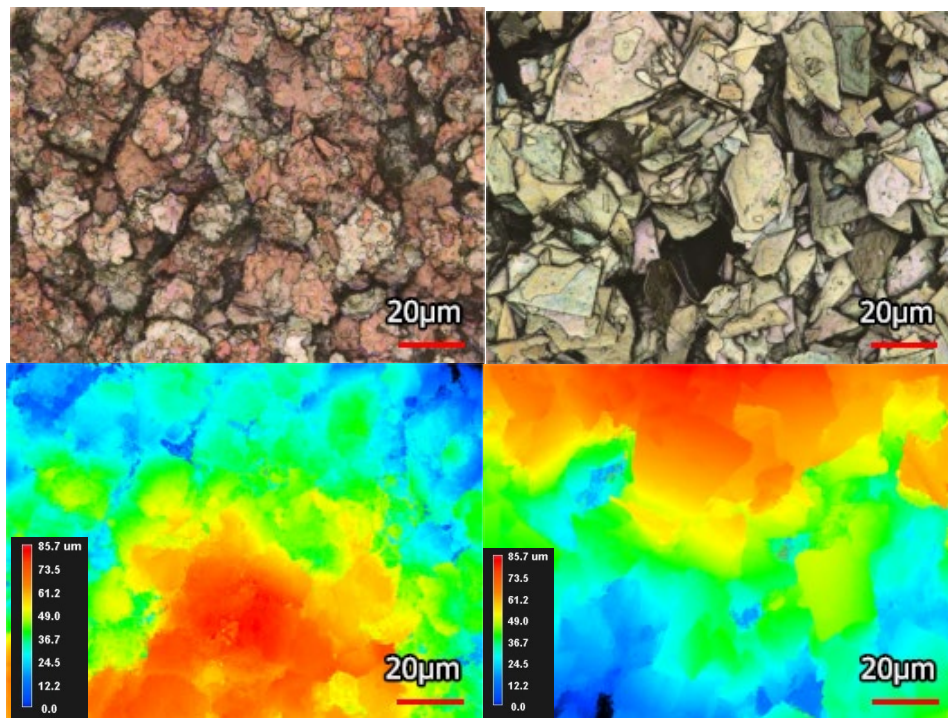


Fig. 2: Images from Laser microscope (top) and topography (bottom) of printed polymeric blend A (left) and B (right)

Furthermore, the prints were evaluated with the SEM. The images shown in figure 3 and figure 4 visualize the difference in shape and size of the two particles used in the polymeric blends. The silver-coated copper particles exhibit a random shape and rather small diameter, while the shape of the silver-coated glass particles really looks like broken glass with very sharp and defined edges. In addition, the thin and longitudinal shape of the larger particles is obvious.

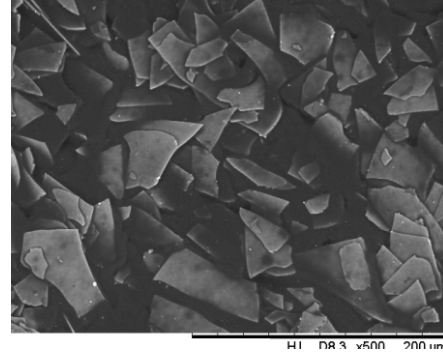
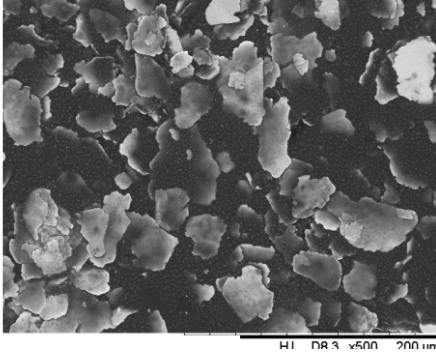


Fig. 3: SEM image of printed polymeric blend A Fig.4: SEM image of printed polymeric blend B

When using the prints for smart textiles, the linear resistance of the meander is the most important property. Overall, the linear resistance only marginally deviated when using one kind of dispersion on one type of fabric. As the design included eight lines of 10 cm each, there was a large number of lines measurable allowing the determination of deviation. For all 10 cm lines as well as for the total 100 cm lines of all 10 samples on one fabric no significant differences were detected within the prints of the same dispersion. Table 4 shows the average linear resistance of 10 measurements for 100 cm lines and 80 measurements of 10 cm lines. The resistance of the blend PAC with the copper particle is significantly lower than with the glass particle, while it is the opposite in the blend with PUR, independent of the chosen fabric. Overall, the results are slightly superior with the PES warp-knit material using PAC, but almost identical using PUR. As described in the introduction, the annealing temperature, which is essential to ensure sufficient crosslinking and adhesion of the binder to the textile material, reduces conductivity due to the increase of crystallinity in the binder matrix. However, this is less significant with PAC, as the polymer used in the described trials is highly branched and therefore probably less prone to an increase in crystallinity from heat treatment. A washing cycle at 40°C increases linear resistance by nearly 100%, but there is no much further change after another four washes.

Table 4: Average linear resistance of 10 printed circuits [ohm]

	100% PES ripstop woven				100% PES warp-knit			
	A PUR/ Cu	B PUR/ GL	C PAC/ Cu	D PAC/ GL	A PUR/ Cu	B PUR/ GL	C PAC/ Cu	D PAC/ GL
Rs 10 cm								
After drying 80°C	10,94	6,39	4,23	12,11	10,27	5,78	2,15	8,81
Rs 100 cm								
After drying 80°C	72,91	47,91	32,45	102,84	78,05	51,57	26,15	77,46
After annealing 150°C	98,75	54,53	39,64	120,54	103,88	75,95	34,87	105,71
After washing 40°C	197,36	160,51	72,54	228,15	186,72	113,97	54,15	158,39
After washing 5x 40°C	205,78	172,88	89,22	232,49	201,75	119,31	68,63	167,02

Conclusion and Summary

With the Procusini 3D food printer electrically conductive patterns can be realized with the described dispenser technique. By choosing the appropriate polymeric binders as well as the optimum shape and size of metal particles the percolation threshold can be reasonably low. With the filler concentration of 20% in PUR and in PAC, the lowest surface resistivity was obtained with the smaller

silver-coated copper flakes compared to the larger silver-coated glass flakes. The results with the copper and the glass particle were slightly better on the more three-dimensional PES warp-knit fabric than on the very thin and light-weight PES ripstop woven fabric. The temperature of annealing has a negative impact on surface resistivity for both particles in both polymer binder blends due to the increase in crystallinity, but the differences from drying at 80°C or annealing at 150°C is less using the glass flakes. It was assumed, that in the coatings with the copper particle, particularly in PAC blends, some corrosion of the flakes occurred, as this could be observed when storing the prepared printing dispersion for longer than 3 to 4 hours.

In conclusion, silver-coated copper particles lead to better results in linear resistance per 100 cm in combination with polyacrylate, while silver-coated glass particles are better in blends with polyurethane. The warp-knit material is superior over the ripstop fabric, annealing increases resistance, however this is required to improve wash-fastness as indicated by the supplier. Overall, the best result, even after washing, was achieved with the dispersion blended with 80 % of the polyacrylate binder at a 15% solid content and 20 % of the 12 µm silver-coated copper particles.

References

- [1] C. Hertler, L. Van Langenhove, Smart textiles: from prototype to commercial product, Autex World Conference, Ljubljana, Slovenia (2016).
- [2] E. Lempa, M. Rabe, L. Van Langenhove, Coating and digital printing electrically conductive paths on textiles under consideration of percolation threshold, Progress Symposium, Bursa, Turkey (2019).
- [3] M. Wagih, Direct-Write Dispenser Printing for Rapid Antenna Prototyping on Thin Flexible Substrates, *14th European Conference on Antennas and Propagation (EuCAP)* (2020) 1-4, Information on: <https://doi.org/10.23919/EuCAP48036.2020.9135625>.
- [4] Y. Wei, X. Wang, R. Torah, J. Tudor, Dispenser printing of electrochromic display on textiles for creative applications, *Electronics Letters*. 53 (2017) 779-781. Information on: <https://doi.org/10.1049/el.2017.0119>.
- [5] T. Greig, R. Torah, K. Yang, Investigation of the Effects of Ink Pigmentation on Substrate Profiling for E-Textile Dispenser Printing, *IEEE International Conference on Flexible and Printable Sensors and Systems (FLEPS)*. (2021) 1-4. Information on: <https://doi.org/10.1109/FLEPS51544.2021.9469756>.
- [6] L. Hyosang et al, Dispenser printing of piezo-resistive nanocomposite on woven elastic fabric and hysteresis compensation for skin-mountable stretch sensing, *Smart Mater. Struct.* 27 (2018) 025017
- [7] T. Greig, R. Torah, K. Yang, Investigation of Nozzle Height Control to Improve Dispenser Printing of E-Textiles. *Proceedings*. 68 (2021) 6. Information on: <https://doi.org/10.3390/proceedings2021068006>.
- [8] M. Rabe et al., Entwicklung selektiv wirksamer Adsorbentextilien zur Entfernung organischer Verbindungen aus Trinkwasser, *Man made fibres congress*, Dornbirn, Austria (2013).
- [9] F. Gubbels et al., Selective Localization of Carbon Black in Immiscible Polymer Blends: A useful tool to design electrical conductive composites, *Macromolecules*. 27 (1994) 1972-1974.
- [10] W. Bobeth, *Textile Faserstoffe, Beschaffenheit und Eigenschaften*, Springer Verlag, Berlin (1993) S. 302-307.
- [11] M. Rabe, *Funktionalisierung als Plattform zur Erzeugung innovativer Technischer Textilien*. Habilitationsschrift, TU Dresden (2017) S. 115. ISBN: 978-3-95908-104-7.
- [12] D. Stauffer, Scaling theory of percolation clusters, *Physics Reports*. 54 (1979) 1-74.

- [13] Y. Mamunya et al., Electrical and thermal conductivity of polymers filled with metal powders, *European Polymer Journal*. 38 (2002) 1887-1897.
- [14] W. Rehnby et al., Coating of textile fabrics with conductive polymers for smart textile applications (Published Conference Proceedings style), in *Proc. Ambience'08 Conf.*, Boras, Sweden (2008).
- [15] K. Kalaitzidou et al., A Route for Polymer Nanocomposites with Engineered Electrical Conductivity and Percolation Threshold, *Materials*. 3 (2010) 1089-1103.
- [16] I. Chodak, I Krupa "Percolation effect and mechanical behavior of carbon black filled Polyethylene", *Journal of Materials Science Letters*, 18 (1999) 1457-1459.
- [17] M. Akerfeldt et.al, Electrically conductive textile coating with a PEDOT-PSS dispersion and a polyurethane binder, *Textile Research Journal*. 83 (2013) 618-627.
- [18] E. Lempa et al. "Electrically conductive textiles under consideration of percolation threshold and polymer crystallinity", *AUTEX Gent, Belgium, Conference Proceedings* (2019).

Novel Knitting Vision - Modern Ways for Integral Knitting of Intelligent Gloves for Tactile Internet Applications

Florian Wieczorek^{1,2,a*}, Hans Winger^{1,2,b}, Philippa Böhnke^{1,2,c},
Jens Wagner^{2,3,d}, Eric Häntzsche^{1,e}, Andreas Nocke^{1,2,f}, Iris Kruppke^{1,2,g},
Chokri Cherif^{1,2,h}

¹TU Dresden, Institute of Textile Machinery and High Performance Material Technology (ITM), Germany

²TU Dresden, Centre for Tactile Internet with Human-in-the-Loop (CeTI), Dresden, Germany

³TU Dresden, Chair for Circuit Design and Network Theory (CCN), Dresden, Germany

^aflorian.wieczorek@tu-dresden.de, ^bhans.winger@tu-dresden.de,

^cphilippa.boehnke@tu-dresden.de, ^djens.wagner@tu-dresden.de,

^eeric.haentzsche@tu-dresden.de, ^fandreas.nocke@tu-dresden.de, ^giris.kruppke@tu-dresden.de,
^hchokri.cherif@tu-dresden.de

Keywords: Weft knitting, smart textile, tactile Internet, conductive yarn, abrasion effects, e-textiles

Abstract. The internet of things is a key driver for new developments in the fields of medicine, industry 4.0 and gaming. Consequently, the interaction of virtual and real world by smart interconnecting of devices in our everyday life is the basis idea of the Cluster of Excellence "Centre for Tactile Internet with Human-in-the-Loop" (CeTI) at TU Dresden. To enable a user-centric approach in CeTI innovative textile structures, mainly knitted smart gloves, and their functionalization by integration of sensors and sensory yarns are focus of research activities.

Introduction

The current Internet has created a key infrastructure component for our modern world, touching almost every aspect of our daily lives. The Internet democratized access to information and has enabled emerging economies to participate in the modern global economy. We are now approaching the next big wave of Internet innovation: the Tactile Internet. The IEEE standard P1918.1 defined the Tactile Internet as following: "A network or network of networks for remotely accessing, perceiving, manipulating or controlling real or virtual objects or processes in perceived real time by humans or machines." [1] Beyond the standard IEEE definition of the Tactile Internet, the key mission of CeTI project [2] at TU Dresden is to discover the new frontiers of the Tactile Internet with Human-in-the-Loop (TaHiL). By explicitly integrating human goal-oriented perception and action as well as human development and expertise as subfields of research into the new technological breakthroughs, TaHiL will allow human users to immerse themselves into virtual, remote, or inaccessible real environments to exchange skills and expertise.

Therefore, new functions (e.g. strain, movement and position detection, haptic feedback [3]) are being integrated into smart textiles (e.g. smart gloves, suits) within CeTI, for human-in-the-loop applications as a communication tools between virtual world and real world. Fundamental interactions between humans and machines, e.g. robots, become possible by the use of smart textiles with integrated sensors and actuators for haptic/tactile user-feedback.

One of the main objects of investigation is an interface device in form of a smart glove, which controls robotic hands and virtual objects. These gloves are manufactured with textile-integrated sensors and leads using electrically conductive yarns. These yarns are used to implement resistive strain sensors that change its resistance during finger flexion. Several developments are necessary for the production of these kind of knitted smart gloves. On the one hand, the damage to the electrically conductive yarn during processing must be investigated, and on the other hand, there are various binding aspects that must be taken into consideration which have a significant influence on the

integrated strain sensor's measurement behaviour. In addition, some manual reworking is still necessary (such as the embedding of electronic components), because especially electrical interconnecting of conductive yarns with conventional circuit boards has not yet been automated.

Materials and Machines

The aim of this project is to develop a smart glove with directly integrated textile sensor technology, which will be extended by an actuator system at a later stage. For this purpose, it is important that the processed electrically conductive yarns are tested for their suitability. This includes, among other things, the knitability depending on the binding technique and the damage potential during processing. Use properties of electrically conductive yarns such as washability [4 – 6] have already been investigated and are not the focus of the investigations here. Two electrically conductive yarns are used for these investigations, a silver-coated PA yarn (Y1) is compared with a stainless steel/polyester hybrid yarn (Y2 cf. Table 1). Within Table 1, the electrical resistance according to the data sheets is compared with measured resistance in unstrained condition of the yarn. For this purpose, an average of 20 samples is taken directly from the bobbin (reference yarn) to perform four-wire resistance measurement. [7, 8]

Table 1 Overview of the yarns used and their basic electrical resistances [7, 8]

	manufacturer/ type/ yarn count	material	linear resistance [Ω/m]	
			data sheet	measured
Y1	Statex – Shieldex 117/17 dtex 2PLY HC+B	PA, Ag-coating	< 300.0	138.6
Y2	Amann – Steel-tech 100 930 dtex	PES, stainless steel	< 90.0	90.0

For the non-conductive basic structure of the smart glove, a polyamide 6.6 yarn (2x78 dtex) as base material is plated with a elastane yarn (135 dtex). For the production of gloves flat knitting machines Shima Seiki SWG 091N2 (gauge E15) [9] and Karl Mayer Stoll ADF 530-32 BW multi gauge (gauge E7.2) [10] are used. The Stoll ADF machine is used for the investigations into the damage behavior of the yarn, as this machine can handle all common feed variants. The Shima SWG has more specialized feeding elements and the results can therefore be transferred less easily to other machine types.

Yarn Damage

Method. The yarn infeed on flat knitting machines is generally from the rear to the front. The bobbins are generally arranged behind the working station and the yarn guides. Above the machine, the feeding elements, yarn control units and feeders are arranged in a superstructure. These elements form the different feed variants (FV). For the investigations, only the paths up to the yarn guides are considered, as in further tests the yarn guide, the needles, the needle bed and the fabric take-off are investigated individually. This is intended to determine crucial machinery components responsible for any yarn damage. In addition, the yarn take-off speed is varied so that different machine speeds can be mapped. The machine elements of each feed variant are listed below:

- FV I: bobbin – feeding elements – Karl Mayer Stoll ADF yarn control unit
- FV II: bobbin - feeding elements – storage feeder Memminger-Iro MSF-3 [11] - Karl Mayer Stoll ADF yarn control unit
- FV III: bobbin - feeding elements – electronic yarn feeder Memminger-Iro EFS920 [12]

The main differences of the used devices are the different modes of action and therefore incoming specific yarn damage. On the yarn control unit (Karl Mayer Stoll Textilmaschinenfabrik GmbH – ADF yarn control unit) the yarn is stressed abrasively by disc brakes and the knot monitor, on the tension unit by yarn accelerations and small deflection angles. On the winding body of the storage feeder (Memminger-Iro GmbH – MSF 3), the yarn is wound by a force controlled winding transport

system. This system has the advantage that no stretching movement of the yarn is caused by the winding of the storage feeder. In contrast, the electronic yarn feeder EFS 920 (Memminger-Iro GmbH) winds the yarn by means of the rotation of a yarn wheel. The geometry and design of the winding body and yarn wheel have different characteristics and therefore indicate results in differences to the damage potential.

Results and discussion. Two yarns with different textures were tested, a silver-coated yarn (Y1: cf. Table 1) and a stainless steel/polyester hybrid yarn (Y2). Regarding the yarn construction, it is to be expected that the damage potential differs enormously between the two variants. The silver coating (which generates the electrical conductivity) of yarn Y1 is inevitably more susceptible to abrasion [13], compared to a yarn that gets its electrical properties from the fiber material alone. The yarn Y2 did not receive any significant damage from the feed variant to the knitting machine, the resistance is approx. $90 \Omega/\text{m}$ for all samples (Fig. 1). It can be observed that the resistance depends on the processing speed and its value at 1.4 m/s is on average 2.4% higher than at 1.0 m/s . This could be related to abrasion of the finishing [14], that can be seen in the SEM images (Table 2). It is exemplified that the fibres of the reference yarn have a strong adhesion and are closer to each other than after processing which led to the slight separation for all three feed variants FV I-III.

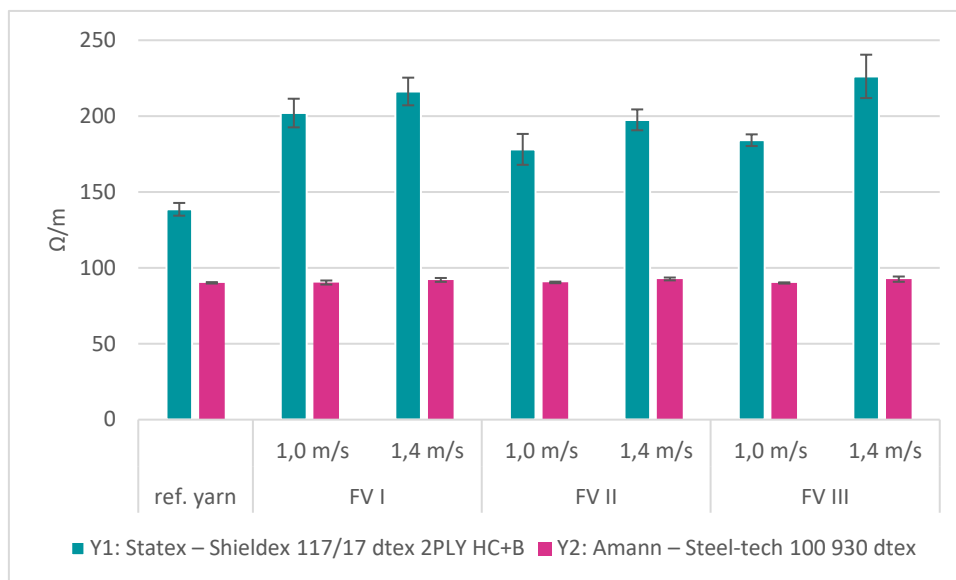
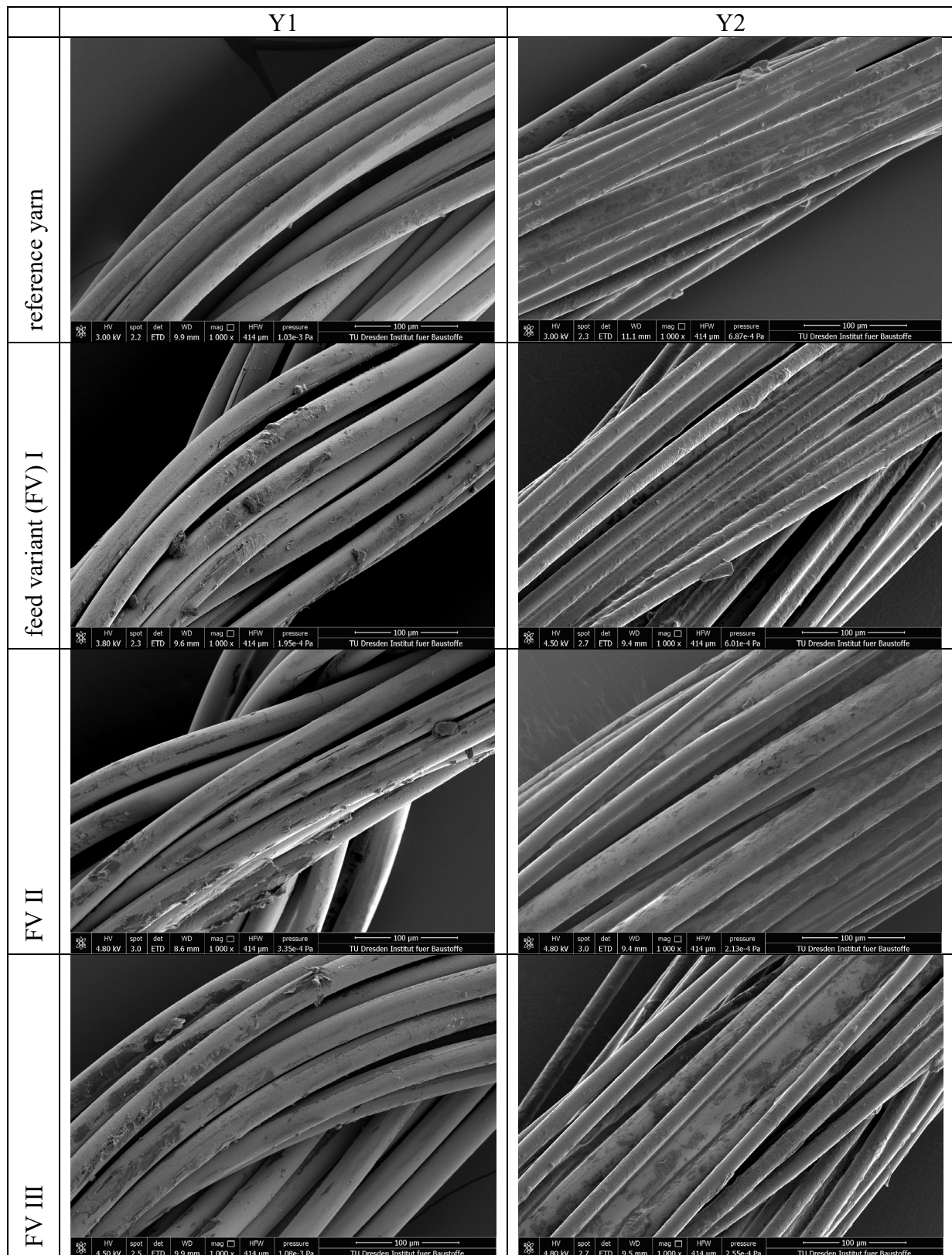


Fig. 1 Lineic resistance of yarns Y1 and Y2 depending on FV and the test speed

More significant differences can be seen with yarn Y1. Due to fiber damage at processing speed of 1 m/s the resulting resistances are on average about 35.7% and at a speed of 1.4 m/s about 53.9% higher than the reference value. These values and the SEM images demonstrate that the increase in resistance is due to damage (abrasion/tearing) of the silver coating. In addition, a correlation between the degree of damage and the test speed can be established. Furthermore, it can be seen that there is a correlation between feed variant (FV) and yarn damage. FV II has a lower impact on the resistance compared to FV I (FV I 56.0% , FV II 42.5%). In this case, the intermediate storage feeder reduces the abrasion by pulling off the bobbin more evenly. The increase in resistance at lower speed with the electronic yarn feeder (FV III) is comparable with FV II, but with an increase in speed to 1.4 m/s the resistance increases by 22.8% to $226.2 \Omega/\text{m}$. It is obvious that this effect is favored by the operating principle and the design of the feeder due to rising friction at increased speeds between the yarns, which are laid in tight coils around a yarn wheel.

Table 2 SEM images of reference yarn and the feed variants (FV) I - III tested at 1.4m/s



Summary. The investigations have shown that the damaging of the electrically conductive coating of the yarn Y1 has a high influence on resistance. Previous studies [6] have shown that an average durability of at least 10 washing cycles is given before the conductivity is significantly reduced. This effect can be transferred in parts, especially the mechanical stress, which is also generated during washing, has a high damage potential for coated yarns. Above all, the high friction with the machine parts is decisive here. The investigations have shown that even the short section between the bobbin

and the yarn carrier infeed has a significant potential for damage. On the other hand, the investigations have also shown that a yarn which is conductive solely due to its material composition (Y2) is not significantly affected by abrasion.

Binding Technique

Method. For the production of a smart glove with textile-integrated sensors for controlling virtual objects or robot arms, the previously mentioned electrically conductive yarns Y1 or Y2 (cf. Table 1) and their improvements are necessary. These are used to implement both sensors and power supply lines, and there binding-related special features that must be taken into due consideration. Thus, the design of a sensor depends on the bond, the structural and material elongation. Among other things, the following requirements are necessary for the production of a smart glove:

- Base material of knitted structure has to be electrically isolating,
- Yarn-based sensor and power supply line should be manufactured integrally on weft knitting machines,
- High elasticity of the sensory yarn to ensure dynamic movement measurement,
- Resistances:
 - Power supply lines should have low resistance ($< 20 \Omega/\text{m}$) for reducing voltage drop,
 - Integral strain sensors need high resistance change for sufficient strain sensing capability.
- Good fit - light, comfortable and thin glove.

Results and discussion. A high number of variants is necessary to assess the function of the sensor design, since the basic operating principle of the knitted sensor setup must first be verified. In order to pick up the movements of the fingers with a smart glove, yarn-based strain sensors are used within this project. The effect bases on change in resistance due to change of the electro-conductive fibers geometry during tensile straining [15]. To demonstrate the functionality of the glove and the change in resistance due to movement, this value is measured with twice for the straight (R_0) and bended (R_1) sensor within the finger of the glove. The relative change can be determined with this differential measurement (Fig. 2 II). There are different textile approaches. On the one hand, the strain sensor is made of a single yarn, since the material's resistance correlates with the strain level and thus, theoretically, a very sensitive sensor can be implemented. A major disadvantage of this sensor design is that the relaxation behavior (decrease of the resistance towards R_0) of the knitted glove structure that is plated with elastane causes a faster relaxation and differs from the non-plated sensor yarn. In contrast, meshed yarn-based strain sensors offer higher structural integrity level, which has a positive effect on the relaxation behavior of the sensor. The principle, the structure of the conductive elements in Fig. 2 I consists of sensor lines (c) and power supply lines (d) which differ in their cross-section geometry and their resistance. The length of the sensor extends to the finger joint (b) with the subsequent power supply line (d), which extends to the structure-integrated electronics. Due to the anatomy of the hand, the length of the individual sensors and supply lines per finger differs. By varying the binding elements (stitch, tuck stitch, integrated warp yarn), sensors with different straining behavior and resistances can be implemented. Thus, the thickness of the sensor and the power supply lines (Fig. 3 G1 and G2) is relevant. Here, limited by the finger width and the binding structure, the respective thickness can be varied between one and three stitches in width. It can be assumed that a thicker power supply line has a lower resistance and thus a minimized unintentional influence on the strain measurement of the major strain sensing area of the integral sensor. In addition, the total resistance is significantly higher using a narrow design of the active measuring sensor lines (c), cf. Table 3. Another significant influencing factor is the use of the binding elements. Thus, the output resistance, for the structures with narrow/thin sensor, is significantly higher than for G1. By bending the finger and measuring the change in resistance, it is clearly visible that there are significant

bond-related differences. For example, plating with the base material causes the sensor structure to solidify, so that a strain-induced change in resistance is marginal. However, because a strain sensor requires a high change in resistance to resolve different finger positions reliably, plating with elastane (G3) is more effective. This sensor design also favors a higher sensitivity of the sensor. As an additional parameter, the yarn material for the sensor is varied. Y1 and Y2 are equally suitable for the functionality of the strain sensor. However, the haptic feel of the structures differs, as the material combination of Y2 results in a noticeably harder and slightly stiffer sensor design.

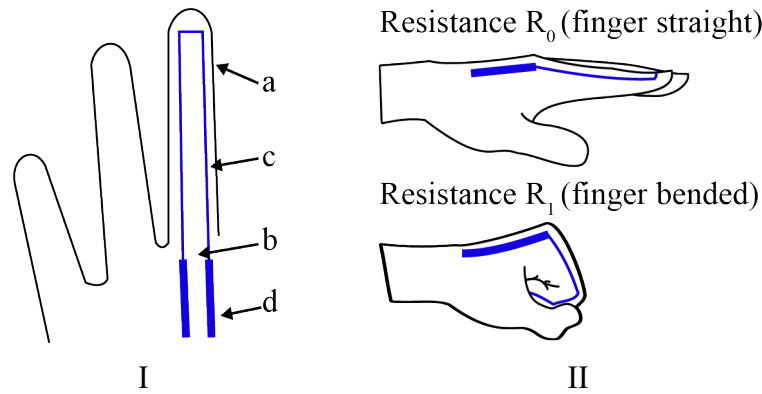


Fig. 2 Scheme of the glove (I) with resistive sensor finger (a), finger joint (b) and strain sensor lines (c) and power supply lines (d) and illustration of the hand positions for determining the resistance change (II)

Table 3 Change in resistance to finger flexing of the different glove versions

	G1	G2	G3	G4
Resistance R_0 finger straight [Ω]	25	78	80	98
Resistance R_1 finger bended [Ω]	29	97	107	103
Relative $\Delta R/R$ change [%]	18	24	34	5



Fig. 3 Different knitted sensor designs Intarsia (G1), Intarsia (different layout; G2), plated with elastane (G3), plated with base material (G4)

Summary. The manufacturing of a smart gloves with textile-integrated sensors is subject to many parameters. It can be stated that the sensor behavior is influenced by the bonding elements, the integration into the carrying knitted structure, the geometry of the sensor threads and the materials. One of the most important findings is that the electrically conductive material must be integrated into the structure and must also have similar elasticity (means by plating with elastane), otherwise the relaxation behavior of the basic structure and the sensor will be different. Due to this different

mechanics, the finger movement cannot be clearly identified by resistance measurement in real time and perspective the control of a robot becomes inaccurate.

Conclusion and Outlook

Integrally manufactured smart textiles, such as smart gloves, can be produced using flat knitting technology. Textile-based resistive strain sensors and the power supply lines can be integrated into the knitted structures during fabric formation process. The selection of a suitable and durable electroconductive yarn material is crucial, because it can be damaged during processing. This damage is increased due to the usage of smart textiles (ageing due wearing), so it is important to develop novel coatings that make the yarn more durable against abrasion during processing and usage. Here, a compromise must be found between abrasion resistance and textile processability, because that higher the coating thickness that higher the yarn stiffness which reduces the diversity of knitting [13]. However, this is necessary to develop sensors with improved usage properties. Since only through an increased abrasion resistance, or a non-aging yarn resistance, despite processing and use of the yarn, a sensor with a long service life can be implemented. Within further test series, the dynamic sensor behavior has finally to be analyzed by recording the signal course of the integrated strain sensor during several load cycles of the sensor glove. Furthermore, the binding technology of the gloves/sensors will be further investigated in order to develop even more sensitive systems. The damage of the electrically conductive yarns during the knitting process will be further investigated. On the one hand, the damage caused by the yarn guide, but also by the needles and the take-down will be examined. Another important object of investigation will be focused on methods and types of electrical interconnection between the textile component and rigid electronic components.

Acknowledgment

Funded by the German Research Foundation (DFG, Deutsche Forschungsgemeinschaft) as part of Germany's Excellence Strategy – EXC 2050/1 – Project ID 390696704 – Cluster of Excellence “Centre for Tactile Internet with Human-in-the-Loop” (CeTI) of Technische Universität Dresden.

References

- [1] IEEE: The IEEE Tactile Internet Standards Working Group (IEEE 1918.1). (ti.standards.comsoc.org/) (2017)
- [2] Technische Universität Dresden: CeTI - Centre for Tactile Internet with Human-in-the-loop. <https://www.ceti.one/>, (18.02.2021)
- [3] F. Wiczorek; H. Winger; C. Sachse; Q. Bollengier; W. Trümper; A. Nocke; C. Cherif: Knitted products for human-in-the-loop applications. Aachen-Dresden-Denkendorf International Textile Conference, Dresden (28. - 29. November 2019), S.263ff.
- [4] V. Gaubert; H. Gidik; N. Bodart; V. Koncar: Investigating the Impact of Washing Cycles on Silver-Plated Textile Electrodes: A Complete Study. *Sensors (Basel, Switzerland)* 20(2020)6,
- [5] S. U. Zaman; X. Tao; C. Cochrane; V. Koncar: E-Textile Systems Reliability Assessment-A Miniaturized Accelerometer Used to Investigate Damage during Their Washing. *Sensors (Basel, Switzerland)* 21(2021)2,
- [6] S. uz Zaman; X. Tao; C. Cochrane; V. Koncar: Launderability of Conductive Polymer Yarns Used for Connections of E-textile Modules: Mechanical Stresses. *Fibers Polym* 20(2019)11, S. 2355-2366
- [7] Amann & Söhne GmbH & Co. KG: Steel-tech. <https://www.amann.com/de/produkte/steel-tech/>, (16.09.2021)

-
- [8] Statex Produktions- und Vertriebs GmbH: Shieldex® 117/17 x2 HCB – Shieldex® – Metallized Technical Textiles – + datasheet. <https://www.shieldex.de/products/shieldex-117-17-x2-hcb/>, (15.12.2021)
- [9] SHIMA SEIKI MFG., LTD.: SWG021N2/041N2/061N2/091N2 WHOLEGARMENT Knitting Machines. https://www.shimaseiki.com/product/knit/swg_n2/, (16.09.2021)
- [10] KARL MAYER STOLL Textilmaschinenfabrik GmbH 2021: ADF 530-32 ki. <https://www.stoll.com/en/machines/adf-family/adf-530-32-ki/>, (16.09.2021)
- [11] MEMMINGER-IRO GMBH: Memminger-Iro - Products - Circular knitting machines - Feeders - MSF 3. <https://www.memminger-iro.de/en/fournisseure/msf-3.php?thisID=181>, (16.09.2021)
- [12] MEMMINGER-IRO GMBH: Memminger-Iro - Products - Seamless machines - Feeders - EFS 920. <https://www.memminger-iro.de/en/fournisseure/efs-920.php?thisID=179>, (16.09.2021)
- [13] SCHÄL, P.; JUHÁSZ JUNGER, I.; GRIMMELSMANN, N.; MEISSNER, H.; EHRMANN, A.: Washing and Abrasion Resistance of Conductive Coatings for Vital Sensors. In: KYOSEV, Y.; MAHLTIG, B.; SCHWARZ-PFEIFFER, A. (Eds.): *Narrow and Smart Textiles*. Cham: Springer International Publishing, 2018. – ISBN 978-3-319-69049-0, pp. 241-250
- [14] T. Textor; L. Derksen; T. Bahnert; J. S. Gutmann; T. Mayer-Gall: Abrasion resistance of textiles: Gaining insight into the damaging mechanisms of different test procedures. *Journal of Engineered Fibers and Fabrics* 14(2019), S. 155892501982948
- [15] C. Breckenfelder: *Mobile Schutzassistenz*. Wiesbaden: Springer Fachmedien Wiesbaden, 2013. – ISBN 978-3-658-01127-7

Development of Actuator Networks by Means of Diagonal Arrangements of Shape Memory Alloys in Adaptive Fiber-Reinforced Plastics

Moniruddoza Ashir^{a*}, Andreas Nocke^b and Chokri Cherif^c

Institute of Textile Machinery and High Performance Material Technology, Faculty of Mechanical Science and Engineering, Technische Universität Dresden, Dresden, Germany

^amoniruddoza.ashir@tu-dresden.de, ^bandreas.nocke@tu-dresden.de,
^cchokri.cherif@tu-dresden.de

Keywords: Adaptive fiber-reinforced plastics, shape memory alloys, weaving.

Abstract. Adaptive fiber-reinforced plastics (FRP) contain actuators that enable the controlled modification of system states and characteristics. The textile-technical integration of actuators, in particular shape memory alloys, into reinforcing fabrics has increasingly been applied in recent years. The objective is to achieve optimum force transmission from shape memory alloy to FRP, long-term stability of adaptive FRP as well as a maximum degree of deformation. This paper presents the development of actuator networks for adaptive FRP, where two shape memory alloys are integrated into reinforcing fabrics by means of open reed weaving technology. After infusion of the functionalized reinforcing fabrics, the deformation behavior of adaptive FRP was characterized with variable actuator switching frequencies (≥ 1 Hz) or actuator activation times (≤ 1 s).

Introduction

Particularly in the last 20 years, fiber-reinforced plastics (FRP) have been used extensively as promising materials for resource-saving mobility. Due to their high stiffness at low mass compared to traditionally used materials, FRP are applied as load-bearing structures for the most dominant modes of transport, such as aviation, road, rail, or ship transport [1]. However, FRP can be used more efficiently and economically by integrating actuator materials for the realization of form variable structures.

Shape memory alloys (SMA) as actuator materials can realize the form variable FRP structures. SMA have the special property of "remembering" their original shape after a permanent plastic deformation below a certain critical temperature by heating them above this temperature. This phenomenon is termed shape memory effect (SME) [2], which is also found in shape memory ceramics (SMC) and shape memory polymers (SMP) [3,4]. However, SMA are more suitable for FRP applications compared SMC and SMP as they offer numerous advantages including considerably higher usable specific energy densities ($2 \cdot 10^3$ J/kg), high actuation stress (10 MJ/m³), malleability, faster response due to thermally induced activation by joule heating, and stability in the high temperature phase [2,5,6]. By means of structurally integrated SMA, single-axis and intrinsic adaptive FRP components can be realized, reducing the number of necessary parts and joints, and therefore resulting in significantly lower assembly costs.

In recent years, research on SMA regarding their application in FRP gained a lot of attention within the composite community [7-11]. In all research efforts, SMA have only been embedded into the matrix of FRP structures. However, to ensure proper force transmission from SMA to FRP and to reduce the delamination of SMA in FRP, it is necessary to integrate SMA into reinforcing fabrics using textile technology.

In previous works carried out by the authors, the textile technical integration of SMA into reinforcing fabrics was implemented by means of the rapier weaving technology [12 – 17] and open reed weaving (ORW) technology [18 – 20]. The suitability of adaptive FRP for use in fast application scenarios has not been reported until now. Hence, this paper reports the deformation behavior of adaptive FRP variable actuator switching frequencies (≥ 1 Hz) or actuator activation times (≤ 1 s).

Materials and Methods

Materials. A market-available SMA wire (Alloy H ox. sa., Memry GmbH, Germany) with a diameter of 0.305 mm and transition temperature of 95-110°C was used in this study for the development of functionalized reinforcing fabric. The wire-shaped SMA was coated with the separating agent Dexcoat 8 (Tag chemicals, Germany) to ensure free and even mobility of SMA within FRP in order to fully exploit the deformation capability of SMA and therefore to increase the deformation potential of FRP structures. The reinforcing material is based on glass fiber rovings (Glasseiden GmbH Oschatz, Germany) of finesses of 1200 tex. In order to prevent the SME during the infusion process, a cold-curing thermosetting matrix system was used. Hence, the commercially available resin system MGS® RIMR 135 was combined with the curing agent RIMH® 137 (Hexion, USA). To increase the flexibility of the matrix material, the modifier Heloxy (Hexion, USA) was mixed with the resin system at a ratio of 7:3 for fabrication of adaptive FRP. Therefore, resin and curing agent were mixed at a ratio of 10:2.4 instead of 10:3.

Development of functional reinforcing fabrics. The functionalized reinforcing fabrics with variable cross-section (pliable area and rigid area) were produced on a rapier weaving machine PTS 4/SOD including two ORW units (Lindauer Dornier GmbH, Germany). The aim of the variable cross-sectional structure is the development of structure integrated joint to increase the deformation potential of adaptive FRP. Here, one set of warp yarn and three set of weft yarn were used. In rigid areas of fabric, three layers of weft yarn are interlaced with one set of warp yarn as angle-interlock weave basis. In the pliable area, every first weft yarn is plain interwoven with warp yarns, while the other two float underneath the woven fabric. By cutting the floating weft yarns of 100 mm length, the variable cross-sectional structure were formed. The SMA was interlaced with weft yarns every 20 mm. The face side of the developed functional reinforcing fabric is shown in Fig. 1.

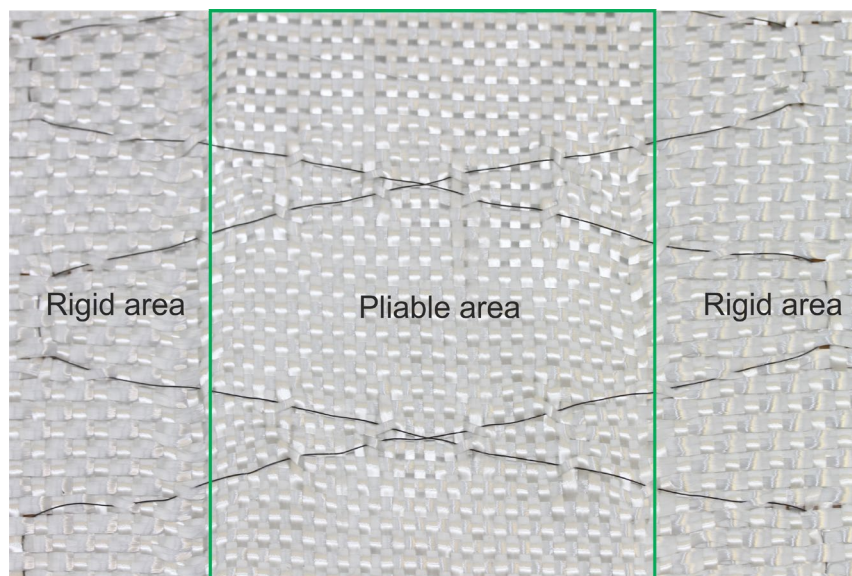


Fig. 1: Face side of the functionalized reinforcing fabrics with SMA. Pliable area is shown by green box.

Impregnation. In a next process step, the functionalized reinforcing fabrics were infused by Seemann Corporation Resin Infusion Molding Process (SCRIMP). Prior to infusion the fabrics were prepared by isolating both SMA in their crossing point using heat shrinking tube as shown in Fig. 2. The free end of the SMA were fixed by screws to the functionalized reinforcing fabrics to prevent slippage of the SMA during thermal induced activation. After the infusion process, the sample were cured for 15 h in a laboratory oven at 50°C to guarantee a proper cross-linking reaction between resin and hardener. Later, the sample were cut using a laboratory wet saw in a size of 240 mm x 30 mm.

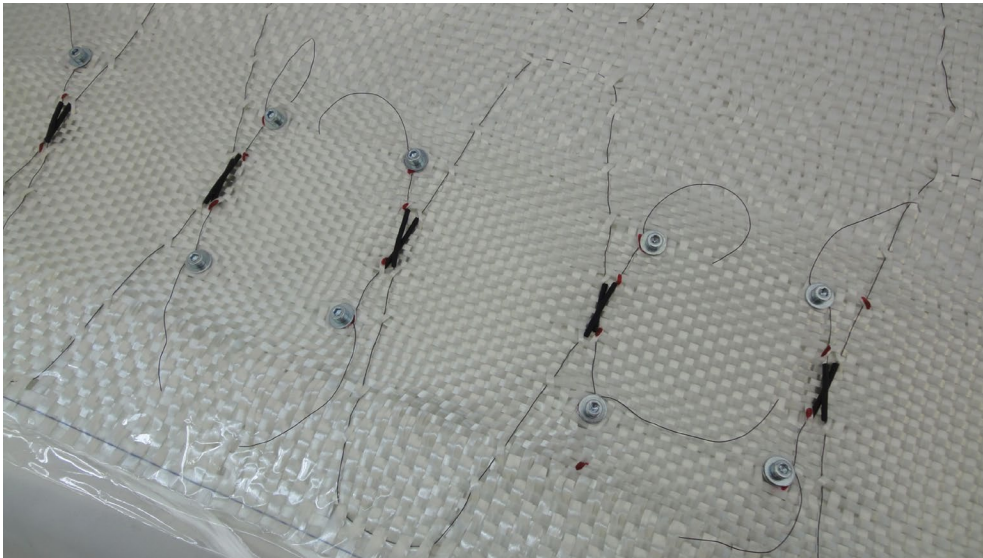


Fig. 2: Preparation of functionalized reinforcing fabrics before infusion.

Characterization of adaptive FRP. An experimental setup for the characterization of adaptive FRP is shown in Fig. 3. A laser triangulator of type LJ-V7200 of (Keyence, America) was used for data collection during thermal induced activation of SMA. The laser triangulation system and the adaptive FRP to be measured were mounted on the test stand. A laboratory power supply unit of type HMP4040 (Rohde & Schwarz GmbH & Co. KG, Germany) realizes the current supply and is equipped with a current controlling system. Thereby, a constant heating (with current flow) and cooling cycle (no current flow) can be set. The surface temperature of adaptive FRP was recorded with an infrared camera of type FLIR E95 24° (FLIR, Estonia). The frame rate of the IR camera during the test is 30 frames/s.

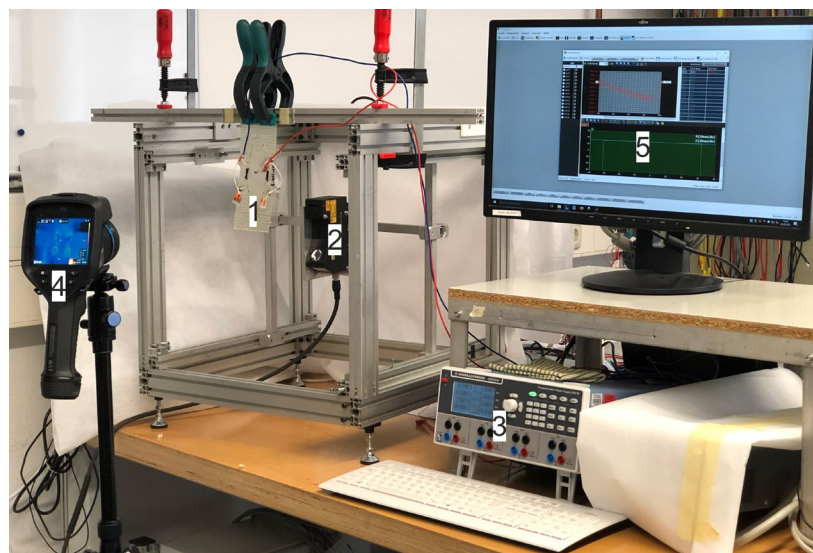


Fig. 3: Test set-up for the characterization of adaptive FRP. 1...adaptive FRP, 2...laser triangulator, 3...power supply unit, 4...infrared camera, 5...data processing.

Results and Discussion

The analysis of the dynamic characteristics of adaptive FRP was performed with variable actuator switching frequencies (≥ 1 Hz) or actuator activation times (≤ 1 s). Example deformation curves of adaptive FRP with activation times in the range 0.2 to 0.8 s at 4.5 V activation voltage are shown in Fig. 4 and the corresponding evaluation in Fig. 5.

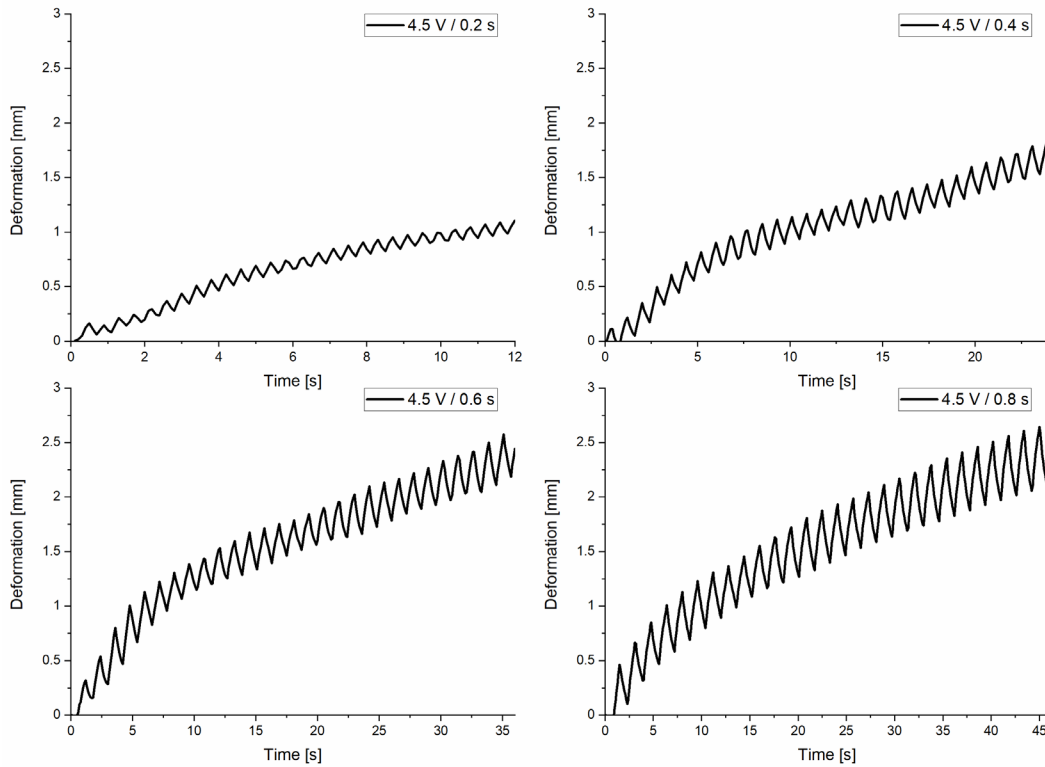


Fig. 4: Deformation curves of adaptive FRP with variable activation time from 0.2 to 0.8 s at an activation and deactivation voltage of 4.5 V and 0 V, respectively.

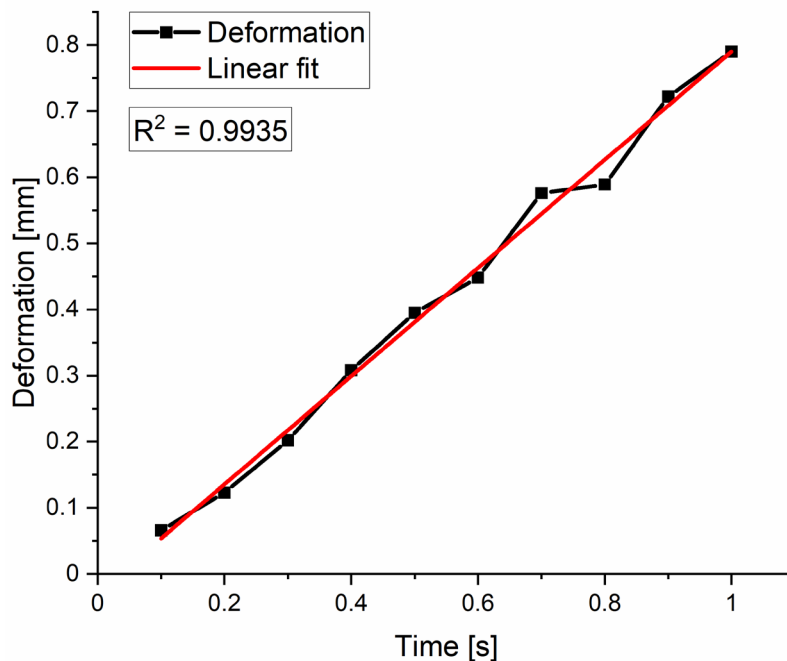


Fig. 5: Relationships between maximum deformation of adaptive FRP and the activation time.

The results show an approximate proportionality between maximum deformation and activation time of adaptive FRP. Thus, the basic proof of adaptive FRP's suitability for use in fast application scenarios is given (≥ 1 Hz), in particular when only small deformations are required. In such applications, the thermal transient behavior should be taken into account, which is indicated in the investigations by a continuous drift of the mean deformation position. This phenomenon can be compensated by active control or sufficiently long run-in times.

Supplementary investigations to analyze the dynamic effects were carried out with the aim of quantifying the influence of activation voltage on achievable deformation paths in this type of fast setting process. For this purpose, the applied voltage was successively increased from 4.5 V to 6 V at an activation time of 1 s and the resulting deformation of adaptive FRP was recorded. The deformation curves are shown in Fig. 6.

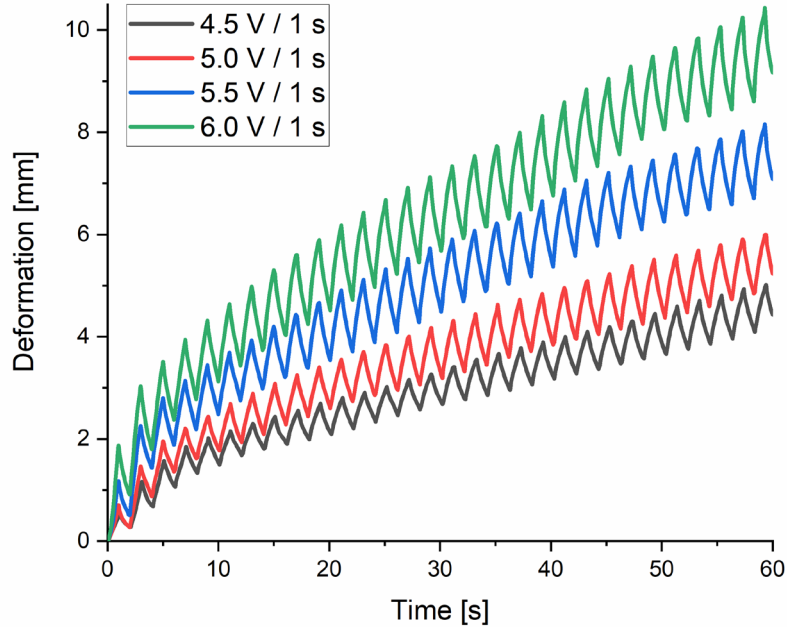


Fig. 6: Deformation curves of adaptive FRP with the activation time of 1 s at varying activation voltages from 4.5 V to 6 V.

The corresponding processed information is shown in Fig. 7 and indicates a linear relationship between applied voltage and resulting deformation of adaptive FRP.

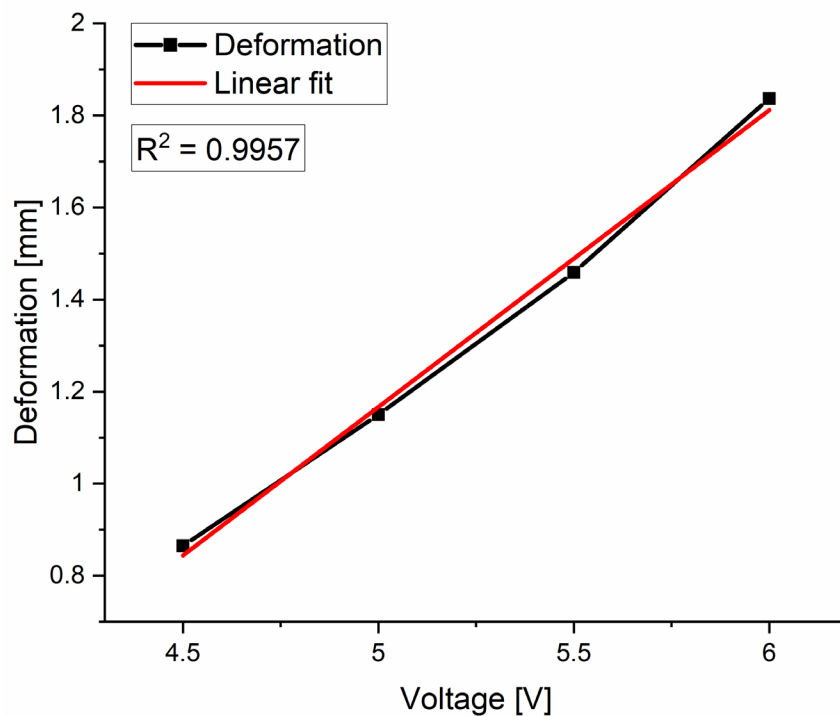


Fig. 7: Relationship between voltage and deformation of adaptive FRP.

The relationship between applied voltage to SMA and resulting deformation of adaptive FRP shown in Fig. 7 is due to the increasing heat input at higher voltage (Joule heating), thus the stronger activation of the SMA. This phenomenon is also confirmed by the near-surface temperature measurements using a thermal imaging camera. The maximum voltage of 6 V considered here produces a temperature of 92°C, which is very close to the transition temperature range of the SMA (95–110°C) used. Thus, the possible maximum deformation for the developed structure with the activation time of 1 s is achieved.

Summary

An actuator network of adaptive FRP was developed by realizing functionalized reinforcing fabrics with diagonal arrangements of two SMA by means of open reed weaving technology. The adaptive FRP were characterized considering their deformation behavior with variable actuator switching frequencies (≥ 1 Hz) or actuator activation times (≤ 1 s) for fast application scenarios. Results reveal an approximate proportionality between maximum deformation and activation time of adaptive FRP. Potential applications scenarios of the developed adaptive FRP are aerodynamic flaps or rudders, medical applications for humanoid kinematics, gripping and tensioning devices or sealing devices (targeted shut-off and control of fluids).

Acknowledgements

The IGF research project 20786 BR of the Forschungsvereinigung “Forschungskuratorium Textil e. V.” is funded through the AiF within the program for supporting the „Industriellen Gemeinschaftsforschung (IGF)“ from funds of the Federal Ministry of Economics and Energy (BMWi) by a resolution of the German Bundestag. The DFG research project 380321452/GRK2430 is supported by the Deutsche Forschungsgemeinschaft (DFG, German Research Foundation). The financial supports are gratefully acknowledged.

References

- [1] H. Amid, A. A. A. Jeddi, M. Salehi, H. Dabiryan, R. Pejman, Investigation of circular woven composite pipes, *AUTEX Res. J.* 16 (2016) 100–108.
- [2] K. Otsuka, C. M. Wayman, *Shape memory materials*, first ed., Cambridge University Press, Cambridge 1999.
- [3] A. Lai, Z. Du, C. L. Gan, C. A. Schuh, Shape memory and superelastic ceramics at small scales, *Science* 341 (2013) 1505–8.
- [4] X. Feng, G. Zhang, S. Zhuo, H. Jiang, J. Shi, F. Li, Dual responsive shape memory polymer/clay nanocomposites, *Compos. Sci. Technol.* 129 (2016) 53–60.
- [5] P. K. Kumar, C. Caer, G. Atkinson, E. Patoor, D. C. Lagoudas. The influence of stress and temperature on the residual strain generated during pseudoelastic cycling of NiTi SMA wires, *Proc. SPIE 7978, Behavior and Mechanics of Multifunctional Materials and Composites 2011*, 79781E (27 April 2011).
- [6] J. M. Jani, M. Leary, A. Subic, M. A. Gibson, A review of shape memory alloy research, applications and opportunities, *Mater. Des.* 56 (2014) 1078–113.
- [7] V. Michaud, Can shape memory alloy composites be smart?, *Scr. Mater.* 50 (2004) 249–53.
- [8] P. Bettini, M. Riva, G. Sala, L. D. Landro, A. Airoidi, J. Cucco, Carbon Fiber Reinforced Smart Laminates with Embedded SMA Actuators—Part I: Embedding Techniques and Interface Analysis, *J. Mater. Eng. Perform.* 18 (2009) 664–71.
- [9] F. Boussu, G. Bailleul, Development of shape memory alloy fabrics for composite structures. *AUTEX Res. J.* 2 (2002) 1–7.

-
- [10] A. Sofla, S. A. Meguid, K. T. Tan, W. K. Yeo, Shape morphing of aircraft wing: Status and challenges, *Mater. Des.* 31 (2010) 1284–1292
- [11] M. Ashir, A. Nocke, C. Cherif, Development of shape memory alloy hybrid yarns for adaptive fiber-reinforced plastics, *Text. Res. J.* 89 (2019) 1371–1380.
- [12] M. Ashir, J. Hindahl, A. Nocke, C. Sennewald, C. Cherif, Development of adaptive pleated woven fabrics with shape memory alloys, *Text. Res. J.* 89 (2019) 2330–2341.
- [13] M. Ashir, J. Hindahl, A. Nocke, C. Cherif, A statistical approach for the fabrication of adaptive pleated fiber reinforced plastics, *Compos. Struct.* 207 (2019) 537–545.
- [14] M. Ashir, M. Vorhof, A. Nocke, Influence of thickness ratio and integrated weft yarn column numbers in shape memory alloys on the deformation behavior of adaptive fiber-reinforced plastics, *Compos. Struct.* 215 (2019) 493–501.
- [15] M. Ashir, A. Nocke, U. Hanke, C. Cherif, Adaptive hinged fiber reinforced plastics with tailored shape memory alloy hybrid yarn, *Polym. Compos.* 41 (2020) 191-200.
- [16] M. Ashir, Activation time-and electrical power-dependent deformation behavior of adaptive fiber-reinforced plastics, *J. Compos. Mater.* 53 (20) 2777-2788.
- [17] M. Ashir, J. Hindahl, A. Nocke, C. Cherif, Development of an adaptive morphing wing based on fiber-reinforced plastics and shape memory alloys, *J. Ind. Text.* 50 (2020), 114-129.
- [18] M. Ashir, A. Nocke, C. Cherif, Maximum deformation of shape memory alloy based adaptive fiber-reinforced plastics, *Compos. Sci. Technol.* 184 (2019) 107860.
- [19] M. Ashir, C. Cherif, Development of shape memory alloy based adaptive fiber-reinforced plastics by means of open reed weaving technology, *J. Reinf. Plast. Compos.* 39 (2020) 563–571.
- [20] M. Ashir, A. Nocke, C. Cherif, Adaptive fiber-reinforced plastics based on open reed weaving and tailored fiber placement technology, *Text. Res. J.* 90 (2020) 981–990.

Effects of Stitch Density, Thread Tension and Using Conductive Yarn as Upper or Lower Thread on Reading Performance of Embroidered RFID Tag Antennas

Mujgan Nayci Duman^{1,a*}, Ismail Usta^{1,b} and Gokhan Bora Esmer^{2,c}

¹Marmara University Technology Faculty Textile Engineering Department, Istanbul, Turkey

²Marmara University Engineering Faculty Electric and Electronics Engineering Department, Istanbul, Turkey

^{a*}mnayci@yahoo.com, ^biusta@marmara.edu.tr, ^cbora.esmer@marmara.edu.tr

^{a*}ORCID ID: <https://orcid.org/0000-0002-6028-723X>

Keywords: RFID tag, embroidered antenna, conductive yarn, stitch density, thread tension, read range

Abstract. Textile-based Radio Frequency Identification (RFID) tags are widely used in different applications such as sensing, localization, and identification applications. Embroidery is one of the methods in textile-based RFID tag production. The embroidered RFID tags are generally used in the follow-up of textile raw material production and inventory, and laundry of commercial textiles. They capture the transmitted electromagnetic wave and generate a new one with a special coding that includes the required information about the item. Therefore, the fabrication parameters of the embroidered antennas are important in terms of durability, cost, and working performance. The conductivity of an embroidered antenna depends on the conductivity of the thread, stitch density, thread tension, and sewing method of the embroidery. In this study, the effect of stitch density, thread tension, and using conductive yarn as needle (upper) or bobbin (lower) thread for embroidered RFID antennas were examined using a polyester yarn twisted with stainless steel that is plain stitched on cotton fabric. The read range performances of the samples were tested with an integrated circuit (IC) by using an indoor RFID reader. It was seen that the optimised stitch density has a significant impact while it was determining the amount of conductive element due to the length of the yarn. Additionally, using conductive yarn as lower thread gave nearly 50% better results in signal strengths.

Introduction

RFID tags are the tags that allow the identification of products over radio frequency (RF) and they have been used in the textile sector for following up the production, stock control, warehousing, distribution, logistics, tracking, and supply chain management. According to the 2018 report of IDTechEx, the apparel companies using RFID tags had many administrative and financial benefits such as preventing administrative errors, theft and shipment errors, having no more multi readings, determining product details, working in combination with barcode, having efficient and instant stock tracking, obtaining 2-20% increase in sales without the need to increase stock quantity, having a reduction in no-stock problems, getting 96% increase in employee productivity, and gaining more than 98% accuracy in inventory follow-up [1]. Textile is the biggest market in RFID technology by volume with 10 billion RFID labels out of 20 billion in total sold in 2019 globally which was only 10% of the total textile market. According to 2029 forecasts, the number of sold RFID tags will continue to grow up to 102 billion units [2]. It was considered that half of the RFID tags sold in the textile market were having embroidered tag antennas. Thus, improving performances in RFID technology and decreasing tag prices are gaining importance.

Embroidery as a tag antenna is preferred in some applications while it is a fast and flexible production method due to the computerized embroidery machines. Antenna patterns are easily designed and can be applied directly to textile products with compact and cost-effective embroidery machines. The size and performance of the tag antenna can be easily obtained by changing the count of the conductive yarn or the ratio of the conductive element.

The embroidered RFID tags are used in several areas like sport, leisure, military, industry, and healthcare [3]–[10]. For example, embroidered RFID tags having wireless sensors can be integrated into a specially designed garment for monitoring vital physiological values in healthcare to transmit the readings to a healthcare professional via a smart phone or an integrated GPS module. Thus, the patients can be followed and cared for at home for reducing costs. Consequently, there is considerable interest in the development of textile-based antenna systems, along with their associated feed networks. Various advantages for these systems include ease of fabrication, the ability to change the fabrication process easily, and conformal systems that give security or safety advantages where non-conformal antennas may be damaged or cause damage.

For textile-based embroidered RFID tag antennas, fabrication parameters of the embroidered antennas are the key points for improving its technology and working performance. The stitching density determines the length of the yarn and so the amount of conducting element used on the embroidery, shown in Fig. 1a, which is related to the reflected signal strength from the tag antenna. Therefore, it has a significant effect on the reading range performance of a RFID tag [11]–[14]. Besides, thread tension has an effect on the length of the thread, and it is related to the amount of conductivity of the antenna. The ratio of the upper and lower thread tensions needs to be set perfectly to get the optimum machine tension. Optimum adjustment of both the upper and lower thread tensions provides the embroidery to have even looking on both sides of the fabric while having some effect on the length of the thread as can be seen in Fig. 1b. Moreover, the threads can break very often because of the friction between the upper and lower threads, unless their tensions are set properly [15]. Furthermore, the less conductive element the yarn on RFID tag antenna contains, the better it curves, but the antenna performance will be degraded. Therefore, by changing the conductive yarn from upper to lower thread on the machine, it is possible to get smooth curves for the conductive element to improve the performance of the antenna to decrease possible thread and needle breakings.

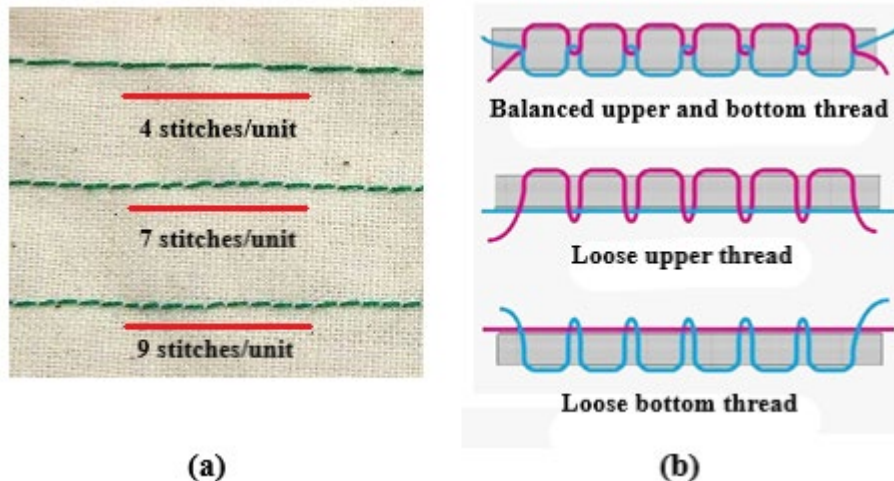


Figure 1. Schematic drawing of stitch density (a) and thread tension (b) of an embroidered yarn.

Literature survey shows that, most of the studies are related to examination of the stitch density effect and structure on improving the embroidered tag antenna performance [16]–[22]. However, thread tension and using conductive yarn as upper or lower thread are also important for antenna performance. In this study, we aimed to investigate the effect of thread tension and using conductive yarn as upper or lower thread along with stitch density in terms of gain and read range performances of the RFID tags. Although most of the studies were conducted with silver twisted or coated yarns, the tag antennas were obtained by embroidery using the stainless-steel twisted polyester yarn in this study. The reason for choosing stainless steel as a conductive element is that it does not corrode and therefore does not need extra protection coating after embroidery, which is important for minimizing the costs.

Materials and Methods

Embroidery yarns having conductive elements are commonly used in the production of RFID tag antennas while they are flexible and can be easily integrated into the product. Low dielectric constant of conductive materials reduces the power of surface waves and provides better frequency responses for the antennas. Several types of conductive yarns can be used as conductive materials in producing embroidered antennas as RFID tags. Synthetic fibers give better results in reflection of the electromagnetic waves than natural fibers due to their molecular structure and surface resistance.

In this work, Coats Gral AST 105 Tex anti-static polyester yarn in combination with stainless steel, 100% cotton fabric, and Pfaff Creative 1,5 computerized embroidery machine have been used in embroidered RFID tag antenna production. Read range tests were performed by using Impinj Monza 4QT IC with 800-bit memory and Alien ALR-F800-EMA RFID reader for the indoor environment in the UHF band at 868 MHz operating frequency. The IC satisfies to the EPC global Class 1 Gen 2 and ISO/IEC 18000-6C specifications. The outpower of the reader was 33 dBm during the read range and gain tests of the tags.

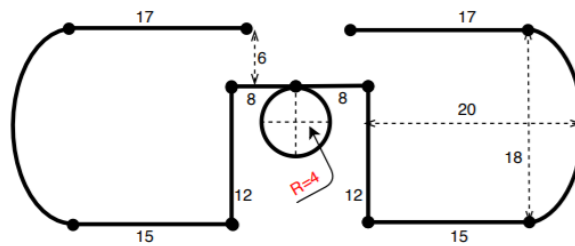


Figure 2. RFID tag antenna design and geometrical parameters (60x18 mm) used for the samples with the numbers showing the dimensions in mm.

Embroidered RFID tag antennas were produced in five different stitch densities as 2, 2.5, 3, 3.5, and 4 mm stitch lengths with RFID antenna design as in Fig. 2, which was optimized in terms of gain. All the samples were tested by attaching the IC by using the RFID reader to find the optimum stitch density to get the best tag performance in terms of read range and gain. Fig. 3 shows the measurement setup of the sample tags. Then the same antenna design was applied with the optimum stitch density in six different thread tensions (2, 3, 4, 5, 6, and 7) by using the conductive yarn as upper and then lower thread at the machine to see the effect of thread tension and conductive yarn using method as upper or lower thread on the tag performance. The samples were tested again with IC by RFID reader and their maximum read ranges were measured 0.5-5 m away in 0,5 m steps in each measurement. The maximum read range is the signal receiving distance that the reader detects the first highest gain from the tag. Also, it is expressed as the maximum reading distance.

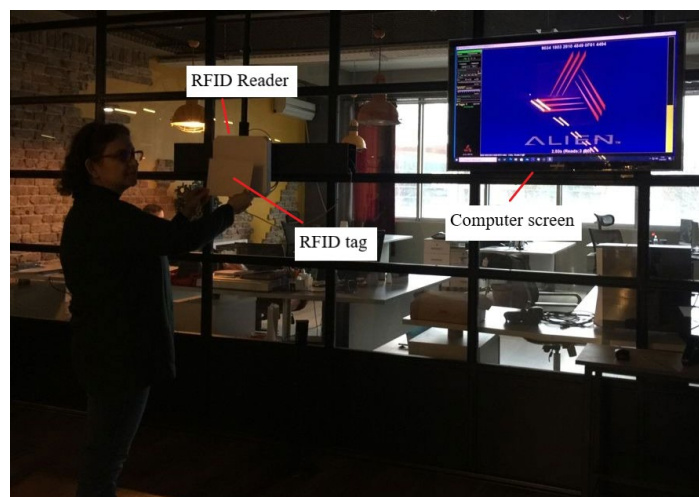


Figure 3. Measurement set up.

The maximum theoretical reading distance (r_{\max}) of the designed tag antenna was obtained with the maximum power transmission coefficient ($\tau=0.7$), was calculated with Frii's free-space equation Eq. 1 by using the parameters of the reader, reader antenna and tag given in Table 1. The parameter r_{\max} was found 27.3 m .

$$r_{\max} = (\lambda / 4\pi) \cdot (P_t \cdot G_r \cdot G_t \cdot \tau / P_{th})^{1/2} [\text{m}]. \quad (1)$$

Where P_t is the power transmitted by the reader, G_r denotes the gain of the receiving tag antenna, G_t stands for the gain of the reader antenna, P_{th} is used for minimum threshold power to power up the IC, and λ refers to wavelength. The employed wavelength is calculated as

$$\lambda = C / f [\text{m}]. \quad (2)$$

Where C is the speed of light, 299,792,458 [m/s], and f is the frequency which was taken as 865.6 [MHz].

Table 1. The technical parameters of the reader, reader antenna and tag.

READER	Type	Alien ALR F800
	Tx: Transmitted Power (P_t)	30 [dBm] = 1 [Watt]
	Rx: Received Power	-84 [dBm] = 0.000025 [Watt]
READER ANTENNA	Type	Circular
	Gain (G_t)	9 [dBi]
TAG	Chip Type	4QT IC
	Tag Materials	Steel/polyester yarn + cotton fabric
	Dimensions	60*18 [mm]
	Threshold Power (P_{th})	-17.4 [dBm] = 0.000018 [Watt]
	Gain (G_r)	2.8 [dBi]

The strength of an RF field decreases when the distance between the tag and reader antenna increases. Actual reading distance is not determined by the communication ability of the tag, but also the location and the materials, which are flexible and porous textiles, used in the antenna are significant effects.

Results and Discussion

When the embroidered tag antenna samples with five different stitch densities were tested by attaching an IC using the RFID reader, the best tag performance in maximum read range was obtained for the sample with 2,5 mm stitch length. Then the embroidered tag antennas with 2,5 mm stitch length were produced by adjusting the thread tension in six different values on the machine (2, 3, 4, 5, 6, and 7) by using the conductive yarn as upper and then lower thread on the machine.

When the test results were evaluated, it was seen that the samples with the conductive yarn as lower thread had more than 50 percent better results than the samples with the conductive yarn as upper thread. It is considered that using the conductive yarn in the bobbin as a lower thread allows the thread to be less bended during the needle movement up and down, decreases the resistance on the conductive thread, and improves the quality of reflected signal [23], [24]. The test results of the samples with conductive yarn as lower thread can be seen in Fig. 4.

The measurements were applied for 5 m distance in 0,5 m steps from the reader. The gains were noted as received signal strength indicator (RSSI) in dBm from the computer connected to the reader. After reaching the maximum static gain at its maximum read distance, the RSSI values of the tags began to fluctuate because of the interference caused by the other tags around as seen in Fig. 4. This is regulated with a computer program in daily use.

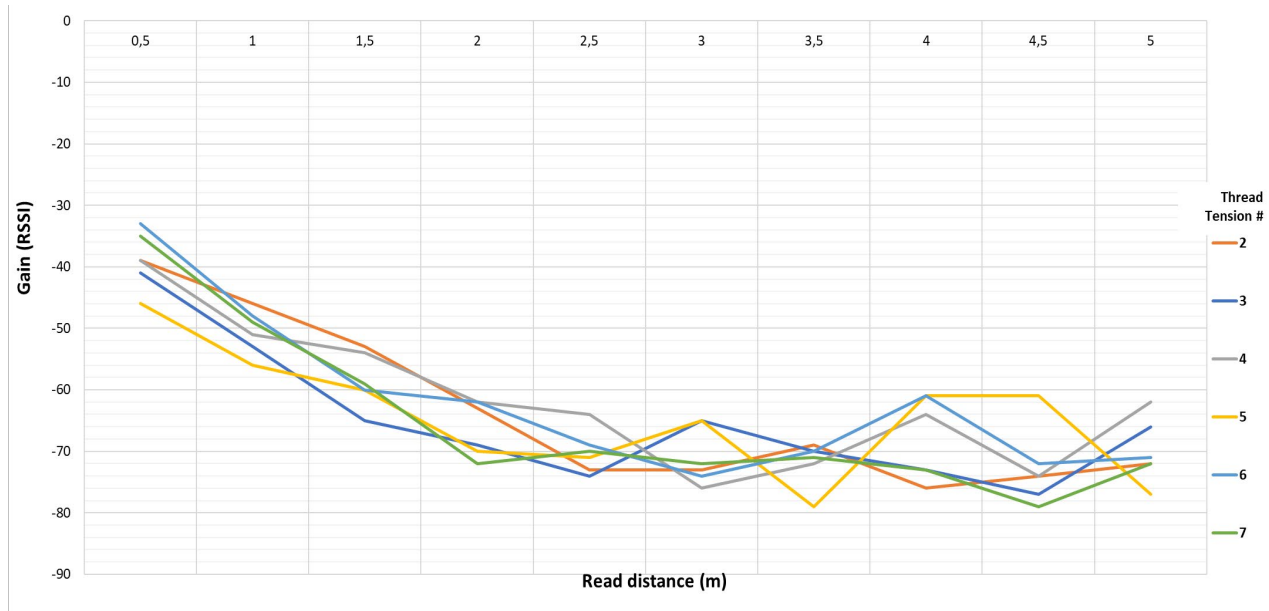


Figure 4. Received signal strength indicator (RSSI) vs. reading distance for the embroidered tag antennas with conductive yarn as lower thread.

When the gain values were considered, it was found that the maximum static gain has been obtained with the tension 4 on the machine for this yarn count as -76 RSSI, which had also the highest reading range. Read ranges of the samples with thread tensions 2 and 3 were 2,5 m, with thread tension 4 was 3 m, with thread tensions 5 and 6 were 2,5 m, and with thread tension 7 was 2 m. The calculated theoretical read range was 27.3 m. The reasons for the differences between the measured and calculated read ranges are listed below:

1. The sensitivity (Threshold Power) of the used IC may not be high,
2. A loss due to mutual coupling mismatch between RFID chip and antenna may exist (there can be no physical connection between them),
3. There may be a loss due to the used material type and dielectric substrate.

Furthermore, threads get flattened due to the tension on the yarns during the embroidery process. Then, the cylindrical shape of the threads becomes flattened and elliptical, and their widths increase. The increased surface area of the conductive yarn, as shown in Fig. 5b, improves the strength of the reflected RF signal [25], and accordingly the maximum read range increases. However, exceeding the optimum thread tension reduces the surface area of the yarn due to stretching as in Fig. 5c and so does the signal strength.

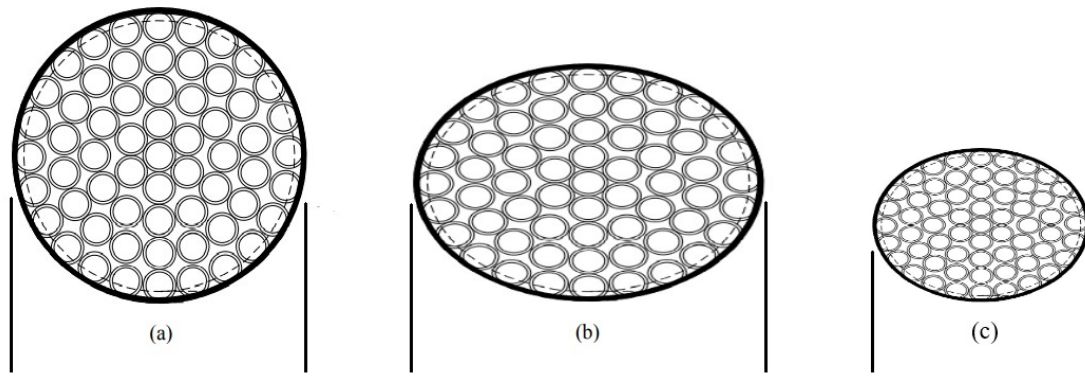


Figure 5. Schematic drawing of the cross-sectional view of the yarns with no tension (a), optimum tension (b), and maximum tension (c).

The optimum thread tension may change due to the yarn count, embroidery machine type, and needle diameter. For example, the optimum thread tension was set 3 on the Brother embroidery machine in a study, which was applied with silver coated conductive yarn [15].

Conclusion

The stitch density and the conductive yarn usage as upper or lower thread have a significant impact on the performance of the maximum reading range for the embroidered RFID tags while the thread tension has relatively less impact than the two others.

The optimum stitch density was obtained with 2,5 mm stitch length for the yarn used. The stitch density in an embroidered antenna determines the length of the yarn on the antenna and so the amount of conducting elements. However, exceeding the optimum level of the conductive yarn amount, a tag performance degradation will occur due to the surface roughness of the embroidery.

The samples with conductive yarn as lower thread had better read ranges and gain values than the samples with conductive yarn as upper thread at the embroidery machine. This is because the lower thread in an embroidery machine bends less and is subjected to less friction than the upper thread. So, these affect the strength of the received signal from the embroidered tag antenna and improve the maximum read range.

Maximum static gain (RSSI) of -76 dBm has been obtained with yarn tension 4 on the machine at a reading distance of 3 m. It is known that a typical tag's RSSI value can range from -30 to -85 dBm and the obtained gain values were ranging from -33 to -76 dBm, so it can be concluded that the tension of the yarn has no significant effect on the signal reflecting the performance of the tag antenna. However, it is important for the proper view of the stitches and also for the washing performance and strength of the embroidery.

Further studies will be performed to analyse the effects of the antenna design, conductive yarn count and tag fabric type.

References

- [1] R. Das, RFID 2018-2028:RAIN and NFC, Market Status, Outlook and Innovations, IDTechEx report (2018).
- [2] R. Das, RFID Forecasts, Players and Opportunities 2019-2029, The Complete Analysis of the Global RFID Industry, IDTechEx report (2020).
- [3] A. Rennane, A. Abdelnour, D. Kaddour, R. Touhami, S. Tedjini, Design of passive UHF RFID sensor on flexible foil for sports balls pressure monitoring IET Microwaves, Antennas Propag. 12 (2018) 2154–2160.

-
- [4] M. Mostafavi, F. Nikseresht, J.E. Resch, L. Barnes, M. Boukhechba, Collision prediction and prevention in contact sports using RFID tags and haptic feedback. arXiv Prepr. arXiv:2102.03453 (2021).
- [5] I.C. Chen, J.S. Sheu, H.L. Chen, Cloud health care system using ZigBee and RFID in SII 2017 - 2017 IEEE/SICE International Symposium on System Integration February 1, (2018) 2018-Janua 429–434.
- [6] C. Turcu, C. Turcu, RFID-based solutions for smarter healthcare. arXiv Prepr. arXiv:1705.09855 (2017).
- [7] T. Nadu, T. Nadu, Implementation of eco-friendly transport system by using Arduino Solenoid , GSM module & RFID card reader Int. J. Emerg. Technol. Eng. Res. 6 (2018) 4–6.
- [8] H. MengXuan, L. LiHua, X. LiJun, S. YanLu, J. LanYing, Application progress of RFID technology in individual animal behaviour recognition. China Poult. 40 (2018) 40–44.
- [9] J.D. Hughes, C. Occhiuzzi, J. Batchelor, G. Marrocco, Miniaturized grid array antenna for body-centric RFID communications in 5G S-band in 2020 50th European Microwave Conference, EuMC 2020 January 12, (2021) 796–799.
- [10] S.F. Khan, Health care monitoring system in Internet of Things (IoT) by using RFID in 2017 6th International Conference on Industrial Technology and Management, ICITM 2017 May 2, (2017) 198–204.
- [11] L. Ukkonen, L. Sydänheimo, Y. Rahmat-Samii, Sewed textile RFID tag and sensor antennas for on-body use in Proceedings of 6th European Conference on Antennas and Propagation, EuCAP 2012 (2012) 3450–3454.
- [12] L. Zhang, Z. Wang, J.L. Volakis, Embroidered textile circuits for microwave devices in Proceedings of the 2012 IEEE International Symposium on Antennas and Propagation (2012) 1–2.
- [13] Z. Wang, L. Zhang, D. Psychoudakis, J.L. Volakis, GSM and Wi-Fi textile antenna for high data rate communications in Proceedings of the 2012 IEEE International Symposium on Antennas and Propagation (2012) 1–2.
- [14] S.P. Pinapati, Magnetic Current Inspired Antennas For Wearable Applications, Doctoral Thesis in School of Electrical and Electronic Engineering at The University of Adelaide, Adelaide Australia, (2018).
- [15] S. Gilliland, N. Komor, T. Starner, C. Zeagler, The textile interface swatchbook: Creating graphical user interface-like widgets with conductive embroidery in International Symposium on Wearable Computers, ISWC (2010) 1–8.
- [16] R. Seager *et al.*, Effect of the fabrication parameters on the performance of embroidered antennas IET Microwaves, Antennas Propag. 7 (2013) 1174–1181.
- [17] Y. Xudong, C. Yingxue, W. Tingting, Z. Yong, H. Jiyong, Effect of stitch structure on the reading performance of fabric-based embroidered UHF RFID tags Fibres Text. East. Eur. 29 (2021) 48–53.
- [18] I. Gil, R. Fernández-García, J.A. Tornero, Embroidery manufacturing techniques for textile dipole antenna applied to wireless body area network Text. Res. J. 89 (2019) 1573–1581.
- [19] T.C. Baum, R.W. Ziolkowski, K. Ghorbani, K.J. Nicholson, Embroidered active microwave composite preimpregnated electronics-pregtronics IEEE Trans. Microw. Theory Tech. 64 (2016) 3175–3186.

- [20] E. Moradi, T. Bjorninen, L. Ukkonen, Y. Rahmat-Samii, Characterization of embroidered dipole-type RFID tag antennas in 2012 IEEE International Conference on RFID-Technologies and Applications (2012) 248–253.
- [21] N. Brechet *et al.*, Cost- and time-effective sewing patterns for embroidered passive UHF RFID tags in 2017 iWAT International Workshop on Antenna Technology: Small Antennas, Innovative Structures, and Applications (2017) 30–33.
- [22] S. Zhang *et al.*, Embroidered wearable antennas using conductive threads with different stitch spacings in 2012 Loughborough Antennas and Propagation Conference (LAPC) (2012) 1–4.
- [23] A.T. Wiri, Automated design optimisation and simulation of stitched antennas for textile devices, Doctoral Thesis in Mechanical, Electrical and Manufacturing Engineering at Loughborough University, Loughborough UK, (2019).
- [24] D.M. de S. Fonseca, Embroidered textile connectors for wearable systems, Doctoral Thesis in Mechanical, Electrical and Manufacturing Engineering at Loughborough University, Loughborough UK, (2019).
- [25] S. Zhang, Design advances of embroidered fabric antennas, Doctoral Thesis in Mechanical, Electrical and Manufacturing Engineering at Loughborough University, Loughborough UK, (2014).

Development and Durability Analysis of the Functionalized Fabric

Elham Mohsenzadeh^{1,2,3,a*}, Hayriye Gidik^{1,2,3,b}, Daniel Dupont^{1,2,3,c},
Axel Hemberg^{4,d} and Driss Lahem^{4,e}

¹ENSAIT, ULR 2461, GEMTEX, F-59000 Lille, France

²Junia, F-59000 Lille, France

³Univ. Lille, F-59000 Lille, France

⁴Materia Nova Materials R&D Centre, 3 Avenue Nicolas Copernic, 7000 Mons, Belgium

^aelham.mohsenzadeh@junia.com, ^bhayriye.gidik@junia.com, ^cdaniel.dupont@junia.com,

^dAxel.Hemberg@MATERIANOVA.BE, ^eDriss.Lahem@MATERIANOVA.BE

Keywords: Photocatalytic activity, Volatile Organic Compounds (VOCs), Titanium dioxide (TiO₂), Textile fabric

Abstract. Nowadays, building insulation must be more and more effective to avoid energy loss. This can result in the lack of ventilation which can cause an increase in the concentration of pollutants in the indoor air, such as Volatile Organic Compounds (VOCs) which are harmful to human health. Different approaches have been proposed to reduce this problem such as ventilation, filtration, depolluting plants, etc. The aim of this study consists of developing functionalized textile substrate allowing the VOCs degradation, ideally into H₂O and CO₂, by the photocatalytic effect under visible light. It is necessary to have photocatalytic activity under visible light for indoor applications as the UV light is filtered by window glasses. To achieve this objective, firstly the samples of woven cotton fabrics are functionalized with the dispersion of silver doped/non-doped TiO₂ in Carboxymethyl Cellulose (CMC) and water by padding process. After that, the treatment sustainability of the functionalized fabric is determined.

Introduction

Indoor spaces are exposed to many types of pollutants, both chemical (formaldehyde, benzene...) and biological (mould, bacteria...) mainly emitted from house aerosols. The desire to prevent energy loss by insulating more effectively buildings increases these pollutants' concentration. Many research confirms that indoor air is often more dangerous than outdoor air due to pollution. Many of these materials are referred to as volatile organic compounds (VOCs), which are abundant, toxic, and hazardous. They originate from different sources; namely, building products (room furnishings, paints, glues, varnishes etc.) and occupant activities. Other air pollutants such as ozone or nitrogen dioxide are mainly generated in outdoor air and are brought indoors via ventilation. Other sources of indoor pollutants include both gaseous and surface chemical reactions that involve oxidants like ozone [1,2].

Indoor air treatment is a complex phenomenon because of the wide variety of potential pollutants and the low level of pollutant concentration. In addition to these, the airflow to treat these VOCs remains modest. The difficulty with this type of treatment is to find an efficient process with low-level selectivity and low cost (investment, energy, and maintenance). Photocatalysis presents a real advantage for indoor air applications as it can treat low concentrations and flow rates [3]. The semiconductor photocatalysis, which is a green technology, has been widely applied in removing the organic pollutants from air [4]. Semiconductor photocatalyst generates electron / hole (e⁻ / h⁺) pair during irradiation of light energy that could be used for initiating oxidation and reduction reactions, respectively. The titanium dioxide (TiO₂) is a semiconductor photocatalyst which can be presented as an effectual, easily available, relatively inexpensive, and chemically stable one. It exhibits three polymorphs, i.e., anatase (tetragonal), rutile (tetragonal), brookite (orthorhombic), at atmospheric pressure. While rutile is stable at all temperatures, anatase and brookite are metastable. However, the

anatase is the more photocatalytic active phase of TiO₂ compared to rutile. In general, TiO₂ has two major inconvenients. Firstly, it can be only triggered by near UV radiation because of its wide band gap (3.2 eV for the anatase phase, 3.0 eV for the rutile phase) and that encompass only about 4–5% of natural solar radiation. Secondly, the photogenerated electron / hole pairs are liable to recombination, leading to low quantum yields [5–7]. To eliminate these disadvantages, its band gap can be reduced using various dopants (nitrogen, silver, vanadium, carbon...) and it can have a photocatalytic activity under visible light [8–10]. In this context, it is suggested to develop textiles that can narrow the amount of these pollutants, to improve indoor air quality (IAQ).

The aim of this study is to develop a functionalized textile substrate with a hybrid photocatalytic material based on Ag doped and non-doped titanium dioxide (TiO₂) and Carboxymethyl Cellulose (CMC), and water (H₂O) to photodegrade VOCs under UV and/or visible light radiation. A cotton (CO) woven fabric was preferred as a textile substrate for indoor applications. In addition to TiO₂, Carboxymethyl Cellulose (CMC) was preferred as the incorporation vector between textile substrate and TiO₂ to increase the binding effect of TiO₂ by encapsulating them into the porous structure of it. The functionalized samples were characterized with different methods (Scanning Electron Microscope (SEM) - Energy Dispersive X-ray (EDX) and Thermogravimetric Analysis (TGA)).

One of the most important aspects to consider when studying these textile structures is durability of their treatment. Although it would be difficult to study it due to the difficulties associated with studying damaging mechanisms.

A textile surface undergoes a variety of stresses during its lifetime. Through these stresses, fabric surfaces become progressively damaged. That's why they must withstand the user's demands throughout their lifetime. There are many types of stresses: traction, shearing, tearing, and maintenance, like washing or drying. Also, they encounter offensives from the environment, such as UV light, chemical compounds, temperature, or humidity. Fabric abrasion and washing are therefore important wear factors. As a result of repeated friction between two fabrics, abrasion wear occurs. As a result, their surface characteristics will change and sometimes they may rupture. In this study, functionalized cotton plain weave samples were going through 1 and 3 washing cycles and after each cycle they are characterized again by TGA and SEM - EDX to analyze their treatment sustainability.

Materials And Methods

100% woven cotton fabric (plain weave) was provided from Subrenat (France). Commercial TiO₂ P25[®] was bought from Evonik (Germany) as a photocatalytic material and it was doped with silver (TiO₂-Ag) at Materia Nova (Belgium) by using physical vapor deposition (PVD) to extend its photocatalytic activity to the visible light domain. Carboxymethyl Cellulose (CMC) was purchased from C. E. Roeper GmbH (Germany) and used as a vector between the cotton substrate and TiO₂.

Preparation of doped TiO₂. TiO₂ P25[®] was doped with silver doping agent. The magnetron sputtering method (R2QU14XGX, Kurt J. Lesker Compant Ltd., UK) was used to produce the doped samples. The powder of TiO₂ P25[®] was used as the substrate for sputtering deposition and the materials for the sputtering targets was Ag. The sample was named Ag-doped TiO₂ P25[®].

Preparation of TiO₂ Suspension. Different dispersion of 1, 2, and 3 g of TiO₂ P25[®] and Ag-doped TiO₂ P25[®] in 40 g water and 1, 2, and 3 g of TiO₂ P25[®] and Ag-doped TiO₂ P25[®] in 10 g of ethanol with 30 g of water and 0.5% in weight of CMC were prepared by using a high-shear disperser (Ultra-Turrax, IKA) with a speed of 7000 rpm during 15 minutes at room temperature. Afterward the suspensions were dispersed in an ultra-sonication bath (BANDELIN, Germany) for 15 minutes at room temperature.

Padding Process. The cotton fabrics were treated with prepared suspensions by using padding process with the applied pressure of 1.8 bar and the roller speed of 7 rpm. After the padding process, the samples were dried and cured at 120 °C and at 150 °C for 1 minute, respectively.

Washing Test. After preparing the samples, to determine the sustainability of the treatment, each sample was washed by a composition of the ECE detergent (5 g/l) in Eco Dyer Rapid (2010 ECO-18/ECO-24, Gate AG Vaduz) following the ISO105-C01:1989 (F) standard, with a short synthetic program of 40 °C, for 30 minutes, with a rotation speed of 25 rpm. Afterward samples were dried in an oven at 70 °C for 10 minutes. All prepared samples were characterized by SEM - EDX and TGA before washing and after 1st and 3rd washing cycles.

Characterizations. Samples were characterized separately by using TGA 4000 thermogravimetric analyzer (Perkin Elmer, USA) in the temperature range of 30-900°C. Non-treated and functionalized cotton samples before and after washing cycles were characterized with same analyzer in the temperature range of 30-700 °C. The heating rate was maintained at 10 °C.min⁻¹. The measurements were made under a constant air flow rate of 20 mL.min⁻¹. The experimental data was collected and analyzed using the Perkin Elmer Pyris Manager software. Each sample was characterized three times to confirm the repeatability of the measurement and homogeneity of the treatments. To observe the TiO₂ particles and their dispersion on the fabric surface, a Scanning Electron Microscope (Phenom ProX, Thermo Fischer Scientific) was used. The identification of different chemical elements in the samples was accomplished with the Element Identification (EID) software package and a specially designed and fully integrated Energy Dispersive Spectrometer (EDS).

Results and Discussion

The weight loss of functionalized samples (%) at 700 °C regarding to non-functionalized sample from TGA analysis are listed in *Table.1* in below.

Table 1. Weight loss of functionalized samples compared to non-functionalized samples – TGA analysis

Sample	Weight loss (%)
TiO ₂ P25 / Water	2.44 ± 0.57 %
TiO ₂ P25 / CMC	3.15 ± 0.01 %
TiO ₂ - Ag / Water	3.95 ± 0.28 %
TiO ₂ - Ag / CMC	4.81 ± 0.92 %

The thermogravimetric analysis showed that the degradation of fabrics started at around 340 °C and reached a maximum rate around 600 °C. From 580 °C onwards, the results show that the weight of residue for treated samples was higher comparing to non-treated samples at 700 °C. As it was presented in our previous study, the binder vector was fully degraded at 600 °C while TiO₂ P25[®] remained stable at this temperature. Thus, the weight loss percentages presented in *Table.1* represent the quantity of TiO₂ on fabric surface [11].

The results can confirm the presence of TiO₂ P25[®] and Ag-doped TiO₂ P25[®] on the surface of the cotton fabrics. The most amount of it, is related to the sample factionalized by silver doped TiO₂ P25[®] with CMC.

The Scanning Electron Microscopy coupled with Energy Dispersive X-ray spectroscopy images of the samples are shown in *Figure.1* with the EDX results listed in the table under each photo.

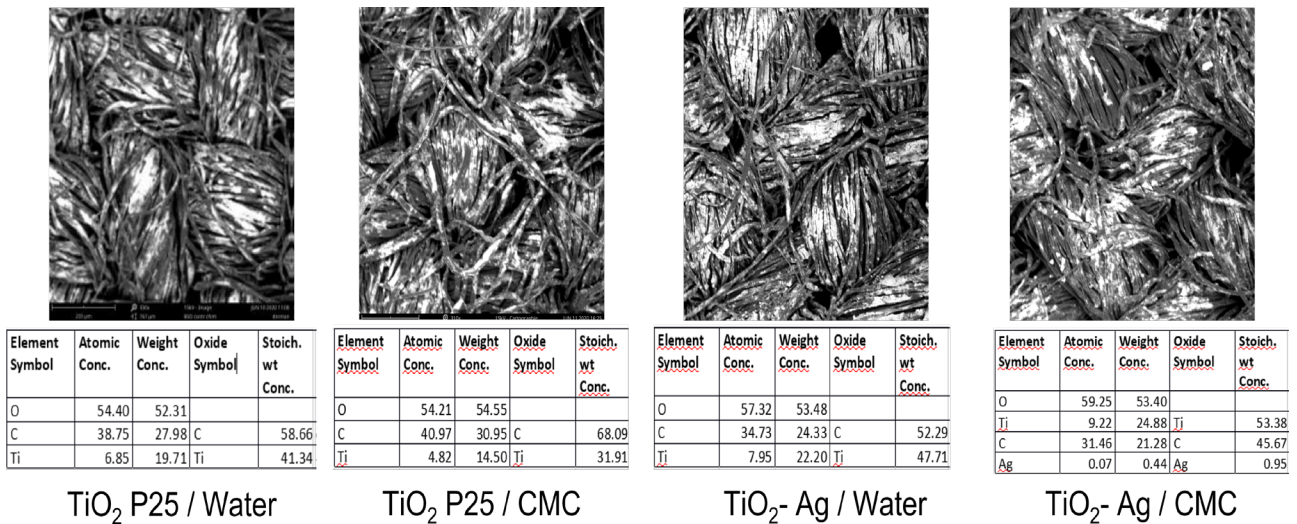


Fig 1. The SEM - EDX analysis results of functionalized samples and non-functionalized samples

The white part of the SEM photos is related to the presence of TiO₂ P25[®] and Ag-doped TiO₂ P25[®] on the surface of the fabric and show us their homogeneity on the textile. On the table below each image, we can see the amount of Ti. These results prove the presence of catalyzer on the fabric.

The SEM - EDX results of the treated cotton sample by 1 g TiO₂-Ag/CMC before washing and after 1st and 3rd washing cycles are presented as an instance in Figure 2.

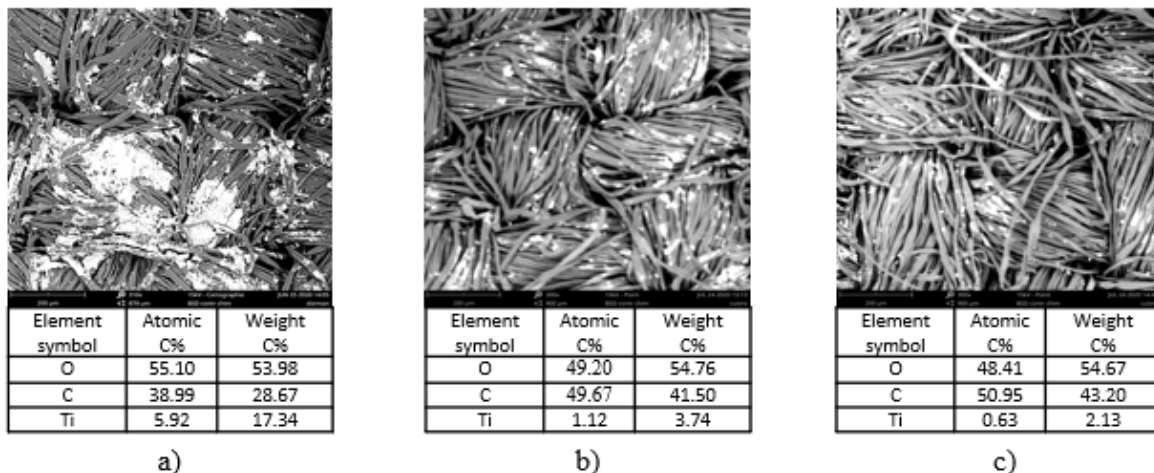


Fig 2. The SEM - EDX analysis results of (a) before washing (b) after 1st and (c) 3rd washing cycles

The loss amount of the treatment after 1st and 3rd washing cycles from TGA and SEM - EDX characterization results are calculated and demonstrated in Figure 3.

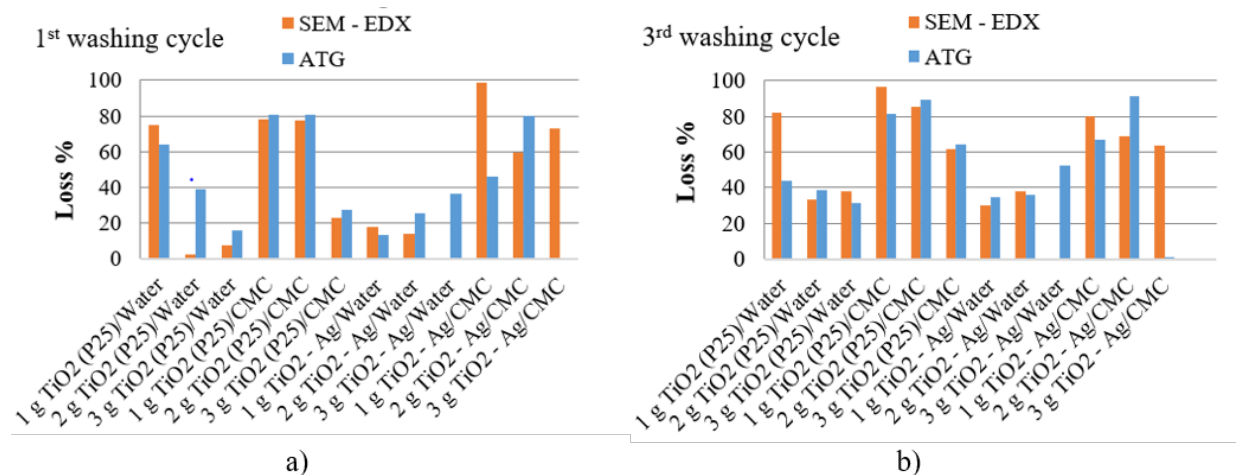


Fig 3. TGA and SEM - EDX results of treated samples after (a) 1st (b) 3rd washing cycles

The results of TGA and SEM - EDX characterizations of the samples after 1st and 3rd washing cycles confirm the presence and durability of the TiO₂ treatment even after 3 washing cycle. It is also concluded that the greater the amount of TiO₂ (3 g) is the less loss happens.

Conclusion

During this study, the TiO₂ P25[®] was doped with Ag to obtain a photocatalytic activity under visible light and CMC was used as the incorporation vector to increase the binding effect of TiO₂ by encapsulating them into its porous structure. A cotton fabric was functionalized with different amount of Ag doped/non-doped TiO₂ in water or CMC dispersion. The first results showed the feasibility of the process and the presence and satisfied durability of TiO₂ on the textile substrate after several washing cycles. The results of TGA and SEM - EDX characterization of the samples after 1 and 3 washing cycles confirm the persistence of the treatment (TiO₂) even after 3 washing cycles. It is also concluded that the greater the amount of TiO₂ (3 g) is the less loss happens. The efficiency of photocatalytic activity will be analyzed by using a measuring unit, which is developed in JUNIA – HEI during this study.

Acknowledgment

This study is realized thanks to the Interreg V France-Wallonie-Vlaanderen program (TEXACOV Project of Portfolio GoToS3). Thus, the authors gratefully acknowledge the European Regional Development Fund (ERDF), the Walloon Region and West Vlaanderen Provincie for their financial support.

References

- [1] T. Brown, C. Dassonville, M. Derbez, O. Ramalho, S. Kirchner, D. Crump and C. Mandin, "Relationships between socioeconomic and lifestyle factors and indoor air quality in French dwellings", *Environmental Research*, vol. 140, 2015, pp 385–396.
- [2] S. Langer, O. Ramalho, M. Derbez, J. Riberon, S. Kirchner and C. Mandin, "Indoor environmental quality in French dwellings and building characteristics", *Atmospheric Environment*, vol. 128, 2016, pp 82–91.
- [3] J. M. Tatibouet, *Plasma non thermique et traitement de l'air, Les composés organiques volatiles dans l'environnement* ed Tec & Doc Lavoisier (Ecole des Mines de Nantes), 1998, pp 41–44.

-
- [4] Ş. Ş. Türkyılmaz, N. Güy, M. Özacar, “Photocatalytic efficiencies of Ni, Mn, Fe and Ag doped ZnO nanostructures synthesized by hydrothermal method: The synergistic/antagonistic effect between ZnO and metals”, *Journal of Photochemistry and Photobiology A: Chemistry*, vol. 341, 2017, pp 39–50.
- [5] M. Vittoria Dozzi, E. Selli, “Doping TiO₂ with p-block elements: Effects on photocatalytic activity”, *Journal of Photochemistry and Photobiology C: Photochemistry Reviews*, vol. 14, 2013, pp 13– 28.
- [6] A. Valentine Rupa, D. Manikandan, D. Divakar, T. Sivakumar, « Effect of deposition of Ag on TiO₂ nanoparticles on the photodegradation of Reactive Yellow-17”, *Journal of Hazardous Materials*, vol. 147, 2007, pp 906–913.
- [7] A. Barmeh, M. R. Nilforoushan, S. Otraj, “Wetting and photocatalytic properties of Ni-doped TiO₂ coating on glazed ceramic tiles under visible light”, *Thin Solid Films*, vol. 666, 2018, pp 137–142.
- [8] P. Donga, F. Yangc, X. Chenga, Z. Huanga, X. Niea, Y. Xiaob, X. Zhang, “Plasmon enhanced photocatalytic and antimicrobial activities of Ag-TiO₂ nanocomposites under visible light irradiation prepared by DBD cold plasma treatment”, *Materials Science & Engineering C*, vol. 96, 2019, pp 197–204.
- [9] A. Javida, M. Kumara, M. Ashraf, J. H. Leed, J. G. Han, “Photocatalytic antibacterial study of N-doped TiO₂ thin films synthesized by ICP assisted plasma sputtering method”, *Physica E: Low-dimensional Systems and Nanostructures*, vol. 106, 2019, pp 187–193.
- [10] G. Rossia, L. Pasquinia, D. Catoneb, A. Piccionia, N. Patellia, A. Paladinic, A. Molinarid, S. Caramorid, P. O’Keeffec, F. Boscherini “Charge carrier dynamics and visible light photocatalysis in vanadium-doped TiO₂ nanoparticles”, *Applied Catalysis B: Environmental*, vol. 237, 2018, pp 603–612.
- [11] H. Gidik, S. Almuhamed, D. Dupont, L. Derue, W. Thielemans, G. Kignelman, D. Lahem, Volatile Organic Compounds (VOCs) Treatment by a Functionalized Textile, *Journal of Fashion Technology and Textile Engineering*, 2018, S5:002.

Heating Filament with Self-Regulation Temperature by Coating a Metallic Yarn with a Conductive Polymer Composite

Louis Marischal^{1,a}, Aurélie Cayla^{1,b*}, Guillaume Lemort^{1,c}, Valentin Laurent^{1,d},
Christine Campagne^{1,e} and Eric Devaux^{1,f}

¹ENSAIT, GEMTEX – Laboratoire de Génie et Matériaux Textiles, 2 Allée Louise et Victor
Champier, 59056 Roubaix Cedex 1, F-59000 Lille, France

^alouis.marischal@ensait.fr, ^{b*}aurelie.cayla@ensait.fr, ^cguillaume.lemort@ensait.fr
^dvalentin.laurent@ensait.fr, ^echristine.campagne@ensait.fr, ^feric.devaux@ensait.fr

Keywords: Smart textile, Heating filament, Self-regulating temperature, melt coating, conductive polymer composite, carbon nanotubes

Abstract. Nowadays, the heating textiles are used in many fields of applications as medicine or comfort. The heating property for the most part of these textiles was ensured by electrical conductive fiber as metallic yarn thanks to Joule Effect. A challenge for heating textile is to have an electrical conductive fiber which has a temperature self-regulation at the comfort temperature. Thanks to this temperature self-regulation, the heating textile reaches more autonomy. To develop this kind of textile, conductive polymer composite (CPC), which is the combination between an insulating polymer and electrical conductivity nanofillers [1], is made by melt spinning. The temperature self-regulation is provided by the positive temperature coefficient (PTC) effect, which allows switching between an electrical conductivity state and an insulating state when the CPC is close to a transition phase temperature (glass transition temperature or melt temperature). However, when the PTC effect can take place at the melting point, the mechanical properties are not involved. So to maintain the final product an immiscible polymer blend was used: one polymer was the CPC and the second polymer was an insulating polymer with a higher melting point than the target temperature. In fact, the CPC involve the electrical conductivity and the PTC effect, whereas the insulating polymer involves the mechanical properties. However, a high electrical conductivity is necessary to reach the comfort temperature (defined around 42°) by Joule Effect. So to reach this temperature, the coating on a metallic yarn by the conductive immiscible polymer blend was used. The electrical conductivity of this product was improved by the metallic yarn and the self-regulating temperature by the PTC effect of the immiscible polymer blend (figure 1). In this paper the immiscible polymer blend used is a polycaprolactone (PCL) filled with multiwall carbon nanotubes (MWCNT) and a polypropylene (PP). In fact, in a previous paper the co-continuity and the selective localisation of the fillers in the PCL for this blend was studied [2]. The influence of the thickness CPC coating and the influence of the structure of metallic yarn were studied on the electrical conductivity, the Joule Effect and PTC effect.

Introduction

Heating textiles allow to protect against cold, to cure the pain by the action of the heat and so there are used in many applications as medical, sport, and comfort. Heat input by textiles are majority ensure by metallic yarn, which only heat by joule effect[3–6]. To regular the temperature, electronic components were added. These components have as consequences an increase in price and a loss of textile properties: flexibility, hand feel and especially washability. In order to reduce these disadvantages, researches have been looking into the development of heating textile with self-regulating temperature.

One solution to is the utilization of coated metallic yarn by Conductive Polymer Composite (CPC), which was a blend composed of an insulating polymer containing electrically conductive fillers [7,8].The heating power was provided by the joule effect of the metallic yarn, which was a high electrical conductivity [3–6]. Indeed, the electrical current is passed thought the CPC, thanks to the

electrical conductivity, to reach the metallic yarn. Then, the self-regulating temperature is ensured by several phenomena associated to the CPC as the positive temperature coefficient (PTC) and the negative temperature coefficient (NTC) [[7,9,10]]. Thanks to these phenomena, it is possible to switch between an electrically conductivity state and an insulating state when the CPC is close to a transition phase temperature (glass or melting temperature). A lot of authors have already studied electrical conductivity of CPC. In these studies, several key factors were found out in order to have electrical conductivity : percolation threshold, which were the minimal content filler allowing the electrical conductivity [11], kind of fillers [8,12–17], the dispersion of fillers, their alignment or process parameters [[6,18–22][6,22]. However, these key factors involved an influence of the PTC effect. Indeed, several studies were made in order to understand the influence of fillers on the PTC effect. The main parameters were the specific area [9], the filler content [23–25], the filler synergy [26], and polymers. Indeed, the PTC effect takes place close to the transition phase temperature (glass temperature or melt temperature) [10]. That is more, this PTC effect depends also on the polymer reticulation [27] and the crystallinity rate [28]. In the literature, Chatterjee *et al.* [29] have done a review of studies in the CPC coating in order to explain different methods of coating and by several electrical fillers for several electrical applications in strain and pressure sensor. They had also found some technical limits which modified electrical, mechanical properties. These limits were the lack of uniformity in coating thickness, filler migration, some coating crack during the processing. They have put forward that it was necessary to find a good compatibility with each component (yarn and the CPC) in order to have the best product. Sup Shim *et al.* [30] have demonstrated that the coating by a CPC for the electrical textile is important. Indeed, they have succeeded to obtain a coated cotton by a CPC based on carbon nanotubes (CNT) with an high electrical conductivity of 25 Ω/cm .

Several kinds of coating (not only melt process) have been used in literature. Ye *et al.* [31] have studied the coating on a metallic yarn, Nickel wire, by steaming carbon nanotubes (CNT) and acid vapor. In their paper, they have noted that the Nickel transported the energy, due to their high electrical conductivity, while the CPC stored charge. Shimizu *et al.* [32] have studied, by an atmospheric pressure micro plasma, the coating of tungsten by carbon nanotube. However, in the literature, there were few studies on the metallic yarn coating by a CPC via melt spinning process and their influence key factors. For example, the CPC formulation and the process parameter have an influence on the properties of the final product. The metallic yarns have also an important influence on the electrical properties like the electrical conductivity and the Joule effect.

The aim of our study is to combine a CPC (for the PTC effect and the electrical conductivity), and metallic yarn (for the heating power) produced by melt spinning coating. Thanks to a previous study [33], a blend was found out. It is a compound of 50 wt. % of polypropylene (PP) and 50 wt. % of polycaprolactone (PCL) filled with 4 wt. % of MWCNT, noted: PP/PCL_{MWCNT}. The coating of the metallic yarn by the PP/PCL_{MWCNT} is examined and, more especially in this study, the influence of the metallic yarn is studied. To understand the influence of the metallic yarn, influence of the spin finish oil and linear density of the metallic yarn is evaluated. Finally, the structure of the metallic yarn between a multifilaments or a spun yarn was studied. In these three cases, the measurement of the electrical conductivity, the measurement of the joule effect and the measurement of the PTC effect was occurring in order to understand each behavior.

1. Materials and Methods

1.1. Materials

The immiscible polymer blend used, which was determined by a previous study [2], is a blend of 50 wt.% of the conductive polymer composite (CPC) and 50 wt.% of insulating polymer. The CPC is a polycaprolactone (PCL) filled with 4 wt.% of multiwalled carbon nanotubes (MWCNT). The PCL, which have a melting point at 60°C, was produced by Perstorp. The MWCNT have an average of length of 1.5 μm , a diameter of 10 nm and a specific area of 250 m^2/g . This MWCNT was supplied by Nanocyl. The insulating polymer is the polypropylene (PP) produced by TOTAL with a melting temperature of 165°C.

Different metallic yarns, which are composed of stainless steel 316L, were used in order to understand the influence of the metallic yarn. One yarn produced by Bekinox, which used spin finish oil during this process: A multifilament (MF) of 505 Tex, which was an assembly of two multifilaments of 275 filaments each with a diameter of each filament of 12 μm . Three metallic yarns supplied by Imattec, which used also spin finish oil but after the process the spin finish oil was removed : a multifilament (MF) of 505 Tex, which was an assembly of two multifilaments of 275 filaments each with a diameter of each filament of 12 μm , a multifilament (MF) of 190 Tex, which was an assembly of two multifilaments of 100 filaments each with a diameter of each filament of 12 μm and a spun yarn (SY) of 11/2 Nm (equivalent at 190 Tex). Table 1 summarizes the different kinds of metallic yarns.

Table 1: Summary of metallic yarns

Supplier	Structure	Spin finish oil	Linear density (Tex)	Number of filaments	Diameter of one filament (μm)
Bekinox	Multifilament	With	505	2 x 275	12
Imattec	Multifilament	Without	505	2 x 275	12
Imattec	Multifilament	Without	190	2 x 100	12
Imattec	Spun yarn	Without	190		12

1.2. Samples preparation

The first compound prepared allows to incorporate and to disperse 4 wt.% of MWCNT in the PCL ($\text{PCL}_{\text{MWCNT}}$) thanks to a co-rotating intermeshing twin-screw extruder from Thermo-Haake PTW 16/25. Then a second extrusion allows to obtain the PP/ $\text{PCL}_{\text{MWCNT}}$ coating to be directly deposited around the metallic yarn with a speed of 100 m/min. The coated yarn was illustrated by the Figure 1. Before the process, polymers were dried at 45°C during 12 hours. All coated yarn obtained by this process was shown by the Table 1.

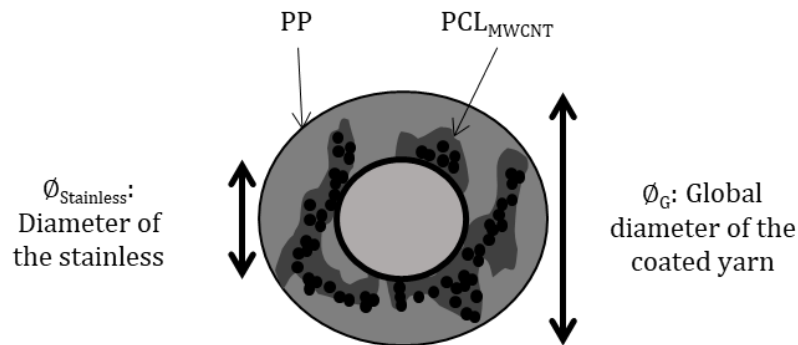


Figure 1: Cross section of coated metallic yarn (in core) by CPC : PP/ $\text{PCL}_{\text{MWCNT}}$

Table 2: Summary of coated yarn by the PP/ PCL_{MWCNT}

Metallic yarn				
Structure	Spin finish oil	Linear density (Tex)	Diameter of the stainless steel (mm)	Global diameter of the coated yarn (mm)
Multifilament	With	505	0.29	0.87
				0.90
	Without	190	0.18	0.48
				0.34
				0.43
				0.48
Spun yarn	Without	190	0.18	0.56
				0.38
				0.45
				0.58

1.3. Methods of characterisation

1.3.1. Electrical conductivity measurement

The electrical measurement was performed by a Keithley 2461 sourcemeter which applied a DC voltage, from -0.5 V to 15 V with an automatic increment of 0.5 V, and measure the current intensity at each point. Each coated yarn was tested about 5 samples between two points spaced by 1 cm. Thanks to the current intensity and the voltage, the electrical conductivity was calculated with the equation (1):

$$\sigma = \frac{L}{R \cdot S} \quad \text{(Equation 1)}$$

Where σ (S/m) is the electrical conductivity, R (Ω) is the resistance, L (m) is the distance between the two electrodes, and S (m^2) is the cross-section area.

1.3.2. Joule effect measurement

The Keithley 2461 sourcemeter and a thermal camera were used to measure the Joule effect for each coated yarn, which were measured at minimum 5 times. The sample was connected by two clamps, spaced by 1 cm, at the Keithley and maintained at 5 cm above the ground. The thermal camera was connected to the FLIR software and placed at a height of 5 cm above the sample and measure the temperature of the centre's sample at any time. During the experiment, the source-meter delivers at 20 V for 300 sec.

1.3.3. CTP effect measurement

A climatic chamber and a Keithley 3701A were used to measure the CTP effect and at least 5 samples were tested by coated yarn. The climatic chamber, with constant relativity humidity at 65 %, had a temperature programme which can be divided into two parts. At first, the temperature increases from 20 °C to 80 °C with an automatic increment of 4°C and a stabilisation time of 2 min by step. Then the temperature decreases from 80 °C to 20 °C with an automatic decrement of 4 °C and a stabilisation time of 2 min by step. The Keithley 3701A measure the resistance (Ω) of the sample during the whole

experiment. For one sample, 5 temperature cycles were made. Thanks to the resistivity of the sample, the electrical resistivity and the electrical conductivity were calculated. Then the sensibility of the sample was calculated with the equation (2):

$$S = \frac{\sigma_t - \sigma_o}{\sigma_o} \quad \text{(Equation 2)}$$

Where S the sensibility of the electrical conductivity, σ_t (S/m) is the electrical conductivity at any time and σ_o (S/m) is the electrical conductivity at the beginning ($t=0$ second).

During this experiment, the sensibility of the sample allows to determine the amplitude of the PTC effect, so when the electrical conductivity sharply decrease at transition phase temperature. This PTC effect amplitude A_{PTC} is described by the equation (3).

$$A_{PTC} = \min(\text{sensibility } S) \quad \text{(Equation 3)}$$

2. Results and discussions

2.1. Influence of the multifilament's spin finish oil

In this paper, the influence of the spin finish oil, which was the combination between water and surfactant, was studied. Two stainless multifilaments were tested (number 1 and 2) with only difference is: one has the spin finish oil; the other had undergone a post-processing to remove the spin finish oil. After the processing of metallic yarns coating, with the same processing parameters, each sample was tested. The electrical conductivity of these experiments is illustrated by the Table 2 and no variation of electrical conductivity is reported.

Table 1: Electrical conductivity of the coated yarn according to the presence of spin finish oil

	With Spin finish oil	Without spin finish oil
Electrical conductivity (log[S/m])	1.28 ± 0.19	1.30 ± 0.09

Measurements of the Joule effect of this coated metallic yarns were made on these samples and these results were illustrated by the Figure 2. The metallic yarn without spin finish oil has involved a Joule effect more important than the metallic yarn with spin finish oil. This difference of Joule effect was explained by the spin finish oil by two hypotheses. The first hypothesis was the spin finish oil had reduced contact point between the stainless and the CPC. In fact, a modification of surface energy of metallic yarn modifies the interface quality. The CPC had not enough electrical conductivity to produce the joule Effect. Otherwise, the electrical conductivity of the metallic yarn, with a low intensity, produces the joule effect. If there were low contacts point, the metallic yarn did not produce Joule effect. The second hypothesis was the spin finish oil had a high thermal conductivity and so involving a high thermal dissipation. However, this hypothesis required further study in order to measure the thermal conductivity of the spin finish oil.

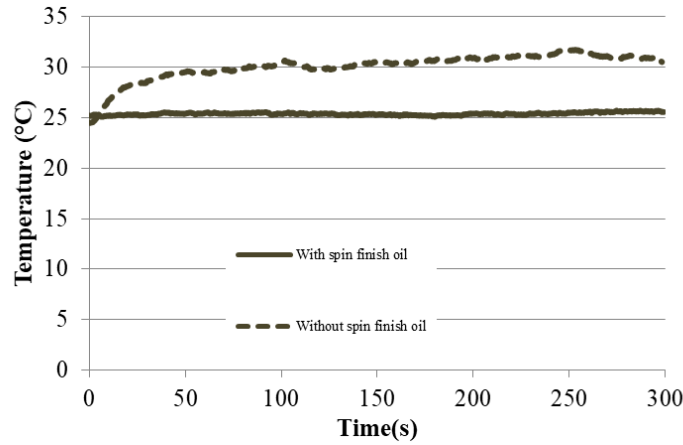


Figure 2: Evolution of temperature of the coated metallic yarn with or without spin finish oil according to the time (Joule effect)

The last experiment made, to understand the influence of the spin finish oil, is the measurement of the PTC effect. Then measurements of the PTC effect are carried out and these results, on the second temperature cycle in order to obtain the stability of the sample, is illustrated in Figure 3 and the amplitude values of the PTC effect for each sample are summarized in Table 3.

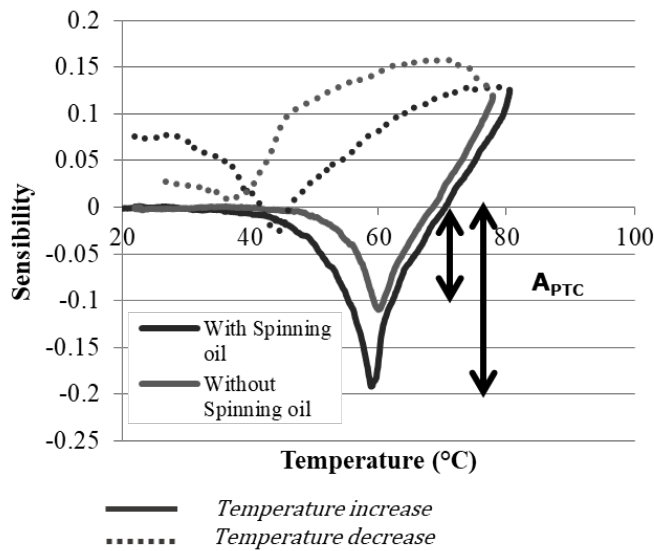


Figure 3: The sensibility of the second temperature cycle according to the temperature of the metallic yarn with or without spin finish oil.

Table 2: The amplitude of the PTC effect of the second temperature cycle according to the presence of spin finish oil on the metallic yarn

	With Spin finish oil	Without Spin finish oil
Amplitude of the PTC effect	-0.1916	-0.11

Figure 3 and Table 3 allow to note that the spin finish oil had an influence on the PTC effect. The amplitude of the PTC effect (A_{PTC}) is higher with spin finish oil than without spin finish oil. That is more; the temperature of the PTC effect is lower with spin finish oil than without spin finish oil. To explain this phenomenon a hypothesis are made and it was when the temperature was increased, the spin finish oil was dissipated under the action of heat and so the CPC had more space for the macromolecular reorganisation. Otherwise, thanks to several studies [[28,34]] , the PTC effect as

dependent on the thermal expansion of the CPC. The dissipation of the spin finish oil, increase the PTC effect.

To conclude, the spin finish oil had an important influence in the development for a heating textile with a self-regulating temperature. As presented, to develop this kind of textile, it was better to use a metallic yarn with no spin finish oil. In fact, without spin finish oil; there was an important Joule effect despite low PTC effect amplitude.

2.2. Influence of initial multifilament's linear density

The linear density of the metallic yarn had also studied thanks to two metallic yarn (stainless multifilament without spin finish oil) but with a linear density and diameter differences. : 505 Tex and a diameter of 0.29 mm and 190 Tex with a diameter of 0.18 mm, both produced by Imattec. During the manufacturing, and in order to compare these yarns, the electrical properties were compared according to the ratio of CPC (R_{CPC}) in the global diameter, calculated with the equation (4) :

$$R_{CPC} = 1 - \frac{\varnothing_{\text{Stainless}}}{\varnothing_G} \quad \text{(Equation 4)}$$

Where R_{CPC} the Ratio of the CPC (%), $\varnothing_{\text{Stainless}}$ (mm) is diameter of the stainless use and \varnothing_G (mm) is the global diameter of the coated yarn.

The measurement of the electrical conductivity according to the ratio of CPC is illustrated by the Figure 4. At the equivalent ratio of CPC (64 – 65%), the electrical conductivity of the coated yarn with an initial linear density of metallic yarn of 190 Tex is a better electrical conductivity than the coated yarn with a linear density of metallic yarn of 505 Tex. A higher initial electrical conductivity allows for a more efficient Joule effect.

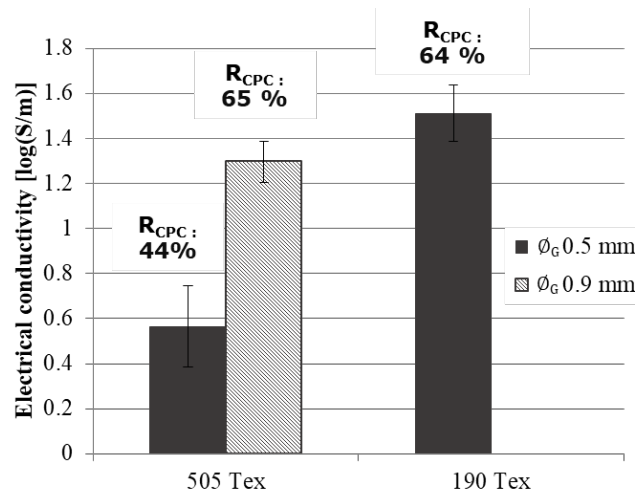


Figure 4: Electrical conductivity according to the initial linear density of the metallic yarn and the global diameter of the coated yarn

2.3. Influence of the structure of the metallic yarn: Multifilament or Spun yarn

The last key factor studied on the metallic yarn was the structure. In fact, like presented in the material section, there were two structures of metallic yarn: one was a multifilament and the other was a spun yarn. Despite the metallic structure, these metallic yarns had the same properties: linear density, chemical composition and without spin finish oil. Electrical conductivity is measured on coated yarn developed by these metallic yarn structures, and illustrated by the Figure 5. The structure of the metallic yarn had an important influence on the electrical conductivity. Indeed, the spun yarn coated allowed to have an electrical conductivity more important than the coated multifilament. This electrical conductivity difference was explained by the structure of the spun yarn and more particularly by the stainless fibrils. During the coating, these fibrils had not a cohesive structure, in

particularly without spin finish oil, so the thickness CPC-metallic yarn is lower for the spun yarn coated than the multifilament coated as illustrated in the Figure 6.

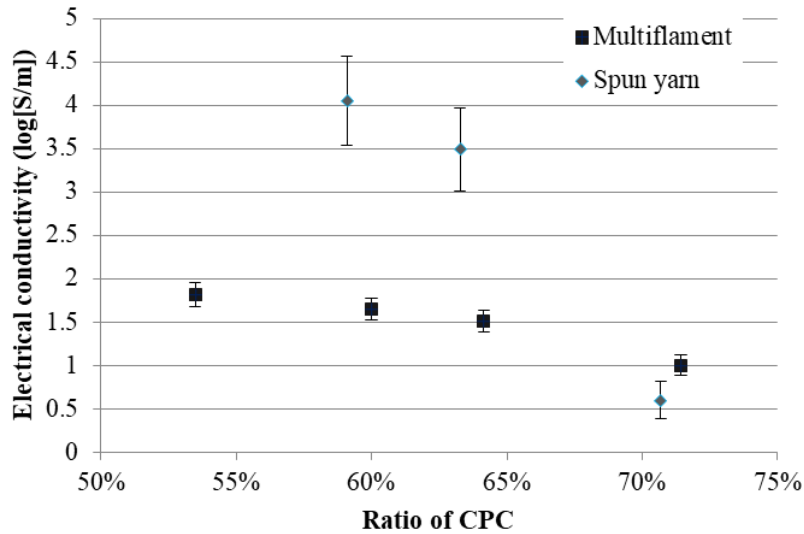


Figure 5: The electrical conductivity of the coated multifilament or the coated spun yarn according to the ratio of CPC in the coated yarn

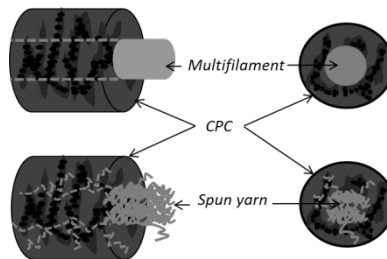


Figure 6: Schematic representation of structure of the coated metallic yarn (multifilament or spun yarn)

All samples were tested in order to measure the Joule effect. However, due to the high electrical conductivity of the spun yarn coated, the protocol used was not adapted. Indeed, due to the high electrical conductivity of the coated spun yarn, there is an important Joule effect which involved the combustion as opposed as the multifilament coated which have not Joule effect. Then the PTC effects were measured and results are reported in the Figure 7 and the Table 4.

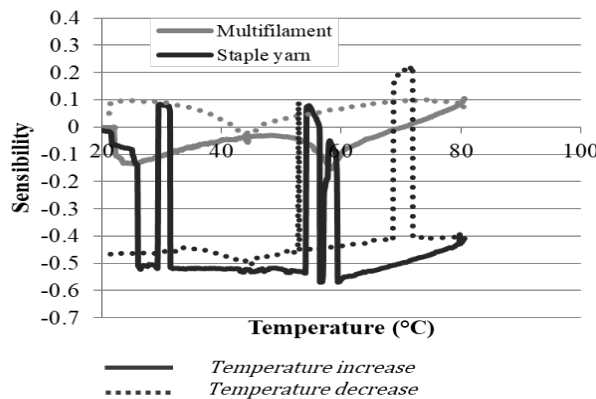


Figure 7 : The sensibility of the second temperature cycle according to the multifilament coated and the spun yarn coated

Table 3: The amplitude of the PTC effect of the second temperature cycle according to the metallic yarn's structure

	Multifilament	Spun yarn
Amplitude of the PTC effect	-0.153	-0.569

During the measurement the coated spun yarn had many variations as opposed as the multifilament coated. During the temperature increase, the internal structure of the coated yarn, and due the action of the heat, have changed and have involved the creation of short circuit with metallic fibrils. This modification had as consequences the modification of the electrical conductivity, so the PTC effect. These various picks have caused by the intensity which pass through these fibrils. The structure of the metallic yarn for a coated yarn is important. Multifilament is better if the goal is to make a heating textile with a self-regulating temperature.

Conclusion

To understand several key factors on the coated metallic yarn to the development for a heating filament with self-regulating temperature, this study is focused on three of these key factors, which is spin finish oil, initial linear density, and the structure of the metallic yarn. All of the parameters during the coating are fixed to compare and analysis each experiment.

At first, spin finish oil is studied and have not directly an influence on the electrical conductivity of the coated yarn. However, on the Joule effect, the spin finish oil is a significant influence. The first hypothesis was the reduction of contact points between CPC and metallic yarn and so involving a decrease of the Joule effect, which was ensured by the metallic yarn. The second hypothesis was the spin finish oil have a high thermal conductivity which have as consequences a thermal dissipation and so a decrease of the global Joule effect. Concerning the PTC effect, the hypothesis is the PTC effect increase with spin finish oil, due to the dissipation of the spin finish oil during the temperature increase involving a more thermal expansion for the CPC, which was a key factor of the PTC effect. Finally, the last key factor was the structure of the metallic yarn more particular the influence if the metallic yarn is a multifilament or a spun yarn. Due to fibrils in the spun yarn, the electrical conductivity and Joule effect are higher in the coated yarn than the multifilament yarn. However, these fibrils involve problem for the PTC effect.

The purpose of this study was the development of a heating filament with self-regulating temperature. Thus in orders to achieve this goal, it was necessary to use a metallic yarn, with a multifilament structure, with no spin finish oil and a low linear density.

Acknowledgment

This work is part of the project FUI AUTOTHERM², financed by the Région Haut-de-France and BPI France.

References

- [1] Dorigato, A., V. Moretti, S. Dul, S.H. Unterberger, A. Pegoretti, Electrically conductive nanocomposites for fused deposition modelling, *Synth. Met.* **2017**, 226, 7–14. doi:10.1016/j.synthmet.2017.01.009.
- [2] Marischal, L., A. Cayla, G. Lemort, C. Campagne, D. Éric, Selection of immiscible polymer blends filled with carbon nanotubes for heating applications, *Polymers (Basel)*. **2019**, 11, 1–16. doi:10.3390/polym11111827.
- [3] G, T., M. N, K. T, Development and Characterization of Electric Heating Fabric Based on Silver Coated Nylon Yarn, *J. Text. Eng. Fash. Technol.* **2017**, 1, 1–3. doi:10.15406/jteft.2017.01.00036.

-
- [4] Asghar, A., M.R. Ahmad, M.F. Yahya, Effects of metal filament's alignment on tensile and electrical properties of conductive hybrid cover yarns, *Fash. Text.* **2016**, 3, 3. doi:10.1186/s40691-015-0055-4.
- [5] Zhang, L., M. Baima, T.L. Andrew, Transforming commercial textiles and threads into sewable and weavable electric heaters, *ACS Appl. Mater. Interfaces.* **2017**, 9, 32299–32307. doi:10.1021/acsami.7b10514.
- [6] E. Cronn, C., Textile based heating apparatus and method, US 2008/0223844 A1, **2008**.
- [7] Feller, J.F., I. Linossier, Y. Grohens, Conductive polymer composites: Comparative study of poly(ester)-short carbon fibres and poly(epoxy)-short carbon fibres mechanical and electrical properties, *Mater. Lett.* **2002**, 57, 64–71. doi:10.1016/S0167-577X(02)00700-0.
- [8] Dorigato, A., M. Brugnara, A. Pegoretti, Synergistic effects of carbon black and carbon nanotubes on the electrical resistivity of poly(butylene-terephthalate) nanocomposites, *Adv. Polym. Technol.* **2017**, 1–11. doi:10.1002/adv.21833.
- [9] Shijian Luo, C.P. Wong, Conductive polymer composites with positive temperature coefficient, in: Proc. Int. Symp. Adv. Packag. Mater. Process. Prop. Interfaces (IEEE Cat. No.99TH8405), IMAPS - Int. Microelectron. & Packaging Soc, **1999**: pp. 311–316. doi:10.1109/ISAPM.1999.757331.
- [10] Park, S.J., H.C. Kim, H.Y. Kim, Roles of work of adhesion between carbon blacks and thermoplastic polymers on electrical properties of composites, *J. Colloid Interface Sci.* **2002**, 255, 145–149. doi:10.1006/jcis.2002.8481.
- [11] Bauhofer, W., J.Z. Kovacs, A review and analysis of electrical percolation in carbon nanotube polymer composites, *Compos. Sci. Technol.* **2009**, 69, 1486–1498. doi:10.1016/j.compscitech.2008.06.018.
- [12] Mamunya, Y.P., V. V. Davydenko, P. Pissis, E. V. Lebedev, Electrical and thermal conductivity of polymers filled with metal powders, *Eur. Polym. J.* **2002**, 38, 1887–1897. doi:10.1016/S0014-3057(02)00064-2.
- [13] Zhang, Q., H. Jin, X. Wang, X. Jing, Morphology of conductive blend fibers of polyaniline and polyamide-11, *Synth. Met.* **2001**, 123, 481–485. doi:10.1016/S0379-6779(01)00354-X.
- [14] Ounaies, Z., C. Park, K.E. Wise, E.J. Siochi, J.S. Harrison, Electrical properties of single wall carbon nanotube reinforced polyimide composites, *Compos. Sci. Technol.* **2003**, 63, 1637–1646. doi:10.1016/S0266-3538(03)00067-8.
- [15] Szeluga, U., B. Kumanek, B. Trzebicka, Synergy in hybrid polymer/nanocarbon composites. A review, *Compos. Part A Appl. Sci. Manuf.* **2015**, 73, 204–231. doi:10.1016/j.compositesa.2015.02.021.
- [16] Kozłowski, M., A. Kozłowska, Comparison of electrically conductive fillers in polymer systems, *Macromol. Symp.* **1996**, 108, 261–268. doi:10.1002/masy.19961080121.
- [17] Xu, H., M. Qu, D.W. Schubert, Conductivity of poly(methyl methacrylate) composite films filled with ultra-high aspect ratio carbon fibers, *Compos. Sci. Technol.* **2019**, 181, doi:10.1016/j.compscitech.2019.107690.
- [18] Mamunya, Y., L. Matzui, L. Vovchenko, O. Maruzhenko, V. Oliynyk, S. Pusz, B. Kumanek, U. Szeluga, Influence of conductive nano- and microfiller distribution on electrical conductivity and EMI shielding properties of polymer/carbon composites, *Compos. Sci. Technol.* **2019**, 170, 51–59. doi:10.1016/j.compscitech.2018.11.037.
- [19] Villmow, T., P. Pötschke, S. Pegel, L. Häussler, B. Kretzschmar, Influence of twin-screw extrusion conditions on the dispersion of multi-walled carbon nanotubes in a poly(lactic acid) matrix, *Polymer (Guildf).* **2008**, 49, 3500–3509. doi:10.1016/j.polymer.2008.06.010.

- [20] Feller, J.F., É. Petitjean, Conductive polymer composites(CPC): influence of processing conditions, shear rate and temperature on electrical properties of poly(butylene terephthalate) / poly(amide12-b-tetramethyleneglycol)– carbon black blends, *Macromol. Symp.* **2003**, *203*, 309–316. doi:10.1002/masy.200351334.
- [21] Király, A., F. Ronkay, Effect of graphite and carbon black fillers on the processability, electrical conductivity and mechanical properties of polypropylenebased bipolar plates, *Polym. Polym. Compos.* **2013**, *21*, 93–100.
- [22] Bhat, N. V., D.T. Seshadri, M.M. Nate, A. V. Gore, Development of conductive cotton fabrics for heating devices, *J. Appl. Polym. Sci.* **2006**, *102*, 4690–4695. doi:10.1002/app.24708.
- [23] Droval, G., P. Glouannec, J.F. Feller, P. Salagnac, Simulation of electrical and thermal behavior of conductive polymer composites heating elements, *J. Thermophys. Heat Transf.* **2005**, *19*, 375–381.
- [24] Feller, J.-F., Conductive polymer composites: Influence of extrusion conditions on positive temperature coefficient effect of poly (butylene terephthalate)/poly (olefin)–carbon black, *J. Appl. Polym. Sci.* **2004**, *91*, 2151–2157. doi:10.1002/app.13337.
- [25] Nakano, H., K. Shimizu, S. Takahashi, A. Kono, T. Ougizawa, H. Horibe, Resistivity-temperature characteristics of filler-dispersed polymer composites, *Polym. (United Kingdom)*. **2012**, *53*, 6112–6117. doi:10.1016/j.polymer.2012.10.046.
- [26] Li, Q., Siddaramaiah, N.H. Kim, G.H. Yoo, J.H. Lee, Positive temperature coefficient characteristic and structure of graphite nanofibers reinforced high density polyethylene/carbon black nanocomposites, *Compos. Part B Eng.* **2009**, *40*, 218–224. doi:10.1016/j.compositesb.2008.11.002.
- [27] Xinfang, C., J. Wentao, T. Hao, Y. Huali, Effect of Irradiation on PTC Performances of Carbon Black Filled Polymer Composites, n.d., 408–413.
- [28] Zhao, Z., W. Yu, X. He, X. Chen, The conduction mechanism of carbon black-filled poly(vinylidene fluoride) composite, *Mater. Lett.* **2003**, *57*, 3082–3088. doi:10.1016/S0167-577X(02)01440-4.
- [29] Chatterjee, K., J. Tabor, T.K. Ghosh, Electrically Conductive Coatings for Fiber-Based E-Textiles, **2019**,. doi:10.3390/fib7060051.
- [30] Shim, B.S., W. Chen, C. Doty, C. Xu, N.A. Kotov, Smart electronic yarns and wearable fabrics for human biomonitoring made by carbon nanotube coating with polyelectrolytes, *Nano Lett.* **2008**, *8*, 4151–4157. doi:10.1021/nl801495p.
- [31] Ye, H., K. Wang, J. Zhou, L. Song, L. Gu, X. Cao, A true cable assembly with a carbon nanotube sheath and nickel wire core: a fully flexible electrode integrating energy storage and electrical conduction, *J. Mater. Chem. A*. **2018**, *6*, 1109–1118. doi:10.1039/C7TA08758F.
- [32] Shimizu, Y., T. Sasaki, C. Liang, A.C. Bose, T. Ito, K. Terashima, N. Koshizaki, Cylindrical metal wire surface coating with multiwalled carbon nanotubes by an atmospheric-pressure microplasma CVD technique, *Chem. Vap. Depos.* **2005**, *11*, 244–249. doi:10.1002/cvde.200406349.
- [33] Marischal, L., A. Cayla, G. Lemort, C. Campagne, É. Devaux, Influence of melt spinning parameters on electrical conductivity of carbon fillers filled polyamide 12 composites, *Synth. Met.* **2018**, *245*, 51–60. doi:10.1016/j.synthmet.2018.08.003.
- [34] Fournier, J., G. Boiteux, G. Seytre, G. Marichy, Positive temperature coefficient effect in carbon black/epoxy polymer composites, *J. Mater. Sci.* **1997**, *6*, 1677–1679. doi:10.1023/A:1018582216002.

Melt Spinning of Elastic and Electrically Conductive Filament Yarns and their Usage as Strain Sensors

Henriette Probst^{1,a*}, Joanna Wollmann^{2,b}, Johannes Mersch^{1,c}
Andreas Nocke^{1,d} and Chokri Cherif^{1,e}

¹Institute of Textile Machinery and High Performance Material Technology (ITM), TU Dresden, Hohe Straße 6, 01069 Dresden, Germany

²Institute of Lightweight Engineering and Polymer Technology (ILK), TU Dresden, Holbeinstraße 3, 01307 Dresden, Germany

^ahenriette.probst@tu-dresden.de, ^bjoanna.wollmann@tu-dresden.de,

^cjohannes.mersch@tu-dresden.de, ^dandreas.nocke@tu-dresden.de, ^echokri.cherif@tu-dresden.de

*corresponding author

Keywords: melt spinning, strain sensor, thermoplastic polyurethane, carbon nanotubes, elastic and electrically conductive filament

Abstract. Electrically conductive fibers are required for numerous fields of application in modern textile technology. They are of particular importance in the manufacturing of smart textiles and fiber composite systems with textile-based sensor and actuator systems. Elastic and electrically conductive filaments can be used as strain sensors for monitoring the mechanical loading of critical components. In order to produce such sensorial filaments, thermoplastic polyurethane (TPU) is compounded with carbon nanotubes (CNT) and melt spun. The mechanical performances of filaments produced at different spinning speeds and containing different amounts of CNT were tested. Furthermore, the correlation between the specific electrical resistance of the filaments and the mechanical strain were analyzed depending on the CNT-content and the spinning speed.

Introduction

In modern textile technology, electrically conductive fibers and filaments are needed for a wide range of applications. Textile-processable sensors and sensor networks, for example, are based on the usage of electrically conductive filaments [1–3]. Moreover, these yarns are indispensable for information transport. Thus, for example, data collected in mechanical structural health monitoring of critical components or in wound monitoring in the medical sector and nursing industry are transported by means of electrically conductive yarns [4–7]. Furthermore, the development of smart textiles and functional fiber composites is inconceivable without electrically conductive yarns, since many functions are based on the transmission of signals and the storage of electrical energy [8, 9].

Highly relevant is the development of smart clothes, which, for example, can be coupled with the smart phone and thus enable the wearer to monitor his vital functions, make inputs or read digital information from his clothing [10–12]. These applications require a high degree of mechanical flexibility, as the garment must deform accordingly to the movements of the human wearer. Also, modern fiber rubber composites which are used in soft robotics, demand electrical conductivity in order to sense environmental conditions and react accordingly [13]. At the same time, the Young's modulus and yield strain of the electrically conductive textile components should be as low as possible in order to minimally restrict motion and enable high deformations [14].

However, in line with the current state of the art, mainly metal-based systems are used to conduct electric current in textiles. For example, fine copper wires or silver-plated yarns are used in woven and knitted fabrics [15–17]. However, these yarns exhibit high Young's moduli, can break at small bending radii and exhibit low durability, since electrically conductive particles are extracted from the surface or coating during use, so that the electrical resistance increases.

In addition to metal-based yarns, some stretchable, electrically conductive fiber materials exist which are either produced by the functionalization of an elastic filament with an electrically

conductive coating, the achievement of structural elongation by tailored geometric arrangement of non-elongatable but electrically conductive yarns or a combination of both possibilities [18]. The coating as well as the geometric arrangement feature several disadvantages. For example, the coating of elastic filaments with an electrically conductive coating solution, that is often based on brittle and stiff conductive particles, requires a multistep process in order to guarantee a stable bond between coating and textile base material [19, 20]. If conductive yarns, on the other hand, are manufactured in a special geometric arrangement, as for example in a helical structure, they can be stretched considerably, but the yarn structures also exhibit great diameters which are negative for several applications and processing variants [21]. The aim of the presented research work is therefore to realize a highly stretchable, textile processable yarn system with electrical conductivity in one production step. For this purpose, thermoplastic polyurethane (TPU) is compounded with carbon nanotubes (CNT) and spun. TPU exhibits a low Young's modulus, but unlike other elastomers, it can be thermally processed so that it can be spun in a melt spinning process. In order to reduce the electrical resistance of the polymeric base material, TPU is compounded with CNT. The melt spinning of TPU-CNT-compounds enables a cost-effective and automatable production process for the manufacturing of elastic and electrically conductive filament yarns.

Materials and Methods

The TPU grade Desmopan 9370A from Covestro AG (Leverkusen, Germany) [22] and the masterbatch TPU 1001 from Nanocyl SA (Sambreville, Belgium) [23] were used in order to produce electrically conductive and highly elastic filaments. The masterbatch TPU 1001 contains 10 wt% CNT. As this filling grade is too high to be processed, the masterbatch and the pure TPU were pre-compounded by hand to a polymeric material containing 1 – 6 wt% CNT. All materials were dried for 24 h at 80 °C before starting the spinning process. A bicomponent melt spinning plant of Dienes Apparatebau GmbH (Mühlheim am Main, Germany), which is present at ITM, TU Dresden, is used for all trials. The tests were performed under a nitrogen atmosphere to avoid the oxidation of TPU. A 60-filament core-sheath spinning die offering a die diameter of 0.6 mm was used and a spinning temperature of 190 °C was selected. The winding speeds were varied between 8 and 650 m/min according to the compound's spinnability.

To determine the melt viscosity, isothermic rheometric measurements were performed on a Haake RheoWin /Thermo Scientific Mars II from Thermo Fisher Scientific Inc. (Waltham, USA) at 200 °C. Tensile tests were performed on a Zwicki Junior from ZwickRoell GmbH & Co. KG (Ulm, Germany) with a clamping length of 62.5 mm and a testing speed of 200 mm/min. For each specification, five samples were tested. The fineness of the melt spun multifilament yarns was determined in accordance with DIN EN ISO 2060. For this purpose, five samples with a defined length of 1 m were taken from each spinning specification. The mass of the samples was then determined using a precision scale R200D from Sartorius (Göttingen, Germany). Microscopic images of the cross section of spun filaments were obtained by means of the light microscope Zeiss Ultra Plus with Axio Imager M1 from Carl Zeiss AG (Jena/Oberkochen, Germany).

In order to measure the electrical resistance depending on the mechanical strain loading of the filaments, tensile tests were combined with a four wire measurement method. Therefore, a current source Voltcraft LRP-1601 (Wollerau, Switzerland), supplying 100 mA, and two multimeters Keithley DAQ6510-7700 from Keithley Instruments Corp. (Solon, USA) were used. The multimeters were used to measure current and voltage at the clamped sample. Then, the electrical resistance was calculated as a function of the testing time. In parallel, the mechanical strains were recorded as a function of time, so that a correlation between electrical resistance and strain is determined. Of each spinning specification, five samples were tested.

Results and Discussion

In order to analyze the rheological properties of the polymer melt, which are important for the melt spinning process, measurements of the viscosities of different TPU-CNT-compounds are presented.

The addition of CNT to TPU leads to a significant rise in the compound's melt viscosity (see Fig. 1). For example, once the CNT content was increased from 1 wt% CNT to 5 wt% CNT, a tenfold increase in viscosity was observed at shear rates of $1 - 10 \text{ s}^{-1}$, which are particularly relevant for the melt spinning process.

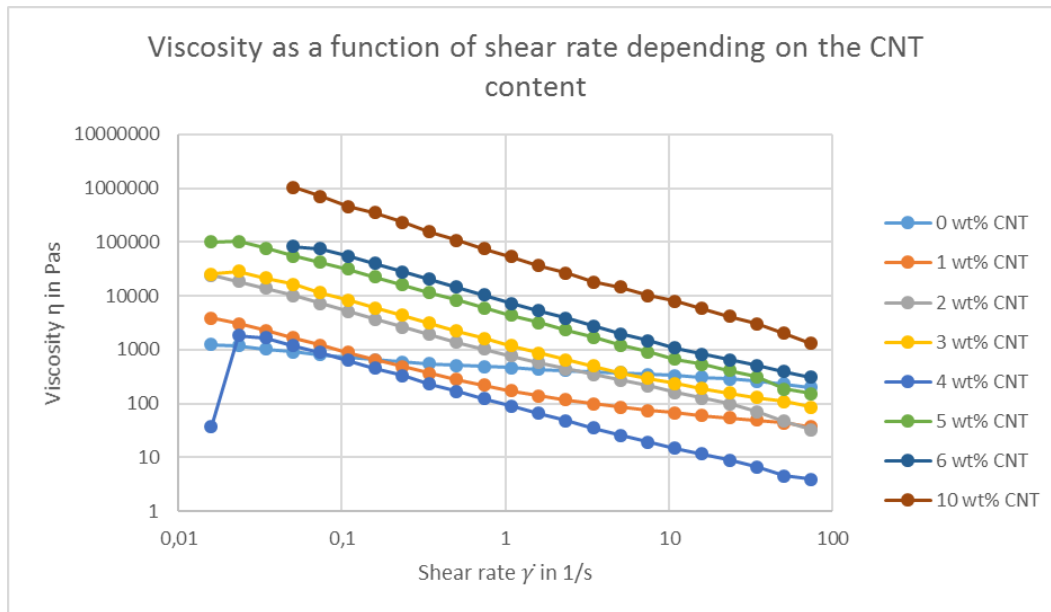


Figure 1: Viscosity of compounds containing different amounts of CNT, measured at a constant temperature of $200 \text{ }^{\circ}\text{C}$

The very high viscosities of up to 100 kPas at filling grades of 5 and 6 % CNT does not only increase the spinning pressure in the process up to 150 bar, they also lead to heterogeneities in the filaments diameter, reduce the possible spinning speed and increase the filament weight. As a result, filaments containing 2 wt% CNT or more must be pulled off at significantly lower speeds compared to pure TPU in order to avoid filament breakage. TPU-CNT-compounds with 0 wt% or 1 wt% offer the potential to be spun at high winding speeds of up to 650 m/min, whereas compounds with 2 wt% or more CNT cannot be spun at speeds exceeding 35 m/min. Compounds with more than 6 wt% CNT are not spinnable, because the viscosity is too high.

At filling grades of 3 % CNT or more, the weight of the spun filaments is too high to be carried by the melt coming out of the spinneret, so filament breakages occur, if the length of the filament exceeds 0.5 m. Therefore, extensive modifications to the spinning machine were required in order to ensure process stability. By means of an additional device, the weight of the solidified filaments was supported shortly below the spinneret so that the melt no longer had to support the entire weight of the filaments. For this purpose, a duo of godets driven by an electric motor was inserted into the spinning shaft 0.3 m below the spinneret (see Fig. 2).

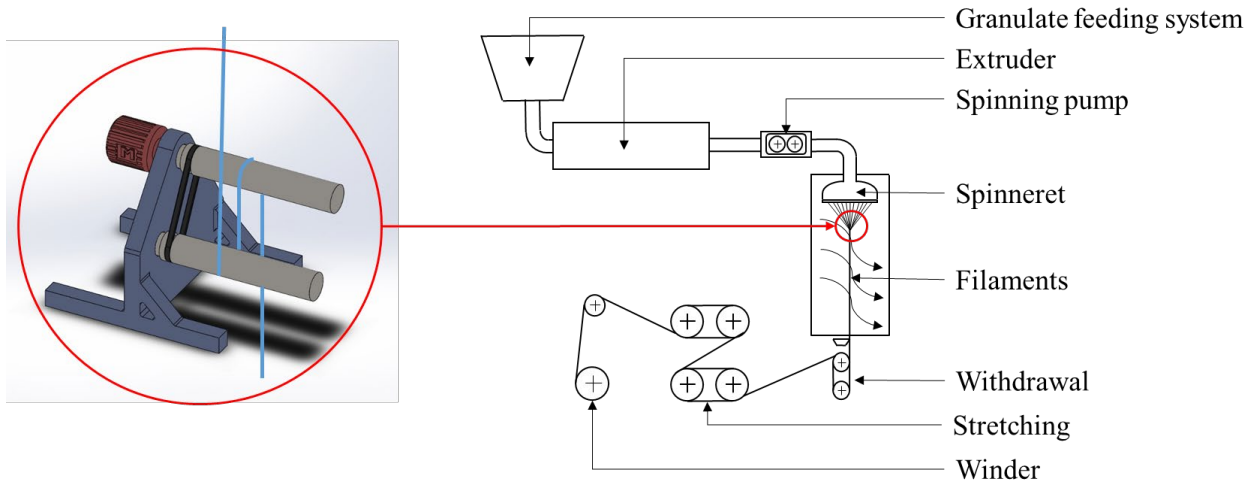


Figure 2: Additional duo of godets and its insertion in the melt spinning process

First, the spun filaments were guided over the lower cylinder and second, they ran vertically upwards while being drawn by the upper cylinder. Due to the staggered arrangement of the cylinders, further deflection points can be avoided to minimize potential effects on the yarn path, the geometry of individual filaments, and the arrangement of filaments in the fiber bundle. Once the spun filaments passed this additional device, they were taken-off and wound up.

The low spinning speed increases the CNT's tendency to agglomerate. The electrically conductive particles attract each other and as long as the polymer matrix surrounding them is in a liquid aggregate state, rearrangement processes within the filament are possible. This means that due to the low take-off speed and the resulting larger filament diameters and higher solidification times, a CNT-rich filament core and a sheath of pure TPU are formed. Even in a monocomponent spinning process, a core-sheath structure with an electrically conductive core and an insulating sheath occurs due to the CNT agglomerations in the filament core. This behavior is increased by the usage of a bicomponent melt-spinning process, which enables the spinning of core-sheath filaments. In this process, the TPU-CNT-compound is spun in the core and the sheath is composed of clear TPU. Fig. 3 shows microscopy pictures of the cross section of TPU-CNT-filaments melt spun in a monocomponent and in a bicomponent spinning process.

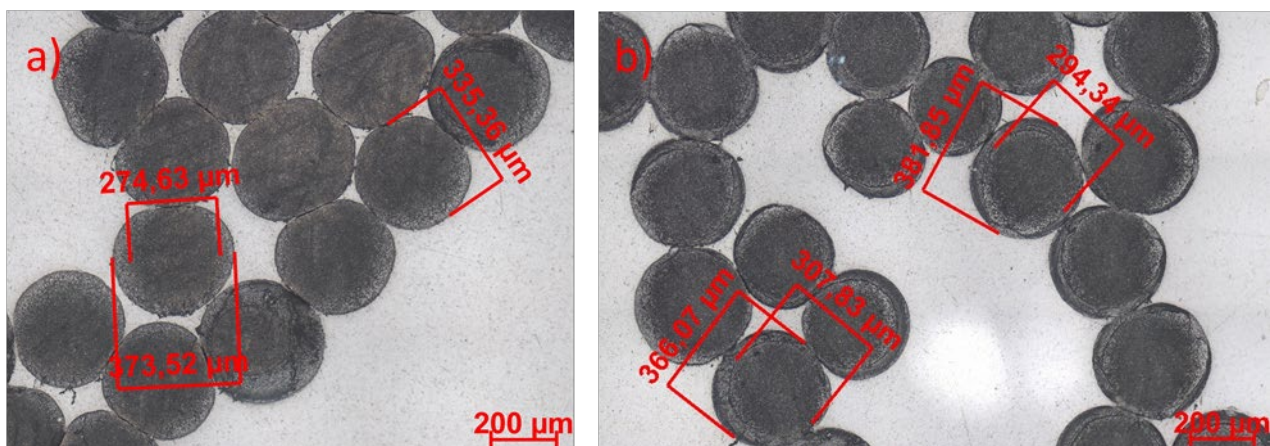


Figure 3: Cross section of filaments made of TPU and CNT; melt spun at 10 m/min, a) monocomponent spinning process, b) bicomponent spinning process

For many applications, it is a great advantage to shield the conductive filament with an insulating sheath. In that case, the probability of short circuits can be minimized significantly. If the filaments spun in a bicomponent process contain the same amount of CNT and are produced at the same spinning parameters (e.g. speed, nozzle diameter, temperature), their outer and inner diameters can be processed in the same range as those of filaments spun in a monocomponent process. In both cases

the diameter of the electrically conductive core, composed of TPU and CNT, is in the range of 270 – 300 μm and the outer diameter is $380 \pm 20 \mu\text{m}$.

The electrically conductive yarns were produced in a multifilament spinning process. Each yarn contains 60 filaments. The multifilament yarns finesses are in the range of 1000 – 3000 tex depending on the spinning speed and the CNT-content. The Young's moduli are below 80 kPa and elongations of up to 400 % can be reached. For more detailed information see [24].

At a constant CNT-content, the reachable stress level and elongation at break increase with decreasing spinning speed, as can be seen in Fig. 4.

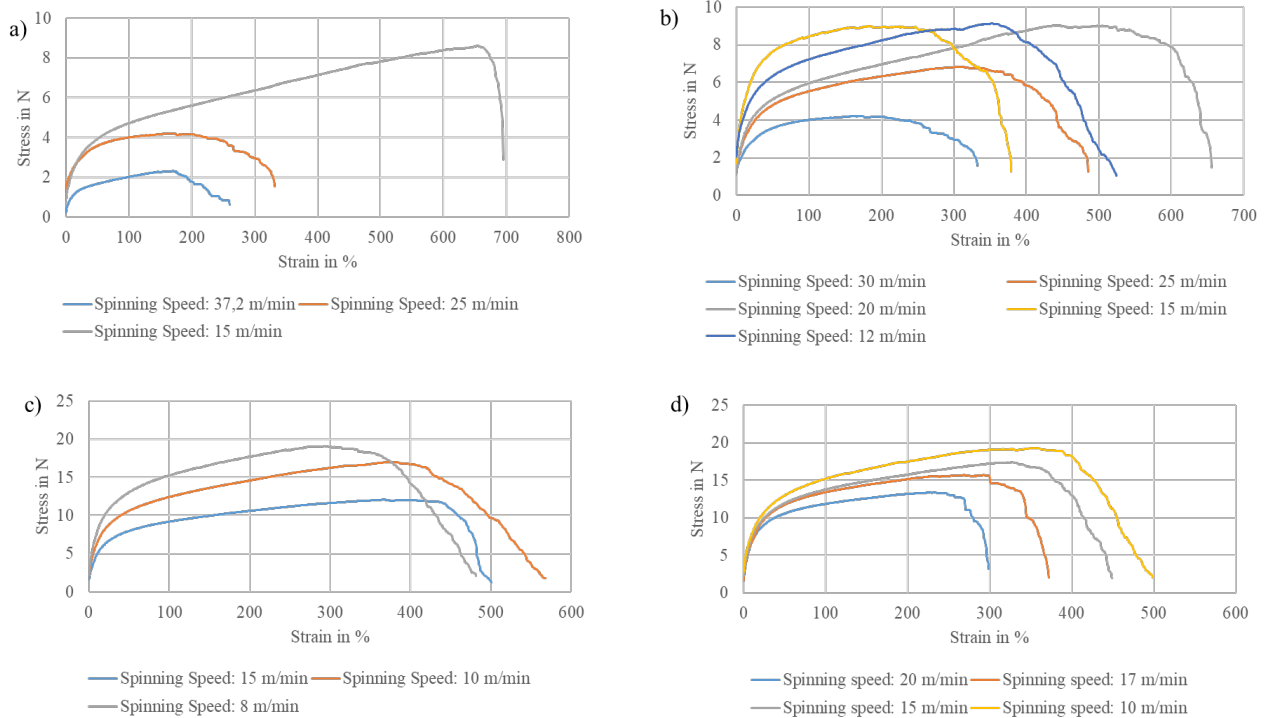


Figure 4: Strain-Stress-Diagrams of multifilament yarns melt spun at different spinning speeds, containing a) 3 wt% CNT, b) 4 wt% CNT, c) 5 wt% CNT, d) 6 wt% CNT

If the spinning speed was kept constant, it can be seen, that the elongations at break decrease with increasing CNT-content. Meanwhile, the achievable stress levels increase, as can be seen in Fig. 5. The curve at 4 % CNT and 15 m/min spinning speed must be regarded as an anomaly. Even though the corresponding tests have been repeated 3 times, the obtained values do not fit within the expected behavior. However, an irregular material behavior at 4 % CNT caused by the material itself seems unlikely from a physical point of view. Probably, a process-related technical peculiarity occurred in the manufacturing of the yarns, which cannot be defined in more detail according to the current state of knowledge. At this point, further investigations are necessary to analyze the strain-stress behavior of the melt-spun TPU-CNT yarns in more detail.

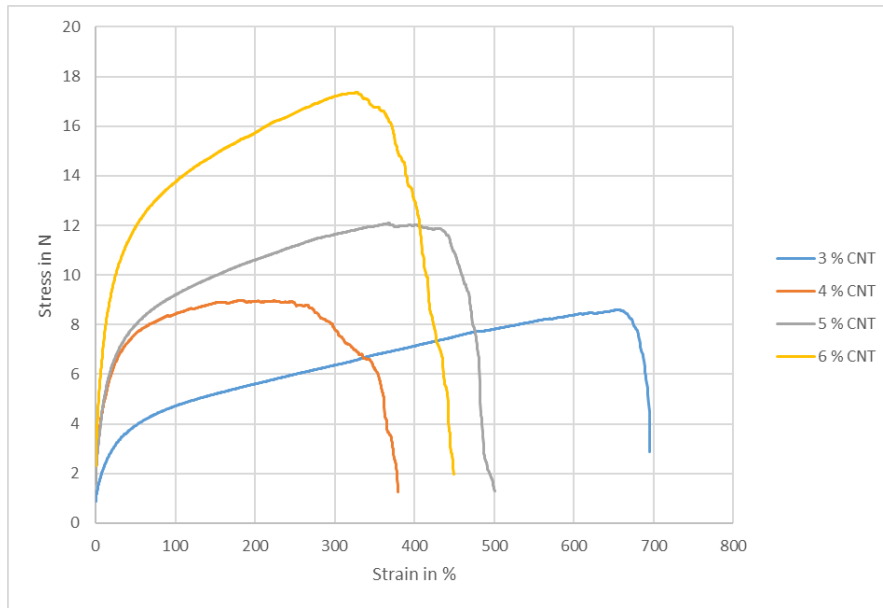


Figure 5: Strain-Stress-Diagrams of multifilament yarns containing different amounts of CNT; all yarns were spun at 15 m/min

The specific electrical resistances increase with decreasing CNT-content and increasing spinning speed. The minimum specific electrical resistance of $110 \pm 39 \Omega\text{cm}$ is found at 5 wt% CNT and a spinning speed of 10 m/min. Compounds containing more than 5 wt% CNT does not offer a lower electrical resistance. The underlying cause is the agglomeration tendency of the CNT, which dominates the electrical properties at higher filling grades.

If the filaments are stretched, the electrical resistance increases, because the electrically conductive particles are pulled away from each other, thus enabling the usage of the melt-spun filaments as strain sensors. Fig. 6 shows the relationship between mechanical strain and specific electrical resistance depending on the CNT-content. The spinning speed during the production of the filaments containing different amounts of CNT was 15 m/min in every case.

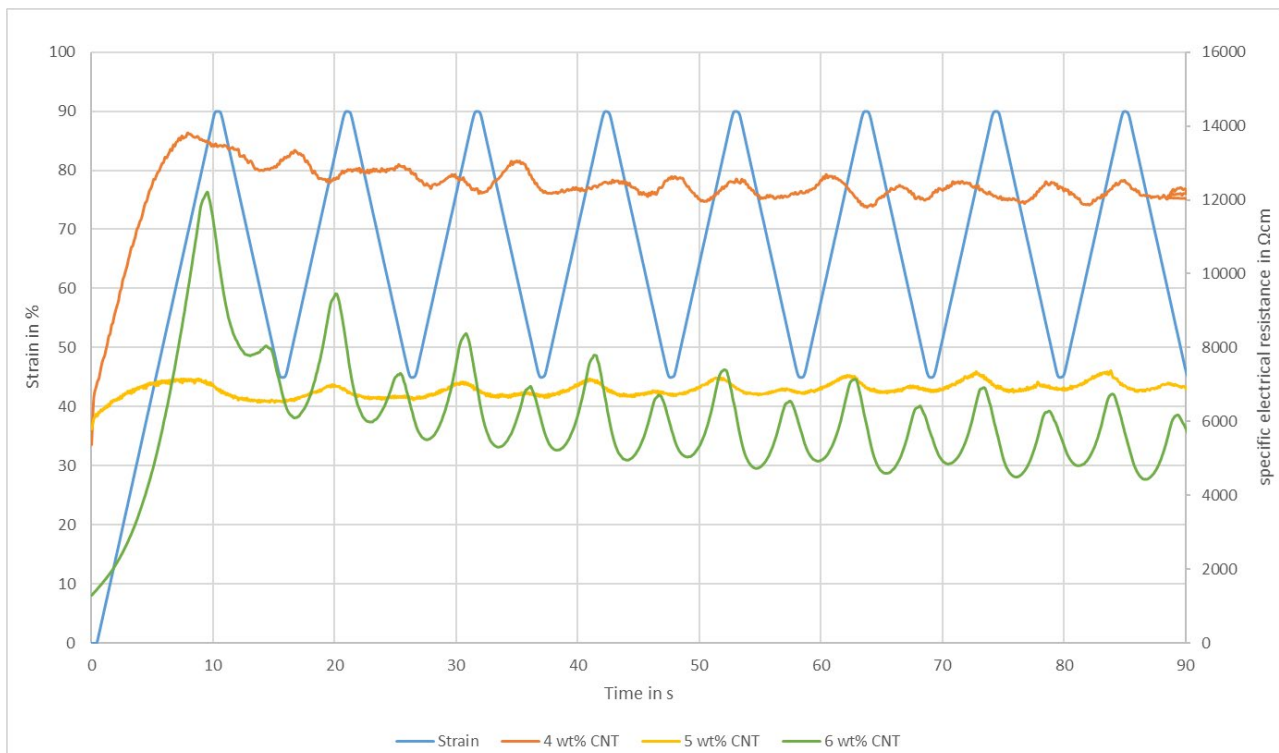


Figure 6: Strain and electrical resistance depending on the testing time; tested at multifilament yarns containing different amounts of CNT

The results of the yarns containing 3 % CNT could not be included in the evaluation because the determined electrical resistance partly exceeded the measuring range of the measurement device and thus no reliable evaluation was possible. The recorded curve of the filaments containing 4 % CNT is suitable for determining a general level of the electrical resistance, but does not accurately represent the course of the electrical resistance as a function of the mechanical elongation. Again, it is apparent that the specification in question has anomalies in the electrical and mechanical properties. Nevertheless, it can be clearly seen that the specific electrical resistance increases with decreasing CNT-content. The filaments containing 4 wt% CNT exhibit the highest mean level of resistance. The corresponding difference between the mean specific electrical resistance of filaments containing 5 wt% CNT and 6 wt% CNT is not very pronounced. This behavior can be explained by the agglomeration tendency of the CNT, which increases with increasing filler content. Due to the formation of agglomerations, the electrical conductivity does not increase further by adding more CNT to the polymer compound.

Especially at a filling grade of 6 wt% CNT, a very pronounced shoulder phenomenon can be seen in the curve showing the electrical resistance. Shoulder phenomena, which mean the existence of local maxima in the electrical resistance at strain minima, can often be seen in filled elastomers under strain loading. This characteristic behavior can be explained with the help of the transverse contractions in the filament induced by the strain loading [25, 26]. The curve of the filaments containing 5 % CNT shows the slightest shoulder phenomenon and thus exhibits an almost direct correlation between elongation and resistance. This direct correlation is particularly important for the usage as sensor, as it allows a direct conclusion to be drawn from the measured change in resistance to the existing strain load. For this reason, the melt-spun filaments containing 5 wt% CNT will be investigated in more detail in the following (see Fig. 7).

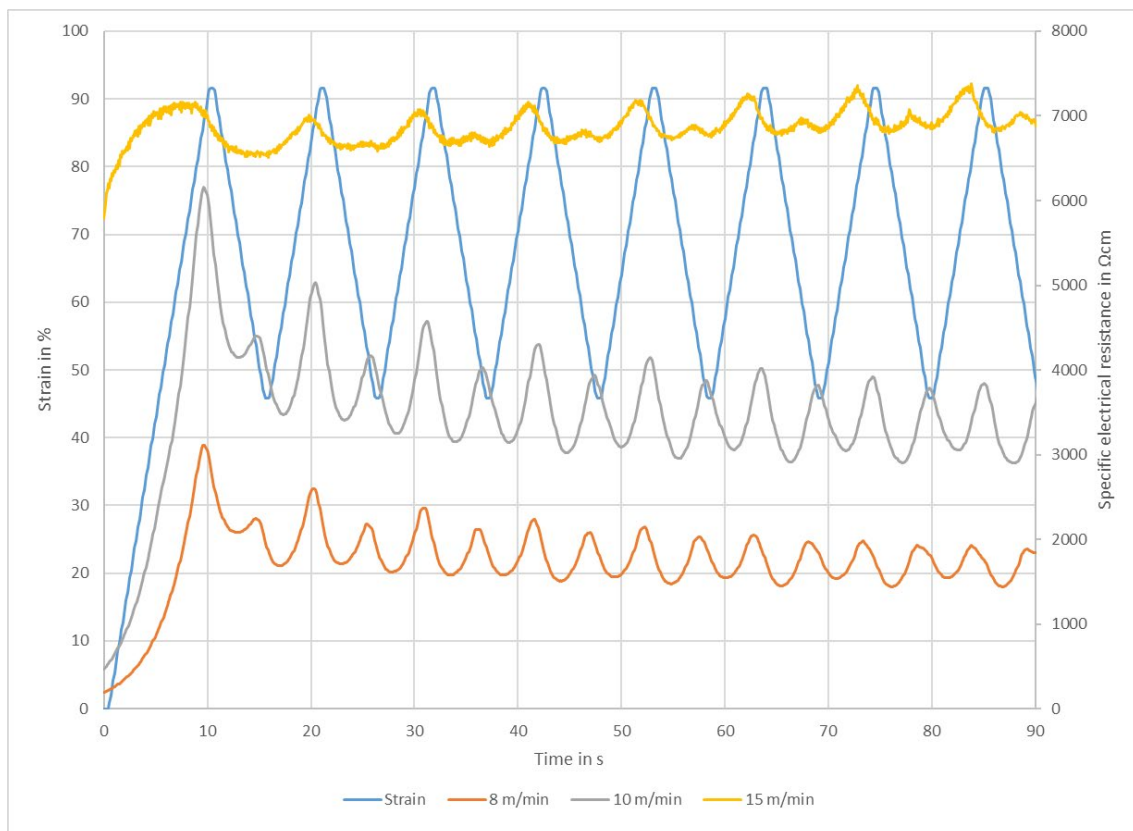


Figure 7: Strain and electrical resistance depending on the testing time; tested at multifilament yarns containing 5 wt% CNT and spun at different spinning speeds

If the CNT-content is kept constant, the specific electrical resistance increases with increasing spinning speed, because during the spinning process and the fiber solidification, the electrically conductive particles are pulled away from each other. Thereby, electrically conductive pathways are

interrupted. It can be seen that the shoulder phenomenon is more concise at lower spinning speeds. The best correlation between mechanical strain and electrical conductivity can be found at a CNT-content of 5 wt% and a spinning speed of 15 m/min but even here, a significant phase shift can be detected. In order to produce reliable resistive strain sensors by melt spinning TPU-CNT compounds, further detailed research is needed.

Conclusion

Polymer compounds composed of TPU and up to 6 wt% CNT can be melt-spun. The resulting filaments exhibited a very high elongation at break while providing mechanical properties in the range of conventional elastic fibers [27] and electrical conductivities in the range of electrically conductive liquid rubbers [28]. At high filling grades and low spinning speeds, the CNT tend to agglomerate in the filament's core, thereby forming an electrically conductive core surrounded by an insulating sheath of clear TPU. This new class of electrically conductive, highly stretchable yarns offers a great potential for strain sensors. The best correlation between mechanical strain and specific electrical resistance can be found in multifilament yarns containing 5 wt% CNT and spun at 15 m/min. In the future, further spinning experiments should be carried out in order to reduce the shoulder phenomenon in other configurations as well, so that elastic yarns with good electrical conductivity can be used to monitor mechanical loads in soft robotics and smart textiles. Furthermore, these yarns could be used in wearable smart textiles for actuation, energy harvesting, computing and communication.

Acknowledgement

The DFG research project 380321452/GRK2430 is supported by the Deutsche Forschungsgemeinschaft (DFG, German Research Foundation). The financial support is gratefully acknowledged.

References

- [1] J. Wendler, A. Nocke, D. Aibibu, C. Cherif, Novel temperature sensors based on strain-relieved braiding constructions, *Textile Research Journal* 5 (2018) 004051751880744.
- [2] I. Jerkovic, V. Koncar, A.M. Grancaric, New Textile Sensors for In Situ Structural Health Monitoring of Textile Reinforced Thermoplastic Composites Based on the Conductive Poly(3,4-ethylenedioxythiophene)-poly(styrenesulfonate) Polymer Complex, *Sensors (Basel, Switzerland)* 17 (2017).
- [3] W.A. Hufenbach, P. Kostka, B. Maron, D. Weck, J. Ehlig, M. Gude, M. Zscheyge, Development and Investigation of a Textile-reinforced Thermoplastic Leaf Spring with Integrated Sensor Networks, *Procedia Materials Science* 2 (2013) 173–180.
- [4] A. Nocke, A. Schröter, C. Cherif, G. Gerlach, Miniaturized textile-based multi-layer ph-sensor for wound monitoring applications, *Autex Research Journal* 12 (2012) 20–22.
- [5] P. Lugoda, T. Hughes-Riley, R. Morris, T. Dias, A Wearable Textile Thermograph, *Sensors (Basel, Switzerland)* 18 (2018).
- [6] E. Haentzsch, T. Onggar, A. Nocke, R.D. Hund, C. Cherif, Multi-layered sensor yarns for in situ monitoring of textile reinforced composites, *IOP Conf. Ser.: Mater. Sci. Eng.* 254 (2017) 42012.
- [7] K. Bremer, F. Weigand, Y. Zheng, L.S. Alwis, R. Helbig, B. Roth, Structural Health Monitoring Using Textile Reinforcement Structures with Integrated Optical Fiber Sensors, *Sensors (Basel, Switzerland)* 17 (2017).
- [8] J.S. Heo, J. Eom, Y.-H. Kim, S.K. Park, Recent Progress of Textile-Based Wearable Electronics: A Comprehensive Review of Materials, Devices, and Applications, *Small (Weinheim an der Bergstrasse, Germany)* 14 (2018).
- [9] B. Wang, A. Facchetti, Mechanically Flexible Conductors for Stretchable and Wearable E-Skin and E-Textile Devices, *Advanced materials (Deerfield Beach, Fla.)* 31 (2019) e1901408.
- [10] V. Koncar (Ed.), *Smart Textiles and their Applications*, Woodhead Publishing, Oxford, 2016.

-
- [11] R.R. Ruckdashel, D. Venkataraman, J.H. Park, Smart textiles: A toolkit to fashion the future, *Journal of Applied Physics* 129 (2021) 130903.
- [12] A. Issatayeva, A. Beisenova, D. Tosi, C. Molardi, Fiber-Optic Based Smart Textiles for Real-Time Monitoring of Breathing Rate, *Sensors (Basel, Switzerland)* 20 (2020).
- [13] E.-F.M. Henke, S. Schlatter, I.A. Anderson, Soft Dielectric Elastomer Oscillators Driving Bioinspired Robots, *Soft robotics* 4 (2017) 353–366.
- [14] D. Rus, M.T. Tolley, Design, fabrication and control of soft robots, *Nature* 521 (2015) 467–475.
- [15] A. Satharasinghe, T. Hughes-Riley, T. Dias, Photodiode and LED embedded textiles for waearable healthcare applications, Ghent, 2019.
- [16] E. Haentzsch, R. Mueller, M. Huebner, T. Ruder, R. Unger, A. Nocke, C. Cherif, Manufacturing technology of integrated textile-based sensor networks for in situ monitoring applications of composite wind turbine blades, *Smart Mater. Struct.* 25 (2016) 105012.
- [17] T. Onggar, G. Amrhein, A. Abdkader, R.-D. Hund, C. Cherif, Wet-chemical method for the metallization of a para-aramid filament yarn wound on a cylindrical dyeing package, *Textile Research Journal* 87 (2017) 1192–1202.
- [18] S. Qin, S. Seyedin, J. Zhang, Z. Wang, F. Yang, Y. Liu, J. Chen, J.M. Razal, Elastic Fiber Supercapacitors for Wearable Energy Storage, *Macromolecular rapid communications* 39 (2018) e1800103.
- [19] Z. Yang, J. Deng, X. Chen, J. Ren, H. Peng, A Highly Stretchable, Fiber-Shaped Supercapacitor, *Angew. Chem.* 125 (2013) 13695–13699.
- [20] C. Cao, S. Burgess, A.T. Conn, Toward a Dielectric Elastomer Resonator Driven Flapping Wing Micro Air Vehicle, *Front. Robot. AI* 5 (2019) 263.
- [21] Z. Yang, Z. Zhai, Z. Song, Y. Wu, J. Liang, Y. Shan, J. Zheng, H. Liang, H. Jiang, Conductive and Elastic 3D Helical Fibers for Use in Washable and Wearable Electronics, *Advanced materials (Deerfield Beach, Fla.)* 32 (2020) e1907495.
- [22] Information on https://solutions.covestro.com/en/products/desmopan/desmopan-9370a-gmp_84876836-05124172?SelectedCountry=DE
- [23] Information on <https://www.nanocyl.com/product/plasticyl-pp2001-2/>
- [24] H. Probst, K. Katzer, A. Nocke, R. Hickmann, M. Zimmermann, C. Cherif, Melt Spinning of Highly Stretchable, Electrically Conductive Filament Yarns, *Polymers* 13 (2021) 590.
- [25] J. Mersch, H. Probst, A. Nocke, C. Cherif, G. Gerlach, Non-Monotonic Sensor Behavior of Carbon Particle-Filled Textile Strain Sensors, *Soft robotics* 1 (2021).
- [26] J. Mersch, H. Winger, A. Nocke, C. Cherif, G. Gerlach, Experimental Investigation and Modeling of the Dynamic Resistance Response of Carbon Particle-Filled Polymers, *Macromol. Mater. Eng.* 305 (2020) 2000361.
- [27] T. Hua, N.S. Wong, W.M. Tang, Study on properties of elastic core-spun yarns containing a mix of spandex and PET/PTT bi-component filament as core, *Textile Research Journal* 88 (2018) 1065–1076.
- [28] Wacker Chemie AG, Powersil 464 A/B: Electrically Conductive Liquid Rubber 2020.

Polymer/CNT Composites and Filaments for Smart Textiles: Melt Mixing of Composites

Müslüm Kaplan^{1,a*}, Beate Krause^{2,b} and Petra Pötschke^{2,c}

¹Faculty of Engineering, Architecture and Design, Bartın University, Bartın, Turkey

²Leibniz-Institut für Polymerforschung Dresden e.V. (IPF), Hohe Str. 6, 01069 Dresden, Germany

^amkaplan@bartin.edu.tr, ^bkrause-beate@ipfdd.de, ^cpoe@ipfdd.de

*Corresponding author

Keywords: carbon nanotube, melt mixing, polyamide 6, polyethylene, composite, electrical conductivity, smart textiles

Abstract. Textile products are of great importance in the dissemination of newly developed communication devices and flexible electronics in conjunction with the advantages of covering the entire human body and being used all day long by all individuals in society. Various approaches have been developed to ensure the required electrical conductivity of textiles. Our research deals with melt spinning of carbon nanomaterial-based composites (CNCs) into electrically conductive filaments. By combining the various composite structures and property profiles with a conductive filler at high concentration, specific morphological structures can be achieved that offer a much higher potential for the development of new functional fibers for different smart textile applications.

This study aims to produce nanocomposites from polyamide 6 (PA6) and polyethylene (PE) matrices with single-walled CNTs (SWCNTs) and multi-walled CNTs (MWCNTs) by using a small-scale mixing device that provides short mixing time, and material savings in the first stage of the research.

Introduction

Developing digital technology and changing consumer demands increase the need for information processing systems that are in connection and interaction with the environment [1, 2]. Textile products are an interface that can be of great importance in the dissemination of newly developing communication devices, flexible electronics, and nanomaterials with the advantages of covering the entire human body and being used all day long by all individuals in society [3]. In addition, textiles provide the highest level of flexibility in system design thanks to their wide range of fibers, yarns, fabrics, and production techniques, thus creating a wearable and comfortable mobile information infrastructure [4]. Thus, studies have shown increased efforts to convey various functionalities to textile fibers, such as electrical conductivity, which is critical for applications such as anti-static protection, electromagnetic interferences (EMI) shielding, sensors, textile electrode material for charge storage systems, or signal transfer [5].

Since textile polymers are largely insulating by nature, several approaches [6] exist on how to enhance the high conductivity of the textiles such as using thin metal wires or hybrid yarns [7] with metalcore in woven or knitted fabrics [8]. An alternative method is to coat the fibers, yarns, or fabrics with a thin metal layer or a conductive polymer [9]. The fabrication of conductive fabrics from metal has been widely studied because of their high conductivity, stability, and low cost [10]. However, there are several disadvantages in using metals, linked e.g., with degradation by wear and tear and durability during textile production or can modify the primary textile properties, such as the washability and hand feel [11]. Corrosion and oxidation may occur, failing due to decreased conductivity. It is known that depending on the layer thickness certain garments can only last for a maximum of 50 wash cycles [12]. Another option is to use intrinsically conducting polymers (ICPs), to which electron donors must be added to conduct electricity. Their disadvantage is that they are difficult to dissolve and almost impossible to melt [13]. Therefore, they must first be dispersed in a matrix polymer. In addition to the high polymer price of ICPs, mixing and processing further

increases the material price, so the study of ICPs for large-scale textile applications is rarely carried out [14].

Carbon nanomaterial-based composites (CNCs) have gained great interest due to their high mechanical, electrical, magnetic, and thermal properties in the last decades [15]. They have a very high potential in different industrial applications in the manufacture of sensors, microelectrodes, electromagnetic shielding materials, electroconductive rubbers, electrostatically paintable materials, parts for automotive engineering, etc. [16]. Thus, their property profile depends on CNT properties, dispersion, and orientation aspects, interfacial adhesion, and matrix properties which can widely vary [17]. The prices of materials such as carbon nanotubes (CNTs) and graphene, whose raw material prices were very high when they were first developed, are falling due to the development of production processes in larger quantities. especially in single-walled CNT (SWCNT) materials, due to the low percolation threshold, the desired properties can be achieved by using very low percentage weight nanoparticles [18]. All this has greatly expanded the application areas of these nanocomposites while reducing production costs.

CNCs can be spun into filaments that have a very high potential in different industrial applications [19]. The structural properties of the filament yarns will primarily depend on the properties of the nanocomposite to be used, its dispersion, orientation, interfacial adhesion, and the properties of the polymer to be used [20]. Our research deals with melt spinning of carbon nanomaterial-based composites (CNCs) into electrically conductive filaments. By combining the various composite structures and property profiles with a conductive filler at high concentration, specific morphological structures can be achieved that offer a much higher potential for the development of new functional fibers for different smart textile applications.

This study aims to produce nanocomposites from polyamide (PA6) and polyethylene (PE) matrices with SWCNTs and multi-walled CNTs (MWCNTs) by using a small-scale mixing device that provides short mixing time, and material savings in the first stage of the research.

Materials and Methods

The polymers as matrices used were PA6 and PE. The carbon-based nanofillers used were MWCNTs, SWCNT (pure), and an SWCNT matrix provided as a masterbatch with 90 wt% PE and 10 wt% SWCNTs. The polymer matrices and nanofillers used in this study are shown in Table 1.

Table 1. Polymer matrices and nanofillers used in this study

Material	Trade Name	Company
PA6	B27E	BASF AG, Ludwigshafen, Germany
PE	Evolve-H	Prime Polymer Co. Ltd., Tokyo, Japan
MWCNT	NC7000	Nanocyl S.A., Sambreville, Belgium
SWCNT	Tuball™ 75%	OCSiAl Ltd., Novosibirsk, Russia
SWCNT masterbatch	Tuball matrix 816 Beta	OCSiAl Ltd., Novosibirsk, Russia

Melt compounding of PA6/CNTs [15] was performed at a mixing temperature of 260 °C, a rotation speed of 250 rpm, and a mixing time of 5 min using a conical twin-screw micro-compounder Xplore15 having a capacity of 15 ccm (Xplore Instruments BV, Sittard, Netherland). After mixing the material was led out as a strand without additional cooling and rotations speed lowered to 50 rpm (Fig. 1). The extruded strands were cut into pieces of some millimeters in length and compression molded into plates. Pressing conditions: 260 °C, 2.5 min pre-melting and 1.5 min pressing under 50 kN pressing force, press PW40EH (Otto-Paul-Weber GmbH, Germany. Electrical measurements were performed on these pressed plates with a thickness of 0.3 mm and a diameter of 60 mm).

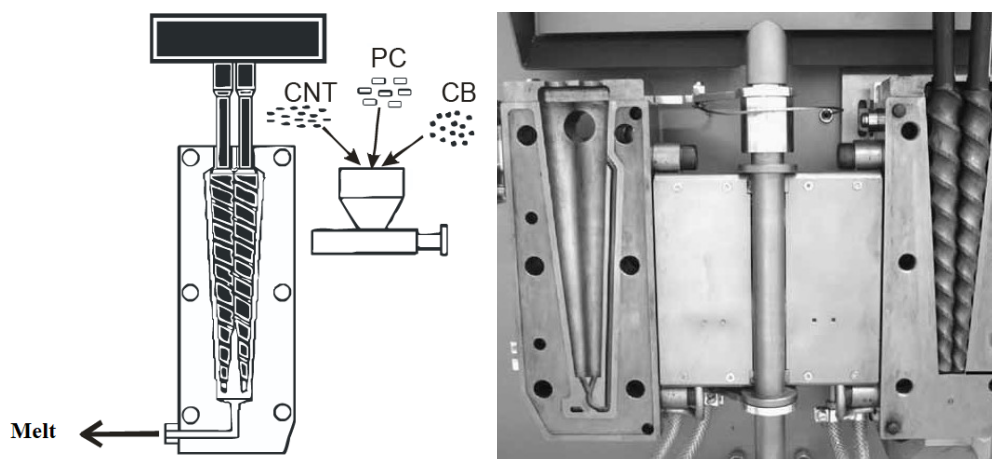


Fig. 1. Conical twin-screw micro compounder Xplore15

Melt compounding of PE/SWCNT was performed using micro-compounder Xplore15 at a mixing temperature of 180 °C, a rotation speed of 20 rpm, and a mixing time of 5 min. After mixing, the material was led out as a strand using a 1 mm nozzle. Melt spinning ability was evaluated using a micro-scale winder (“Micro Fiber Spin Device” - Xplore Instruments BV, Sittard, Netherland) set up directly after the extruder nozzle and by drawing a monofilament of PE/SWCNT of at least 50 m. Fiber diameters ranged from 0.4 to 0.9 mm depending on SWCNT content.

To measure the electrical volume resistivity of PA6/CNT compression-molded plates a Keithley 6517a electrometer combined with a Keithley 8009 test fixture (Keithley Instruments, USA) was used for all pressed plates. For resistances lower than 10^{11} Ω cm, the measurements were carried out on strips (length of 20 mm, wide of 6 mm, cut from the plates) using a 4-point test fixture having gold electrodes combined with Keithley electrometer E6517A and Keithley multimeter DMM 2001 (for resistances lower than 10^6 Ω cm recommended to use DMM 2001). The electrical resistance of PE/SWCNT was measured directly on single filaments with a length of about 100 mm using a DT-61 digital multimeter from MASTECH (Multimeter Warehouse, Walnut, CA, USA).

The state of CNT macrodispersion in the PA6/CNT composites containing 1 wt.% CNT was determined using light transmission microscopy. Thin sections with 5 μ m thickness were prepared from the extruded strands using a Leica RM 2265 microtome (Leica Microsystems GmbH, Germany) and were fixed with Aquatex® on glass slides. The samples were characterized with a microscope BX53M in transmission mode combined with a camera DP74 (Olympus Deutschland GmbH, Germany). The area ratio A_A (%) of the area of filler agglomerates related to the total area of the images was calculated using an image analysis process.

Results and Discussion

The electrical volume resistivity of polymer/CNT composites and filaments at a filler content of 0.1-10 wt % is given in Table 2.

Table 2. Electrical volume resistivity of polymer nanocomposites containing different CNTs

CNT Content (wt %)	Electrical Volume Resistivity (Ω cm)		
	PA6/MWCNT*	PA6/SWCNT*	PE/SWCNT ⁺
0.1	-	3.89E+05	-
0.25	-	1.65E+04	-
0.5	2.95E+14	1.32E+03	-
1.0	1.07E+14	2.10E+02	-
2.0	9.15E+07	1.30E+02	-
3.0	1.35E+06	1.09E+02	-
4.0	1.66E+05	1.07E+02	-
5.0	9.43E+03	2.51E+01	-
8.0	-	-	1.1E+02
10	-	-	1.7E+03

*Measured on plates ⁺ measured on filaments.

The results of volume resistivity measurements show the significantly lower electrical percolation threshold of the PA6/SWCNT as compared to the PA6/MWCNT composites. The resistivity value of PA6/SWCNT achieved at the loading of 0.1 wt % already lower than 10^6 Ohm cm and at 0.25 wt % addition, values lower than 10^4 Ohm cm are reached. Similar resistivity values were achieved for PA/MWCNT loadings of 4-5 wt %. However, characterization of the state of macrodispersion has shown that the area of agglomerates is much larger in PA6/SWCNT composites compared to PA6/MWCNT composites.

The results of volume resistivity of PE/SWCNT filaments which loading was less than 8 wt % could not be measured because the percolation threshold has not been exceeded. This may be due to the worse CNT dispersion in PE even when using a masterbatch combined with the elongation of the network during the drawing of filaments, resulting in a resistivity increase above the measuring range of the equipment.

Transmission light microscopy (LM) was used to characterize the state of macrodispersion of CNTs in extruded strands. The state of agglomerate macrodispersion in the three CNT composites is representatively shown in two different magnifications in Fig. 2.

It is clear from the micrographs (Fig. 2) that the area of agglomerates is much larger for CNT TUBALL™ in comparison to the NC7000. To evaluate the area rate of remaining agglomerates and to compare between three CNT composites, the optical microscopic images of high magnification (200 μ m scale bar) were quantitatively analyzed using an image analysis process. The area of agglomerates is much larger for SWCNT TUBALL™ (5.07 \pm 3.4%) in comparison to the MWCNT NC7000 (1.23 \pm 0.7 %). For CNT TUBALL™, the area ratio of remaining agglomerates, the largest remaining agglomerates of all investigated CNTs, was 5.07 \pm 3.4%.

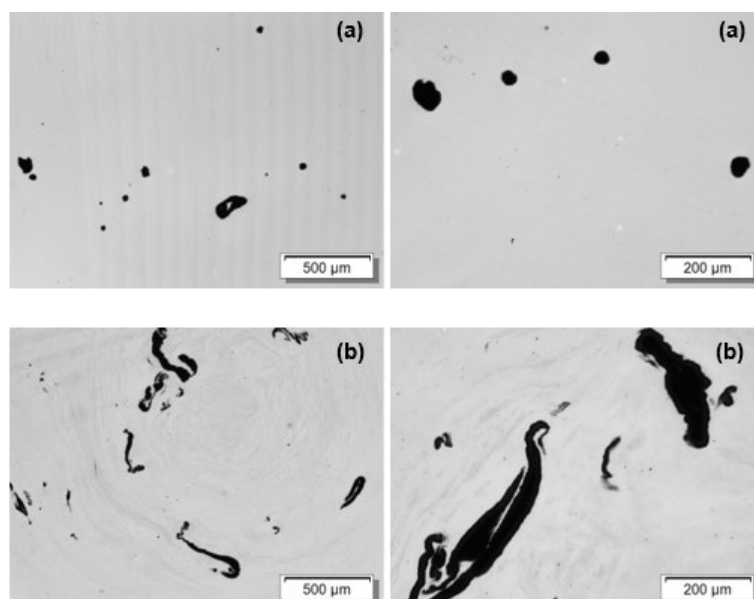


Fig. 2. Optical microscopy images of PA6/CNT composites with 1 wt % filler a) Nanocyl™ NC7000, b) CNT TUBALL™

Conclusion

We have produced nanocomposites from PA6 and PE matrices with SWCNTs and MWCNTs by using a small-scale mixing device. PA6/SWCNT composites show lower electrical volume resistivity than PA6/MWCNT composites at the same loading. Macrodispersion characterization has shown that the area of agglomerates in PA6/SWCNT composites is substantially larger than in PA6/MWCNT composites. This underlines the need for further and more detailed investigations on the effects of mixing conditions for PA6/SWCNT composites. The PE composites, measured directly as filaments, need much higher SWCNT contents to reach similar resistivity values, suggesting that these filaments could be used for the development of antistatic textiles. We observed that the strength of the filaments decreased with increasing SWCNT loads. The focus of futures studies will be to also investigate PA6 based filaments, to analyse the nanocomposite materials in more detail, and to systematically analyse the influencing parameters (compounding, melt-spinning, filtering, drawing) of the melt spinning process chain. Nanocomposite filaments will be further processed into structures such as woven and knitted fabrics to investigate the multi-functionality of CNT-based textiles. As well as anti-static textiles, CNT-modified materials could be developed as EMI shielding, sensors, textile electrode material for charge storage systems, or signal transfer.

Acknowledgment

The author, M.K., would like to acknowledge the support of COST Action CA15107 (MultiComp) Short Term Scientific Missions (STSMs) for his stay at IPF Dresden, Germany. Author M.K. was funded by ITC Conference Grant COST-CA17107-2452 within the COST Action CA17107 - European Network to connect research and innovation efforts on advanced Smart Textiles (context).

References

- [1] *Electronic Textiles*: Elsevier, 2015.
- [2] A.K. Yetisen, H. Qu, A. Manbachi, H. Butt, M. R. Domeci, J. P. Hinestroza, S. H. Yun, Nanotechnology in textiles. *ACS nano* (2016), 10(3), 3042-3068. doi: 10.1021/acsnano.5b08176.
- [3] Myant, *Vision Page – DW Page Updated - Myant*. [Online]. Available: <https://myant.ca/vision-page-dw-page-updated/> (accessed: Oct. 14 2021).

-
- [4] S. Park, S. Jayaraman, "Smart Textiles: Wearable Electronic Systems," *MRAS Bulletin* (2003), vol. 28, no. 8, pp. 585–591, doi: 10.1557/mrs2003.170.
- [5] E. Nilsson, M. Rigdahl, B. Hagström, "Electrically conductive polymeric bi-component fibers containing a high load of low-structured carbon black," *J. Appl. Polym. Sci.* (2015), vol. 132, no. 29, doi: 10.1002/app.42255.
- [6] C. R. Cork, "Conductive fibres for electronic textiles," in *Electronic Textiles*: Elsevier (2015), pp. 3–20.
- [7] M. Kaplan, "Hybrid Yarns For Thermoplastic Composites: Manufacturing Methods and Properties," *Tekstil ve Mühendis* (2016), vol. 23, no. 101, pp. 61–79, doi: 10.7216/1300759920162310106.
- [8] A. Bedeloglu, N. Sunter, B. Yildirim, and Y. Bozkurt, "Bending and tensile properties of cotton/metal wire complex yarns produced for electromagnetic shielding and conductivity applications," *Journal of The Textile Institute* (2012), vol. 103, no. 12, pp. 1304–1311, doi: 10.1080/00405000.2012.677568.
- [9] A. M. Grancarić, I. Jerković, V. Koncar, C. Cochrane, F. M. Kelly, D. Soulat, X. Legrand, "Conductive polymers for smart textile applications. *Journal of Industrial Textiles* (2018), 48(3), 612-642. doi: 10.1177/1528083717699368.
- [10] Y. Zhang, H. Wang, H. Lu, S. Li, and Y. Zhang, "Electronic fibers and textiles: Recent progress and perspective," *iScience* (2021), vol. 24, no. 7, p. 102716, doi: 10.1016/j.isci.2021.102716.
- [11] İ. Borazan, M. Kaplan, and B. M. Üzümcü, Eds., *Utilization of Metallic Fibers In Textiles*, International Congress of Innovative Textiles. (2019).
- [12] J. Slade, M. Agpaoa-Kraus, J. Bowman, A. Riecker, T. Tiano, C. Carey, P. Wilson, Washing of electrotexiles. *MRS Online Proceedings Library (OPL)* (2002), 736.
- [13] C. O. Baker, X. Huang, W. Nelson, and R. B. Kaner, "Polyaniline nanofibers: broadening applications for conducting polymers," *Chemical Society reviews* (2017), vol. 46, no. 5, pp. 1510–1525, doi: 10.1039/c6cs00555a.
- [14] L. Jingcheng, V. S. Reddy, W. A. D. M. Jayathilaka, A. Chinnappan, S. Ramakrishna, and R. Ghosh, "Intelligent Polymers, Fibers and Applications," *Polymers* (2021), vol. 13, no. 9, doi: 10.3390/polym13091427.
- [15] B. Krause, C. Barbier, J. Levente, M. Klaus, and P. Pötschke, "Screening of Different Carbon Nanotubes in Melt-Mixed Polymer Composites with Different Polymer Matrices for Their Thermoelectrical Properties," *J. Compos. Sci.* (2019), vol. 3, no. 4, p. 106, doi: 10.3390/jcs3040106.
- [16] W. Khan, R. Sharma, and P. Saini, "Carbon Nanotube-Based Polymer Composites: Synthesis, Properties and Applications," in *Carbon Nanotubes - Current Progress of their Polymer Composites* (2016), M. R. Berber and I. H. Hafez, Eds.: InTech,.
- [17] B. Krause, C. Barbier, K. Kunz, and P. Pötschke, "Comparative study of singlewalled, multiwalled, and branched carbon nanotubes melt mixed in different thermoplastic matrices," *Polymer* (2018), vol. 159, pp. 75–85, doi: 10.1016/j.polymer.2018.11.010.
- [18] B. Krause, R. Boldt, L. Häußler, and P. Pötschke, "Ultralow percolation threshold in polyamide 6.6/MWCNT composites," *Composites Science and Technology* (2015), vol. 114, pp. 119–125, doi: 10.1016/j.compscitech.2015.03.014.
- [19] J. R. Bautista-Quijano, "Mechanical, electrical and sensing properties of melt-spun polymer fibers filled with carbon nanoparticles," PhD, Der Fakultät Maschinenwesen, Technischen Universität Dresden, Dresden, Germany, 2018.
- [20] B. A. Weise, K. G. Wirth, L. Völkel, M. Morgenstern, and G. Seide, "Pilot-scale fabrication and analysis of graphene-nanocomposite fibers," *Carbon* (2019), vol. 144, pp. 351–361, doi: 10.1016/j.carbon.2018.12.042.

Dynamic Qualities of Smart Textiles: Study of Stimuli Magnitude with Chromic Pigments

CABRAL Isabel^{1,a*} and SOUTO António Pedro^{1,b}

¹2C2T – Centro de Ciência e Tecnologia Têxtil, University of Minho, School of Engineering, Campus Azurém 4800-058 Guimarães, Portugal

^adiascabral@gmail.com, ^bsouto@det.uminho.pt

Keywords: Smart Textiles, Hydrochromics, Photochromics, Thermochromics, Textile Design

Abstract. Smart textile behaviour encompasses changes over time, which are triggered upon a sensed stimulus. With a focus on dynamic qualities, this research sought to study how gradual and reversible transitions of smart textiles can be influenced by the activation variable – stimuli magnitude. Taking into account an analysis of different external stimuli for the same property change, the experimental work was conducted with Colour Change Materials, namely textiles screen printed with thermo, photo and hydrochromic pigments. The results attained demonstrate how stimuli magnitude can affect textile temporal expressions, in this case: hue, saturation and lightness, as well as pace change. In addition, different considerations also arose in respect to each stimulus' energy type and interdependencies between stimuli types. Contributing to the understanding of dynamic qualities of smart textiles and chromic materials' properties, this research also discusses further alternatives to explore textile behaviour towards new design possibilities for smart textiles as dynamic interfaces.

Introduction

Considering that smart textiles are able to sense and react reversibly to an external stimulus [1], they present a behaviour that can be described as dynamic and interactive, due to their property change ability and the response being triggered upon a sensed stimulus. In this sense, designing smart textiles includes exploring and working with the properties and qualities of the smart textile behaviour.

Dynamic behaviour is not a familiar dimension in conventional textiles. It is found more comprehensively in fields such as dance, music and even robotics, namely addressing time and movement concepts. For example, the design of a robot movement, besides concerning the trajectory definition that is accomplished by a physical medium, can also be described according to the movement properties and expressions, namely if the movement appears more organic or mechanical, if it occurs in a perceived fast or slow pace.

Therefore, as an emergent dimension in textile design and engineering, smart textiles behaviour presents new opportunities and challenges, including to provide new means to extend textiles conventional functions and expressions; to create new potential to interact with our environment and transform it; as well as to add new variables and competence requirements design research and practice [2-6].

To study the dynamic qualities of smart textiles, it is important to focus on how the materials changes between one state to another and the variables that can influence their expressions during gradual transitions and in different states. Previous research was conducted to study how the combination of smart materials and their integration processes in textile substrates can affect their expressions and behaviour [7-8], which was developed with stimulus-sensitive colourants.

The present research sought to study how gradual and reversible transitions of smart textiles can be influenced by the activation variable – stimuli magnitude. Taking into account an analysis of different external stimuli for the same property change, the experimental work was conducted with Colour Change Materials, namely textiles screen printed with photochromic (PC), thermochromic (TC) and hydrochromic (HC) pigments, which react to Ultraviolet (UV) radiation, heat and water, respectively [9].

Considering the intrinsic dynamic behaviour of each pigment type, PC are colourless in the stimulus absence, acquiring their predefined colour when exposed to it; the colour of TC textiles fades away above their activation temperature and returns to colourized below it; HC are opaque in dried state, changing to transparent when exposed to water [10-11]. Analysis on chromic behaviour conducted in this study, encompassed textile samples development and exposure to different stimulus types that address different magnitude levels for each pigment studied.

Materials and Methods

The chromic pigments handled were: SFXC water based PC dispersion yellow (PCy), magenta (PCm) and blue (PCb); SFXC water based HC ink white; ATUSMIC water based TC dispersion red with activation temperature of 27°C. PC and HC were supplied as ready-made pastes, and TC screen printing paste was formulated with 10% pigment and 90% Gilaba vinyl acrylic binder.

Samples were screen printed on a Zimmer Mini MDF R541 table. After being screen printed, each sample completed a process of drying and thermo setting in a laboratory oven with time and duration parameters according to the materials applied: 150°C during 3 minutes for TC; 130°C during 3 minutes for PC and HC pigments.

The experimental work consisted of two phases for each pigment type. The first phase studied the effect of activation magnitude in the textile expressions of each stimulus sensitive material, and the analysis was conducted with samples screen printed with individual pigments' colours. The second phase studied the speed in which the textiles change between states according to the stimuli conditions.

Colour change behaviour was studied through a qualitative analysis by direct observation and video recording, which also enabled the comparing of results attained through video frame images and the evaluation of pace of change.

For the study with UV radiation stimulus, PC samples were produced with a 100% cotton plain weave substrate and the conditions defined to analyse textile behaviour included natural and artificial light. Experiments in natural light encompassed direct and indirect exposure. In artificial light, the tests were conducted with a standardized light booth under the exposure of three lighting conditions: D65, UV and D65 combined with UV. The light source D65 is a CIE Standard Illuminant that represents average daylight, referring to diffuse skylight without direct sunlight and has a colour temperature of 6504 K [12].

Heat stimulus activates chromatic changes of TC pigments, leading to a decolourization process with changes from a coloured to a colourless state. Depending on the way the heating source activates the changes, dynamic textile patterns can be distinguished as direct or reported – concepts that were introduced by Worbin [2]. Direct patterns account for colour change as a direct response to the thermal stimulus, while reported patterns involve the use of conductive and electronic components, which are programmed to induce temperature variation through resistive heating.

This work discusses a section of the studies conducted with reported activation [6], which were developed with a textile sample woven with conductive threads. The TC sample was woven in the Jacquard Vamatex loom with 41.2 tex cotton warp and 14.7 tex polyester weft, integrating the Karl Grimm High Flex 3981 conductive thread in the weft of a plain weave structure at 1 cm distance each (13 picks PES and 1 pick conductive thread per cm). Conductive thread insertion in the weaving was programmed through the loom software.

TC sample activation through resistive heating was conducted with a DC power supply and different electrical current values were tested, enabling temperature transfer from the conductive threads to the textile chromic surface at different magnitude levels. To study sample temperature during activation, thermal images were also recorded with a Testo 876 Infrared camera and analysed with Testo IRSoft software.

The study with the HC pigment analysed textile behaviour of opacity decrease, when exposed to water and colour return upon drying through different environmental conditions, namely direct sunlight at 30 and 27°C and shadow at 25 and 20°C. Considering that this pigment was commercially available just in white, the HC sample used in this study was developed through overprinting process

with a 100% cotton plain weave substrate previously screen printed with ATUSMIC Magnaprint black H3B.

Results and Discussion

PC pigments. Experiments conducted with PC samples yellow, magenta and blue exposed to different light conditions, which present different UV radiation levels, were video record and frames of each sample in the colourized state was combined in image frameworks. Fig.1 shows the PC samples under natural light – direct, indirect exterior and interior – where different colour saturation was attained in the 3 samples – PCy, PCm and PCb. Variations reflect that the higher the stimulus magnitude, the more saturated is the PC pigment colour, as observed through samples in direct sunlight activation. When PC samples are exposed to indirect sunlight, either in interior or exterior environment, colour strength is considerably lower and, in the case of PC blue pigment, besides colour saturation, differences appear to regard also to hue: instead of blue, colour observed is a very light greenish shade.



Fig. 1. PC samples exposed to different natural lighting conditions.

Artificial lighting conditions also interfered in textile PC behaviour in respect to saturation and hue, as observed in Fig.2. Samples under D65 illuminant present a very low colourization, particularly with yellow and blue pigment. With UV light, the blue light colour does not allow perception of the samples activated colour, rather, lightness dimension differentiates chromic behaviour results ranging from darker to lighter with magenta, yellow and blue PC samples, respectively, as depicted in Fig.2 – 2nd column. When D65 is combined with UV light, the last enables a higher UV radiation and, whereas it still assigns a blue shade to the samples' colour, D65 light enables hue perception.

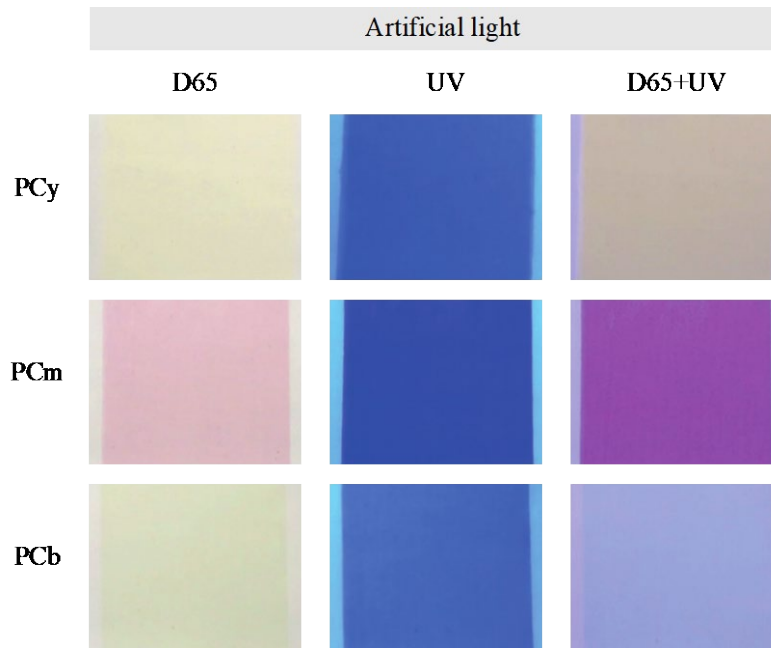


Fig. 2. PC samples exposed to different artificial lighting conditions.

Regarding the pace of change, when PC pigments are activated by direct sunlight, they appear to almost immediately change colour to their fully saturated state. With other lighting conditions that present lower UV stimuli magnitude, the chromic behaviour can be perceived overtime through a more gradual transition. With natural light, the colouration process was more obviously perceived previously to the first seconds 5'' for direct exposure and in between 15 to 20'' to exterior and interior indirect exposure (Fig.3).



Fig. 3. Dynamic behaviour of PC pigments, upon different natural lighting conditions.

The time required for the PC to return to its colourless state, after exposure with natural light, was difficult to quantify, as samples have to be contained from UV light, but exposed to other lighting to be observed. In addition, PC pigments show a residual colour according to its hue, which also interferes in the analysis. Nevertheless, the study highlighted that a higher stimulus magnitude triggers faster changes, but it can also slow down the pace at which the textile returns to the initial colour.

For artificial light with D65, dynamic behaviour occurred during approximately 40'' in the colourization process (Fig.4 left). Regarding decolourization, pace of change is observed slowly, also being difficult to identify by direct observation when the transition is complete. In the D65 test, 1'20'' appear to be required for the decolourization process with PC magenta, whereas with PC yellow and PC blue, the decolouration appears to be complete at approximately between 40'' and 1'(Fig.4 right).

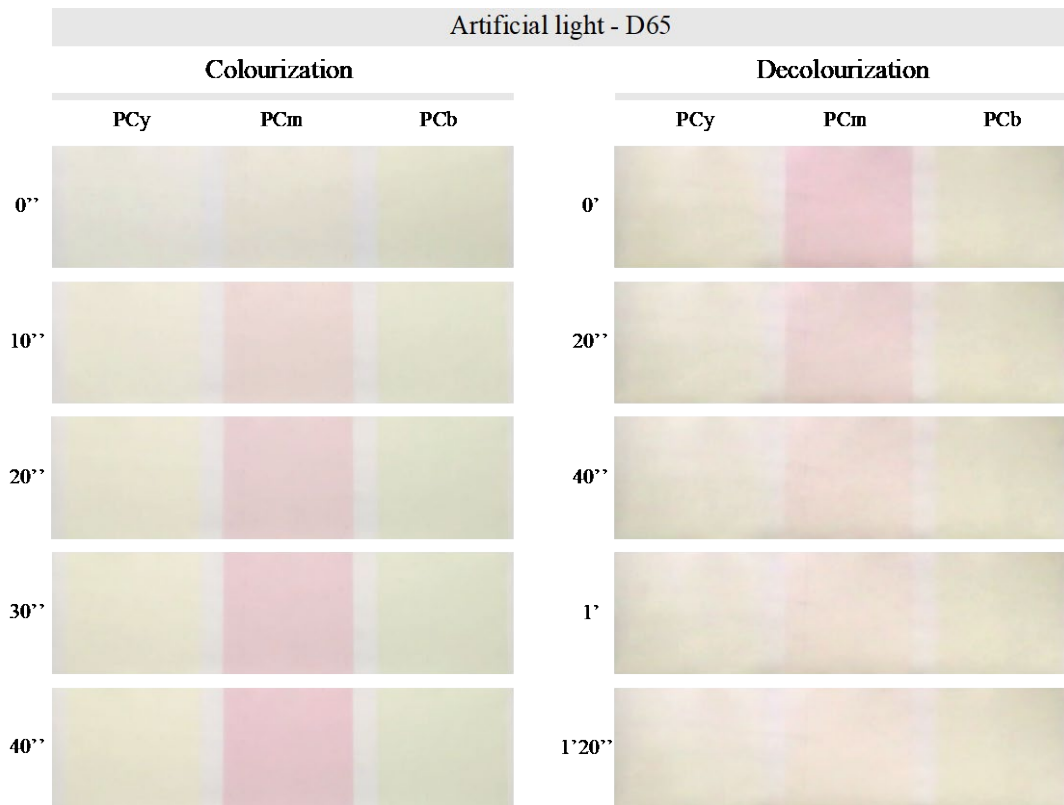


Fig. 4. Dynamic behaviour of PC samples under D65 standard illuminant.

The results attained with natural and artificial light stimulus, also highlight the possibility to design colour change behaviour that can perform transitions with different chromatic expressions by combining two or more PC pigments' colours and according to the stimulus magnitude supplied, as they present different saturation levels and change rates.

TC pigments. The study of magnitude stimulus influence on TC textile behaviour report to resistive heating activation experiments [6]. In the initial test, the objective was to study the influence of the electrical current value in the heating process of the TC sample. The test setup was defined with 1' duration of power supply, after which colour return was analysed during the same period. The electrical current values tested ranged between 1 and 1,5A and the experiments were all conducted at a room temperature of 20°C.

Fig.5 presents the results attained with 1,3A and displays frames of the video record and IR images at each 15'' of the timeline. When power supply was switched ON, the conductive thread pattern was revealed through the transition from textile solid colour to parallel colourless lines. This change was perceived in the 1st 15'' of activation, after which thermal expansion in the textile areas in between the conductive threads, performed a slower pace, until attain an overall colourless expression, after 1' of activation. When power supply was interrupted, colour return occurred slowly, through a more blurred expression than on heating.

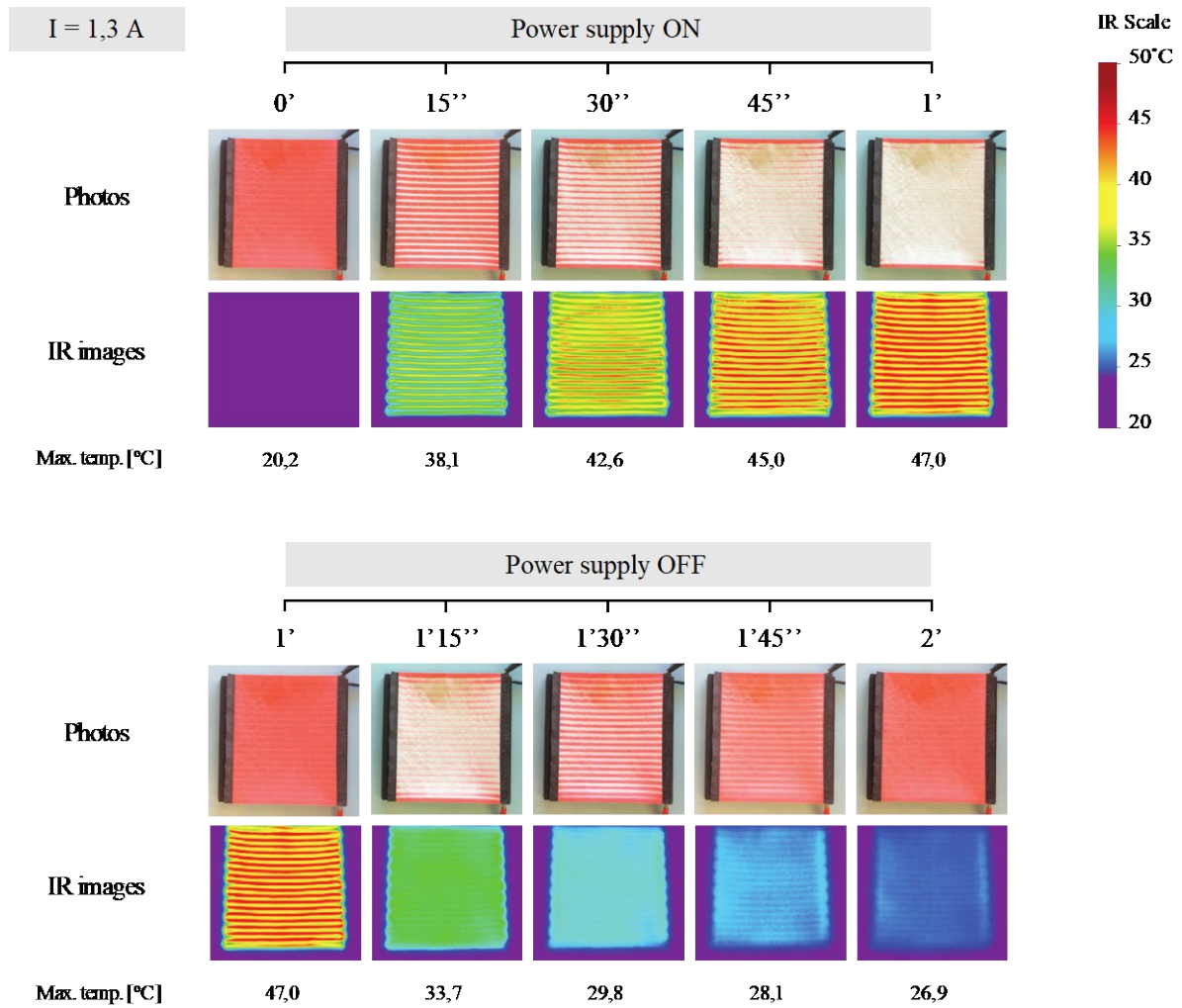


Fig. 5. Dynamic behaviour of TC sample, during and after activation with 1,3 A.

Comparing the results of the experiment with different electrical current values presented in Fig.6, it was observed that they affect the pace and the expressions of colour change. In experiments with 1,2A or lower, full colour change was not attained with 1' power supply. The temperature on the conductive threads changed the textile colour, but was not sufficient to heat up the textile areas between them above 27°C (TC pigment activation temperature). When power supply was switched OFF, textile temperature affected colour return, which was incomplete in tests with 1,4 and 1,5 A.

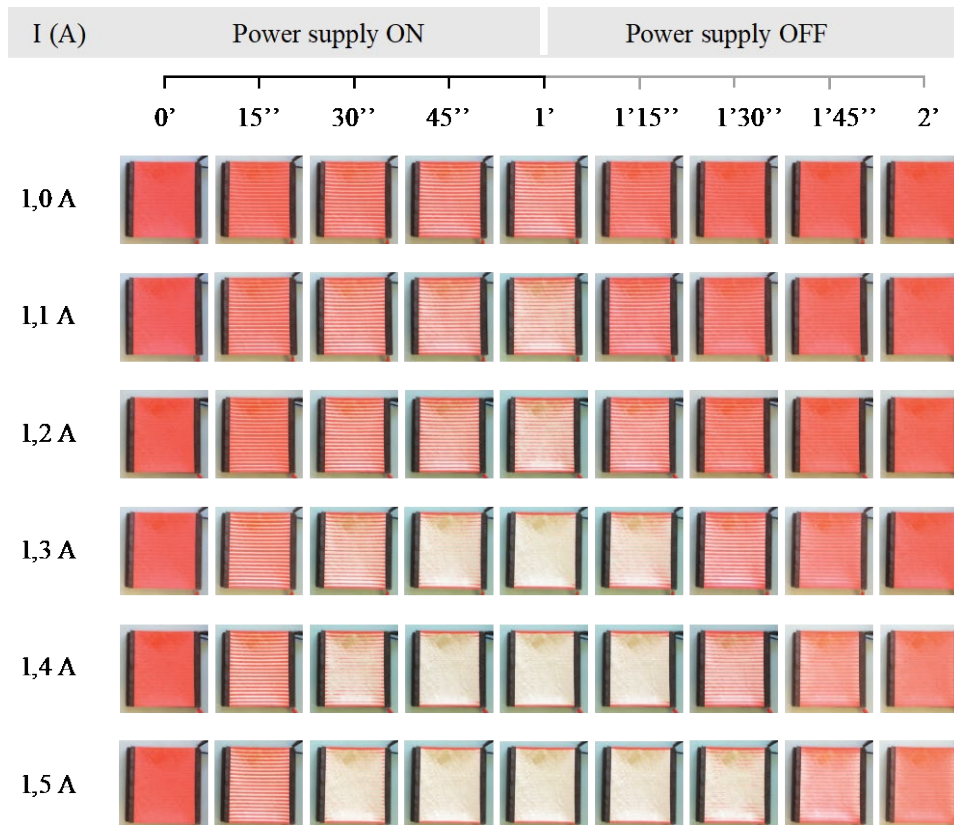


Fig. 6. Dynamic behaviour of TC sample during and after activation through different electrical current values.

Experiments with different room temperatures were conducted, which have shown to significantly affect duration of change. Fig.7 presents the time and maximum temperature measured on TC sample activated with 1,4A electrical current at a room temperature of 16°C and 20°C. Results comparison show that with 16°C room temperature, colour change occurred much slower than in the test at 20°C; while colour return was slightly faster, stressing their influence on both chromic transitions between colourized and decolourized states.



Room Temp. [°C]	Heating		Cooling	
	Time	Max. Temp. [°C]	Time	Max. Temp. [°C]
20	1'15''	50,1	1'15''	26,9
16	2'30''	49,9	1'	25,3

Fig. 7. Dynamic behaviour of TC sample with 1,4 A activation, at room temperature of 20 and 16°C.

HC pigments. The experiments on HC behaviour encompassed an initial analysis on chromic activation either in an environment with different relative humidity properties and wetting possibilities. It was observed that the stimulus magnitude does not present an obvious effect on HC pigment decolourization. For example, when the dried samples were exposed to different humidity levels, no visual differences were observed. To identify colour change, the pigment required to be wet, which can occur regarding different scale areas of the printed surface, attaining different

expressions such as presented in Fig. 8: sprayed pattern with small droplets, stained area with the HC surface partially or fully wet. In addition, as the other pigments' types, kinetic behaviour of this material is also incomplete, showing a residual opacity.

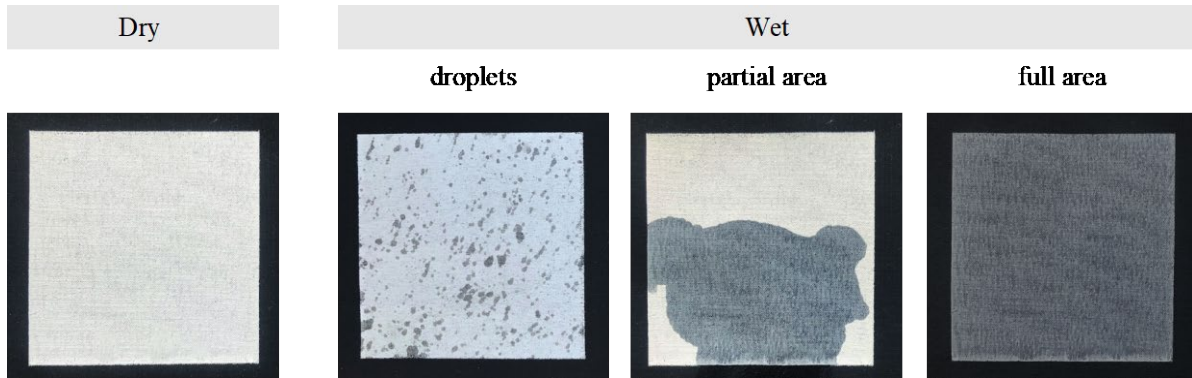


Fig. 8. HC sample at dry and wet states.

After direct water contact, time required to observe colour change is almost immediate, while colour return holds interdependencies between different stimuli conditions, as colourization of HC encompasses a drying process.

Two setups were tested involving direct sunlight and shadow, both comprising of different temperatures, each measured with a thermometer placed in the sample surface. Conditions were 30°C and 27°C in direct sunlight and 25°C and 20°C in shadow. Time results required for the HC textile surface to become completely colourized are presented in Fig.9, where it can be observed that environmental conditions significantly affect the pace of HC colourization: samples in direct sunlight required 10 to 12 minutes to fully colourized and in shadow, time varied between 45 and 125 minutes.

The analysis highlights that to design dynamic behaviour of HC textiles, it is important to take into consideration that pace of change during decolourization occurs at the seconds rate, while colourization involves minutes or even hours.

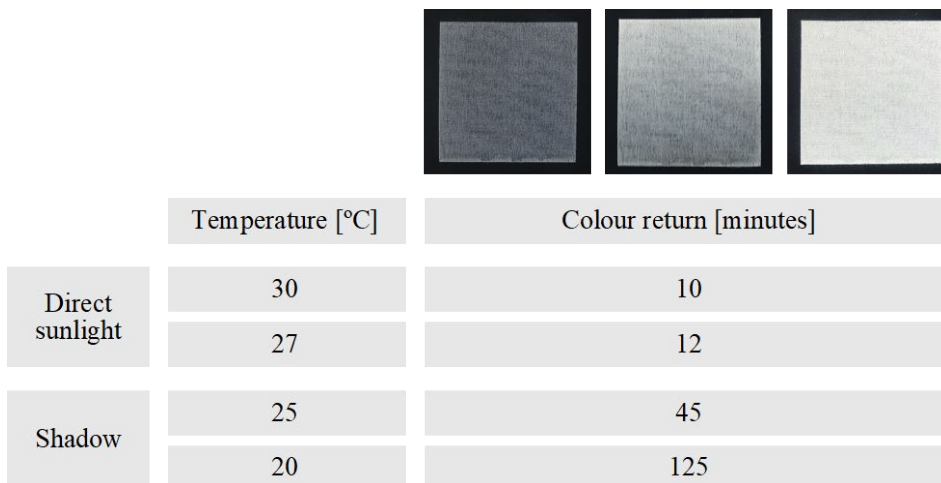


Fig. 9. Dynamic behaviour of HC at different lighting and temperature conditions.

Results obtained highlight that whereas designers can select specific colours for a given textile expression, various chromatic possibilities can arise in dependence of the stimulus type and respective magnitude. For all pigments tested it was observed that the pace of changes is also directly influenced to the stimuli magnitude. A high intensity activation triggers faster changes, but it can also slow down the pace at which the textile returns to the initial state. This relationship holds interdependencies between different stimuli conditions. For example, the stimulus absence in HC textiles involves the

drying of the textile sample, thus pace change is also related to temperature, light exposure condition, as well as textile substrate properties.

Conclusions

Stimuli variables are an important consideration in smart textiles design, as they are responsible for triggering textile behaviour, as well as affecting how textile expressions evolve overtime.

The research conducted provides a framework that articulates relationships between stimuli magnitude and dynamic qualities of smart textile behaviour, with stimuli-sensitive colourants. Through this process, the framework can be extended over research with other variables that play an active role the textile performance as well as with other smart materials.

The findings also contribute to understanding of chromic materials properties and behaviour, which enable designers to further explore different rhythms of change, designing dynamic and interactive textiles.

Future work encompasses development of research prototypes to demonstrate colour change effects and potential to design textile behaviour with distinct dynamic qualities. It is also of crucial importance to combine this qualitative study with quantitative analysis of colour change, dependent on stimulus magnitude variable, through colourimetric measurements.

Acknowledgment

This work is financed by Project UID/CTM/00264/2020 of 2C2T – Centro de Ciência e Tecnologia Têxtil, funded by National Funds through FCT/MCTES.

References

- [1] X. Tao, Smart technology for textiles and clothing – introduction and overview, in X. Tao (Ed.), *Smart fibres, fabrics and clothing: fundamentals and applications*, Woodhead, Cambridge, 2001, pp. 1-6.
- [2] L. Worbin, *Designing Dynamic Textile Patterns*, Doctoral thesis, University of Borås, *Studies in Artistic Research*, no. 1., 2010.
- [3] J. Redström, On technology as material in design, in M. Redström, J. Redström, & R. Mazé (Eds.), *IT+Textiles*, The Interactive Institute and the Swedish School of Textiles, Borås, 2010, pp. 12-29
- [4] A. Vallgård, Giving form to computational things: developing a practice of interaction design *Personal and Ubiquitous Computing*, 18(3) (2014), 577-592.
- [5] A. Mossé, Self-actuated textiles, interconnectivity, and the design of the home as a more sustainable timescape, in D. Schneiderman & A. Winton (Eds.), *Textile technology and design: from interior space to outer space*, Bloomsbury Academic, New York, 2016, pp. 121-134.
- [6] I. Cabral, A.P. Souto, L. Worbin, *Dynamic Light Filters: Smart Materials Applied to Textile Design*, Springer, Cham, 2020.
- [7] I. Cabral, A.P. Souto, Dynamic colour in textiles: combination of thermo, photo and hydrochromic pigments. *IOP Conf. Ser.: Mater. Sci. Eng.* 827 (2020), 012059.
- [8] H. Gauche, F.R. Oliveira, C. Merlini, A.P. Hiller, A.P.G.V. Souto, I.D. Cabral, F. Steffens, Screen Printing of Cotton Fabric with Hydrochromic Paste: Evaluation of Color Uniformity, Reversibility and Fastness Properties, *J. Nat. Fibers* (2020) 1-12.
- [9] M. Visková, Type of Chromic Materials, in M. Visková (Ed.), *Chromic Materials: Fundamentals, Measurements, and Applications*, Apple Academic Press, Waretown, 2019, pp. 35-108.

- [10] P. Bamfield, M. Hutchings, *Chromic phenomena: technological applications of colour chemistry*, third ed., Royal Society of Chemistry, Cambridge, 2018.
- [11] A.A. Merati, *Application of Stimuli-Sensitive Materials in Smart Textiles*, in Shahid-ul-Islam, B.S. Butola (Eds.), *Advanced Textile Engineering Materials*, Scrivener Publishing, Beverly, 2018, pp. 3-30.
- [12] R.H. Wardman, *An Introduction to Textile Coloration: Principles and Practice*, Wiley, Hoboken, 2018.

Study on Electrical Characteristics of Flexible Textile Aluminium-Air Battery / Wetness Sensor and Their Applications

Uģis Briedis^{1,a}, Aleksandrs Valiņevskis^{1,b*}, Miguel Carvalho^{2,c}

¹Riga Technical University, Institute of Design Technologies, Kipsalas 6, Riga LV-1048, Latvia

²University of Minho, Textile Engineering Department, Campus de Azurém 4800-058
Guimarães, Portugal

^augis.briedis@rtu.lv, ^baleksandrs.valisevskis@rtu.lv, ^cmigcar@det.uminho.pt

*corresponding author

Keywords: textile battery, self-powered wetness sensor, smart diapers, smart safety bracelet

Abstract. The field of smart textiles has been steadily growing throughout the last decades. Wearables and garments with integrated electronics being one of the major sections of this area. One of the components that virtually any such product has is a power source. This paper focuses on one such option, which employs only non-toxic materials, which can be safely used in close proximity to human body. The paper builds on previously developed flexible textile aluminium-air battery prototype. New electrical measurements are provided, which show possibilities and limitations of the developed primary battery, as well as niches, where it can be used. This paper focuses on testing the battery in real-world application conditions, by repeatedly activating and deactivating it for short periods of time in order to test its useful life period. From that point useful practical applications can be determined, which take into account limitations of the battery. The measurements show that the battery is best suited for use in emergency and alarm systems, where the system is activated for relatively short period of time in order to change system's state or transmit an alarm message. Some examples are smart diapers with smart monitoring capabilities and anti-drowning safety bracelets.

Introduction

Wearable/smart textiles are still an active research topic in scientific community, but are uncommon for consumers because of limited availability in retail stores. This is due to the relatively small number of products, and one of the reasons for that could be difficulties with industrial production, with the complex integration of sensors and energy sources into textile materials. Both electronic components and energy sources (usually electrochemical batteries) must be integrated into the textile, and they must all be interconnected with conductive lines. It poses numerous challenges, and in this study we focus on one of them, which is related to power supply. We propose a safe human-friendly energy source, which contains no harmful or dangerous substances, uses relatively cheap materials, which can be disposed of with the textile product.

The study has started in 2016, when we were working on the development of enuresis alarm system, in which electronic elements were integrated, using embroidery technology [1]. The original prototype used an Li-ion secondary battery, which was integrated directly into child's shirt. This raised concerns due to safety issues, so the new goal was to develop an energy source, that would contain no harmful substances and that would be easily to integrate into textiles. During this study, the idea of using a battery based on aluminium-air technology was first tested.

An aluminium-air cell is a promising battery technology, in which aluminium anode oxidation and atmospheric oxygen cathode reduction is used to produce electricity. These batteries have one of the highest energy densities, which however is difficult to obtain practically because of a number of challenges, mostly related to aluminium reactivity [12]. Besides that, aluminium is much cheaper than materials commonly used in other popular battery designs, e.g. lithium.

After a few iterations the final battery design was developed [2, 3]. The battery is made of only textile materials, combined using embroidery technology, and is integrated in inactivated "dry" state – without the electrolyte. This makes it possible to store the battery for indefinite time before it is

activated by adding liquid electrolyte from the *outside*. As a result, the first prototypes of flexible textile batteries were made and tested to prove the applicability of the technology. The results were positive and can be studied in detail in previous papers [4]. Based on the obtained results, a patent has been applied for [5]. Besides the dry battery design used in this paper because of the requirements of the original product, a number of other designs of flexible and textile batteries are available as well, for example see [6, 7, 8, 9].

Structure of the Battery

The structure of the primary cell is shown in Fig. 1. It utilizes only textile-based materials: Mtex® aluminium-textile composite fabric is used for aluminium anode; cathode current collector is made using Shieldex® Budapest fabric, which is 99% pure silver-plated polyamide fabric. Silver plating makes it particularly resistant to oxidation; outer shells are made of common cotton fabric, which ensures necessary tactile characteristics of the whole package. Optional NaCl can be added to the air cathode. Its use and concentration should be evaluated based on the liquid, which is expected to activate the battery. Should its ion concentration not be enough to act as an electrolyte, NaCl should be added accordingly. The distance between the anode 1 and cathode current collector 2 is determined by the thickness of carbon granule layer 3 and is just around 2 mm, which was maintained the same for all the cells produced.

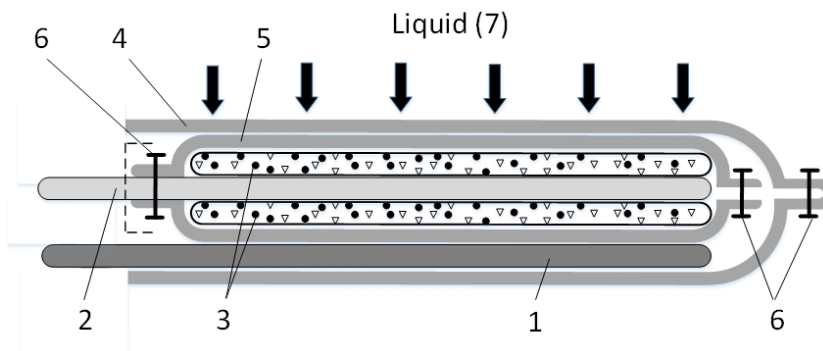


Fig. 1. Flexible textile Al-Air battery cell

1 – aluminium anode, Mtex® aluminium-textile composite material; 2 – cathode current collector, Shieldex® Budapest conductive textile; 3 – carbon granule and optional NaCl mixture to increase its concentration in electrolyte; 4 – cotton enclosure of the cell; 5 – cotton enclosure of the cathode; 6 – sewn joints; 7 – activating liquid from outer environment that is applied to the cell and that acts as an electrolyte.

The developed cells can be combined into multi-cell batteries in order to reach necessary electrical characteristics. The modular design of the battery enables one to choose an arbitrary number of cells and their arrangement on the plane. Since one cell of the chosen type produces about $0.7V$, a number of prototypes has been produced each made of 4 cells, connected in series. This arrangement should quadruple the potential and give an output voltage of about $2.8V$, which is enough for most low-power semiconductor electronics and sensors.

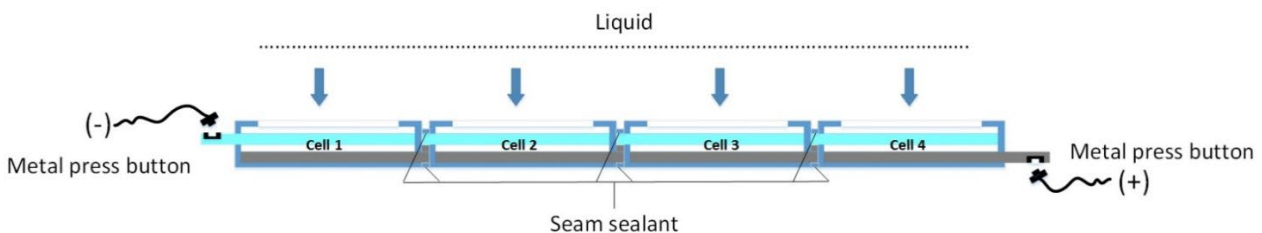


Fig. 2. Multi-cell battery design, side view

Fig. 2 shows the basic diagram for cell arrangement on plane. Three different prototypes have been prepared with 1x4 or 2x2 cell arrangement, see Fig. 3 and 4. The cells are arranged on a plane and are adjacent to each other in a way that the cathode of one cell overlays the anode of the next cell. Since the materials are textile-based, the connection is made by sewing the electrodes together with conductive thread.

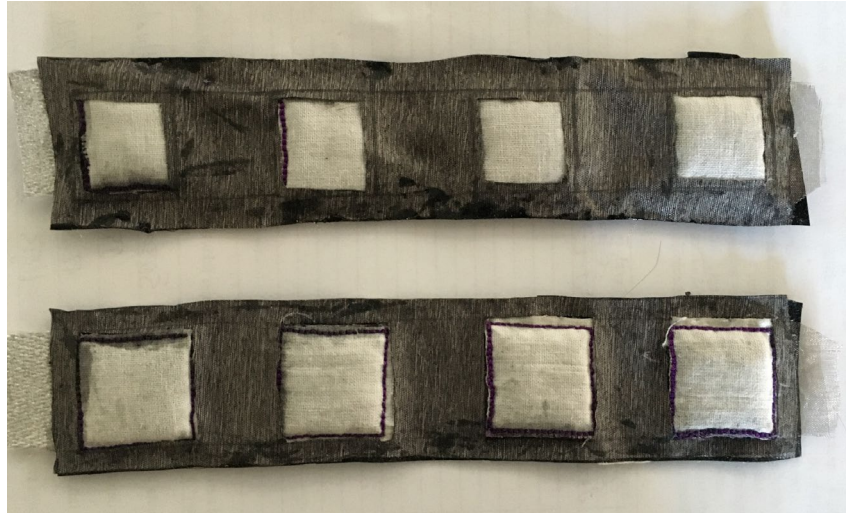


Fig. 3. Prototypes of multi-cell flexible textile Al-Air batteries with 1x4 cell arrangement



Fig. 4. Prototype of a multi-cell flexible textile Al-Air battery with 2x2 cell arrangement



Fig. 5. Inner structure of a multi-cell battery with sealant applied

The cells are encapsulated into two layers of non-permeable fabric, using commercially available seam sealer. The lower layer is made of solid rectangular piece of fabric and the upper layer is made of the same fabric with four openings that allow electrolyte to reach the cells. The sealant is applied on the cathode/anode connection area and around the cells, in order to insulate them. The fabric has hydrophobic coating, which minimizes electrolyte accumulation on the upper layer of the battery and detrimental connection bridges, as well as it enables the electrolyte to be distributed among the cells. On the other hand, the enclosure of the cathode (pos. 5, Fig. 1) is made of permeable cotton. Thus,

the electrolyte (pos. 7, Fig. 1) can be poured directly on the battery. Afterwards it travels through cathode enclosure and cathode current collector (pos. 2, Fig. 1) to reach the aluminium anode (pos. 1, Fig. 1), which activated the battery. The only non-insulated electrodes are the anode of the first cell and the cathode of the last cell, which are the poles of the multi-cell battery. Inner structure of the battery can be seen in Fig. 5.

The advantages of the developed battery over traditional alternatives can be summarized as follows:

1. Conventional metal elements (anode, cathode) replaced by human-friendly textile-based materials.
2. Thanks to the use of textiles, automated embroidery technology can be used in the production of the prototype, allowing the battery to be assembled and connected to peripheral elements.
3. Unlike lithium-ion batteries and other commercially available electrochemical energy sources, there are no harmful or hazardous substances.
4. Unlimited storage time before activating the element. Aluminium-air batteries are one of the fastest growing areas and is among the promising technologies that might replace lithium-ion technology. One of the biggest obstacles is the rapid oxidation and degradation of aluminium. The proposed technology eliminates this problem by postponing the introduction of electrolyte until the moment when the battery needs to be activated.
5. The amount of energy obtained is greater than that of non-chemical (mechanical, photoelectric) energy sources of similar size/weight and is sufficient to operate semiconductor devices immediately after activation.

The proposed design enables to use the battery as a self-energized moisture sensor – the element is energized when the liquid is introduced and starts to generate electricity, so does not need an external power supply. An important novelty is the textile materials used, which replaces the conventional aluminium- and silver-containing materials, resulting in a human-friendly, flexible product. Another novelty is the size and shape of the sensor/battery, which can be arbitrary arranged and made suitable for installation in diapers. A special cathode unit was designed, which ensures optimal supply of oxygen molecules for the redox reaction, and incorporates a current collector made of Ag textile and carbon granules. Another important innovation is the battery manufacturing technology – it is made with an embroidery machine using embroidery technology, which means that the battery parts are assembled using threads. Conductive threads are used for inner battery connections.

Study of Battery Behaviour in Realistic Applications

According to previous results [4], the battery can be practically used for relatively short periods of time, measured in dozens of minutes or a few hours at most. See Fig. 6 and 7 for more details. These figures show the battery voltage and current change over time with 22Ω load applied. The 22Ω load was chosen arbitrarily, with the rationale being that it constitutes a sufficiently high load to limit the battery operating time. For the experiments shown in Fig. 6 and 7, the battery was connected to *PicoScope 3204B* digital oscilloscope for voltage measurements and *Extech EX330* multimeter for current measurement. Subsequently 2.8M sodium chloride water solution was applied to the battery (until it was soaked). Measurements were taken 5 minutes apart during the first 30 minutes and 15 minutes apart until the end of the experiment.

Thus, the battery is not suitable for continuous operation, but only for applications, where it needs to be activated for a short period of time in order to activate an alarm unit or transmit a signal. Examples are smart diapers, anti-drowning safety bracelets, textile sensors wrapped around underground pipes, thawing alarm for frozen foods, which changes the state of an e-ink display in case of freezing equipment failure etc.

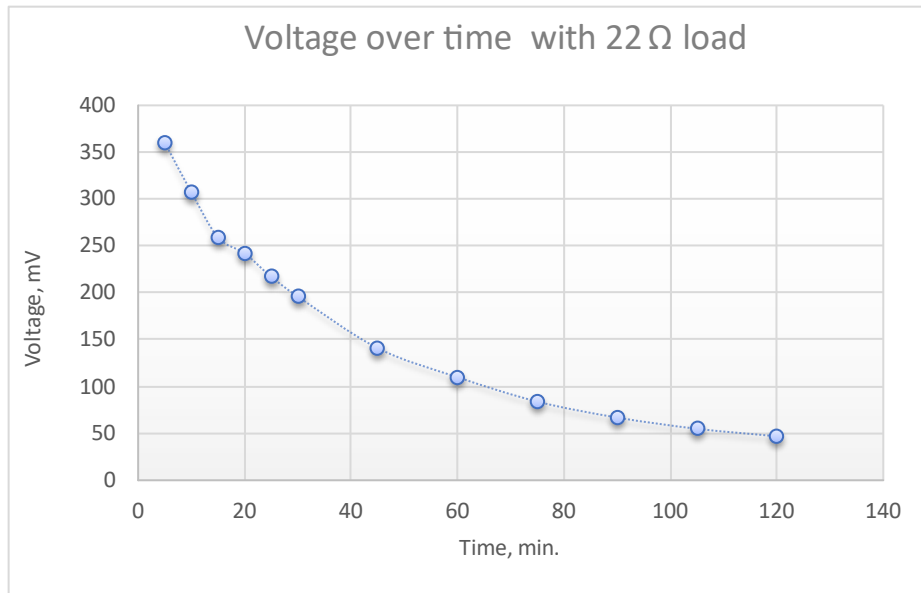


Fig. 6. Voltage change over time of a 4-cell battery with 22Ω load applied

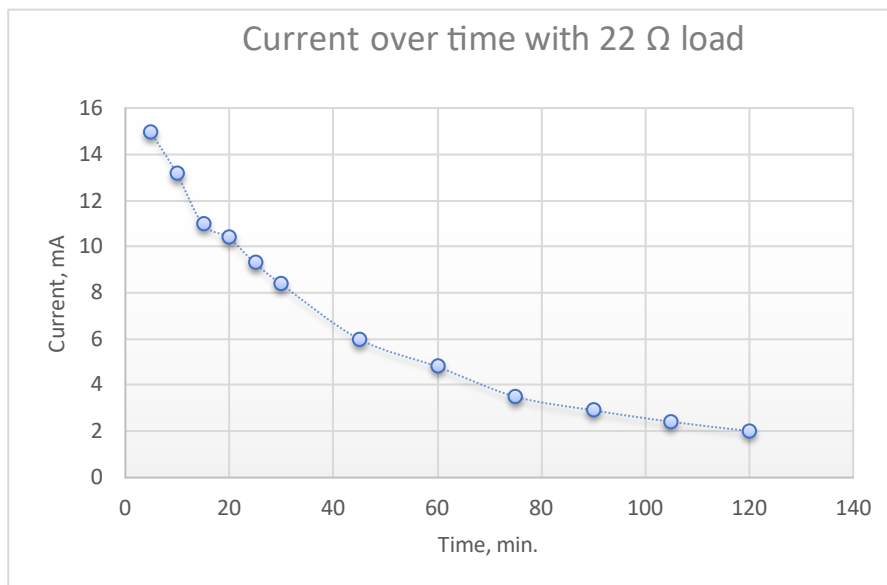


Fig. 7. Current change over time of a flexible textile battery with 22Ω load applied

Taking into account this limitation, it would be advantageous to know how many times a battery can be repeatedly activated and deactivated (by flushing an electrolyte or separating the anode). In order to answer this question, the following experiment has been designed.

Experiment plan:

Objects being tested: 1x4 battery prototype, 2x2 battery prototype was skipped due to reasons explained below.

Steps of the experiment:

1. Initial voltage (V) and current (mA) of the battery are measured.
2. Battery is flushed with fresh water in order to slow down redox reaction.
3. Battery is activated by applying saline solution, which acts as an electrolyte.
4. Voltage (V) and current (mA) of the battery are measured.
5. Battery is kept active for three minutes.
6. Voltage (V) and current (mA) of the battery are measured.
7. Battery is flushed with fresh water in order to slow down the redox reaction.
8. Battery is kept in inactive state for five minutes.

9. If the measurements have not dropped under usable limits, go to step 3, otherwise stop the experiment.

Results of this experiment are shown in Fig. 8 and 9.

Only results for prototype with cell arrangement of 1x4 are shown on the diagrams. The reason is that the performance of battery with configuration 2x2 is subpar, as is shown in Fig. 10. Most likely this can be explained by defective assembly, since there are no reasons for the configuration itself to introduce any disadvantages. The experiments shown in Fig. 10 were conducted using a setup similar to that described in the beginning of this section – 2.8M sodium chloride water solution was applied to the battery; afterwards open-circuit/short-circuit voltage and current were measured, along with a number of intermediate resistances in order to obtain the intermediate points of the graph.

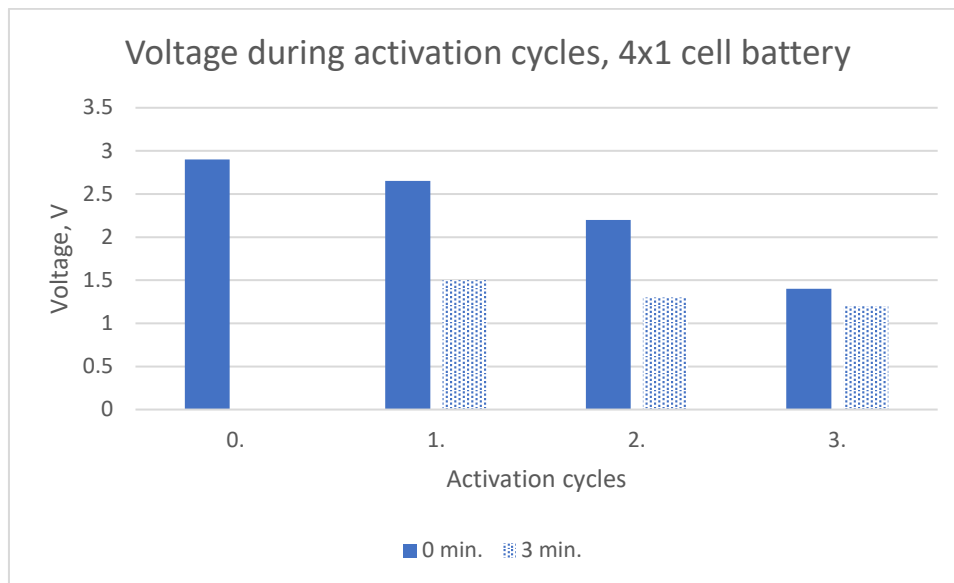


Fig. 8. Repeated activation of battery, Voltage

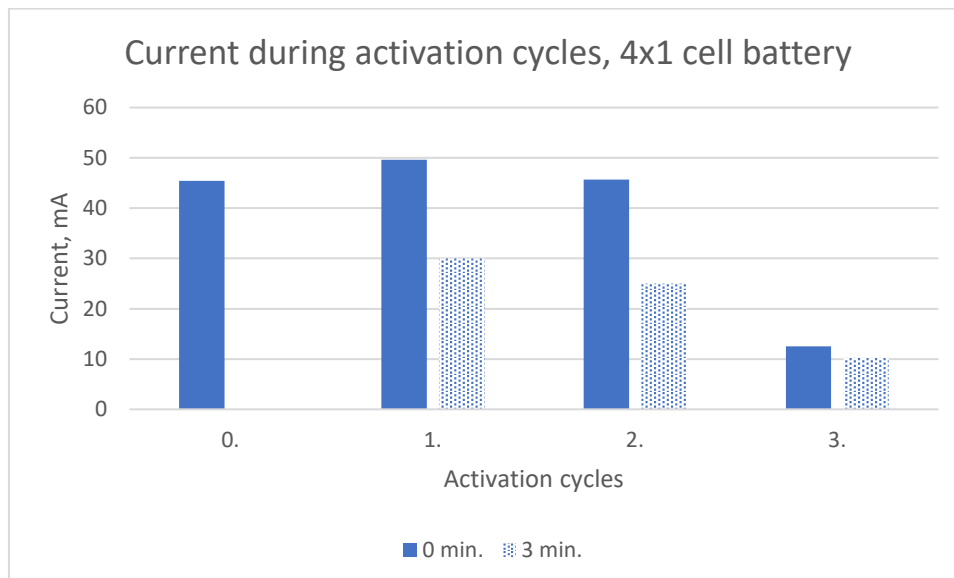


Fig. 9. Repeated activation of battery, Current

The first column of Fig. 8 and 9, marked as “Cycle 0” shows the initial characteristics of the battery. This is followed by three groups, each containing two bars. The first, darker bar, indicates measurement at the start of the cycle, the second, lighter bar, indicates measurement after three minutes, at the end of the cycle. At the start of Cycle 3 voltage has dropped about twice, so it was decided to end the experiment there.

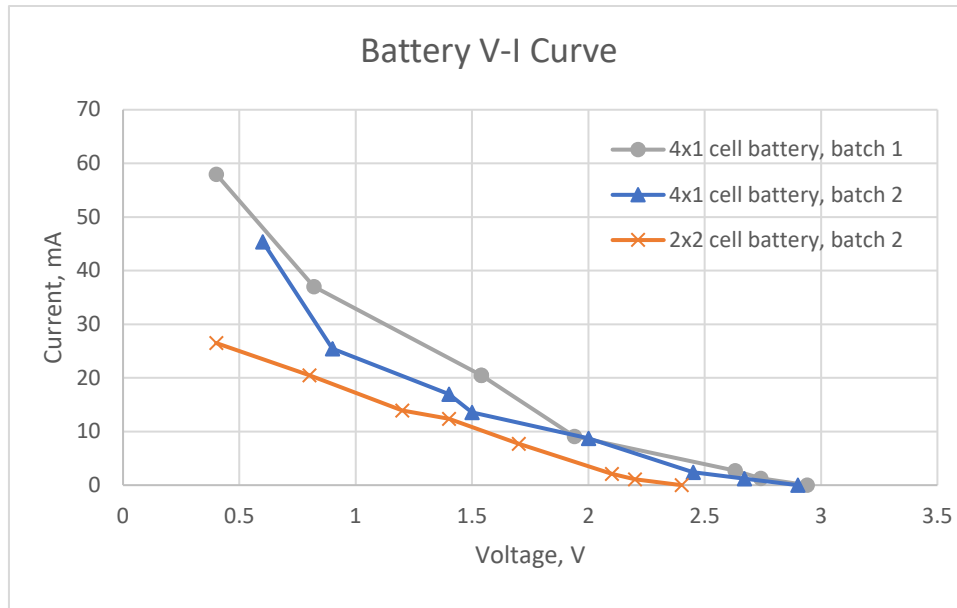


Fig. 10. V-I curve of the three prototypes

Possible Applications/Commercialisations

As was mentioned before, one of the possible applications of the proposed battery/sensor is integration into smart diapers with moisture monitoring system. The battery should be inserted into the 3rd moisture absorbent layer, in order to be activated when the diaper is full and needs to be changed. The battery is connected to alarm unit, which either gives a visual indication or sends a wireless signal to the receiving unit (Fig. 11).

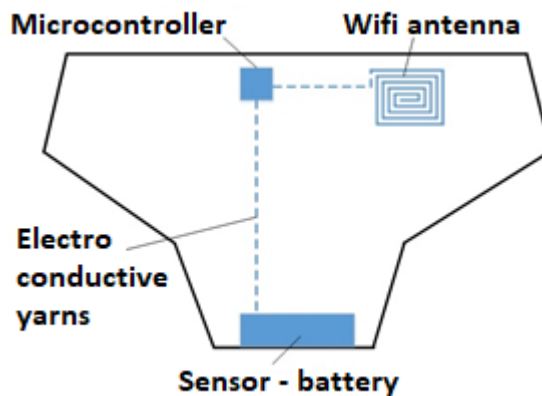


Fig. 11. Smart diaper with monitoring system

The idea of determining the moisture level of diapers is not new. Relatively common are chemical indicators that are integrated into diapers and show when they need to be changed. Determining the humidity level has financial benefits too, because it allows to make full use of diapers and reduce waste and costs.

Currently two types of smart diapers are available on the market and in research studies: 1) with an external moisture sensor – these are commercialized and available on the market; 2) with diaper-integrated sensor or self-energized sensor, which currently are found in scientific studies, but not as commercialized products. Various researchers have proposed to integrate wetness sensors into diapers. Researcher from Tokyo University have developed a wet sensor and control chip based on chip printing technology, which is powered by an external battery for diapers [10]. Researchers from Sweden Johan Sidén, Andrei Koptioug and Mikael Gulliksson have proposed to create a diaper sensor/battery with inkjet printing technology, with the sensor inside and the other elements (antenna and chip) attached to the diaper from the outside [11].

Several smart diaper products with electronic diaper moisture indicators have also appeared, some of which are: O'PRO9 Adult SmartDiaper, DiaperSens Adult Diaper, Geecare Smart Baby Diaper, Pampers Lumi, etc. All these diapers have an external module that is attached to the front of the diaper and is removed and replaced with new diapers when replaced. These modules contain a chemical battery and measure moisture from the outside by determining the surface moisture. In the diaper design that is made possible by using the battery proposed in this paper, the sensor/battery can be integrated into the last, 3rd layer, which usually is filled with moisture to a critical level after about 4-5 wetting times, when the diaper should be replaced with new one. This means that the sensor/battery must detect moisture and report it.

Another possible application of the proposed sensor/battery is integration into a smart water safety bracelet that will warn parents about child's hand coming into contact with water (which can indicate sudden immersion in water). Information about the wetting of the bracelet can be transmitted to the receiver wirelessly, using an integrated antenna. The experiments presented in previous section and shown in Fig. 8 and 9 indicate that such a device can be activated about three times, before the battery needs to be restored, e.g., by replacing the aluminium anode.

Results and Discussion

This paper is based on previous research made in the field of power sources for smart textiles. It focuses on determining electrical characteristics of the developed batteries, when they are used in real-world applications.

The battery has a number of advantages, such as:

- 1) the battery is made entirely, using traditional textile technology (sewing, embroidery) includes only textile-based materials, providing greater flexibility and fusion with textile materials;
- 2) the four-cell battery is capable of producing 3V upon activation, which enables it to power semiconductors without the need of additional voltage conversion or energy accumulation;
- 3) the proposed batteries can be integrated into smart textiles and can stay in inactive state for unlimited time (with electrolyte separated from electrodes), before liquid is introduced to activate the battery;
- 4) this type of battery shows great potential as energy storage solutions for different applications in healthcare products, cold storage, safety products etc.

Several important limitations have been determined as well:

- 1) short-term use – battery stays in usable state for 20-30 minutes – enough for emergency activation, but not suitable for long-term powering of electronic devices;
- 2) use for single activation applications (or not more than 2-3 activations) - e.g. enuresis alarms, smart diapers, drowning alarm bracelets, frozen product thawing alarms, underground pipe leakage alarms.

As can be seen, the developed battery is not of universal type, it has some advantages, as well as limitations. Thus, this should be taken in consideration when deciding on a possible application or suitability of the battery for a particular product. Although it should be kept in mind that the battery can be restored, e.g., by replacing the deteriorated aluminium anode.

Conclusion

This paper deepened the understanding about the characteristics and behaviour of the developed flexible textile Al-Air batteries in real-world situations. The battery has obvious advantages, but several important limitations have been highlighted as well. This data makes it easier to decide on the applicability of the proposed battery for a particular system. Most promising areas of application are emergency systems, which are characterized by long stand-by times and short activity times upon activation. A number of examples are presented in the paper as well.

Further plans include developing a carbon ink for screen-printing and replacing the carbon granule layer with printed layer in order to reduce thickness.

References

- [1] Briedis, U., Vališevskis, A., Grecka, M. Development of a Smart Garment Prototype with Enuresis Alarm Using an Embroidery-machine-based Technique for the Integration of Electronic Components, *Procedia Computer Science*, Volume 104, 2017, Pages 369-374, ISSN 1877-0509, <https://doi.org/10.1016/j.procs.2017.01.147>.
- [2] Briedis, U., Vališevskis, A., Zelča (2017). Z. Flexible Aluminium-Air Battery for Enuresis Alarm System. In: 16th International Scientific Conference "Engineering for Rural Development": Proceedings. Vol.16, Latvia, Jelgava, 24-26 May, 2017. Jelgava. pp.619-624. ISSN 1691-3043. Available from: doi:10.22616/ERDev2017.16.N123.
- [3] Vališevskis, A., Briedis, U., Juchnevičiene, Ž., Juciene, M., Carvalho (2019). M. Design improvement of flexible textile aluminium-air battery. *The Journal of the Textile Institute*, Vol.12 No.2019, 1.-6.lpp. ISSN 0040-5000. e-ISSN 1754-2340. Available from: doi:10.1080/00405000.2019.1676521
- [4] Vališevskis, A., Briedis, U., Carvalho, M. et al. Development of flexible textile aluminium-air battery prototype. *Mater Renew Sustain Energy* 10, 6 (2021). <https://doi.org/10.1007/s40243-021-00191-z>
- [5] Patent No. LV15477B. Active wetness sensor comprising textile. A. Vališevskis, U. Briedis, 2021.
- [6] Avoundjian, A.; Galvan, V.; Gomez, F.A. (2017). An Inexpensive Paper-Based Aluminum-Air Battery. *Micromachines*, 8, 222.
- [7] Normann M, Kyosev Y, Ehrmann A, et al. (2016) Multilayer Textile-Based Woven Batteries. In: Y. Kyosev (Ed.): *Recent Developments in Braiding and Narrow Weaving*, Springer International Publishing, 129–136.
- [8] Resuli, R., Turhan, I., Ehrmann, A., Blachowicz, T. (2018). Textile-based batteries with nanofiber interlayer. *AIMS Energy*. 6. 10.3934/energy.2018.2.261.
- [9] Jost, K., Pérez, C., McDonough, J., Presser, V., Heon, M., Dion, G., Gogotsi, Y. (2011). Carbon coated textiles for flexible energy storage. *Energy Environ. Sci.*. 4. 5060-5067. 10.1039/C1EE02421C.
- [10] H. Fuketa et al., "30.3 Organic-transistor-based 2kV ESD-tolerant flexible wet sensor sheet for biomedical applications with wireless power and data transmission using 13.56MHz magnetic resonance," 2014 IEEE International Solid-State Circuits Conference Digest of Technical Papers (ISSCC), 2014, pp. 490-491, doi: 10.1109/ISSCC.2014.6757525.
- [11] J. Siden, A. Koptioug and M. Gulliksson, "The "smart" diaper moisture detection system," 2004 IEEE MTT-S International Microwave Symposium Digest (IEEE Cat. No.04CH37535), 2004, pp. 659-662 Vol.2, doi: 10.1109/MWSYM.2004.1336073.
- [12] Li, Q., Bjerrum, N.J. Aluminum as anode for energy storage and conversion: a review. *Journal of Power Sources* 110 (2), pp. 1-10, 2002. ISSN: 03787753.

Improving Adhesion of Graphene Nanoplatelets to Cotton-Based Knitted Fabrics Using Plasma Treatment

Luisa M. Arruda^{1,a*}, Inês P. Moreira^{1,b}, Inês Boticas^{1,c}, João Bessa^{1,d}
and Raul Fangueiro^{1,2,e}

¹Centre for Textile Science and Technology (2C2T), University of Minho, 4710-057 Guimarães, Portugal

²Department of Mechanical Engineering, University of Minho, 4710-057 Guimarães, Portugal

^aluisamendesarruda@gmail.com, ^bines.moreira@fibrenamics.com, ^cinesboticas@fibrenamics.com
^djoabessa@fibrenamics.com, ^erfangueiro@dem.uminho.pt

Keywords: Smart Textiles, Plasma treatment, Graphene nanoplatelets, Electrical resistance values

Abstract. This work aims to analyse the effect of plasma and alkaline pre-treatment to improve the adsorption of GNPs onto 100% cotton knits. For this purpose, in one approach, 2% GNPs were dispersed in an aqueous/ethyl-based solution, in another approach the same concentration of said nanoparticles were dispersed in different % of PEG (10%, 30% and 50%, w/ v). The functionalised samples with and without plasma pre-treatment were characterized by Field Emission Scanning Electron Microscopy (FESEM), Contact Angle, Ground State Diffuse Reflectance (GSDR), and Attenuated Total Reflectance-Fourier Transform Infrared Spectroscopy (ATR-FTIR). Electrical and washability properties until 10th wash cycles were also evaluated. The doped samples obtained semiconductor values, and the ones that received the plasma treatment became hydrophilic, which contributed to excellent absorption bands. However, it is necessary to carry out more in-depth studies that contribute not only to better adsorption, as well as an adequate anchoring of nanoparticles in textile substrates.

Introduction

The history of fibrous structures is analogous to the *Homo sapiens* survival on Earth, who used them as a body layer of protection against the bad weather, acting as a second skin. Adding to the quality of protection, these fibrous structures have undergone substantial changes in the last 50 years regarding their functionalities and properties, such as the ability to capture biochemical and physical signals from the human body, as pressure [1, 2, 3, 4]. In line with this perspective, the concept of smart textiles appeared, which relates to textiles that can detect and sometimes react to different stimuli. Beyond that, there is a substantial increase on the need of smart textiles with medical applicability, which, in addition, need to include safety standards, such as the required cytotoxicity parameters under the ISO 10993 norm [5].

Fibrous matrices in their conventional form do not present responsiveness characteristics, thus they need to be functionalised, to act as identifiers of any stimulus. This functionalisation can be accomplished through chemical or physical processes and, in many cases, nanoparticles arise as a promising material to grant such functionalities to textiles. When it comes to detecting physical signals, as body pressure, carbon-based materials are an adequate resource, mainly due to their thermal and mechanical properties, along with their piezoresistive behavior, that is, the ability to change its electrical resistance from a mechanical deformation. Among these, graphene nanoplatelets (GNPs) have a more affordable price when compared to other carbon-based materials, making it more applicable on an industrial scale [6, 7]. However, two points need to be highlighted when it comes to chemical functionalisation in textile substrates, in this case with GNPs: first, it is noteworthy that due to the Van der Waals forces, the GNPs are less stable, tending to a difficult dispersion [8]; on the other hand, when dealing with textiles based on natural fibres, such as cotton, the hydrophobic impurities found in their cuticle layer, especially waxes, affect the uptake of dyeing and finishing solutions [9].

In view of the above, there is a growing economic and environmental demand to find solutions so that the textile finishing industry can make substrates more adsorptive, reinforcing their functionalisation efficiency through low % of the specified material, as exemplified by Ribeiro *et. al* [10], avoiding the waste of NPs in the bath, while it is possible to reduce the production of wet chemical residues in the production chain. In line with this perspective, the state of the art has presented plasma treatment as an important alternative to meet such specified demand [11, 12, 13].

Plasma treatment is a surface treatment of different materials that takes place from the equal discharge of positively and negatively charged particles [11]. Treatment with oxygen plasma in textiles produces radicals, functional groups, and increases the roughness textile surface due to ionic bombardment, which tends to increase their wettability, thus improving their adsorption capacity in processes of coating. Dielectric barrier discharge (DBD) is faster and more environmentally friendly than chemical surface modification techniques, that act exclusively on the surface of the material without affecting the volume properties. Beyond, when the DBD plasma is operated in air, without the use of expensive carrier gases, this technique is very economical [10]. Some studies address this issue and indicate that since such treatment is a solvent-free technique, it can be an alternative to wet pre-treatment methods [12].

Thus, this work aims to study the effect of DBD plasma technique on the adsorption of graphene nanoplatelets to cotton substrates. For this, we firstly carry out a comparison between plasma and a conventional wet pre-treatment widely used in the finishing industry, namely the alkaline treatment. Then, we verify whether the influence of the plasma treatment is valid when the substrate is functionalised in two different solutions: in aqueous/ethyl base, and in polymeric base, more specifically in different % of polyethylene glycol (PEG).

Experimental

Materials and methods

Materials. The fabrics used in this work were made of 100% cotton fibres (CO), with a mass per unit area of 145.6 g/m² and a thickness of 0.48 mm, provided by Impetus (Barqueiros, Portugal). The GNPs used were provided by Graphenest (Aveiro, Portugal), with 8-30 layers, a thickness of 3-10 nm, and layers' lateral dimensions of 0.5-0.2 μm. PEG with molecular weight of 35,000 g mol⁻¹, were provided by Sigma Aldrich (Germany). As solvents, distilled water and ethanol 96 % (Portugal) were used. For the alkaline fibre pretreatment, Sodium hydroxide (99% NaOH) was purchased from Normax Chem (Marinha Grande, Portugal).

Fabrics pre-treatment. In one approach, 100% CO knitted fabric specimens were submitted to an alkaline pre-treatment. To execute this procedure, the knitted fabrics were immersed in an aqueous solution with NaOH (1M) and kept there for 60 minutes under stirring by orbital shaker. At the end, the samples were washed under running water to remove all residues and dried for 60 min at 80 °C.

The DBD plasma treatment was performed at atmospheric pressure and room temperature in a semi-industrial prototype machine (Softal GmbH/University of Minho, Guimarães, Portugal), using metal electrodes coated with ceramic and counter electrodes coated with silicon. The electrodes, with a 50 cm effective width and gap distance of 3 mm, produced the discharge at low frequency (40 kHz) and high voltage (10 kV). The speed of the machine and discharge power of the electrodes could be modified, with a maximum speed of 60 m·min⁻¹ and discharge of 1.5 kW. In this study, the machine was operated at 1 kW power and a velocity of 4 m·min⁻¹, and the samples were subjected to five discharge cycles on each side of the substrate.

Functionalisation of the fabrics with graphene nanoplatelets. In one approach, powdered GNPs (2% w/v) were added to a solution composed of 70% distilled water and 30% ethanol under magnetic stirring and kept at 350 rpm overnight, followed by 30 minutes in an ultrasound bath. In another approach, different concentrations of PEG (10%, 30%, and 50% w/v) were slowly added to distilled water under magnetic stirring at 200 rpm for 3 hours. After the PEG has been properly dissolved, 2% GNPs were added to the previous solution under magnetic stirring and kept at 200 rpm overnight, followed by 30 minutes in an ultrasound bath. To summarise, 4 solutions were obtained (1 in aqueous/ethyl base and 3 in PEG base). The samples were divided into 3 groups: those that received

alkaline pre-treatment, those that received plasma pre-treatment, and those without any type of pre-treatment. The three groups of knitted fabrics were functionalised by the dip-pad-dry method, where 5 consecutive impregnations were carried out with a roller pressure of 80 Pa, followed by drying in an oven at 100 °C for 10 min. This method is diagrammed in (Figure 1)

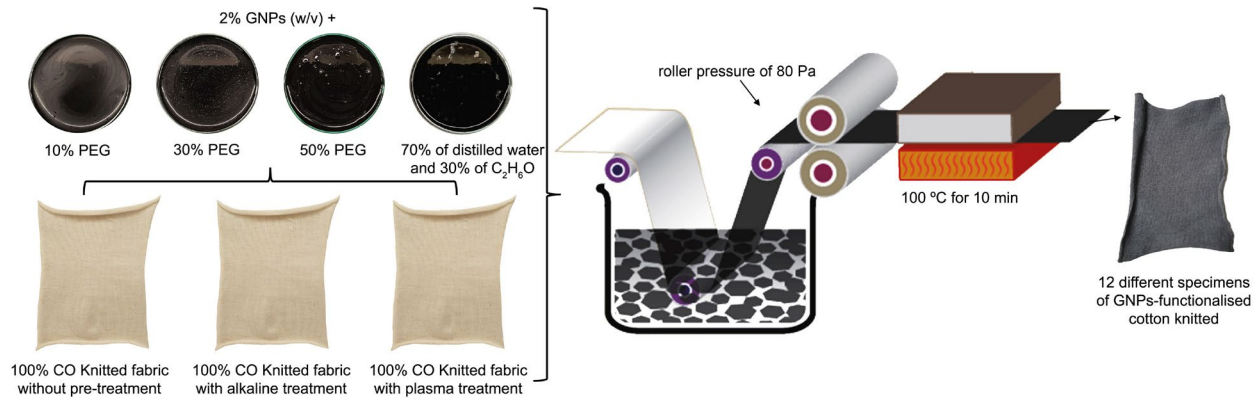


Figure 1. Illustrative scheme of the dip-pad-dry impregnation method on the different samples

Sample characterization

Field Emission Scanning Electron Microscopy (FESEM). In order to study the impregnation and the degree of dispersion of the GNPs into the knitted substrate, FESEM analysis was carried out. The surface morphology and cross sections of the samples was analysed by FESEM using the NOVA 200 Nano SEM equipment from FEI Company (Hillsboro, OR, USA). All samples were sputter-coated with a palladium-gold (Pd-Au) film (20 nm) to make them conductive.

Ground-State Diffuse Reflectance (GSDR). In addition to validating the presence of GNPs in the knitted fabric, GSDR was performed to identify differences in the absorption spectrum for functionalised samples that received the aforementioned pre-treatments. The knitted fabric samples' GSDR spectra were recorded in the 200 to 800 nm wavelength range, using a Spectrophotometer UV 2501PC Shimadzu. Each sample was analysed in three different places to ensure homogeneity. The remission function ($F(R)$) was calculated according with the Kubelka-Munk Eq.1:

$$F(R) = \frac{(1-R)^2}{2R} = \frac{K}{S}. \quad (1)$$

Attenuated Total Reflectance-Fourier Transform Infrared Spectroscopy (ATR-FTIR). Chemical composition of the knitted samples was studied by ATR-FTIR analysis using an IRAffinity-1S, SHIMADZU equipment (Kyoto, Japan). Each spectrum was obtained in transmittance mode using a diamond ATR crystal cell by accumulation of 45 scans with a resolution of 4 cm^{-1} from 400 to 4000 cm^{-1} .

Water contact angle. To evaluate the hydrophobic character of the cotton knitted, without pre-treatment, with alkaline treatment and with plasma treatment, WCA measurements were performed. For this, a contact angle system was carried out through the Dataphysics instrument (Filderstadt, Germany), coupled to a high-resolution camera, using OCA20 software (Germany). A volume of 5 μL distilled water was dispensed from the syringe onto the fibrous substrate's surface. For each sample, the contact angle was measured at 10 different locations, and the average and standard deviation for each test were calculated.

Electrical Resistance test. To verify the electrical resistance values of the functionalised samples, with and without GNPs, the I-V curves (electric current intensity – voltage curves) method was performed. For this purpose, an electrical source (Keitley 487 Picoammeter/Voltage Source), applying a potential difference between -0.8 V to 0.8 V with a step of 0.1 V at room temperature, was connected to the specimens by conductive electrodes. This set-up is composed of 4 conductive copper plates with an area of ($5 \times 10 \text{ cm}^2$), and an electrode distance of 2 cm. The samples have an area of

10x10 cm², and they are sandwiched by the electrodes. The electrical resistance values were determined by the slope of the I-V curves.

Durability test: wash fastness. In order to quantify the stability of the samples to the domestic washing process, they were subjected to 10 washing cycles, and at the end of the 5th and 10th, their electrical resistance value was measured according to the method described previously. The procedure was carried out in accordance with the standard ISO6330–Textiles, Domestic washing and drying, procedures for textile testing.

Results and Discussion

Morphological Characterization. Considering the possible changes caused in the textile substrate topography by the pre-treatments, SEM observations were important. The appearance of cracks and grooves in the order of 2 μm in the samples with plasma treatment can be explained by the presence of H and OH species in the DBD plasma discharge, causing extensive etching of the surface, and leading to the formation of microcraters, as previously noted by Molina, R. [14]. It is also possible to observe an increase in roughness in the samples that received the corrosion treatment with NaOH, due to the extraction of low molecular weight materials and the presence of lignin in them [15]. Otherwise, cotton fibres without treatment present a smoother appearance, as can be seen in Figure 2.

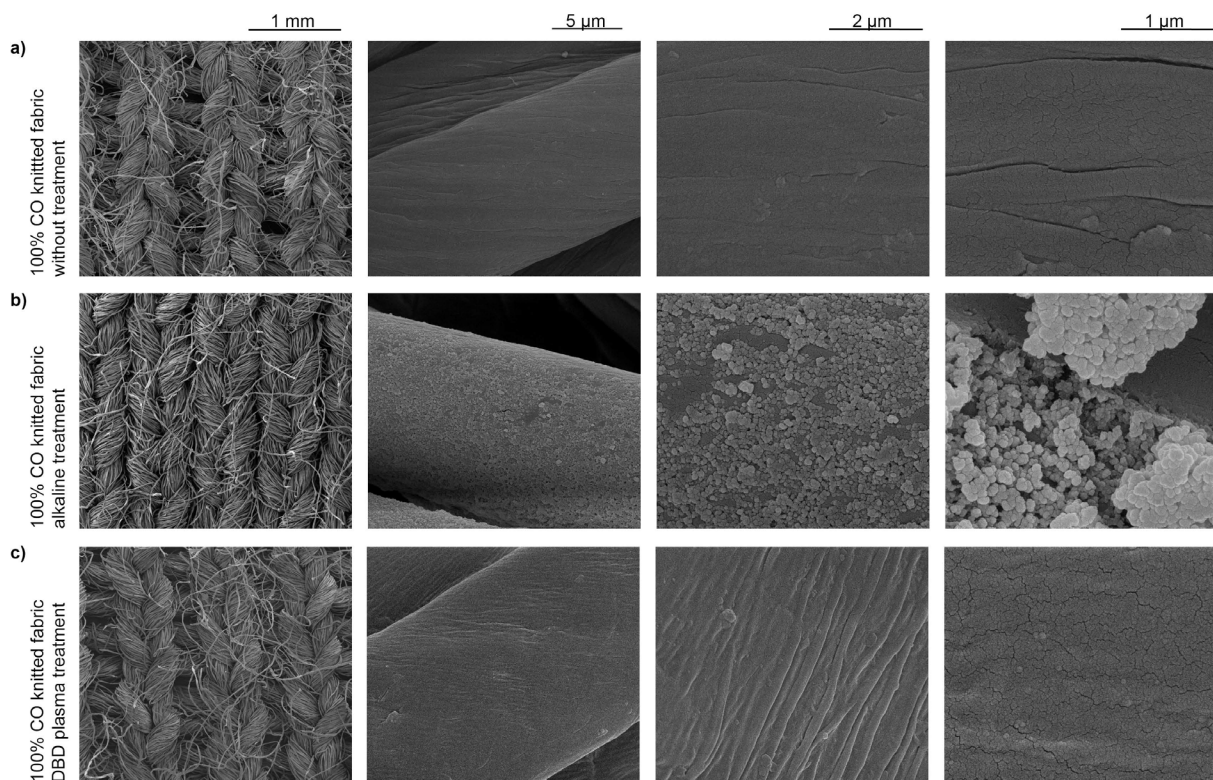


Figure 2. FESEM images of a) 100% CO knitted fabric surface; b) 100% CO knitted fabric surface with alkaline treatment; c) 100% CO knitted fabric surface with plasma treatment

Physicochemical characterization. In order to evaluate the hydrophobicity of the knits in question after said pre-treatments, water contact angle measurements were carried out (Figure 3). According to the literature, hydrophilic surfaces have a contact angle below 90 degrees, while hydrophobic surfaces have a contact angle larger than 90 degrees. In addition, surfaces with over 150 degrees of contact angle are considered super hydrophobic [16].

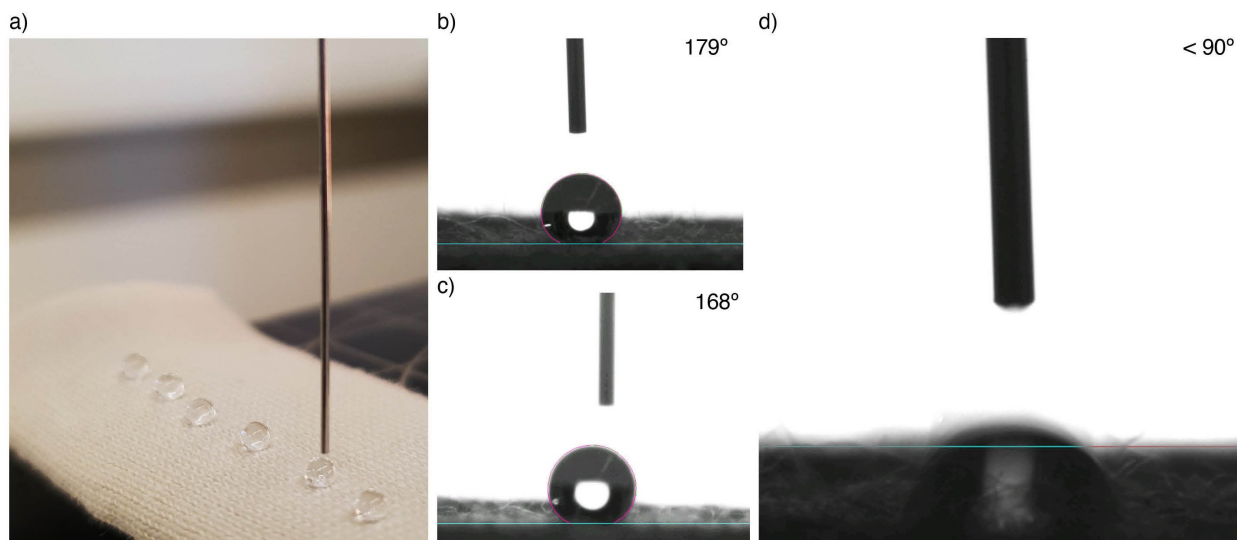


Figure 3. a) Representative image of the knitted fabric hydrophobicity; WCA measurements of b) the knitted fabric without pre-treatment; c) the knitted fabric with alkaline pre-treatment; d) the knitted fabric with plasma pre-treatment

The 100% cotton knit without any type of treatment is superhydrophobic (WCA $179.8^\circ \pm 0.1225$), which can be explained considering the presence of hydrophobic elements such as lignin and waxes. After receiving the alkaline pre-treatment, a not very significant reduction occurred with respect to this property (WCA $168.84^\circ \pm 6,8200$), in addition to presenting a high standard deviation. This fact may indicate that the crystalline region of lignocellulose was not deeply destroyed, in addition, it can be related to the exposure time and the concentration of NaOH used, as previously stated by Wang et al.[17]. However, after receiving the plasma discharge, the knit became superhydrophilic, as the liquid spreads almost to a zero-contact angle on the textile surface. This behavior can be explained by the partial decomposition of the hydrophobic layer, causing the formation of new hydrophilic groups on the surface, that increase the surface energy value and, therefore, the decrease of contact angles [12]. In this regard, plasma treatment proved to be the most effective.

After chemical and physical pre-treatment of the cotton knits, the functionalisation was performed with the abovementioned GNPs. The Kubelka–Munk remission functions (Figure 4), show an evident formation of a new peak at approximately 255 nm in all functionalised samples, which differs from the control sample. It has been previously reported that the presence of these peaks is associated to the $\pi \rightarrow \pi^*$ transition of C=C bond in graphitic structure of GNPs [18]. In this sense, this result confirms the incorporation of said nanoparticles on the knitted fabric surface. Furthermore, there is an increase in the absorption band of all functionalised samples, which indicates a reduction in the reflectance band. Such behavior is occurring considering that GNPs are dark pigments in nanoscale, with low reflective index. Furthermore, for the samples doped with GNPs in solutions with 10% and 30% PEG (w/v), there was no significant difference in the absorption bands for those that received pre-treatments. However, for samples functionalised with the solution made with 50% PEG and for samples functionalised with aqueous + ethyl base, there was a significant difference in the absorption band relative to the pre-treatment used. For the former, a superior absorption band is visible for alkaline pretreatment, while for the latter, a superior absorption band is patent for plasma treatment. This is in line with previous reports that show a more efficient cotton surface modification upon the addition of (deuterated) water on DBD atmospheric pressure plasma, when compared to a plasma treatment, which is due to the incorporation of polar functional groups on the cotton surface [14]. Therefore, in addition to indicating a greater absorption range for the plasma-treated sample, it may justify larger Remission Function $F(R)$ for aqueous and ethyl-based solutions, when compared to said polymer-based solutions.

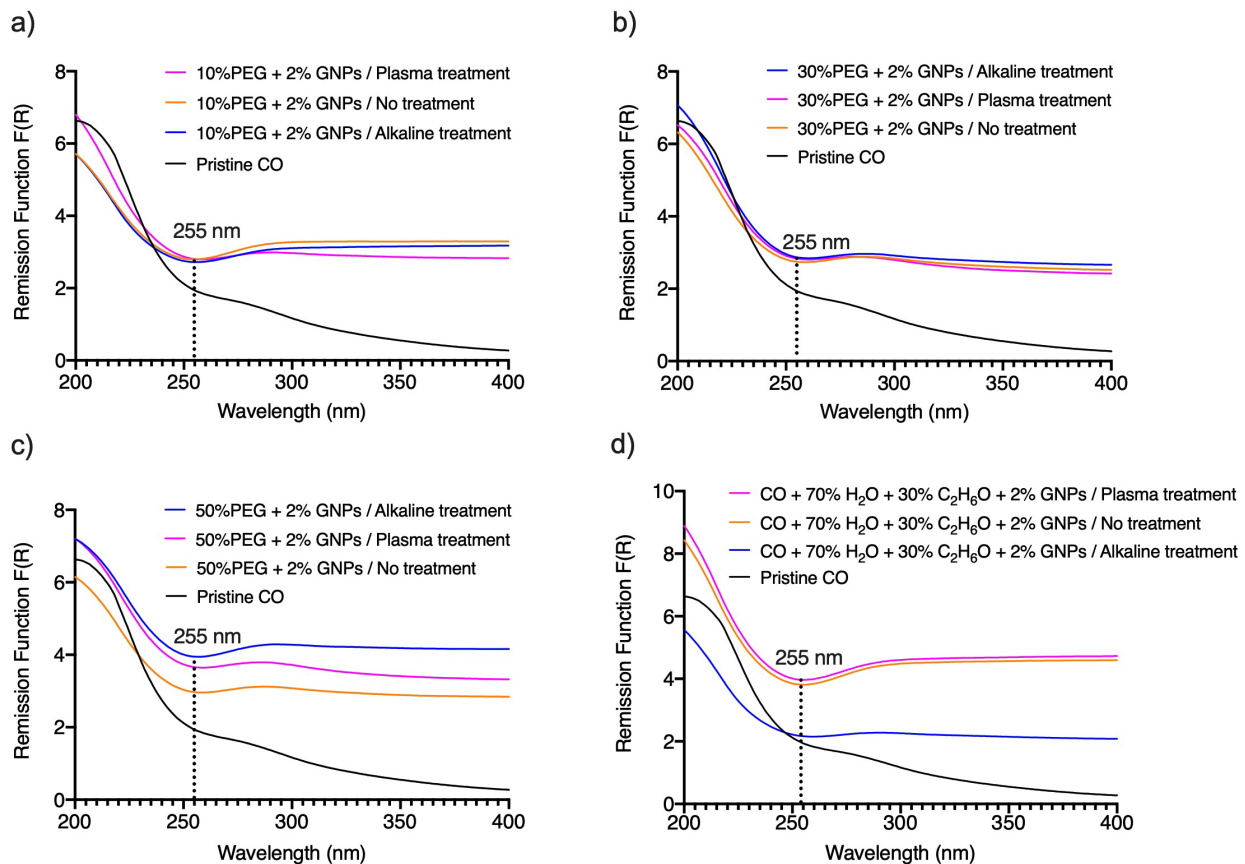


Figure 4. GSDR spectra of a) samples functionalised with 2% GNPs in 10% of PEG; b) samples functionalised with 2% GNPs in 30% of PEG; c) samples functionalised with 2% GNPs in 50% of PEG, and d) samples functionalised with 2% GNPs in aqueous/ethyl solution

The cotton knit ATR-FTIR spectrum (Figure 5) shows the presence of the typical bands of natural cellulosic fibers: cellulose, hemicellulose and lignin. The band appearing at approximately 1028cm^{-1} can be attributed to the asymmetric C-H stretching vibration of cellulose and hemicellulose [9]. In turn, the peak at 1315cm^{-1} can be associated to the CH wagging [9, 12], and the one at approximately 3334cm^{-1} to the O-H stretching, both related to the hydroxyl groups from cellulose and lignin [20, 21]. The peak around 2895cm^{-1} , corresponds to symmetric CH_2 stretching: long alkyl chain, and is related to the cotton impurities, such as waxes and pectins [19, 22]. The FTIR spectra did not show significant differences between the knitted fabrics with treatments and without any type of treatment, which can be justified by the fact that this technique only measures the bulk composition of fabrics. Waxes and pectins from non-cellulosic components are located at the cuticle and primary wall of the cotton fibers, and plasma and alkaline treatment act exclusively on the material surface without affecting the bulk properties [15]. Regarding the samples functionalised with GNPs dispersed in aqueous and ethylic solution, the peak located at approximately 2112cm^{-1} is reinforced and can be associated with the spectrum of powdered GNPs.

When comparing the spectroscopy of the CO knitted samples functionalised by the PEG + GNPs solution, with the pristine CO, the characteristic peaks of the natural fiber remain, as well as the peak corresponding to the GNPs. The peak previously located at 1028cm^{-1} have been moved slightly to the right, and can be attributed to the -CH out-of-plane bending vibrations of PEG [22]. In addition, the peaks located at approximately 1340cm^{-1} , 1278cm^{-1} , and 1240cm^{-1} , are due to CH, CH_2 and CH_3 bending vibrations, respectively [23]. It is noteworthy that the peaks located at 2895cm^{-1} , intensified in samples functionalised with solutions made with 30 and 50% PEG, which may indicate that the bonds are strengthening from these concentrations.

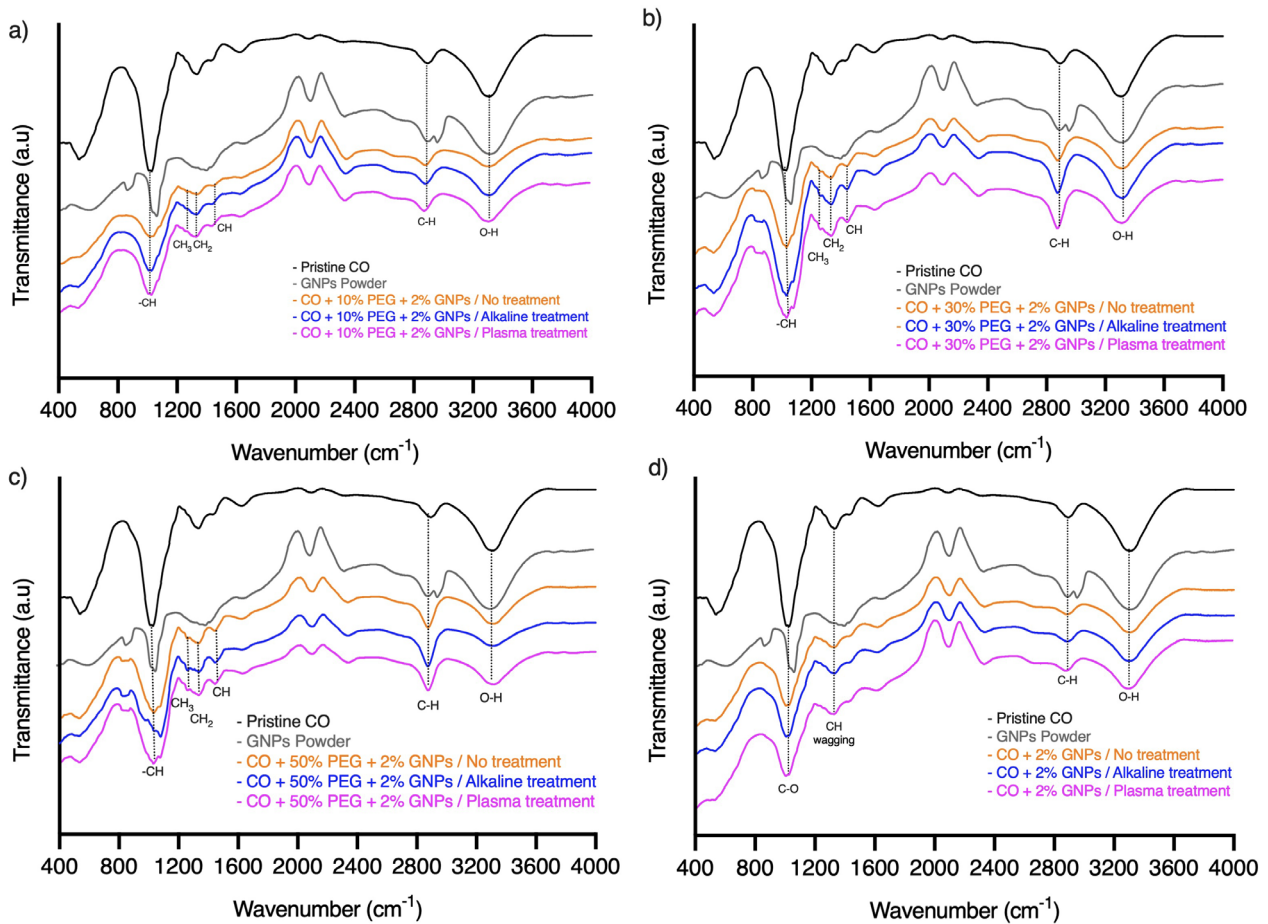


Figure 5. ATR-FTIR spectra of a) samples functionalised with 2% GNPs in 10% PEG; b) samples functionalised with 2% GNPs in 30% PEG; c) samples functionalised with 2% GNPs in 50% PEG; d) samples functionalised with 2% GNPs in aqueous/ethyl solution

Electrical Resistance Characterization. The electrical resistance of textile substrates is directly related to their water absorption mechanisms [24], as well as the specific area of the fibres used in a fabric construction [25]. In this sense, a study by Wang et. al relates the electrical resistance values of cotton and polyester, and shows that since cotton is a material with hydrophilic properties that rapidly absorbs and diffuses water through the fibre, its electrical resistance values are lower when compared to the aforementioned synthetic substrate [25]. Furthermore, the results presented by the author indicated that cotton knitted has electrical resistance values in the order of $k\Omega$, which varies according to their Moisture regain (M). The higher their moisture recovery rate, the greater their electrical resistance. In line with these previous results, the value of $1.67 \times 10^4 \Omega$ is identified for the 100% CO knitted fabric (pristine CO) analysed under this work, (Figure 6). Therefore, we proceeded with the analysis of the electrical resistance of cotton knits submitted to functionalisation in polymeric and aqueous/ethyl base (so far without the addition of nanoparticles). When cotton knitted fabrics were doped with different concentrations of PEG, lower resistance values were observed for all samples that received alkaline pre-treatment. This result may indicate that, in addition to PEG contributing to the reduction of electrical resistance values, when compared to plasma treatment, alkaline treatment made the substrate more reactive for PEG bonds.

For samples functionalised with aqueous/ethyl-based solution, a lower electrical resistance value is found for samples that received the plasma treatment. This result confirms the data obtained in the Ground-State Diffuse Reflectance and Contact Angle of this sample, considering that polar functional groups on the surface of the cotton substrate by the addition of water, added to the plasma discharge, make the cotton knitted fabric more adsorptive and hydrophilic, therefore, contributed to their electrical resistance value reduction (Figure 6)

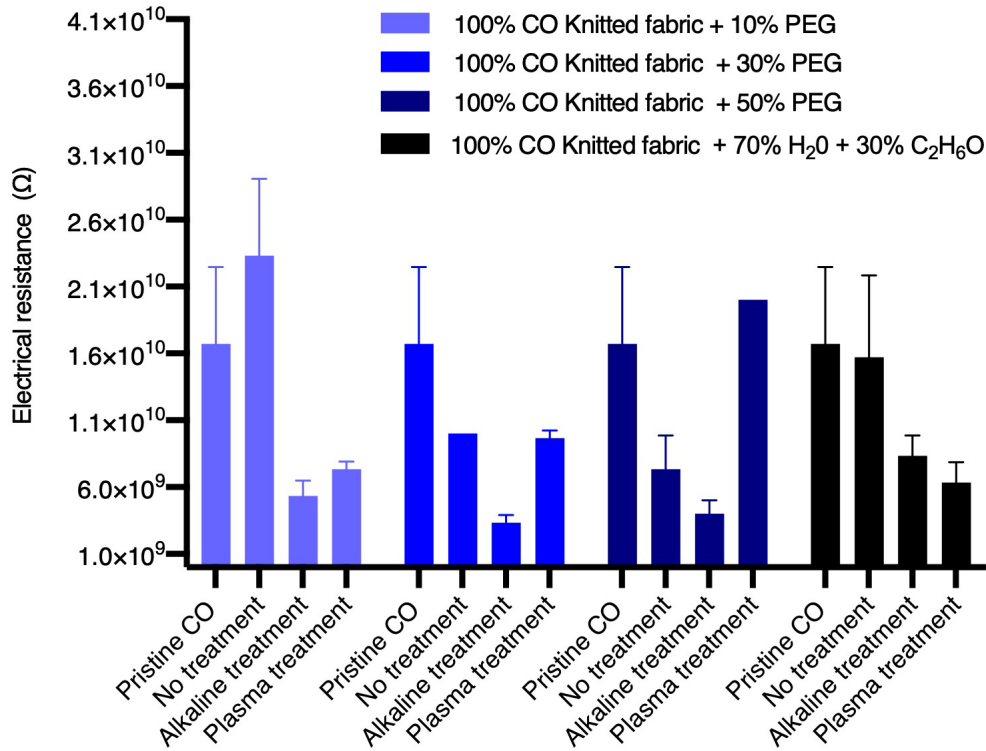


Figure 6. Electrical resistance values of samples functionalised with PEG solutions at different concentrations, and with the aqueous/ethyl based solution, pre-treated with the aforementioned methods that are being analysed in this study.

In addition, we sought to identify changes in electrical resistance values from the addition of 2% GNPs in the samples. For specimens in which GNPs were dispersed in PEG solutions, the alkaline treatment also presented lower electrical resistance values, namely $3 \times 10^9 \Omega$, $2 \times 10^9 \Omega$, $2 \times 10^9 \Omega$, for 10%, 30% and 50% PEG, respectively. This result also indicates that 30% and 50% of PEG are more suitable concentrations for better dispersion of said nanoparticles. For samples that were doped with GNPs dispersed in aqueous/ethyl solution, $3 \times 10^9 \Omega$ and $3 \times 10^{10} \Omega$ of electrical resistance values were obtained for those with alkaline and plasma pre-treatment, respectively. This last value may indicate that, although the plasma treatment has reduced the electrical resistance value of the substrate when compared, under the same conditions, to the alkaline treatment, these GNPs may not have properly dispersed in an aqueous/ethyl base, thus, increasing its electrical resistance value.

In other words, for specimens with plasma treatment, the electrical resistance values increase as well as their absorption band, which once again indicates that the plasma treatment has played an important role in the enhanced adsorption of these nanoparticles when compared to the wet pre-treatment. However, once again, as the GNPs are not properly dispersed, good electrical resistance values were not obtained. (Figure 7).

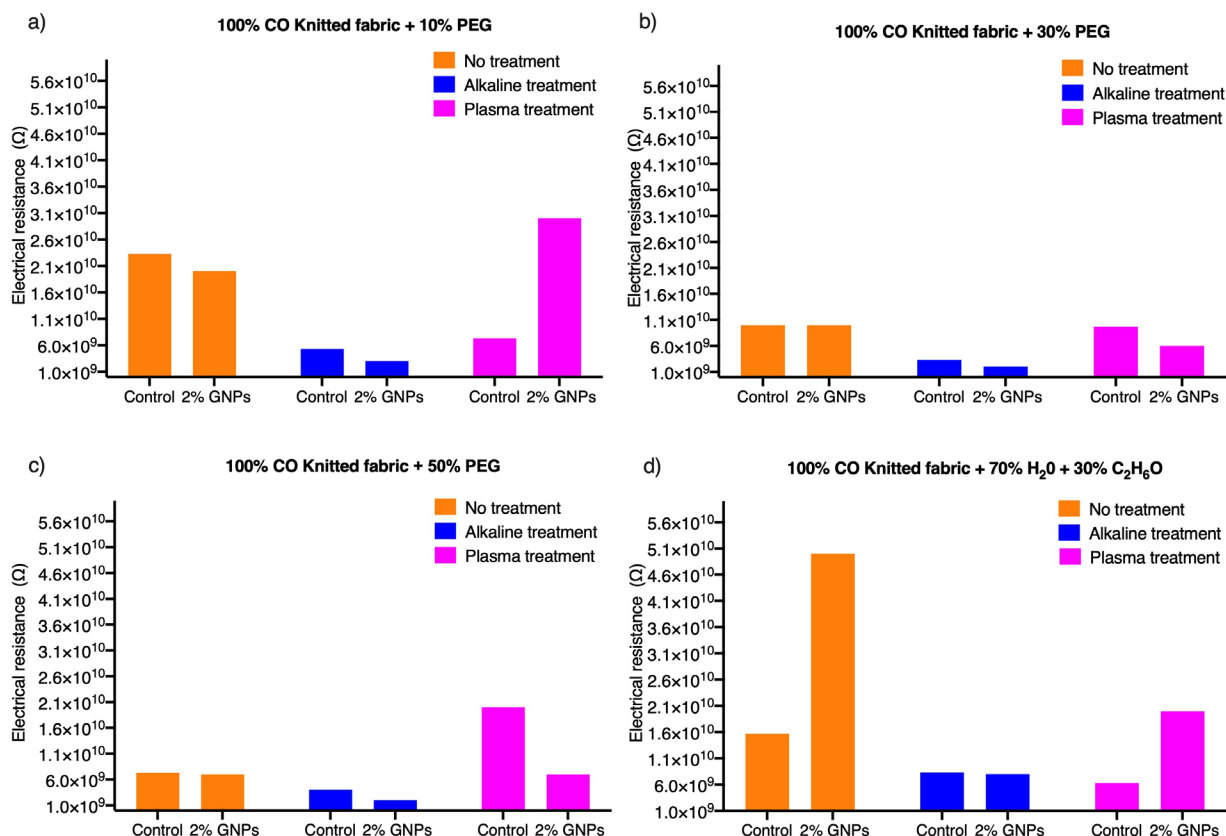


Figure 7. Electrical resistance values of 100% CO knitted fabrics, without pre-treatment, with alkaline treatment and with plasma treatment, functionalised with a) 10% PEG + 2% GNPs; b) 30% PEG + 2% GNPs; c) 50% PEG + 2% GNP; d) aqueous/ethyl solution + 2% GNP

Durability test: wash fastness. In order to evaluate the resistance to washing, the samples were submitted to 10 test cycles that mimic the domestic washing procedure. After the 5th washing cycle, all samples showed similar electrical resistance values, in the order of 10^8 Ω, (Figure 8). This may suggest that, after undergoing a certain mechanical agitation, some nanoparticles moved to the surface of the fibrous substrate, a fact that contributes to better acquisition of electrical signals. Until the 10th cycle, they maintained a certain constancy in the range of values obtained and, from then on, the electrical resistance values were higher than the values obtained before washing, which may indicate the loss of said nanoparticles in the bath, which suggests that the samples have resistance up to the 10th cycle.

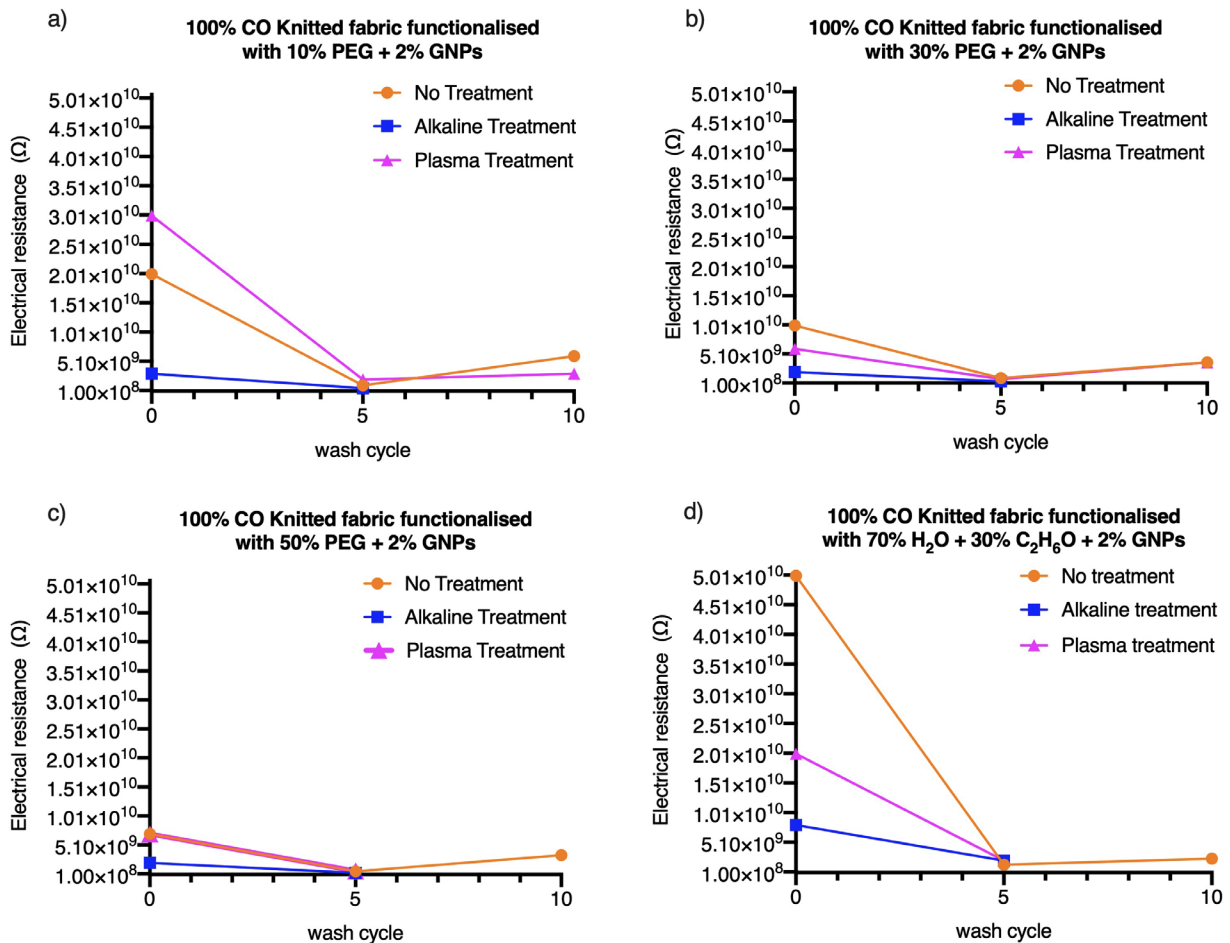


Figure 8. Electrical resistance values after 10th wash cycles of the samples functionalised with a) 10% PEG + 2% GNPs; b) 30% PEG + 2% GNPs; c) 50% PEG + 2% GNP; d) aqueous/ethyl solution + 2% GNPs

Conclusion

In this study, 100% CO knitted fabrics treated with plasma and alkaline treatment, were functionalised with 2% GNPs dispersed in polymeric and aqueous/ethyl-based solutions. These depositions were confirmed by the results of GSDR and ATR-FTIR. The results of SEM and contact angle showed that plasma treatment, by causing extensive etching of the surface, and leading to the formation of microcraters, made a substantial modification by making the knitted fabric more hydrophilic, when compared to a wet pre-treatment method, thus contributing to a better adsorptive property.

In addition, cotton samples that received the plasma pre-treatment and that were doped with aqueous/ethyl-based solutions, showed more intense absorption bands compared to polymer-based solutions. This result proves a more efficient modification of the cotton surface with the addition of water (deuterated) added to the plasma DBD. However, it should be noted that alkaline treatment made the substrate more reactive for PEG bonds, which contributed to a better dispersion of these nanoparticles, as well as lower electrical resistance values.

That said, the effectiveness of the plasma treatment in contributing to the improvement of finishing processes by making substrates more adsorptive is undeniable. However, it still cannot be seen as a replacement method for the conventional wet method.

Within the scope of this research, new tests will be carried out with the alteration of the plasma discharge exposure time, as well as the insertion of gases.

Acknowledgments

The authors acknowledge the financial support of the project 4NoPressure, with the reference n. POCI-01-0247-FEDER-039869, co-funded by Operational Programme for Competitiveness and Internationalization (COMPETE 2020), under the PORTUGAL 2020 Partnership Agreement, through the European Regional Development Fund (ERDF).

References

- [1] M. Liu *et al.*, Large-Area All-Textile Pressure Sensors for Monitoring Human Motion and Physiological Signals, *Adv Mater.* 29 (2017) 1–9.
- [2] C. Guignier, B. Camillieri, M. Schmid, R. M. Rossi, and M. A. Bueno, E-Knitted textile with polymer optical fibers for friction and pressure monitoring in socks, *Sensors.* 19 (2019) 31–33.
- [3] J. Deng *et al.*, A tactile sensing textile with bending-independent pressure perception and spatial acuity, *Carbon.* 149 (2019) 63–70.
- [4] L. Yu *et al.*, Flexible Multi-Material Fibers for Distributed Pressure and Temperature Sensing, *Adv. Funct. Mater.* 30 (2020) 1-8.
- [5] M. A. Ali and A. Shavandi, Medical textiles testing and quality assurance, in: Wang, L. (Eds.), *Performance Testing of Textiles: Methods, Technology and Applications*, Woodhead Publishing, Sawston, 2016, pp. 129-153.
- [6] L. Yue, G. Pircheraghi, S. A. Monemian, and I. Manas-Zloczower, Epoxy composites with carbon nanotubes and graphene nanoplatelets - Dispersion and synergy effects, *Carbon.* 78 (2014) 268–278, 2014.
- [7] P. Pereira, D. P. Ferreira, J. C. Araújo, A. Ferreira, and R. Figueiro, The potential of graphene nanoplatelets in the development of smart and multifunctional ecocomposites, *Polymers.* 12 (2020)2-18.
- [8] Y. Wang, W. Dai, Y. Song, D. Wang, L. Zeng, and N. Jiang, Enhanced Thermal and Electrical Properties of Epoxy Composites Reinforced With Graphene Nanoplatelets, *Polym. Compos.* 16 (2014) 101–113.
- [9] C. Chung, M. Lee, and E. K. Choe, Characterization of cotton fabric scouring by FT-IR ATR spectroscopy, *Carbohydr. Polym.* 58 (2004) 417–420.
- [10] A. I. Ribeiro *et al.*, Antimicrobial efficacy of low concentration PVP-Silver nanoparticles deposited on DBD plasma-treated polyamide 6, 6 fabric, *Coatings.* 9 (2019) 1–14.
- [11] W. Raslan, A. El-Halwagy, and H. Elsayad, Recent Advances in Plasma/Nanoparticles Treatments of Textile Fibers, *J. Text. Color. Polym. Sci.* 17 (2020) 87–105.
- [12] H. A. Karahan and E. Özdoğan, Improvements of surface functionality of cotton fibers by atmospheric plasma treatment, *Fibers Polym.* 9 (2008) 21–26.
- [13] N. V. Bhat, an Netravali, av Gore, mp Sathianarayanan, ga Arolkar, and rr Deshmukh, Surface modification of cotton fabrics using plasma technology, *Text. Res. J.* 81 (2011) 1014–1026.
- [14] R. Molina, R. Bitar, P. Cools, R. Morent, and N. De Geyter, Effect of liquid impregnation on DBD atmospheric pressure plasma treatment of cotton, *Cellulose.* 27 (2020) 7847–7859, 2020.
- [15] P. Nguyen-Tri, F. Altiparmak, N. Nguyen, L. Tuduri, C. M. Ouellet-Plamondon, and R. E. Prud'Homme, Robust Superhydrophobic Cotton Fibers Prepared by Simple Dip-Coating Approach Using Chemical and Plasma-Etching Pretreatments, *ACS Omega.* 4 (2019) 7829–7837.

-
- [16] A. Marmur, C. Della Volpe, S. Siboni, A. Amirfazli, and J. W. Drelich, Contact angles and wettability: Towards common and accurate terminology, *Surf. Innov.* 5 (2017) 3–8.
- [17] J. Wang, Y. Zheng, and A. Wang, Effect of kapok fiber treated with various solvents on oil absorbency, *Ind. Crops Prod.* 40 (2012) 178–184.
- [18] S. S. Shazali, S. Rozali, A. Amiri, M. N. M. Zubir, M. F. M. Sabri, and M. Z. Zabri, Evaluation on stability and thermophysical performances of covalently functionalized graphene nanoplatelets with xylitol and citric acid, *Mater. Chem. Phys.* 212 (2018) 363–371.
- [19] J. C. Araújo, D. P. Ferreira, P. Teixeira, and R. Figueiro, In-situ synthesis of CaO and SiO₂ nanoparticles onto jute fabrics: exploring the multifunctionality, *Cellulose*. vol. 1 (2020) 1123–1138, 2020.
- [20] M. Bakri and E. Jayamani, Comparative Study Of Functional Groups In Natural Fibers : Fourier Transform Infrared Analysis (FTIR), *International Journal of Current Engineering And Scientific Research.* 3 (2016) 154-161.
- [21] S. M. Costa, D. P. Ferreira, A. Ferreira, F. Vaz, and R. Figueiro, Multifunctional flax fibres based on the combined effect of silver and zinc oxide (Ag/zno) nanostructures, *Nanomaterials.* 8 (2018) 1–21, 2018.
- [22] S. Naghibi *et al.*, Mortality response of folate receptor-activated , PEG – functionalized TiO₂ nanoparticles for doxorubicin loading with and without ultraviolet irradiation, *Ceram. Int.* 40 (2014) 5481–5488.
- [23] S. Luo, A. F. Wang, and A. Z. Shi, Preparation of highly active photocatalyst anatase TiO₂ by mixed template method, *J Sol-Gel Sci Technol.* 52 (2009) 1–7.
- [24] J. Hu, Y. Li, K. Yeung, A. S. W. Wong, and W. Xu, Moisture Management Tester : A Method to Characterize Fabric, *Text. Res. J.* 75 (2005) 57-62.
- [25] X. Wang, W. Xu, W. Li, and W. Cui, Study on the Electrical Resistance of Textiles under Wet Conditions, *Text. Res. J.* 79 (2009) 753–760.

Curing Adhesives with Woven Fabrics Made of Polymer Optical Fibre and PET Yarn

Jan KALLWEIT^{1,a*}, Robert SEEWALD^{2,b}, Mark PÄTZEL^{1,c},
Alexander SCHIEBAHN^{2,d}, Uwe REISGEN^{2,e} and Thomas GRIES^{1,f}

¹Institut für Textiltechnik, RWTH Aachen University, Otto-Blumenthal-Straße 1, 52074 Aachen, Germany

²Welding and Joining Institute, RWTH Aachen University, Pontstraße 49, 52062 Aachen, Germany

^ajan.kallweit@ita.rwth-aachen.de, ^bseewald@isf.rwth-aachen.de,

^cmark.paetzel@ita.rwth-aachen.de, ^dschiebahn@isf.rwth-aachen.de, ^ereisgen@isf.rwth-aachen.de, ^fthomas.gries@ita.rwth-aachen.de

Keywords: POF, woven fabrics, adhesives, photocuring

Abstract. UV bonding technology's biggest limitation is the need of a transparent joining part to be able to cure the adhesive with an external light source. This is to be solved with ribbon fabrics made with polymer optical fibres (POF) which guide the UV light into the adhesive bond. On the basis of previously published experiments, a set of POF fabrics with different thread densities and weft materials is evaluated optically regarding the emitted UV light intensity and mechanically regarding the shear strength of the adhesive bonds. A factorial experiment plan indicates that higher tensile lap-shear strength comes with lower weft fineness and higher weft density. The maximum shear strength achieved was 8.3 MPa with potential room for improvement due to non-cohesive failure, relatively high weft densities and a comparatively low powered UV light source.

Introduction

An essential deficit of the adhesive technology is the long curing time of the adhesives. Besides properties such as dimensional stability, transparency, low shrinkage and a high chemical resistance, radiation-curable materials enable curing within seconds or minutes on demand [1]. There are two different types of radiation-curing mechanisms: radical curing and cationic curing [2]. In the case of radical curing, the light is absorbed by photoinitiators, which start a chain-growth polymerization based on radicals. In cationic curing systems, the radiated light is absorbed which releases reactive substances in the adhesive that initiate curing process. Despite the cationic process can proceed without further radiation, the radical curing process is advantageous due to the much faster curing times which is one of the essential benefit initially mentioned [3]. Most radiation-curing adhesives are cured at wavelength of 405 nm, 365 nm and below which is why they are also referred to as UV adhesives. UV adhesives are applied in many fields like electronics (e.g. for touch screens), industrial assembly (e.g. for solar panels) and glass bonding (e.g. for windshield repair) [4, 5]. However, all these application have in common that a transparent part is being bonded so that the adhesive can be cured with an external UV light source. Thus, according to the current state of the art, the use of UV-curing adhesives is therefore not possible for two non-transparent joining parts which drastically limits their applicability [6, 7].

In order to use UV-curing adhesives in combination with non-transparent joining partners, polymer optical fibres (POF) are embedded in the adhesive to guide UV light into the adhesive joint. POF are usually bicomponent fibres made of transparent amorphous polymers which can guide light via the principle of total internal reflection (TIR) at the core-cladding interface [8]. Their typical applications are in short distance data transfer, sensor technology and illumination [9]. A potentially infinite light guidance is limited by losses in the POF. These can happen due to external causes during production like impurities or inhomogeneities in the fibre which cause scattering. But there is also inevitable attenuation caused e.g. by molecular vibration which leads to absorption of optical power [10]. Despite the lower attenuation of glass optical fibres, the focus has been laid on optical

fibre made of polymers since their mechanical properties like the Young's modulus are closer to the ones of the adhesive which are polymers as well in their cured form. High differences in Young's modulus would lead to stress peaks which weaken the adhesive bond [1, 11].

For the UV light to be emitted laterally into the uncured adhesive TIR must be hindered to a certain extent. This can be referred to as sidelight activation. There are different mechanisms like bulk scattering, bending, surface perforation and luminescence used for sidelight activation [12, 13]. For the purpose of curing UV adhesives, a trade-off between on the one hand a sufficiently intensive and on the other hand a sufficiently homogeneous lateral light emission from the fibre must be made. In case of a uniform sidelight activation, the attenuation losses and the side emission losses both exponentially decay the optical power guided in the POF. Therefore, the sidelight activation needs to be intensified with increasing distance to the light source to ensure uniform curing of the adhesive [14].

Previous experiments showed that typical POF diameters of 1.0 mm are too large for standard adhesive joints [6]. However, single POFs with a smaller diameter cannot transmit enough optical power and lead to too long curing times or insufficient curing. Therefore, as a new approach, a multitude of small-diameter POF in woven fabrics are further investigated as suggested in [6] (see Figure 1). This leads to new research and implementation questions besides the bonding process itself regarding how to weave the POF: POF as warp or weft, materials and fibre fineness (titre), weave, warp and weft densities etc.

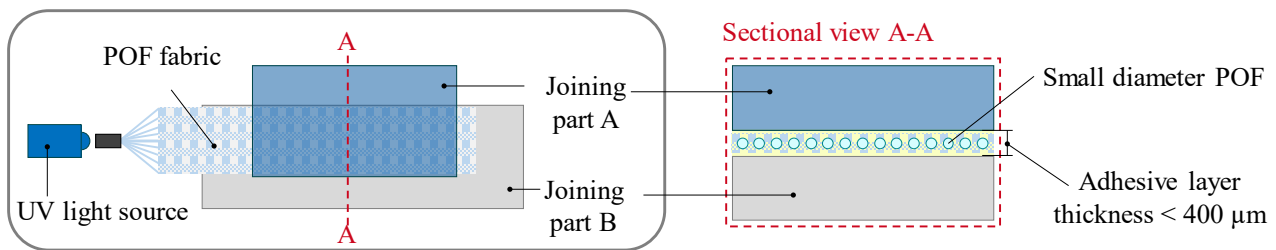


Figure 1: Schematic diagram of an adhesive bond using a woven fabric made of polymer optical fibres

Materials and Methods

In the following study, with regard to the process parameters mentioned, focus is laid on the influence of weft titre and density. For this purpose, two PET yarns with different fineness as well as two different weft densities for each yarn were used: 167 dtex, F036/2 by TWD Fibres GmbH, Deggendorf, Germany and 1110 dtex, F192 by BRILEN TECH, S.A., Barbastro, Spain. This corresponds to the design of experiment matrix in Table 1 to determine the influence of weft density and weft fineness on the radially emitted optical power and, based on this, on the achievable tensile strengths of an overlap bond. PET as weft yarn material was chosen due to its chemical polarity leading to a potentially strong adhesive bond [15]. Besides PET yarns are available in various specifications, usually cost efficient and recyclable.

Table 1: Full factorial experiment plan with the parameters weft fineness and density being varied

No.	Weft fineness	Weft density
1	167 dtex	7 /cm
2	1110 dtex	5 /cm
3	167 dtex	3 /cm
4	1110 dtex	3 /cm

To examine the fabric parameters mentioned above, the other parameters are left as constant as possible. Therefore, all fabrics were produced as plain weave fabrics. Moreover, a commercially available sidelight POF “VB-500P” by Asahi Kasei Corp., Tokyo, Japan was used as warp for all trials. It is a multi-core POF with 37 PMMA cores and has a total diameter of 0.5 mm. The weaving

trials were performed with a ribbon loom system “NH2 53” by Jakob Müller AG, Frick, Switzerland. The POF fabrics consist of 20 POF filaments resulting in a width of ~15 mm. They were cut in 150 mm long probes. Over a length of 50 mm, the weft threads were removed in all probes in order to bundle the POF in a ferrule. Then the POF ends are polished. F-SMA905 connectors were used to ensure reproducible coupling to a DELOLUX50 UV LED spot lamp by DELO Industrie Klebstoffe GmbH & Co. KGaA, Windach, Germany (491 mW) respectively to a laser diode by InsaneWare-Deluxe, Gladbeck, Germany (749 mW), both with a peak wavelength of 405 nm. Figure 2 depicts the fabric surfaces illustrating the different yarn titres and weft densities.

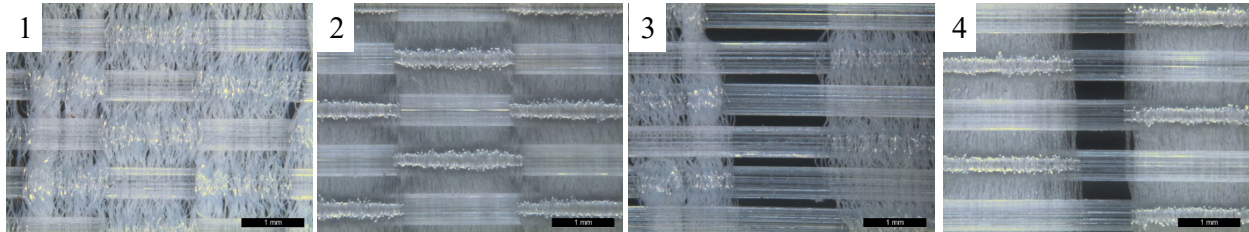


Figure 2: Microscopy images of the surfaces of the four fabric types

With one POF fabric four adhesion tests can be done because the non-transparent anodized aluminium test specimina are bonded on an adhesive area of 25 mm x 12.5 mm. A UV adhesive “Photobond FB4175” by DELO Industrie Klebstoffe GmbH & Co. KGaA, Windach, Germany based on a modified acrylate is used for the bonding tests. All test specimen are pre-treated with a Nd:YAG (neodymium-doped yttrium aluminium garnet) laser with 20 W at 1064 nm to improve the surface energy for adhesion. The adhesion procedure in five steps can be seen in Figure 3.

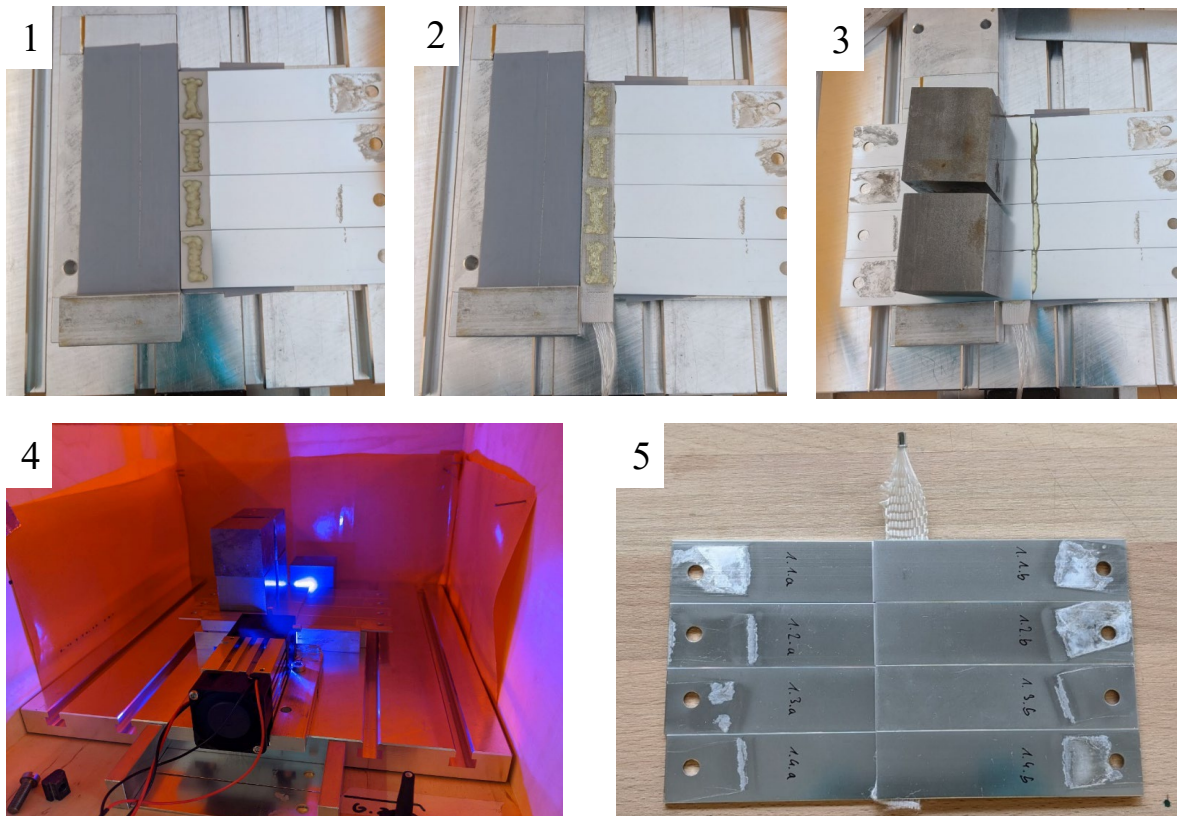


Figure 3: 5-step bonding procedure: 1) the lower joining parts are positioned and the adhesive is applied, 2) the POF fabric is inserted and again an adhesive layer is applied onto the fabric, 3) the upper joining parts are positioned on top and fixed with weights, 4) the fabric is coupled to the light sources and the UV curing is done in a UV tight box (curing time of 5 minutes), 5) the individual adhesion samples are separated and subsequently tested.

A UV meter by Dr. Höhle AG, Gräfelfing, Germany was used to determine the UV intensity of the different fabrics. The aim is to compare the performance of the LED spot lamp and the UV laser diode in combination with the different fabric types. The tensile lap-shear strength was measured with a universal tensile testing machine Z010 by ZwickRoell GmbH & Co. KG, Ulm, Germany according to European norm DIN EN 1465.

Results and Discussion

The target value to be optimized is the achievable shear strength of an overlap bond which is measured and discussed for all four fabric types hereafter. Beforehand, the sidelight intensity of the fabrics as an intermediate parameter with a huge impact on the shear strength [6] is examined using a UV meter.

Optical measurements. The test setup which was used for the optical measurements is shown in Figure 4. The intensity of the emitted UV light was recorded with a measuring head, which is positioned directly beneath the test fabric. For each test fabric, four measuring sections are defined at equidistant intervals of 25 mm which equals the sample width for the adhesive tests later on.

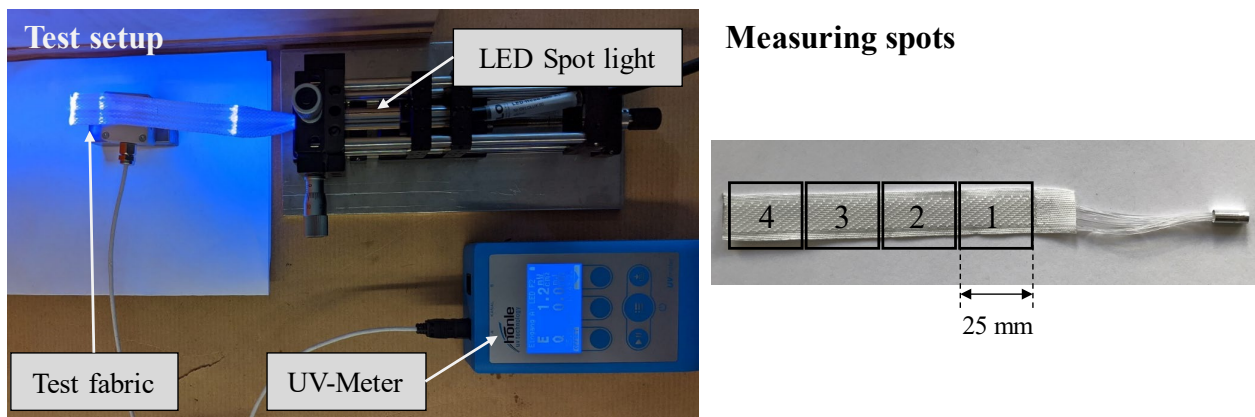


Figure 4: Test setup and measuring spots for determination and comparison of the UV intensity, which is emitted by the different fabrics

The UV meter measurements are shown in Figure 5. The optical intensity is plotted averaged over the four measuring spots. Both sides of the fabrics were measured, indicating that the difference between the top and bottom is negligible which is anticipated since the fabrics are plain weaves. Thus, there is an equal amount of POF on both sides.

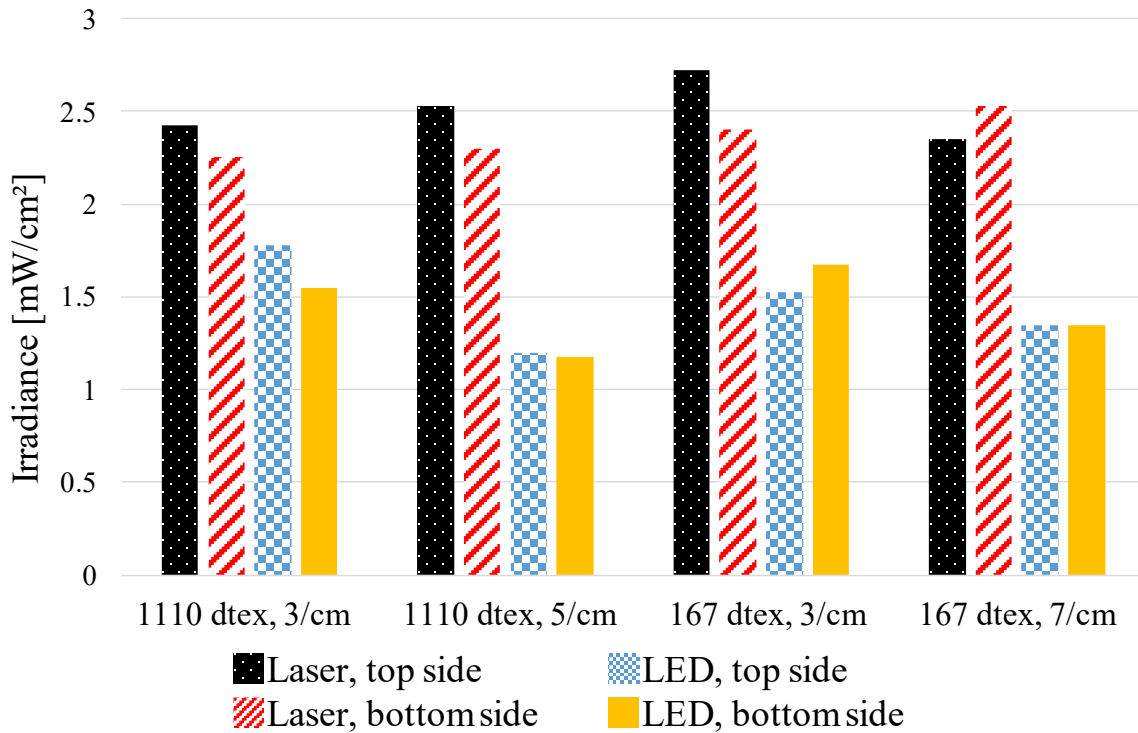


Figure 5: UV measurements of the laterally emitted UV irradiance

With regard to the fabric parameters, the tendency is shown that a lower fineness results in a higher irradiance, which applies to both the weft densities and the light sources. However, a clear statement cannot be made for the weft density, as the results for the two light sources and the two weft threads are different. A reason for this ambiguous characteristic might be an interdependency between both parameters (weft density and weft fineness) so that their individual impact and their combined impact on the irradiance differ due to reciprocal effects between the parameters. A closer look at this parameter has to be taken in the future.

Bonding trials. As second and main evaluation, adhesion tests are carried out as described before and the tensile lap-shear strength is measured. The results of the tensile tests are shown in Figure 6.

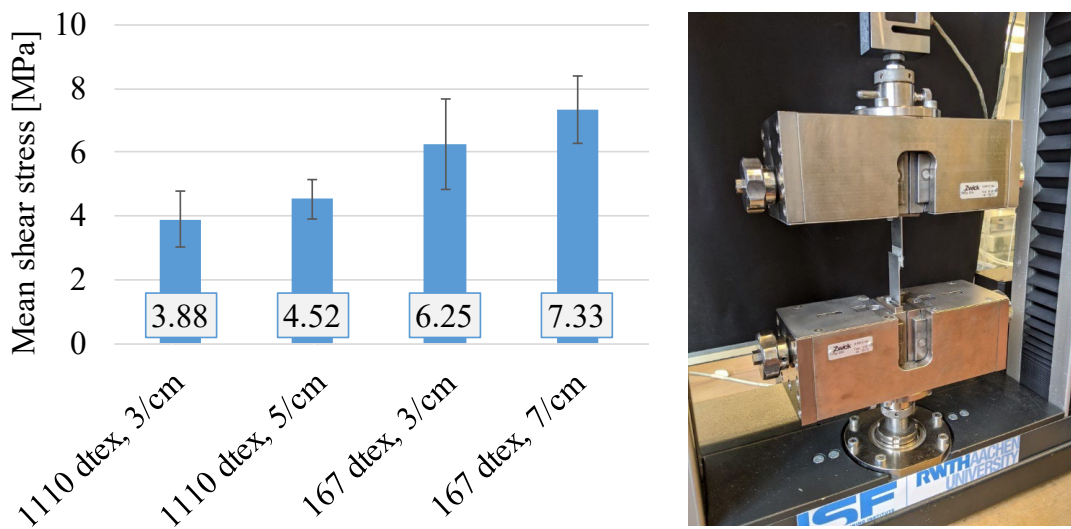


Figure 6: Tensile lap-shear strength measurements and tensile testing machine during a measurement

As described before, the LED spot lamp has been used for the adhesion tests. In accordance with the irradiance measurements, a higher lap-shear strength was measured for the adhesives bonds using

the fabrics with a lower weft fineness and therefore higher irradiance. However, the bonding tests also show that a higher lap-shear strength can be achieved by means of a higher weft density. A higher weft thread density usually can be associated with a higher undulation of fibres in a woven fabric. Thus, the POF are bent more frequently within the same section resulting in a lower bending radius. Both effects (more frequent bends and smaller bending radius) eventuate in a stronger sidelight emittance as the conditions for total internal reflection of the POF are no longer met [14, 16].

Since with lower weft titres higher weft thread densities in the fabric can be achieved (see Table 1) this can also be part of the reason why the weft yarns with lower titres perform better. However, in factor experimental designs, usually only interpolation can be performed, not extrapolation [17]. Since a medium titre of 167 dtex was chosen rather than a low setting of weft fineness, it remains unclear as to whether the positive effect of a low titre on irradiance and lap-shear strength also applies to small titres, e.g., below 50 dtex. In the future, further weaving trials with lower titres need to confirm the trend of the result and might increase irradiance and lap-shear strength.

The fracture patterns in the shear-tension tests show mostly adhesive failure between adhesive and fabric (see Figure 7) which means that the additional adhesive interface weakens the overall strength of the bond when compared to a standard adhesive bond. Possible explanations are too low curing degree and a too high viscosity of the adhesive hindering an impregnation of the fabric. Furthermore, the fracture patterns show that the adhesion on the surface of the textile fabric is weaker than the adhesion on the metallic surface.

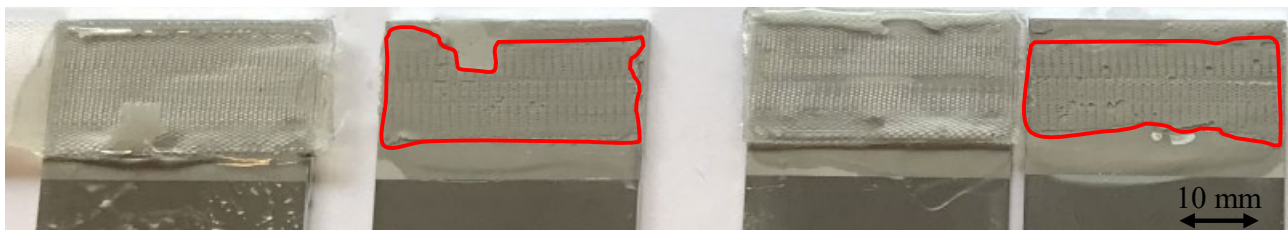


Figure 7: Examples of non-cohesive failure between fabric and adhesive

The irradiance measurements showed that a higher initial optical power also leads to higher irradiances. It is anticipated that a higher irradiance could lead to higher curing degrees of the adhesive in shorter irradiation times as well as to higher final strengths of the bond. This is made plausible by the fact that exposure times with external UV light sources for curing through transparent parts are much shorter (~5–30 seconds, depending on adhesive, adhesive thickness, wavelength, transparency and other parameters) and final strengths are higher. For instance, for the tested adhesive the compressive shear strength is 21 MPa for an adhesive bond between glass and aluminium according to its datasheet [18]. Compressive shear strengths and tensile lap-shear strengths cannot be compared directly with each other, but they are well suited for a quantitative comparison. It can therefore be assumed that further potential can be exploited through further investigations and optimisation of the process.

Another source of higher irradiance can be a higher sidelight efficiency. As stated in the introduction, there is a trade-off between high intensity and high homogeneity of the laterally emitted light. The non-uniform sidelight activation, which is used to enhance the length of homogeneously emitted light intensity, implies that the POF are designed for a certain illumination length. The commercially available sidelight POF show a very homogeneous irradiance over a long distance, but at a low level. Therefore, for future bonding trials the POF are to be sidelight activated for the specific task of high and homogenous irradiance over a length of 150 mm. A subsequent sidelight activation of the fabric after the weaving process is possible, especially surface perforation with various processes, and can simplify the handling and homogeneity [14, 19]. Impairment to the weft yarn must be investigated, especially if particularly fine weft yarns are used.

Summary

Polymer optical fibres are woven into ribbon fabrics with different weft finesses and densities. Irradiance measurements indicate a higher potential for weft yarns with low titre. The POF fabrics are successfully integrated into adhesive joints for external curing. A technological feasibility has been proven. Adhesive bonding trials and subsequent tensile lap-shear measurements confirm the better performance of weft yarns with lower titre and complement a better performance for higher weft densities. Tensile lap-shear strengths of up to 8.3 MPa are achieved. However, mostly adhesive failures occur between adhesive and fabric. This shows that there is still room for improvement in the bond between fabric and adhesive until pure cohesive failures occur and thus, the maximum strength of the adhesive is achieved. Approaches for improvement include finer weft yarns, higher initial optical power of the light source, and higher sidelight activation efficiency so that a greater fraction of the optical power coupled into the POF is emitted laterally to cure the adhesive and finally reduce the curing times.

Acknowledgments:

The presented results were developed during the research project FiberKleb, IGF-No. 20382 N. The project was funded by the Arbeitsgemeinschaft industrieller Forschungsvereinigungen "Otto von Guericke" e.V. (AiF) from funds of the Federal Ministry of Economic Affairs and Energy (BMWi) based on a decision of the German Bundestag and is supported by DVS - Deutscher Verband für Schweißen und verwandte Verfahren e.V. The authors thank the aforementioned institutions for their support.

References

- [1] J. Camillo, What's New With UV-Cure Adhesives, *Assembly* 60 (2017) 34-37.
- [2] A.D. Alobaidani, D. Furniss, M.S. Johnson, Optimization and spectroscopic experiments of cationic epoxy formulations for the application of photocuring of deep resin mediums using side emitting optical fibres, *Proceedings, International Committee on Composite Materials (ICCM) 17*, Edinburgh, Scotland, 2009.
- [3] S. Wellmann, J.d, N. Nuyts, Lichthärtung auch im Schattenbereich, *Adhäsion: Kleben & Dichten* 50 (2006) 29-32.
- [4] R. Søndergaard, M. Hösel, D. Angmo, T.T. Larsen-Olsen, F.C. Krebs, Roll-to-roll fabrication of polymer solar cells, *Mater Today* 15 (2012) 36-49.
- [5] C.-H. Park, S.-J. Lee, T.-H. Lee, H.-J. Kim, Characterization of an acrylic polymer under hygrothermal aging as an optically clear adhesive for touch screen panels, *Int J Adhes Adhes* 63 (2015) 137-144.
- [6] R. Seewald, J. Kallweit, J. Weiland, A. Schiebahn, T. Gries, U. Reisinger, Use of UV-Curing Adhesive Systems on Non-transparent Joining Parts by Using Sidelight Activated Polymer Optical Fibres, in: L. F. M. da Silva, R. D. Adams, C. Sato, K. Dilger (Eds.), *Industrial Applications of Adhesives*, Springer Singapore, Singapore, 2021, pp. 1–14.
- [7] A. Choudhary, E. Prasad, *UV Curable Resin Market by Resin Type (Acrylated Epoxies, Acrylated Polyesters, Acrylated Urethanes, Acrylated Silicones, and Others) and Application (Coating, Packaging, Printing, Adhesives & Sealants, and Others): Global Opportunity Analysis and Industry Forecast, 2019–2026*, first ed., Allied Market Research, Portland, 2019.
- [8] C.-A. Bunge, M. Beckers, B. Lustermann, Basic principles of optical fibres, in: C.-A. Bunge, T. Gries, M. Beckers (Eds.), *Polymer Optical Fibres: Fibre Types, Materials, Fabrication, Characterisation and Applications*, Elsevier, Amsterdam, 2017, pp. 47–118.

-
- [9] S. Kulkarni, Application of polymer optical fibers, in: M. A. Estes, A. C. Faria Ribeiro, S. C. George, A. R. Abraham, A. K. Haghi (Eds.), *Optical and molecular physics: Theoretical principles and experimental methods*, Apple Academic Press Inc., Palm Bay, 2021, pp. 153-174.
- [10] J. Zubia, J. Arrue, Plastic Optical Fibers: An Introduction to Their Technological Processes and Applications, *Opt. Fiber Technol.* 7 (2001) 101–140.
- [11] H. Pan, Introduction: Why Plastic Optical Fibers, in: M. M. Werneck, R. C. da Silva Barros Allil (Eds.), *Plastic Optical Fiber Sensors: Science, Technology and Applications*, CRC Press, Boca Raton, 2019, pp. 1-20.
- [12] J. Spigulis, Side-Emitting Fibers Brighten Our World, *Opt. Photon. News* 16 (2005) 34–39.
- [13] V. Koncar, Optical Fiber Fabric Displays, *Opt. Photon. News* 16 (2005) 40–44.
- [14] J. Kallweit, M. Pätz, F. Pursche, J. Jabban, M. Morobeid, T. Gries, An Overview on Methods for Producing Side-Emitting Polymer Optical Fibers. *Textiles* 1 (2021) 337-361.
- [15] G. Habenicht, *Kleben: Grundlagen, Technologien, Anwendungen*, 6th ed., Springer-Verlag Berlin Heidelberg, 2009.
- [16] J. Wang, B. Huang, B. Yang, Effect of weave structure on the side-emitting properties of polymer optical fiber jacquard fabrics, *Text. Res. J.* 83 (2013), 1170–1180.
- [17] R. H. Myers, D. C. Montgomery, C. M. G. Anderson-Cook, *Response Surface Methodology: Process and Product Optimization Using Designed Experiments*, 4th ed., John Wiley & Sons, Hoboken, 2016.
- [18] DELO Industrie Klebstoffe GmbH & Co. KGaA, Technical Datasheet: DELO® PHOTOBOND® FB4175, as of 27.07.2020.
- [19] J. Shen, C. Chui, X. Tao, Luminous fabric devices for wearable low-level light therapy, *Biomed. Opt. Express* 4 (2013), 2925–2937.

Emi Shielding of the Copper/Nickel-Coated Polyester Nonwoven

Sundaramoorthy Palanisamy^{1,a*}, Veronika Tunakova^{1,b}, Yuanfeng Wang^{1,c},
Daniel Karthik^{1,d} and Jiri Militky^{1,e}

¹Department of Material Engineering, Faculty of Textile, Technical University of Liberec, Liberec
46117, Czech Republic.

^asundaramoorthy.palanisamy@tul.cz, ^bveronika.tunakova@tul.cz, ^cyuanfeng.wang@tul.cz,
^ddaniel.karthik@tul.cz, ^ejiri.militky@tul.cz

Keywords: Electromagnetic radiation, ultrathin nonwoven, shielding effectiveness, copper/nickel coating, strips.

Abstract. Electric and electronic devices are mainly emitting electromagnetic radiation, and shielding from radiation is essential. Electrically conductive materials are suitable for radiation shielding applications. The designing of the textile material for the radiation shielding is challenging because of its open area and design. In general, more open area has transmit the radiations tend to lesser in shielding. Another factor is the laying angle of the textile material also plays important role beyond open area. In this study, the effect of laying angle and open area was analysed for effective utilization of conductive materials. The conductive nonwoven fabric was used to form as strips to simulate the various textile structures for shielding application. The Cu/Ni coated ultrathin polyester nonwoven fabric sample is taken to form two-layers strips and test for electromagnetic shielding effectiveness. In experimental design, three factors of strips which are strips laid angle, strip thickness, and gap between the strips are taken at three levels. The strip cover area and aperture area were calculated geometrically for each design and significant difference on shielding effectiveness was noticed.

Introduction

This world is full of radiations; most of the radiations are under electromagnetic (EM) waves categories. There are seven categories in the EM spectrum: low frequency, radiofrequency, microwaves, infrared, ultraviolet, x-rays, and gamma cosmic rays[1]. In the range of radiofrequency to microwaves categories, most electronic devices like FM radios, wireless devices, computers, mobile phones, microwave ovens, and remote controls are functioning[2]. Electronic devices emit EM radiation due to their work functions and cause EM interference (EMI). EMI is disturbing the function of electronic devices, and sometimes it damages the electronic parts; some studies say that it is harmful to living beings (mainly birds are affected by cell phone towers)[3]. It's impossible to avoid EM radiations due to their requirement in day-to-day life, so shielding is the efficient method to protect electronic devices and living beings from EM radiations[4].

EM shielding is possible with reflection and absorption of the EM waves[5]. Most electrically conductive materials like copper, silver, gold, aluminum, iron, steel, nickel, carbon, graphite, and intrinsically conductive polymers reflect and absorb the EM waves [6]. EM shielding with textile materials is developing nowadays because of its flexibility, high strength, wearability, feasibility to develop any design, and lightweight. Conventional textile materials are non-conductive and need to impart conductive material coating or fibers blending to make them conductive materials [7]. The textile woven structures with different grid size of conductive yarn is formed and studied for electromagnetic shielding. It was noticed that the grid open area has affecting the shielding effectiveness [8].

In this work, the copper/nickel-coated polyester nonwoven fabric was taken and form as strips at different open areas. The different open area was formed by changing the strips laid angle, strips thickness, and gap between the strips. Developed strips samples are studied for EM shielding effectiveness (SE) as per ASTM standard and analyzed its EM SE concerning the open area.

Materials and Methods

Nonwoven Material. The Cu/Ni coated polyester cross-laid nonwoven (Cu-Ni NW) sample procured from BOCHEMIE a.s., Bohumin, Czechia, and its parameters are given in Table 1.

Table 1. Cu/Ni NW fabric parameters and their values.

Parameters	Values
GSM [gram per sq. meter]	24.56 ± 2.69
Thickness [mm]	0.087 ± 0.006
Tensile strength in MD [N/50mm]	25 [9]
Tensile strength in CD [N/50mm]	16 [9]
Surface resistivity [Ω]	2.1 ± 0.28

Sample Preparation and Coding. The Cu-Ni NW sample was cut to prepare the strips at 3-, 6-, and 9 mm thick. It was arranged in plain paper (sticking on paper with cello tape) at 3-, 6-, and 9-mm gaps between the strips to form a single layer sheet. The two single layer sheets was laid on each other at different angles to form double layer. The double layer of the 9 mm thick strips at a 3 mm gap between the strips laid at 0° , 45° , and 90° angles as shown in Figure 1. The graphic design was created with the help of CREO® CAD software (see fig. 1). Like-wise 9 mm thick strips, the 3- and 6 mm thick strips were arranged at three levels of laid angle and three levels of gap between the strips which codings are given in the table 2.

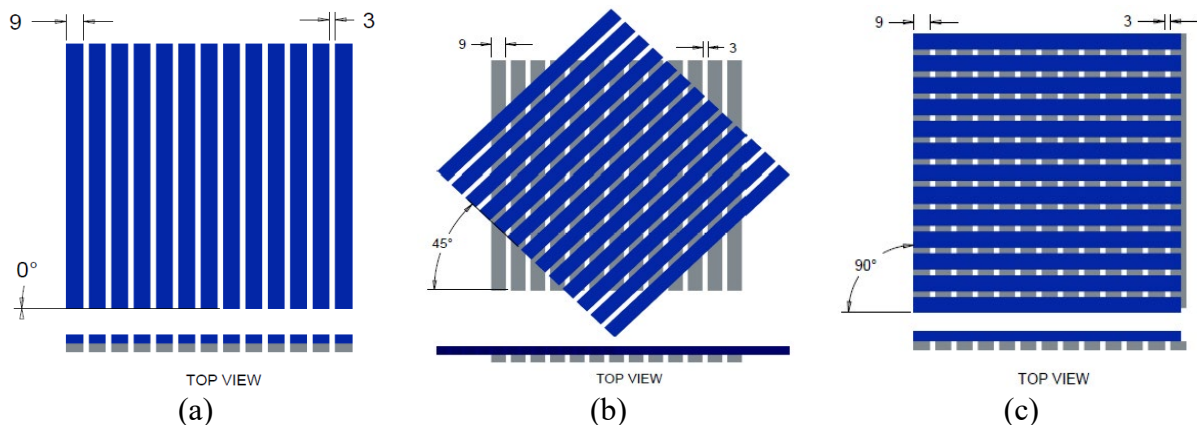


Figure 1. The graphic image of two-layer Mc Cu/Ni NW strips of 9 mm thickness arranged at 3 mm gap and laid at (a) 0° (TL30), (b) 45° (TL345), and (c) 90° (TL390), angles.

Table 2. Arrangement of the two layers of 9 mm thick strips and its sample codes.

The angle between the two layers	The gap between the strips in a single layer	Strip thickness		
		3 mm	6 mm	9 mm
0°	3 mm	TS30	TM30	TL30
	6 mm	TS60	TM60	TL60
	9 mm	TS90	TM90	TL90
45°	3 mm	TS345	TM345	TL345
	6 mm	TS645	TM645	TL645
	9 mm	TS945	TM945	TL945
90°	3 mm	TS390	TM390	TL390
	6 mm	TS690	TM690	TL690
	9 mm	TS990	TM990	TL990

EM SE Test Method. The electromagnetic shielding effectiveness (EM SE) of the sample set was measured according to the ASTM D4935-18 [10], for the planar materials using a plane-wave, the far-field EM wave at the temperature $T = 21^\circ\text{C}$, and the relative humidity $\text{RH} = 54\%$ [11]. SE of the samples was measured over the frequency range of 30 MHz to 1.5 GHz. The set-up consisted

of a sample holder connected to the network analyzer with its input and output [12]. A shielding effectiveness test fixture (Electro-Metrics, Inc., model EM-2107A) was used to hold the sample. The design and dimension of the sample holder follow the ASTM method mentioned above.

Cover Area and Aperture Area Calculation. The strip cover area and the aperture areas of the samples are calculated from the design created with the help of CREO® CAD software. The measured areas are theoretical values calculated geometrially with help of CAD software.

Results and Discussion

EMSE versus Frequency. The EM SE of Cu/Ni NW fabric and its strips samples are tested with the coaxial transmission line method as per ASTM standard [10], and the results are shown in figure 2.

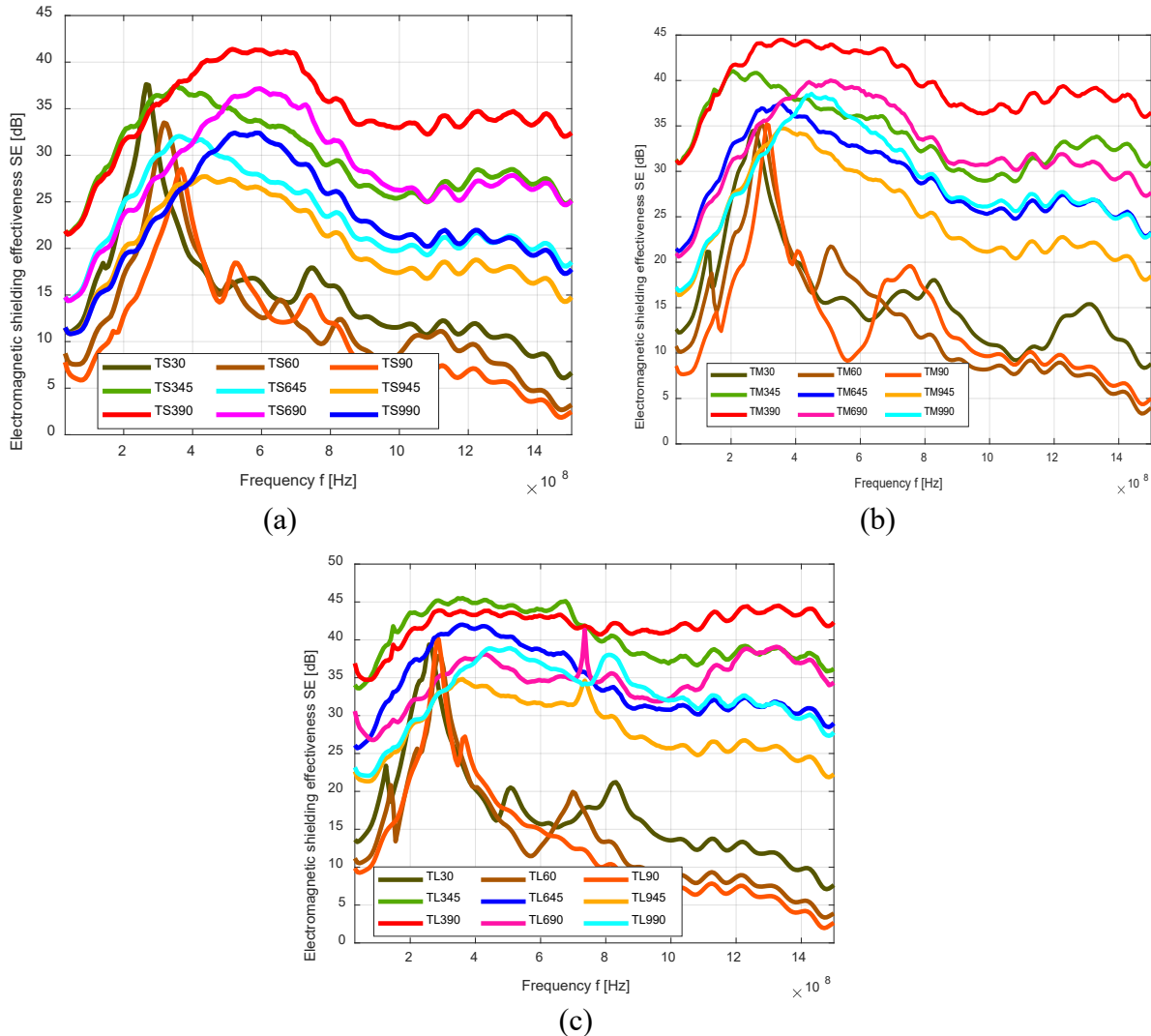


Figure 2. Frequency (30 MHz~1.5 GHz) versus EM SE in dB of the two-layer Cu-Ni NW strips at the thickness of (a) 3mm, (b) 6 mm, and (c) 9 mm.

All the samples were tested from 30 MHz to 1.5 GHz frequency, and the SE is shown in dB. Cu/Ni NW samples made of 3 mm thick strips were prepared of two-layers (TS) using various gaps between strips as well as various laying angles, and their SE [dB] versus frequency graph is shown in figure 2(a). From this graph, the SE is increasing with increasing angles and a decrease in the gap. All the two-layer strip samples show that the SE is increasing steeply to the frequency range of 400 – 600 MHz, where the global maximum of SE (from 27 to 42 dB for all TS samples) is observable. The arrangement of two layers of 6 mm thick strips (TM) SE versus frequency results are in figure 2(b). SE of the samples increases from 30 MHz – 300 MHz frequencies and then slowly decreases until 1.5 GHz frequency. The global maximum of SE for all samples is located (SE = 35 – 45 dB). Another peak of SE is formed between 1.2 GHz to 1.35 GHz frequency, and it

has an SE of 9 – 40 dB range. When studying the highest frequency (1.5 GHz), SE is in the range from 18 to 37 dB. In figure 2(c) shows the SE versus frequency graph for 9 mm thick strips of Cu/Ni NW sample of two-layers (TL). Observing the SE frequency dependence, SE is steeply increasing from the starting frequency till the 200 – 450 MHz, where the global maximum of SE for all samples is located (SE = 37 – 46 dB). Another peak of SE is formed between 980 MHz to 1.25 GHz frequency, and it has SE of 18 – 35 dB range. When studying the highest frequency (1.5 GHz), SE is in the range from 22 to 42 dB. The samples laid at 0° angle show significantly less SE from 300 MHz – 1.5 GHz because of disconnection between the strips layer. The connection between the layers of the strip has a higher SE.

Cover Area versus SE. The calculated strips cover area (A_c) versus SE at 1.5 GHz of the samples are given in figure 3. The strip cover area (A_c) increases with the increase in the laid angle of the strips; also, an increase in SE is noted with an increase in A_c . The gap between the strips decreases the A_c and SE. Figure 3(a) shows the A_c versus SE at 1.5 GHz of 3 mm thick strips, linear regression analysis showing that the A_c has a high correlation with SE and its coefficient of determination (R^2) is higher than 0.96. Maximum SE of 32 dB is achieved at 75% A_c . The 6 mm, thick strips samples show excellent R^2 of > 0.97 value for 45° and 90° laid angle samples, but R^2 is 0.7 for 0° laid angle. So the correlation between the A_c and SE is excellent at higher laid angles. Maximum SE of 36 dB is achieved at 88% A_c . In figure 3(c), the correlation between the A_c and SE is excellent; R^2 is greater than 0.96 for all the laid angles. A maximum SE of 42 dB is achieved at 94% A_c . In common, the A_c value for 45° and 90° degree laid angle at different distances is the same, but the SE values are higher for 90° laid angle samples. The area per aperture was calculated to identify the difference in SE value for the same cover area, and the results are analyzed below.

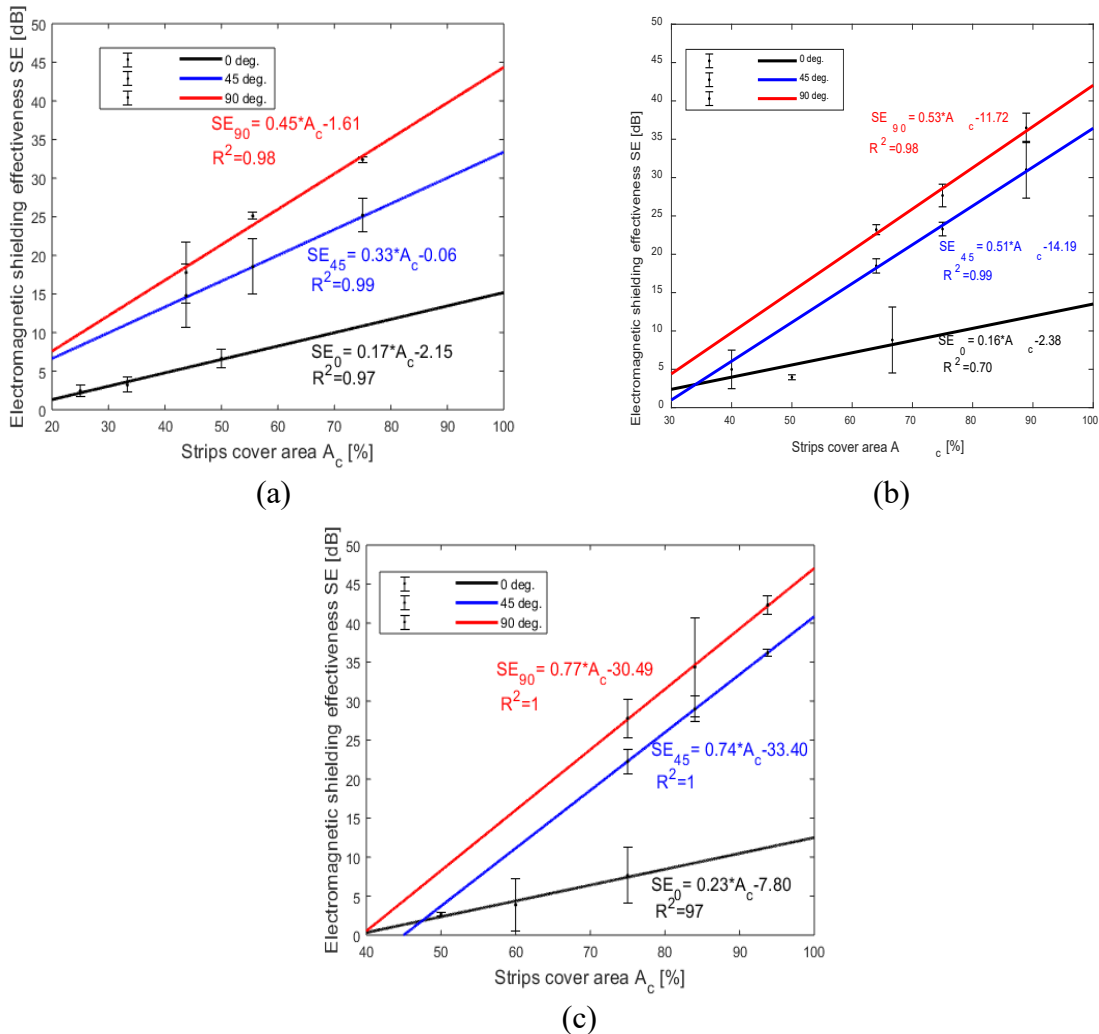


Figure 3. Strips cover area (A_c) versus EM SE in dB versus frequency (30 MHz to 1.5 GHz) of the two-layer Cu-Ni NW strips at the thickness of (a) 3mm, (b) 6 mm, and (c) 9 mm.

Area per Aperture versus SE. The area per aperture (A_a) was calculated geometrically by identifying one repeat of the design. The A_a increase decreases the SE (at 1.5 GHz) values, as clearly seen in figure 4—also, the increase in the angle of laying decreases the A_a . Figure 4(a) shows that the 'TS' series of samples' SE value decreases with an increase in A_a ; the maximum SE (1.5 GHz) of 32 dB is recorded at A_a of 10 mm². The 'TM' series of samples' SE values decrease with an A_a increase, as shown in figure 4(b). Maximum SE of 36 dB at 1.5 GHz frequency was recorded for 10 mm² A_a . Also, SE values are decreased with an A_a increase for the 'TL' series of samples, as seen in figure 4(c). Maximum SE of 42 dB at 1.5 GHz frequency was recorded for 10 mm² A_a . In general, the 0° laid angle has very little SE because of disconnection between the strips. The 3 mm gap and 90° laid angle ('390' series) have the highest SE value and lowest A_a values, which also has higher A_c among all samples.

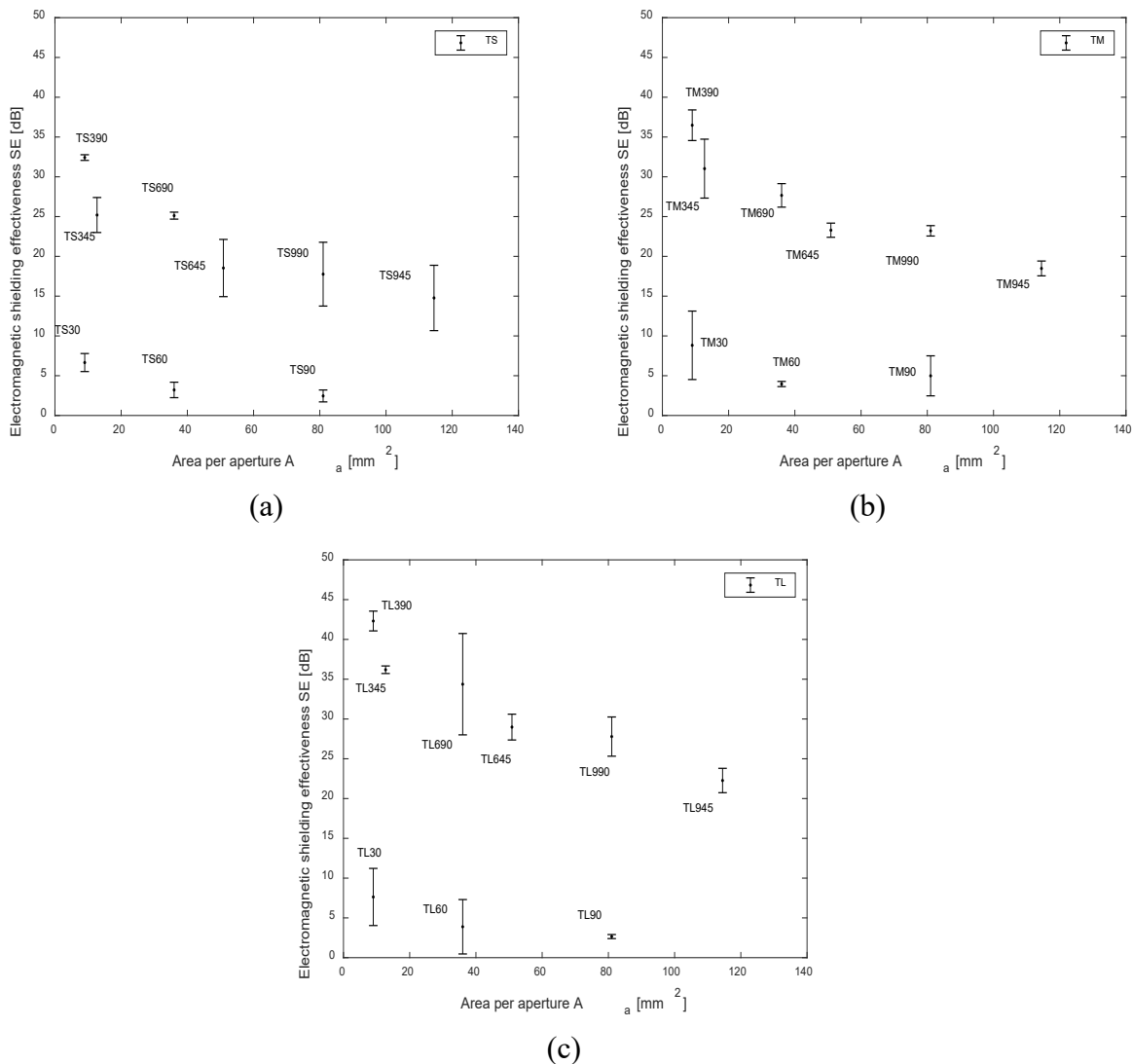


Figure 4. Area per aperture (A_a) versus EM SE in dB versus frequency (30 MHz to 1.5 GHz) of the two-layer Cu-Ni NW strips at the thickness of (a) 3mm, (b) 6 mm, and (c) 9 mm.

Summary

The Copper/Nickel coated 100% polyester cross-laid nonwoven fabric was taken in this study. Among TL samples, TL390 exhibits the highest SE of 42 dB at 1.5 GHz frequency. The EM SE (at 1.5 GHz frequency) is increasing with an increase in percent strips cover area (A_c) for the TL samples; A linear correlation between A_c and EM SE has been found ($0.98 \leq R^2 \leq 1$). A maximum A_c of 94% for TL3 series samples and recorded the highest SE value. An increase in area per aperture (A_a) of the TL samples has decreased in EM SE value. TS and TM samples also exhibit SE

of 32 dB and 36 dB at 1.5 GHz frequency with 75% and 88% strip cover area. An increase in strip cover area and decreases in area per aperture have increased the SE values. Hence, the highest shielding effectiveness is the two-layer strips with a 90° laid angle and 3 mm gap. The higher A_c and lower A_a also exhibit the higher SE. The interconnection between the conductive layers also improves the SE. This design will be helpful to achieve efficient material usage for preparing the samples for electromagnetic applications.

Acknowledgment

This work was supported by the project Hybrid Materials for Hierarchical Structures [HyHi, Reg. No. CZ.02.1.01/0.0/0.0/16_019/0000843] and also supported by the 'Student Grand Competition' project number: SGS-2021-6008.

References

- [1] R.B. Schulz, V.C. Plantz, D.R. Brush, Shielding theory and practice, IEEE Trans. Electromagn. Compat. 30 (1988) 187–201.
- [2] H.W. Ott, Electromagnetic Compatibility Engineering, John Wiley & Sons, Inc., Hoboken, NJ, USA, 2009.
- [3] J.C. Lin, ed., Electromagnetic Fields in Biological Systems, Taylor & Francis Group, Boca Raton, Florida, USA., 2012.
- [4] F.S. Barnes, B. Greenebaum, eds., Bioengineering and Biophysical Aspects of Electromagnetic Fields, Third, Taylor & Francis Group, Boca Raton, Florida, USA., 2006.
- [5] K. Lai, R.J. Sun, M. Yu Chen, H. Wu, and X. Zha, Electromagnetic Shielding Effectiveness of Fabrics with Metallized Polyester Filaments, Text. Res. J. 77 (2007) 242–246.
- [6] S. Palanisamy, V. Tunakova, J. Militky, Fiber-based structures for electromagnetic shielding – comparison of different materials and textile structures, Text. Res. J. 88 (2018) 1992–2012.
- [7] M. Tian, M. Du, L. Qu, S. Chen, S. Zhu, G. Han, Electromagnetic interference shielding cotton fabrics with high electrical conductivity and electrical heating behavior: Via layer-by-layer self-assembly route, RSC Adv. 7 (2017) 42641–42652.
- [8] V. Šafářová, J. Militký, Electromagnetic shielding properties of woven fabrics made from high-performance fibers, Text. Res. J. 84 (2014) 1255–1267.
- [9] MEFTEX 20, BOCHEMIE a.s, Czech Republic. (2020). <https://www.meftex.cz/en/meftex-20/p-3/> (accessed October 1, 2020).
- [10] ASTM D4935-10, Standard Test Method for Measuring the Electromagnetic Shielding Effectiveness of Planar Materials, West Conshohocken, PA, 2010.
- [11] B.P. Saville, Physical testing of textile, Woodhead publishing limited, England, Cambridge, England, 1999.
- [12] S. Geetha, K.K.S. Kumar, C.R.K. Rao, M. Vijayan, D.C. Trivedi, EMI shielding: Methods and materials-A review, J. Appl. Polym. Sci. 112 (2009) 2073–2086.

Flexible Textile Printed Piezoresistive Pressure Sensors

E. Oßwald^{2,a}, H. Carvalho^{1,b*}, I. Cabral^{1,c}, A.P. Souto^{1,d}, A. Cunha^{1,e}

¹Univ. of Minho, Centre for Textile Science and Technology, Guimarães, Portugal

²Reutlingen University, Department of Textil & Design, Reutlingen, Germany

^aelena.osswald1@googlemail.com, ^bhelder@det.uminho.pt, ^cdiascabral@gmail.com,
^dsouto@det.uminho.pt, ^eanacunha98.ac@gmail.com

Keywords: Sensors, piezoresistive, smart textiles, pressure sensors, flexible sensors

Abstract. The combination of sensor technology and textiles substantially extends the range of textile applications. Smart textiles, especially clothing, might increasingly be equipped with pressure sensors. They could be used in the sports or health sector to measure body activities or other activities which are close to the body. Therefore, it is essential to develop flexible sensors which allow to adapt to the properties of textile materials which are in contact with the body or surrounding it. In this paper a pressure sensor based on piezoresistive ink and conductive fabric with high flexibility is reported. Preliminary pressure sensors have been fabricated and tested on a universal testing machine. The sensors show to be functional, but also showing some aspects to improve, such as its hysteretic behaviour.

Introduction and State-of-the-Art

One of the methods for manufacturing a textile piezoresistive pressure sensor is based on a 3-layer structure. The outer layers form the electrodes through which the electrical conditioning circuit is connected. A conductive, moreover piezoresistive layer is placed between the electrodes. A piezoresistive material is able to change its electrical resistance if pressure is applied to it. The variations of resistance in the piezoresistive layer are proportional to the pressure applied on it, and thus an appropriate signal conditioning circuit is able to convert these variations into an electrical signal. Figure 1 shows a setup in which the inner layer is a polymeric piezoresistive film [1].

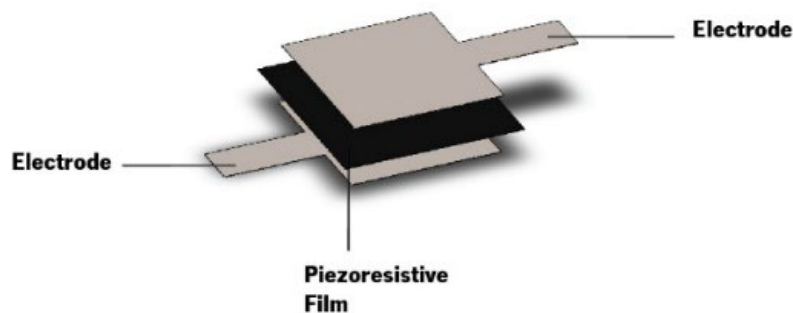


Figure 1. Construction of the flexible pressure sensors [1]

To realize the pressure sensitive layer, several piezoresistive materials can be used, which are able to change their resistance under mechanical deformation. To obtain a piezoresistive textile, various conductive materials are applied on textile fabrics or fibers, such as carbon nanoparticles [2], metallic nanoparticles or nanowires [3] and conductive polymers [4].

A piezoresistive material can be made out of conductive nanoparticles which are placed in a matrix of non-conductive polymer. When pressure is applied to this material, the particles move closer together and thus resistance between the electrodes decreases as the current is conducted more easily through the particles, which is explained in Figure 2 [5].

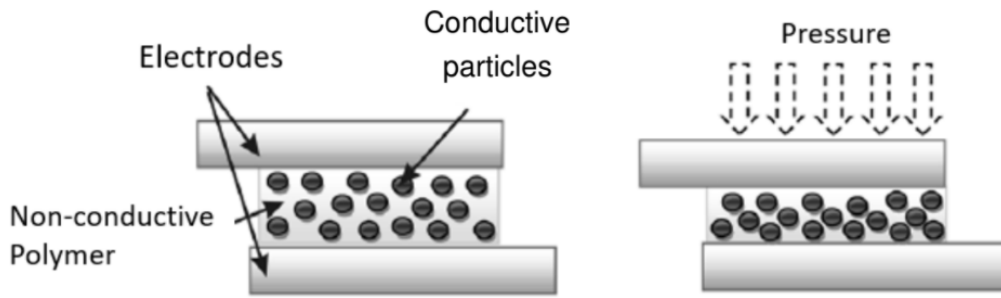


Figure 2. Functionality of the piezoresistive effect [5]

One of the most known and utilized materials is Velostat by 3M. It is a common piezoresistive material, which consists of a carbon loaded polymeric foil [4]. In [6], a setup using Velostat with silver-plated woven polyamide fabric is described. Earlier work [1] has been presented using this setup, as well as copper film and knitted polyamide silver-plated fabric as electrodes. In [7] a similar configuration using copper fabric and Velostat is described. The EeonTex fabric produced by EEONYX has revealed piezoresistive properties as well. In [8], a pressure sensing matrix using this fabric as piezoresistive layer and striped copper-based conductive fabrics to form the electrode matrix have been proposed.

Another possibility of producing pressure sensor using piezoresistive materials is using interdigitated electrodes, as shown in Figure 3 [6]. In this case, conduction is made between electrodes places on the same plane, as opposed to conduction in the z direction that occurs in the previously presented works.

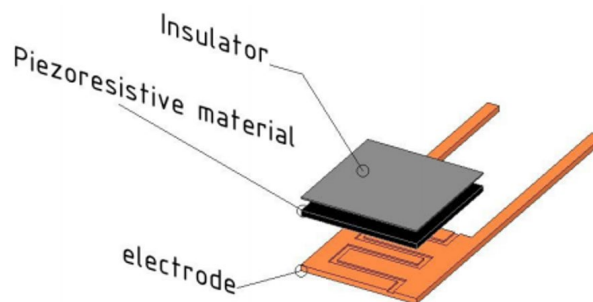


Figure 3. Piezoresistive sensor using interdigitated electrodes [6]

In this work, conductive fabrics are used combined with a piezoresistive ink printed on cotton fabric using a screen-printing process. To achieve a mechanical stability between layers of the sensor, a net-shaped adhesive is used between layers. This should allow achieving stable performance of the sensor even in sensors with larger areas.

Materials and Methods

In this work, piezoresistive ink from Nanopaint, commercial name PR 2, is printed on a cotton plain weave to achieve a piezoresistive layer. First tests showed that the piezoresistive sensor exhibits very low resistance after a certain level of applied force, which makes signal conditioning tricky in these ranges. For this reason, a non-conductive additive provided by Nanopaint, with the intention of increasing resistance values and thus measurement ranges, was used in some experiments.

As studied in [9], woven structures result in more stable sensors regarding reproducibility and dynamic properties of the measured signals, when compared to knitted structures. Therefore, a plain weave is used as first choice for this work. Cotton is chosen as material due to its thermal stability, considering that the printing and bonding processes to which the material is subjected induce some

thermal stress that should not impair the original fabric properties. The fabric has been tested and has the following properties

Table 1. Properties of fabric used for printing of piezoresistive layer

Property	Value	Test method
Yarn fineness	Warp: 19,5 tex Weft: 21 tex	DIN EN ISO 2060:1995-04
Thickness	0,54 mm	DIN EN ISO 5084
Mass per unit area	116,2 g/m ²	DIN EN 12127
Weave density	Warp: 30 threads/cm Weft: 25 threads/cm	DIN EN ISO 1049-2

The application of the piezoresistive ink on the textile is accomplished by screen-printing. Before using, the ink is subjected to mechanical stirring between 30-60 minutes. It is at this time that the additive is mixed with the ink, in various mixture ratios.

A screen with the mesh size of 81 Threads Per Inch (TPI) is used. Samples were screen printed on a Zimmer Mini MD-F R541, a flat screen-printing table with a magnetic system that allows the rolling of a metallic rod-squeegee over the screen, applying the ink at an even pressure, as shown in Figure 4. The magnetic field level can be chosen from a range of 1 to 6, low to high pressure respectively, therefore affecting the ink's layer thickness. The dimensions of the printed sensors are 3 x 3 cm.

The economical screen-printing process is perfectly qualified for the production of mass articles. The opportunities for designs are unlimited and the textile properties remain unchanged by screen printing. Screen printing is considered a direct printing process because the ink is applied directly to the textile through the screen, as can be seen in Figure 4.

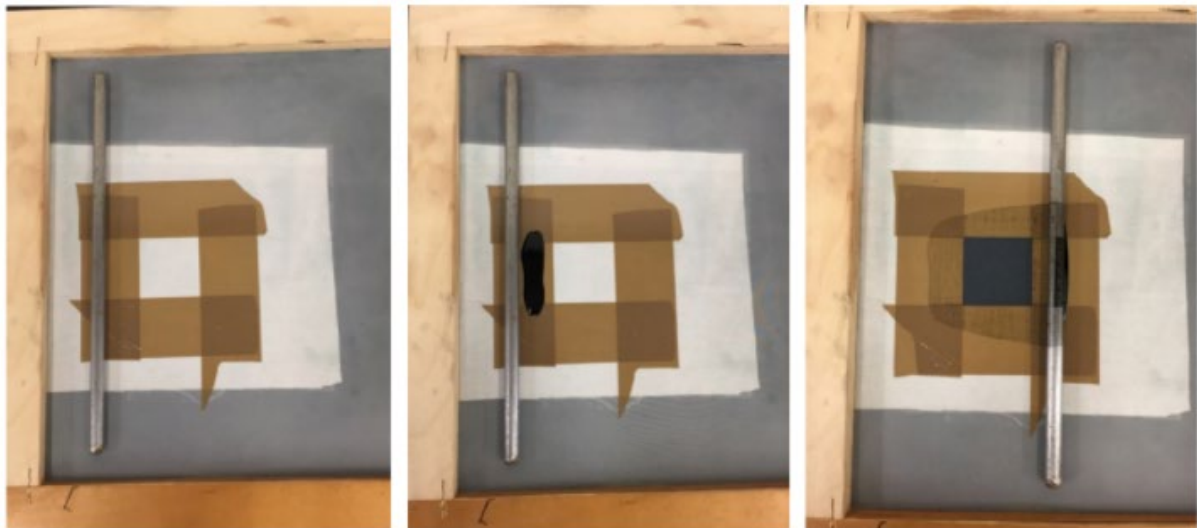


Figure 4. Printing the piezoresistive ink on the cotton fabric

After printing, the ink has to be cured in an oven for 10 minutes at 60°C.

To allow the electrical connection to the piezoresistive layer a silver-plated woven nylon fabric (Statex Bremen from Shieldex) is proofed to be functional as an electrode material. The woven silver fabric has high conductivity and is extremely flexible, fully preserving the textile properties required in this work.

In order to stabilize the assembly of fabrics, the individual layers should be joined in some way. With the use of the silver-plated conductive fabric, however, joining the layers by sewing is not functional. By stabbing the fabric with a needle, individual threads can be damaged and pulled through the seam hole to the other side. This causes a short circuit between the electrodes.

To overcome this problem, a thermoplastic bonding net, UT1 from Protechnic, shown in Figure 6, is used to bond the silver fabric and the cotton together. The material is non-conductive. However, as it is in a net shape, there is still electrical contact between the electrodes and the ink, which is fundamental for the sensor to work. The electrode fabric layers must be smaller than the middle layer in order to avoid a short circuit. The bonding net consists of polyurethane ester aliphatic which is very elastic and transparent. This thermoplastic bonding net, therefore, is supposed to have an excellent bonding on TPU, PVC, polyamide, polyester, fabrics and leather. Since the material for the electrodes is based on polyamide and the piezoresistive ink is printed on cotton fabric, this bonding material promises to be quite suitable for this application.

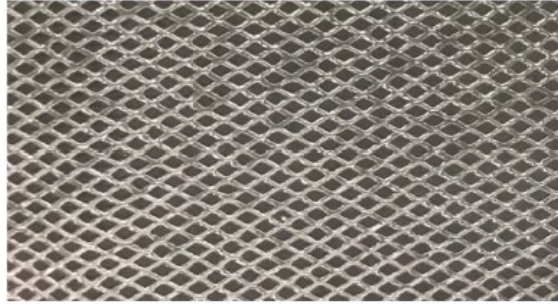


Figure 6. Thermoplastic bonding net

For bonding the 3 layers of the sensor the bonding net is placed on both sides of the piezoresistive layer and pressed in a heating press at 110°C for 10 seconds at a pressure of 2.5 bar (Figure 7). Although the melting point of the thermoplastic net is reached at lower temperature, a sufficient cross-linking is only achieved with the mentioned settings.

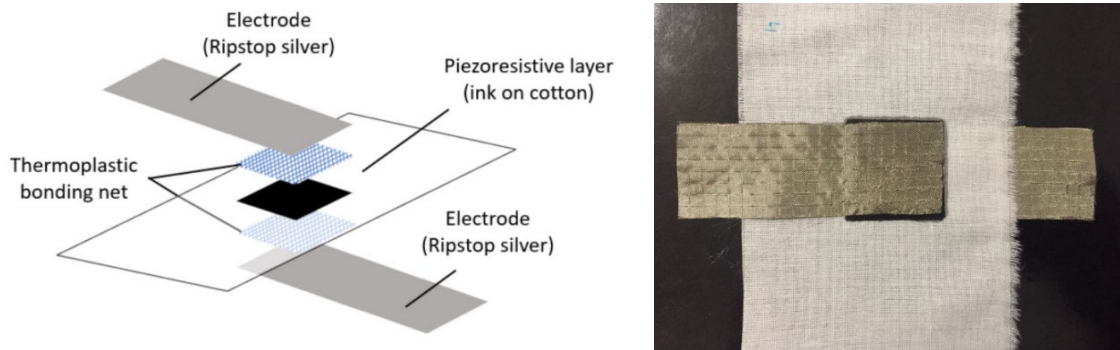


Figure 7. Exploded view of the sensor (left) and sensor (right)

Using the described materials, sensors are manufactured and tested in the further course. During the manufacturing process, different parameters such as piezoresistive ink layer thickness are varied in order to gain knowledge about the design showing the best functionality.

The fastest way to test the sensors for simple functionality is to use a multimeter to which the electrodes are connected, and the resistance is measured. This enables immediate determination of whether sensors are functional by changing their resistance as soon as pressure is applied. If this does not happen and the resistance is close to 0 or remains the same when pressure is applied, it indicates that the sensor is not functional, and a short circuit probably occurred. For more detailed and significant measurements, the Hounsfield universal testing machine is used. This method is used to test the behavior of the sensor when a force is applied in a cyclic process, shown in Figure 8.

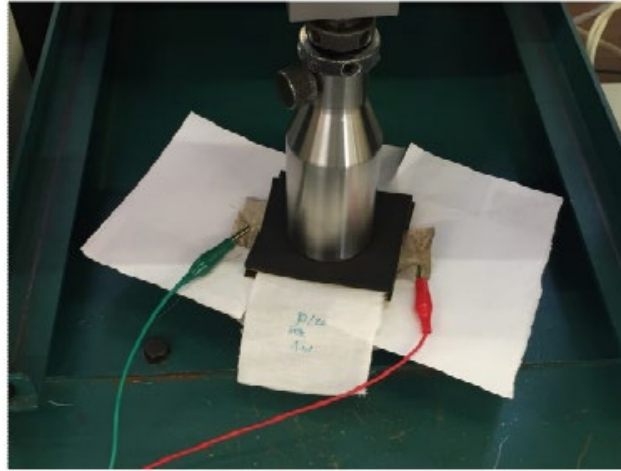


Figure 8. Setup for compression test

The printed pressure sensor is subjected to a cyclic compression test in a Hounsfield universal testing machine. To protect the sensor and the equipment from mechanical impairment during the test, as well as to distribute pressure evenly over the surface of the sensing area, a layer of 3 mm EPDM (ethylene propylene diene monomer rubber) is placed on each side of the sensor.

The machine is equipped with a movable traverse with adjustable speed. For the compression test, a 2.5 kN force cell and a compression stamp are attached on the bottom of the traverse. As a counterpart a fixed plate is used on the bottom of the machine on which the sensor is placed. By connecting the electrodes to a multimeter or to the sensor signal conditioning equipment, the sensor is tested using a speed of 30mm/min and force ranges between 0 to 200N. Resistance is measured by a multimeter connected to a PV via RS-232, whilst the signal conditioning circuit described in Figure 9 outputs a voltage that is acquired with a data acquisition board (DAQ) and software developed in LabVIEW. The output voltage depends on the resistance R and on the sensor's resistance R_s (Figure 9).

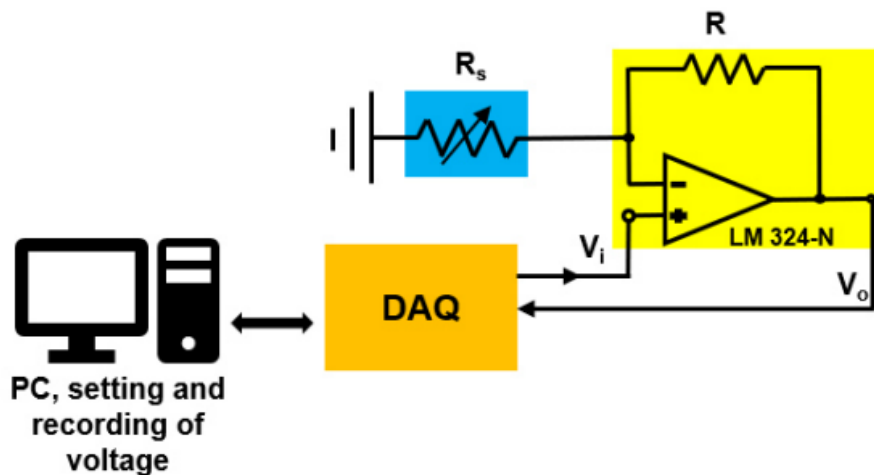


Figure 9. Conditioning circuit for the piezoresistive sensors, implemented with a non-inverting amplifier with gain dependent on the sensor resistance R_s

The relation between the sensor's resistance (R_s) and the voltage output (V_o) for the circuit used is expressed by equation 1:

$$V_o = V_i \left(1 + \frac{R}{R_s}\right). \quad (1)$$

with

V_o : Output voltage (V)

V_i : Input Voltage (V)

R_S : Sensor resistance (Ω)

R : Feedback resistance (Ω)

The force is recorded by the Universal testing machine, voltage and force signals are later synchronised in the developed Labview software.

Results and Discussion

The first result obtained is that of resistance versus force, depicted in Figure 10.

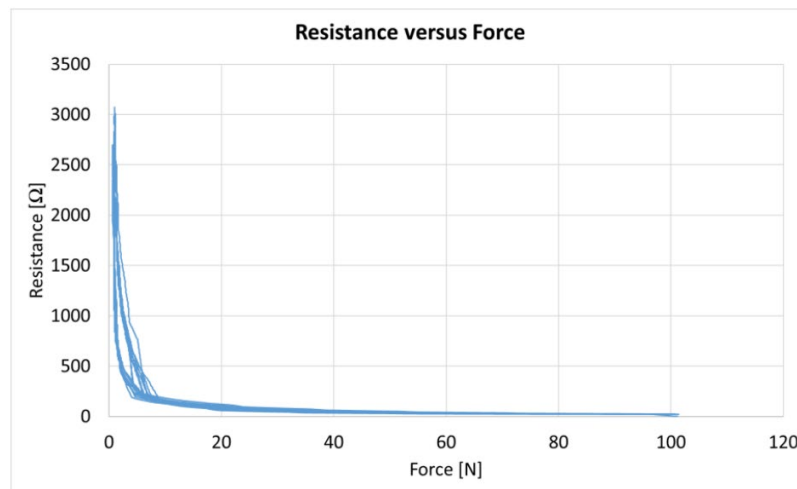


Figure 10. Characteristic of resistance versus force in a cyclic test

As can be observed, the characteristic is highly non-linear, and sensitivity is much higher at low forces than at higher ones. The processing of these variations becomes much easier when the sensor is connected to the signal conditioning circuit and output voltage is measured. The transfer function of the circuit, when applied to the characteristic that can be observed in Figure 10, has the ability to linearize the force-output voltage relation to a certain extent. A typical relation is shown in Figure 11.

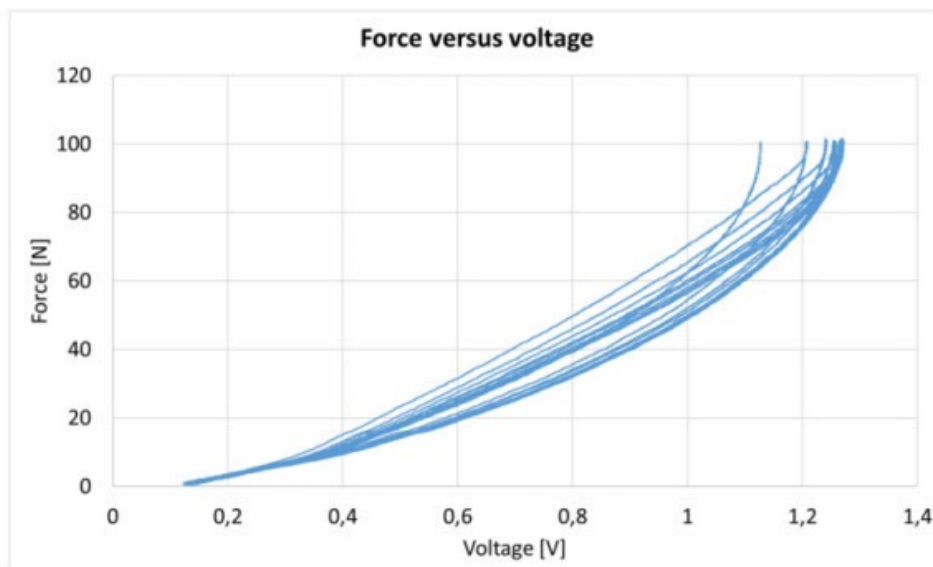


Figure 11. Force-Voltage diagram

Although the sensor is functional, it shows some hysteresis during the cyclic compression test, which is marked in red in Figure 12. In general, hysteresis is a phenomenon in physical systems, which describes that a physical property, caused by a change of another variable, is delayed. In addition, the output variable is not only dependent on the input variable, but also on the previous state of the output variable. In this case, a reason why the hysteresis appears, could be that the sensor layers do not fully recover from compression before new pressure is applied in the cyclic compression test.

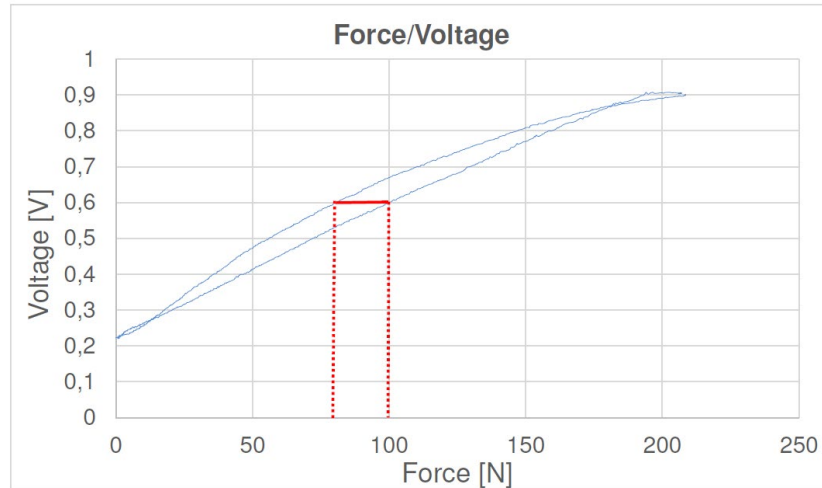


Figure 12. Hysteresis (red)

Hysteresis is a problem, because it is not possible to determine exactly at which force a certain voltage occurs.

Furthermore, with increasing number of cycles the voltage signal shows an increase of the peak magnitude that results from a decrease of the resistance (Figure 12). This behavior was observed for all the manufactured sensors and had already occurred with other sensors using Velostat. It is most probably due to mechanical creep of the piezoresistive material and substrate.

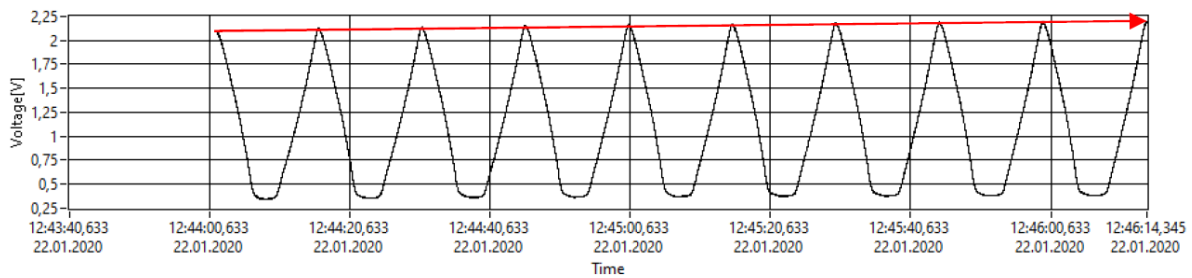


Figure 13. Time signal of output voltage over several cycles - Increase of the voltage peak

Nevertheless, some very interesting results could be obtained using several percentages of additive and using bonding. Figure 14 shows the comparison of a non-bonded (sensor layers not joined using the bonding net, just superimposed) versus a bonded sensor produced using ink with 20% of additive:

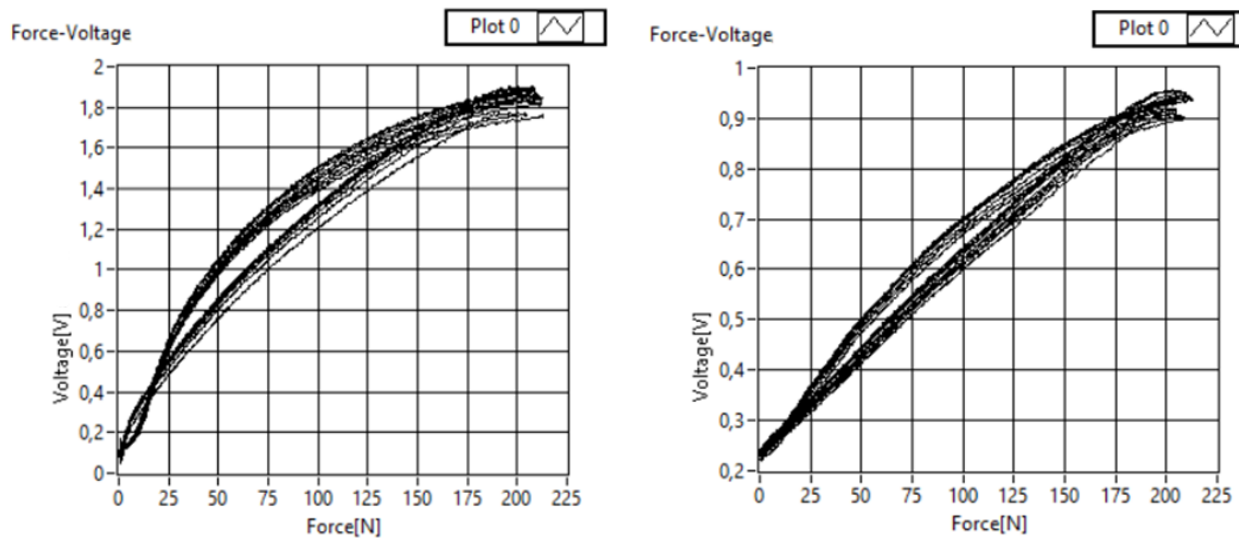


Figure 14. Sensor using ink with 20% of additive, non-bonded (left) and bonded (right)

As can be observed, the voltage range produced by the bonded sensor is lower than that of the non-bonded sensor. This is due to the effect that the bonding net has on the resistance of the sensor, increasing it and thus lowering the output voltage (see Equation 1). This is no actual problem, because it can be easily solved by increasing the gain of the amplifier using a larger resistance R .

On the other side, bonding shows to contribute to lower hysteresis and a more linear characteristic of the sensor, besides the improved mechanical stability of the sensor. It can also be observed that the sensor is more stable for low forces (between 0 and 20 N).

Conclusions and Future Work

The main goal of the present research work was to create a textile based flexible piezoresistive pressure sensor for the integration into smart textiles. To achieve this, a basic overview and understanding about the existing methods and materials was inevitable. The research shows that the materials currently used for the manufacture of sensors for smart textiles do not yet meet all requirements for flexibility, washability and other desired properties.

Measurement results show almost linear behavior for sensors with lower conductivity in the ink and using bonding. Furthermore, an interesting range of resistance could be measured, from over $3\text{k}\Omega$ to under 200Ω which allows the sensor to be used in different areas of sensitivity. However, hysteresis, some non-linearity and spreading of the measurement results are still existing and are to be improved. In conclusion, the piezoresistive ink is proved to be functional to produce a flexible, piezoresistive pressure sensor with reasonable stability and accuracy.

For further applications of flexible textile pressure sensors, it is recommended to perform the same test procedure with other materials and compare their results. In sectors where natural fibers are not or only barely used, the cotton material could thus be replaced by synthetic alternatives such as polyester. This material exhibits different properties than cotton and may therefore be used advantageously. Polyester is considered to be very easy-care and dries very quickly. Due to its high flexibility and strength, polyester is particularly suitable for bedclothes or clothing in outdoor areas. Up to now, only textiles in the form of woven fabrics have been considered in this work. In future investigations, experiments with knitted fabrics or nonwovens could provide further insights.

In this research work, sensors with an area of 9 cm^2 were manufactured and examined. In the future it is expected that the knowledge gained from these results can be used to produce wide-area sensors, to be applied in sports and health applications.

The next step could be a punctiform pattern application of the ink. If the electrodes continue to cover the entire surface, the measurement principle remains the same, but the manufacturing process becomes cheaper and more sustainable by using less ink.

Besides pressure sensors, extension sensors are also feasible using this ink. Different combinations of materials and forms of textiles could result in sensors with the ability to behave in a very specific way and thus applicable in very specific applications.

References

- [1] H. Carvalho, Y. Yao, L.M. Gonçalves, Flexible force sensors for e-textiles, IOP Conference Series: Materials Science and Engineering, 254 (2017) 072007.
- [2] J. C. Ferreira, J. Oliveira and S. Ribeiro, Nanopaint, 2016. [Online]. Available: <http://www.nanopaint-tech.com/>. [Accessed: 21 12 2019].
- [3] Z. Zhou, Y. Li, J. Cheng, S. Chen, R. Hu, X. Yan, X. Liao, C. Xu, J. Yu and L. Li, Supersensitive all-fabric pressure sensors using printed textile electrode arrays for human motion monitoring and human-machine interaction, Journal of Materials Chemistry C, 6(48) (2018) 13120-13127.
- [4] R. Bohne, Making things wearable, O'Reilly Verlag GmbH & Co.KG, Köln, 2012.
- [5] M. Bücherl, Druckempfindliche textile Sensorfläche, Patent, DE202015004254U1 (2015) [Online]. Available: <https://patents.google.com/patent/DE202015004254U1/de?q=textiler&q=drucksensor&oq=textiler+drucksensor>. [Accessed: 14 12 2018].
- [6] C.B. Goy, V. Menichetti, L. M. Yanicelli, J. B. Lucero, M.A.G. López, N.F. Parodi, M.C. Herrera, Design, fabrication and metrological evaluation of wearable pressure sensors, Journal of Medical Engineering and Technology, 39(3) (2015) 208-215.
- [7] D.A. Valle-Lopera, A.F. Castaño-Franco, J. Gallego, A.M. Hernandez, Test and fabrication of piezoresistive sensors for contact pressure measurement, Revista Facultad de Ingeniería, 82 (2017) 47-52.
- [8] I. Baldoli, T. Mazzocchi, C. Paoletti, L. Ricotti, P. Salvo, V. Dini, C. Laschi, F. Di Francesco, A. Menciassi, Pressure mapping with textile sensors for compression therapy monitoring, Proceedings of the Institution of Mechanical Engineers. Part H, 230(8) (2016) 795-808.
- [9] L. Possanzini, M. Tessarolo, L. Mazzocchetti, E. G. Campari, B. Fraboni, Impact of Fabric Properties on Textile Pressure Sensors Performance, Sensors 19(21) (2019) 4686.

Textile Heat Flux Sensor Used in Stress Detection of Children with CP

TLEMSANI Fatima Zohra^{1,2,3,a*}, GIDIK Hayriye^{1,2,3,b},
MOHSENZADEH Elham^{1,2,3,c}, DUPONT Daniel^{2,3,d}

¹ENSAIT, ULR 2461, GEMTEX, F-59000 Lille, France

²Junia, F-59000 Lille, France

³Univ. Lille, F-59000 Lille, France

^{a*}fatima-zohra.tlemsani@junia.com, ^bhayriye.gidik@junia.com, ^celham.mohsenzadeh@junia.com,
^ddaniel.dupont@junia.com

Keywords: Textile heat fluxmeter; E-textile; Heat transfer; Mass transfer; Stress.

Abstract. This work is part of the European project MOTION (Interreg 2 Seas Mers Zeeën), which aims to develop an exoskeleton for children with cerebral palsy (CP). The developed exoskeleton is equipped with a smart garment in order to detect the stress (e.g. physical, physiological) during the rehabilitation. Five different sensors, i.e. electrocardiogram (ECG), respiratory rate (RR), pressure, galvanic skin response (GSR) and textile heat fluxmeter (THF), are integrated into this smart garment for stress detection. This paper focuses on the development of the textile heat fluxmeter. Several researchers used heat fluxmeters in physiological studies to measure the body heat exchanges with the environment. However, the non-permeability of such fluxmeter gives inaccurate measurements in wet condition. Innovative flexible textile heat fluxmeter may detect, analyze, and monitor the heat and mass transfers with minimum disturbance due to its porosity. Moreover, it is desirable to have flexible sensors when they need to be in contact with the human body, in which the flexibility and non-irritability requirements are of utmost importance.

Introduction

Many technological devices have been developed to assist children with neurological diseases in physical rehabilitation, particularly robotic trainers [1-3] and exoskeletons [4]. These devices can also cause discomfort for children, due to their weight or because children are not used to this form of therapy [5, 6]. This can cause either physical discomfort such as pain, fatigue, itching, insomnia, hot/cold sensation, or psychological discomfort such as uncertainty, fear, stress, anxiety, and depression [7].

Previous studies on the stress of children with multiple disabilities have used audio signals to detect screams [8, 9], they have also tested social stress [10], and adopted some subjective instruments during rehabilitation [11-13]. These methods may have worked well, however, many children with motor problems, such as cerebral palsy (CP), also have cognitive problems. For them, it may be difficult to answer questions and express their feelings, and these methods do not measure the level of discomfort in real time. Therefore, measuring discomfort continuously and objectively can be very useful when using technological devices during rehabilitation.

When children are under physical or psychological stress, their physiological and vital signs, such as heart rate, blood pressure, respiratory rate, and skin temperature, change significantly [14-16]. For this reason, the measurement of physiological parameters during rehabilitation is integrated into new rehabilitation technologies using electronic textiles (e-textile). Different sensors can be integrated into these e-textiles, such as electrocardiogram (ECG) [17, 18], respiratory rate sensors [19, 20], temperature sensors [21, 22], blood pressure sensors [25], heat flux sensors [23, 24].

In this study, we focus on the development of textile-based heat flux sensors for stress detection. The stress often generates a changing in heat losses and an increase of the sweat on the skin surface. That is why, instead of temperature sensors that reveal only the abnormal state of the body's health, the heat flux sensor can also reveal the level of comfortability.

Heat flux sensors currently available in the market are impermeable and prevent the evaporation of sweat, thus they give incomplete results for the energy balance in a humid environment. Moreover, due to their semi-rigidity, they can only be used on flat or semi-flat surfaces. Indeed, to allow an accurate measurement, heat flux sensor need to have a good contact with the support surface. The textile heat flux sensor can take into account the humidity and it can be used for complex surfaces due to its permeability and flexibility. Therefore, it is possible to measure, analyze and monitor thermal and hydric transfers with minimal disturbance.

The first part of this work presents the development of this Textile Heat Fluxmeter (THF) and the second part explains the experimental setup used for characterization and in the end, the results are presented and analyzed.

Materials and Methods

Principle of THF

The THF consists of two components: (i) textile substrate and (ii) metallic wire that forms a number of thermocouples connected in series, also called a thermopile.

The operating principle is based on the Seebeck effect (Fig. 1). When there is a temperature difference between the thermocouple junctions, an output voltage is delivered between the metallic wire's terminals (Eq. 1) (Fig. 2). In this work, we used a thermocouple of constantan-copper (Cn-Cu).

$$\Delta V = N \times \alpha \times \Delta T. \quad (1)$$

Where, N is the number of thermocouples, α is the Seebeck coefficient ($\mu\text{V} \cdot \text{K}^{-1}$) and ΔT is the temperature difference between the thermocouple junctions (K).

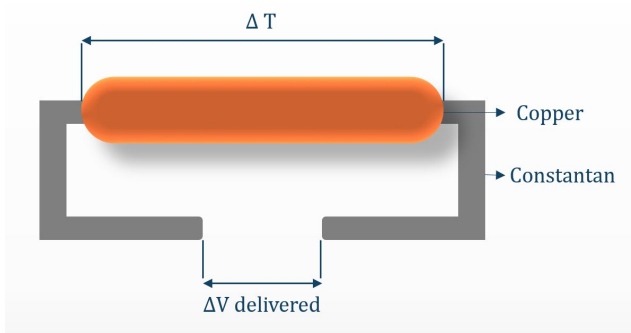


Fig. 1. Seebeck effect principle

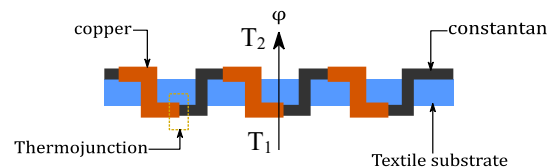


Fig. 2. Schema of the thermopile

THF development

The THF was developed following two major steps: (i) the weaving process and (ii) the post-treatment.

A 24-frame weaving loom (50 cm), ARM AG (Swiss), was used for weaving process. A 100% polyester (PES) yarn was used for both warp and weft yarns. Then, a constantan wire (Omega Engineering, USA) with a diameter of 76 microns was inserted between each PES yarn as weft floats (1.7 cm equal to covering 5 wrap yarns).

The structure adopted to develop the sensor is the satin 5, weft effect, ($S_y=3$) structure as presented in Fig. 3, which is, according to our previous work [24], the most suitable and efficient structure.

The aim of the post-treatment is to transform the textile structure to a sensor (thermopile) by obtaining the Cn-Cu junctions on both faces of the sample. The sensor was made by the local electrochemical deposition of copper (Cu) achieved by masking a local zone (Fig. 4). A polymer (QUECODUR DM 70, THOR, Germany) was used for local masking.

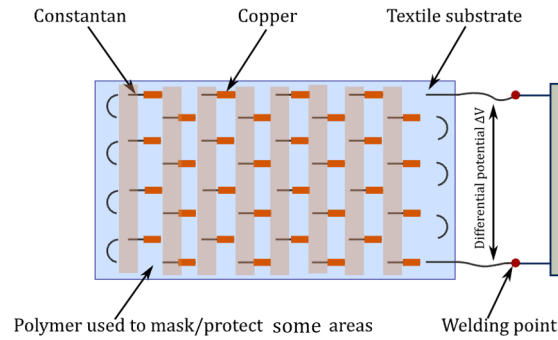
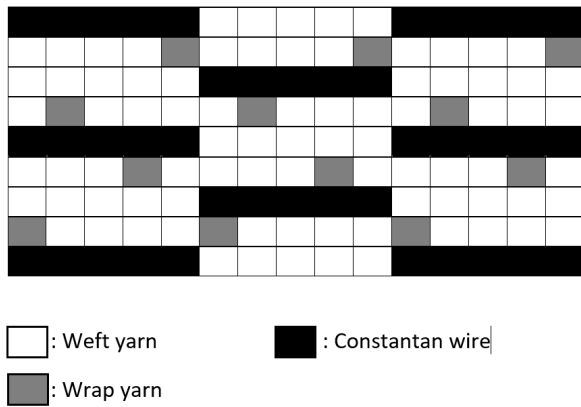


Fig. 2. THF structure

Fig. 4. The post-treatment with local masking and copper deposition

The size of the developed THF was $2\text{ cm} \times 2\text{ cm}$, supported by a textile substrate whose thickness was 15 mm all around the THF perimeter as presented in Fig. 5.

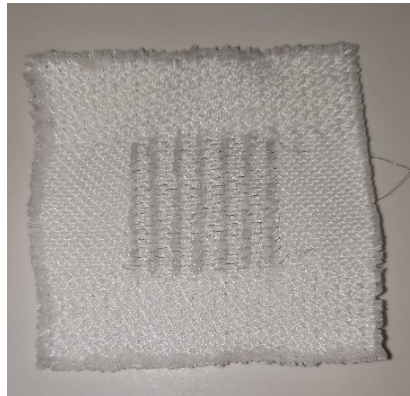


Fig. 5. The developed THF

Experimental setup for characterization

A sketch of the experimental setup used in this study is presented in Fig. 6. The setup is composed of two insulated and thermally regulated hot plates made from aluminum. Each one of them is connected to a temperature control system (Julabo, Germany). A space of 5 cm is left between the two hot plates to be used for piling up and placing the THF and the gold standard commercial heat fluxmeter (Captec[®], France). Then, a metallic piece, made also from aluminum, is added to fill up the gap between the sensors and the hot plate, and the whole space is insulated with a 5 cm layer of polystyrene. Four temperature probes T_{L1} , T_{L2} , T_{L3} and T_{L4} are put to measure the “in” and “out” temperatures of the THF, the Captec[®] and the aluminum piece, respectively. The setup is connected to a data acquisition system (DAQ, Keithley 2700 controlled by ExcelLNKS software) and a PC control to collect the voltage delivered by fluxmeters and temperatures given by temperature probes.

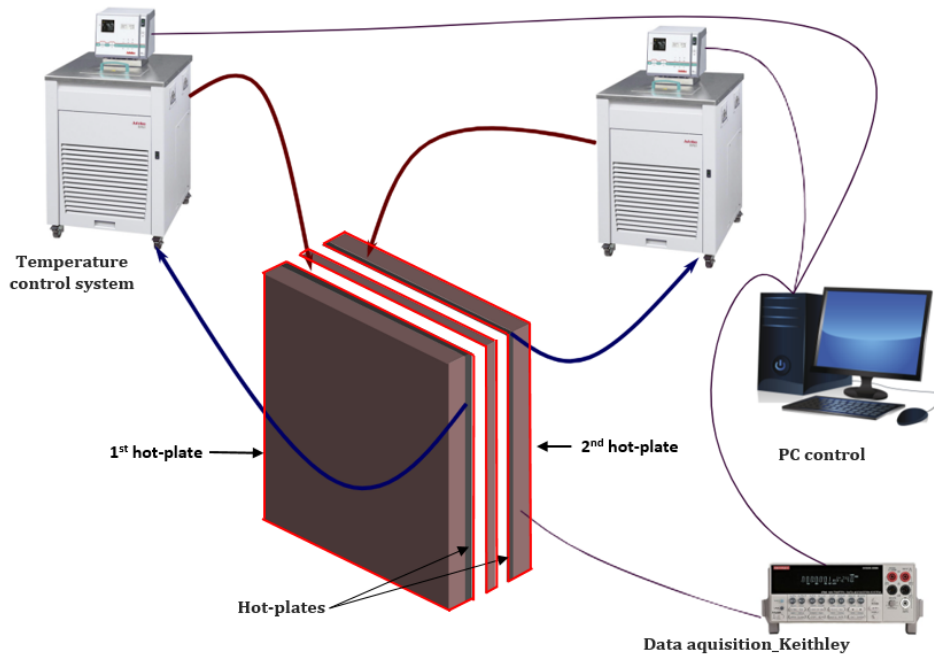


Fig. 6. Experimental setup developed at HEI

To evaluate the performance of the THF and determine its sensitivity, a transient heating was carried out using the above-mentioned setup. The textile sensor was tested in both dry and moisturized state to analyze the effect of moisture on the heat flux transfer. To do so, different temperatures were imposed to the hot plates. The first one, T_s , simulates the behavior of the skin temperature and the other one, T_a , simulates the ambient temperature. The temperatures used for skin and ambient [T_s , T_a] were [303, 303], [309, 300], [309, 309], [313, 309], [309, 309] (K), respectively. We moved from a range to another one when the steady state was reached.

The temperature was uniform on the hot plates' surfaces and we assumed that the heat transfer was unidirectional along the horizontal (x) axis. Thus, it was considered that all the heat flux was dissipating through both THF and Captec[®]. The sensitivity of the THF was calculated using the sensitivity of Captec[®] ($4.01 \mu\text{V}\cdot\text{W}^{-1}\cdot\text{m}^{-2}$) given by supplier) (Eq. 2).

$$\varphi_{\text{THF}} = \varphi_{\text{Captec}} = \frac{\Delta V_{\text{THF}}}{S_{\text{THF}}} = \frac{\Delta V_{\text{Captec}}}{S_{\text{Captec}}} \quad (2)$$

Where, S is the sensitivity ($\mu\text{V}\cdot\text{W}^{-1}\cdot\text{m}^{-2}$), φ ($\text{W}\cdot\text{m}^{-2}$) is the heat flux density and ΔV is the voltage (μV).

Furthermore, different levels of moisture were added to the THF, i.e. 10 %, 30 % and 50 %, to examine their effect on the global heat transfer and on the textile sensor's behavior. This time, more temperature ranges were applied on the hot plates to better understand the THF behavior as presented in the Table 1. T_a simulates the average temperatures of a sunny day while T_s simulates, at each range of time, the variation of skin's temperature from a normal to an abnormal one.

Table 1. Experimental procedure followed in wet conditions

Range of Time	1	2	3	4	5	6	7	8	9	10	11	12
T_a [K]	294		297			295			289			
T_s [K]	309.5	312	310	310	312	310	310	312	310	310	312	310

Results and Discussion

Sensitivity of THF

Fig. 7 presents the output voltage of both THF and Captec[®] for different temperature ranges.

When the same temperature is set on the two hot plates, the measured output voltage was 0 for both fluxmeters (Eq. 1). The tendency between THF and Captec[®] was the same when a temperature difference was applied to the hot plates. The obtained output voltage increased by increasing temperature difference. Captec[®] gave slightly higher values than the THF for the output voltage and THF revealed a sensitivity of $3.87 \pm 0.04 \mu\text{V}/(\text{W}\cdot\text{m}^{-2})$ which is similar to the sensitivity of Captec[®]. The THF output voltage evolution follows perfectly the evolution of Captec[®] output and of the system's temperature that reflects the proper and accurate functioning of the THF. Thus, this sensor can be considered as a promising solution.

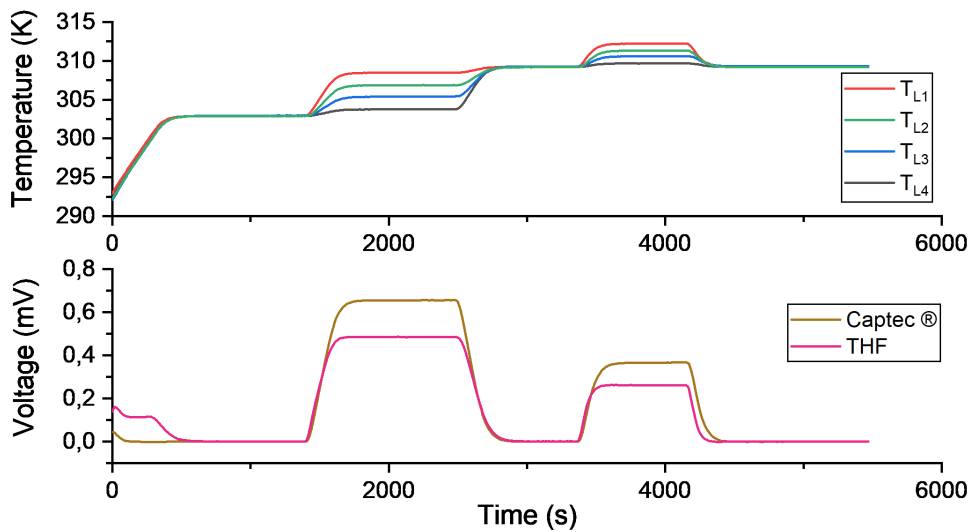


Fig. 7. Output voltage obtained for THF and Captec[®]
(For colors interpretation, please refer to the electronic version)

Effect of moisture on the heat flux transfer measured by the THF

Fig. 8 presents a comparison between the output voltage of the two involved sensors when different levels of moisture were applied to the THF. Results showed that most of the time the output voltage of the THF decreases by increasing the level of humidity, which can be explained by the presence of a cooling process that slowed down the heating. Furthermore, the signal becomes noisier when the humidity increases, and this indicates the involvement of the convection that disturbs the heat transfer. Besides, when the level of moisture increases, the voltage difference between the THF and Captec[®] becomes higher. This could be related to several complex phenomena, and it may also reflect a recovery phenomenon inside the heating system. This phenomenon increases the heat transfer rate in the area nearby the Captec[®] when it is slowed down around the THF. Thus, these results confirm that all the heat flux was dissipating through both THF and Captec[®].

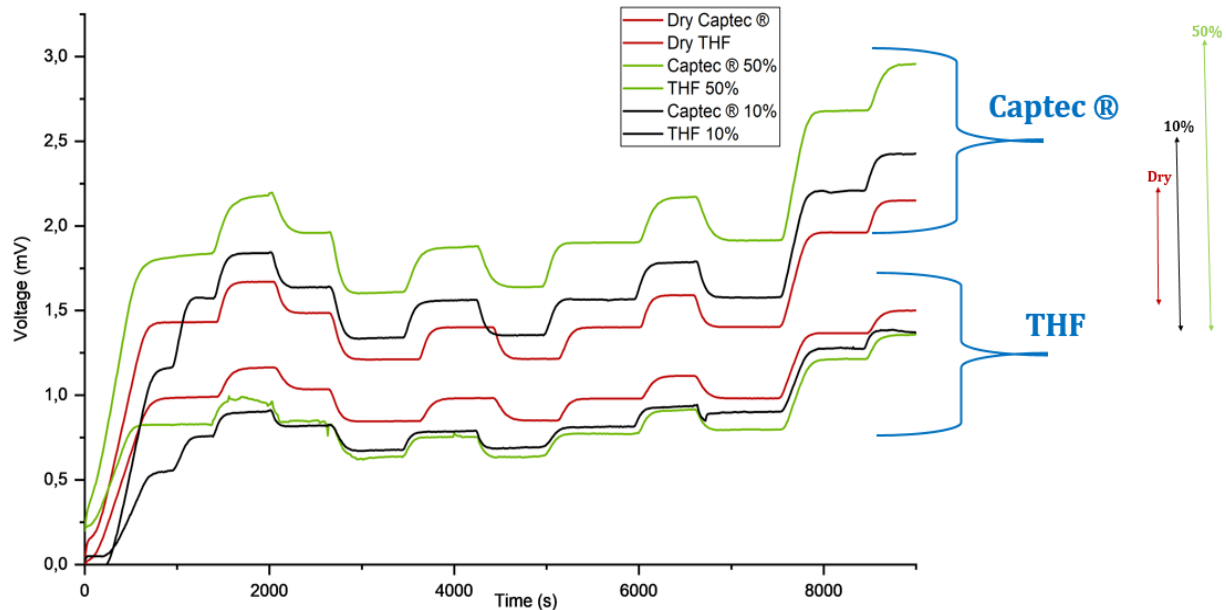


Fig. 8, Effect of moisture on the voltage output behavior of both THF and Captec[®]
(For colors interpretation, please refer to the electronic version)

Conclusion

In this work, a textile heat flux sensor was developed and characterized. Results showed that this sensor has the same tendency as a commercial heat fluxmeter (i.e. Captec[®]), with a very close sensitivity. As the mass transfer affect the heat flux exchanges, the behavior of the moisturized THF was studied. As it is a complex phenomenon, the results should be completed with a numerical study for better understanding. Thus, future studies will focus on analyzing the coupled heat and mass transfer and their modeling. Moreover, the THF will be tested on human bodies to determine its ability to detect the stress. Finally, it will be integrated into a smart garment with other sensors (i.e. ECG, RR, GSR, pressure). Afterwards, the obtained results from different sensors will be merged and analyzed to detect the stress of children with CP during the rehabilitation.

Acknowledgment

This study is realized thanks to the Interreg 2 Seas Mers Zeeën program (Project MOTION).

References

- [1] R. Gassert, V. Dietz, Rehabilitation robots for the treatment of sensorimotor deficits: a neurophysiological perspective, *Journal of NeuroEngineering and Rehabilitation*. 15 (2018) 46.
- [2] C. Bayón, T. Martín-Lorenzo, B. Moral-Saiz, Ó. Ramírez, Á. Pérez-Somarriba, S. Lerma-Lara, I. Martínez, E. Rocon, A robot-based gait training therapy for pediatric population with cerebral palsy: goal setting, proposal and preliminary clinical implementation, *Journal of NeuroEngineering and Rehabilitation*. 15 (2018) 69.
- [3] K.P. Michmizos, H.I. Krebs, Pediatric robotic rehabilitation: Current knowledge and future trends in treating children with sensorimotor impairments, *NeuroRehabilitation*. 41 (2017) 69–76. <https://doi.org/10.3233/NRE-171458>.
- [4] T.C. Bulea, Z.F. Lerner, A.J. Gravunder, D.L. Damiano, Exergaming with a pediatric exoskeleton: Facilitating rehabilitation and research in children with cerebral palsy, *IEEE Int Conf Rehabil Robot*. 2017 (2017) 1087–1093.

-
- [5] J.-S. Bourseul, S. Brochard, L. Houx, C. Pons, M. Bué, I. Manesse, J. Ropars, D. Guyader, P. Le Moine, A. Dubois, Care-related pain and discomfort in children with motor disabilities in rehabilitation centres, *Annals of Physical and Rehabilitation Medicine*. 59 (2016) 314–319.
- [6] E.A. Lyons, D.E. Jones, V.M. Swallow, C. Chandler, An Exploration of Comfort and Discomfort Amongst Children and Young People with Intellectual Disabilities Who Depend on Postural Management Equipment, *J Appl Res Intellect Disabil*. 30 (2017) 727–742.
- [7] S. Ashkenazy, F. DeKeyser Ganz, The Differentiation Between Pain and Discomfort: A Concept Analysis of Discomfort, *Pain Management Nursing*. 20 (2019) 556–562.
- [8] L. Abou-Abbas, H. Fersaie Alaie, C. Tadj, Automatic detection of the expiratory and inspiratory phases in newborn cry signals, *Biomedical Signal Processing and Control*. 19 (2015) 35–43.
- [9] A. Rosales-Pérez, C.A. Reyes-García, J.A. Gonzalez, O.F. Reyes-Galaviz, H.J. Escalante, S. Orlandi, Classifying infant cry patterns by the Genetic Selection of a Fuzzy Model, *Biomedical Signal Processing and Control*. 17 (2015) 38–46.
- [10] C. Kirschbaum, K.-M. Pirke, D.H. Hellhammer, The ‘Trier Social Stress Test’ – A Tool for Investigating Psychobiological Stress Responses in a Laboratory Setting, *NPS*. 28 (1993) 76–81.
- [11] A.D. Deacy, L.A. Gayes, S. De Lurgio, D.P. Wallace, Adaptation of the State-Trait Inventory for Cognitive and Somatic Anxiety for Use in Children: A Preliminary Analysis, *J Pediatr Psychol*. 41 (2016) 1033–1043.
- [12] N.C. a. C. Oliveira, C.M. Gaspardo, M.B.M. Linhares, Pain and distress outcomes in infants and children: a systematic review, *Braz. J. Med. Biol. Res*. 50 (2017) e5984.
- [13] (PDF) The Utility of Measures of Child and Adolescent Anxiety: A Meta-Analytic Review of the Revised Children’s Manifest Anxiety Scale, the State–Trait Anxiety Inventory for Children, and the Child Behavior Checklist, ResearchGate. (n.d.). 10
- [14] I. Locher, Technologies for system-on-textile integration, Doctoral Thesis, ETH Zurich, 2006.
- [15] (PDF) Stress Detection Using Physiological Sensors, ResearchGate. (n.d.).
- [16] G. Vila, C. Godin, S. Charbonnier, E. Labyt, O. Sakri, A. Campagne, Pressure-Specific Feature Selection for Acute Stress Detection From Physiological Recordings, in: *IEEE International Conference on Systems, Man, and Cybernetics, IEEE SMC 2018, Mysaki, Japan, 2018*. <https://hal.archives-ouvertes.fr/hal-01971692> (accessed September 22, 2020).
- [17] R. Paradiso, G. Loriga, N. Taccini, A wearable health care system based on knitted integrated sensors, *IEEE Transactions on Information Technology in Biomedicine*. 9 (2005) 337–344.
- [18] M. Di Rienzo, F. Rizzo, G. Parati, G. Brambilla, M. Ferratini, P. Castiglioni, MagIC System: a New Textile-Based Wearable Device for Biological Signal Monitoring. Applicability in Daily Life and Clinical Setting, in: *2005 IEEE Engineering in Medicine and Biology 27th Annual Conference, 2005*: pp. 7167–7169.
- [19] L. Hu, M. Pasta, F. La Mantia, L. Cui, S. Jeong, H.D. Deshazer, J.W. Choi, S.M. Han, Y. Cui, Stretchable, Porous, and Conductive Energy Textiles, *Nano Lett*. 10 (2010) 708–714.
- [20] C. Rovira, S. Coyle, B. Corcoran, D. Diamond, F. Stroiescu, K. Daly, Integration of textile-based sensors and Shimmer for breathing rate and volume measurement, in: *2011 5th International Conference on Pervasive Computing Technologies for Healthcare (PervasiveHealth) and Workshops, 2011*: pp. 238–241.

- [21] E.S. Kolosovas-Machuca, M.A. Martínez-Jiménez, J.L. Ramírez-GarcíaLuna, F.J. González, A.J. Pozos-Guillen, N.P. Campos-Lara, M. Pierdant-Perez, Pain Measurement through Temperature Changes in Children Undergoing Dental Extractions, *Pain Res Manag.* 2016 (2016) 4372617.
- [22] S. Jung, T. Ji, V.K. Varadan, Point-of-care temperature and respiration monitoring sensors for smart fabric applications, *Smart Mater. Struct.* 15 (2006) 1872–1876.
- [23] H. Gidik, D. Dupont, G. Bedek, Development of a radiative heat fluxmeter with a textile substrate, *Sensors and Actuators A: Physical.* 271 (2018).
- [24] H. Gidik, G. Bedek, D. Dupont, C. Codau, Impact of the textile substrate on the heat transfer of a textile heat flux sensor, *Sensors and Actuators A: Physical.* 230 (2015) 25–32.
- [25] C.-T. Huang, C.-L. Shen, C.-F. Tang, S.-H. Chang, A wearable yarn-based piezo-resistive sensor, *Sensors and Actuators A: Physical.* 141 (2008) 396–403.

Scalable Flexible Electromagnetic Interference Shielding Textiles Based on MWCNTs and PEDOT:PSS

Ana Rita Sousa^{1,2,a}, Renata Matos^{2,b}, José R. M. Barbosa^{3,c},
O. Salomé G.P. Soares^{3,d}, João Ferreira^{4,e}, Gilda Santos^{4,f}, Augusta Silva^{4,g},
José Morgado^{4,h}, Patrícia Soares^{5,i}, Sergey A. Bunyaev^{1,j}, Gleb N. Kakazei^{1,k},
Cristina Freire^{2,l}, M. Fernando R. Pereira^{3,m}, André M. Pereira^{1,n*},
Clara Pereira^{2,o*}

¹FIMUP - Institute of Physics for Advanced Materials, Nanotechnology and Photonics, Physics and Astronomy Department, Faculty of Sciences, University of Porto, Rua do Campo Alegre s/n, 4169-007 Porto, Portugal

²REQUIMTE/LAQV, Chemistry and Biochemistry Department, Faculty of Sciences, University of Porto, Rua do Campo Alegre s/n, 4169-007, Porto, Portugal

³LSRE-LCM, Department of Chemical Engineering, Faculty of Engineering, University of Porto, Rua Dr. Roberto Frias, 4200-465 Porto, Portugal

⁴CITEVE - Technological Centre for the Textile and Clothing Industry of Portugal, Rua Fernando Mesquita, 2785, 4760-034 Vila Nova de Famalicão, Portugal

⁵Cottonanswer, Rua dos Combatentes do Ultramar, 50, 4750-047 Lijó, Barcelos, Portugal

^aanarita.sousa@fc.up.pt, ^bup201303853@fc.up.pt, ^cjrbarbosa@fe.up.pt, ^dsalome.soares@fe.up.pt,
^ejferreira@citeve.pt, ^fgsantos@citeve.pt, ^gasilva@citeve.pt, ^hjmorgado@citeve.pt,
ⁱpatricia.soares@cottonanswer.pt, ^jbunyayev@fc.up.pt, ^kgleb.kakazei@fc.up.pt, ^lacfreire@fc.up.pt,
^mfpereira@fe.up.pt, ⁿampereira@fc.up.pt, ^oclara.pereira@fc.up.pt

Keywords: Electromagnetic shielding, carbon materials, carbon nanotubes, conductive polymers, functional textiles, dip-pad-dry process, coating process

Abstract. With the rise of electromagnetic radiation-based technologies, considerable attention has been drawn to developing and implementing innovative electromagnetic shielding materials. Carbon nanomaterials and conductive polymers have been appealing to both academia and industry as promising alternatives for the traditionally used metallic materials, owing to their lightness, flexibility, easy processability and resistance to corrosion, which are of special importance for textile applications. In this work, multiwalled carbon nanotubes (MWCNTs) and poly(3,4-ethylenedioxythiophene):polystyrenesulfonate (PEDOT:PSS) have been applied to cotton textile substrates by straightforward scalable dyeing and coating processes, respectively. These processes led to uniform and homogeneous coatings with distinct properties: the fabric coated with MWCNT presented higher thickness and lower loading of incorporated material than the textile coated with PEDOT:PSS (thickness: 995 μm vs. 208 μm ; material loading: 9.4 wt.% vs. 70.7 wt.%). The electromagnetic shielding properties were outlined for each shielding textile in the frequency range of 5.85–18 GHz: an average shielding effectiveness of ~ 35.6 dB was obtained for MWCNT@tex, while PEDOT:PSS@tex reached ~ 38.3 dB. Thus, PEDOT:PSS provided enhanced radiation shielding with lower coating thickness, while the MWCNTs led to improved attenuation with less material usage. Shielding effectiveness values above 30 dB were obtained for both electromagnetic interference shielding textiles, which corresponds to an excellent classification for general use applications, such as casual clothing and maternity wear.

Introduction

Electromagnetic (EM) radiation has been used overtime in order to fulfil the civilization needs for superior and faster technologies. EM radiation located in the radiofrequency range is especially used in several indispensable applications, such as radio, telecommunications, wireless internet and radars.

Currently, the global society is witnessing the worldwide implantation of 5G wireless technologies. Thus, in a near future, EM radiation that relies on higher frequencies (when compared to the previous 4G technology) will be used [1]. Besides that, the “Internet of Things” market is rising, where smarter technologies and automation will boost EM radiation exposure. This undesired radiation exposure may create issues either by affecting electronic equipment operation or by affecting human health [2]. To overcome these issues, electromagnetic interference (EMI) shields are under development.

The attenuation ability of a shield is given by the shielding effectiveness (SE), expressed in decibel (dB). The mechanisms of EMI shielding involve reflection, absorption and multiple reflections contributions, with the latter being usually negligible. In order to achieve enhanced SE , there are three intrinsic parameters of the shielding material of extreme importance: electrical conductivity (σ), electrical permittivity (ϵ) and magnetic permeability (μ). Additionally, the thickness (t) of the shield plays an important role in the absorption mechanism, thus increasing the overall SE .

The textile sector has been consistently investing in research and development of innovative functional textiles. As so, textile-based EMI shields represent a useful solution for consumer protection by conjugating radiation protection functionality with the aesthetic advantages of lightness, flexibility and comfort. Most commercial textile-based EMI shielding solutions are based on metallic materials fabricated through conventional approaches, including plating, combination of metallic fibers/yarns and textile-based fibers/yarns through weaving and knitting processes, etc. [3]. Although metals very effectively attenuate EM radiation, they present several disadvantages, such as their high density, weight, corrosion tendency, being usually expensive and difficult to process. Moreover, the mechanism of EMI shielding by metals is mainly through reflection, causing adverse EM pollution to the surrounding environment. For this reason, researchers are turning their ways to alternative materials, such as conductive polymers and carbon materials [4–10].

Intrinsically conductive polymers (ICPs) are polymers in doped states that present increased electrical conductivity. The presence of mobile charges (*e.g.*, polarons, bipolarons and solitons) and bound charges (*e.g.*, dipoles) is responsible for the EM shielding properties of ICPs [11]. Additionally, contrarily to metallic materials, polymers have lower density, higher corrosion resistance, flexibility and are easy to process and handle. Polyaniline (PANI), polypyrrole (PPy) and PEDOT:PSS are examples of ICPs that have been investigated for this application. For instance, Qiu *et al.* synthesized PANI by chemical oxidation using different doping acids (hydrochloric acid, camphorsulfonic acid and phosphoric acid) [12]. The highest electrical conductivity of 1.28 S cm^{-1} was obtained with the camphorsulfonic acid doping. A SE of 20.7 dB was obtained for the same sample for a thickness of only 0.35 mm. Kim *et al.* prepared PPy- and PEDOT-coated polyethylene terephthalate (PET) fabrics by *in situ* chemical polymerization of the monomers in the presence of the textiles [13]. The PPy-coated PET displayed electrical properties superior to those of PEDOT-based one at lower ICP content. For both samples, a decrease in the volume resistivity was observed as the ICP loading increased. Moreover, that decrease was accompanied by the increase of the SE , reaching values of up to 36 dB, measured in the frequency range of 50 MHz to 1.5 GHz. Gosh *et al.* fabricated polyethylene glycol (PEG)/PEDOT:PSS-treated fabric by dip-coating process followed by a drying step at $70 \text{ }^\circ\text{C}$ [8]. The sample prepared with 25 dipping cycles presented an electrical conductivity of 82.7 S cm^{-1} , a thickness of 0.45 mm and a SE of 65.6 dB evaluated over 8–12 GHz.

Carbon materials (CM) have been investigated for EMI shielding due to their remarkable properties, namely high electrical conductivity, high surface area, low density and high chemical, thermal and mechanical stability. Carbon black, multiwalled carbon nanotubes (MWCNTs) and graphene are examples of carbon materials that demonstrated good EM radiation attenuation. For instance, Song *et al.* studied graphene aerogels–carbon texture (GA-CT) hybrids for EMI shielding [14]. The authors reported a SE of 37 dB for 3 mm thickness in the frequency range of 8–12 GHz. Dai *et al.* used dip-coating processes to incorporate waterborne polyurethane and different loadings of fillers containing 80 wt.% of carbon nanotubes (CNTs) and 20 wt.% of graphene into textile substrates [15]. The sample containing 3 wt.% filler loading with a thickness of 0.35 mm presented an electrical conductivity of 0.64 S cm^{-1} , low reflectivity and a SE of 35 dB between 8.2 and 12.4 GHz. Xu *et al.* developed an asymmetric EMI shield based on an ultra-thin CNT film, by e-beam deposition of a copper nanolayer

on one side of the CNT film followed by electrospinning of nylon-6 nanofibers on both surfaces (PCCP) [16]. A SE of ~ 40 dB was obtained for the pure CNT film, while for the final PCCP textile (thickness of $20\ \mu\text{m}$) a SE of up to 50 dB was obtained in the frequency range of 1.5–5.85 GHz. Summarily, ICPs and CM have been reported to be promising materials for EMI shielding to be applied in textiles. However, most of the reported works rely on complex processes or involving multiple steps concerning the functionalization of textiles to yield EMI shielding properties. This work aims to provide solutions that are easy, scalable and quickly to be employed in the textile industry, while avoiding metallic materials. Herein, the goal was to create EMI textile-based shields with superior properties: thin, lightweight and flexible with good radiation absorption properties in the radiofrequency band. For this reason, two types of shields were produced and compared: a) MWCNTs impregnated on cotton textile by dip-pad-dry process (already reported in a previous work [17]) and b) PEDOT:PSS applied by coating into cotton substrate. The produced shields were evaluated and compared concerning the amount of incorporated material, thickness, electrical conductivity and EMI shielding properties. Moreover, the EM shielding mechanisms were unveiled.

Materials and Methods

In this work, two EMI shielding textiles were produced (Fig. 1):

MWCNT@tex: In this procedure, 100% cotton American fleece textile (thickness: $\sim 677 \pm 83\ \mu\text{m}$; areal density: $450\ \text{g m}^{-2}$) was used, provided by Cottonanswer S.A. (Portugal), as well as MWCNT NC7000TM from Nanocyl and sodium cholate hydrate (SCH, 99%) surfactant from Alfa Aesar. The fabrication process, as already reported in a previous work [17], was initiated with the preparation of an aqueous MWCNTs dispersion using SCH as surfactant under sonication. The cotton textile was impregnated through the dip-pad-dry process, which was repeated 6 times: the substrate was dipped into the dispersion, submitted to a padding process and then dried at $100\ ^\circ\text{C}$ after each step.

PEDOT:PSS@tex: In this fabrication process, 100% cotton Jersey textile (thickness: $\sim 140 \pm 13\ \mu\text{m}$; areal density: $90\ \text{g m}^{-2}$) provided by Cottonanswer S.A and commercial PEDOT:PSS paste CLEVIUS STM V4 from Heraeus were used. The PEDOT:PSS was applied through coating with a laboratory knife over roll coating unit type SV from Mathis AG. The sample was dried at $100\ ^\circ\text{C}$ and finally thermofixed at $140\ ^\circ\text{C}$ for 3 min.

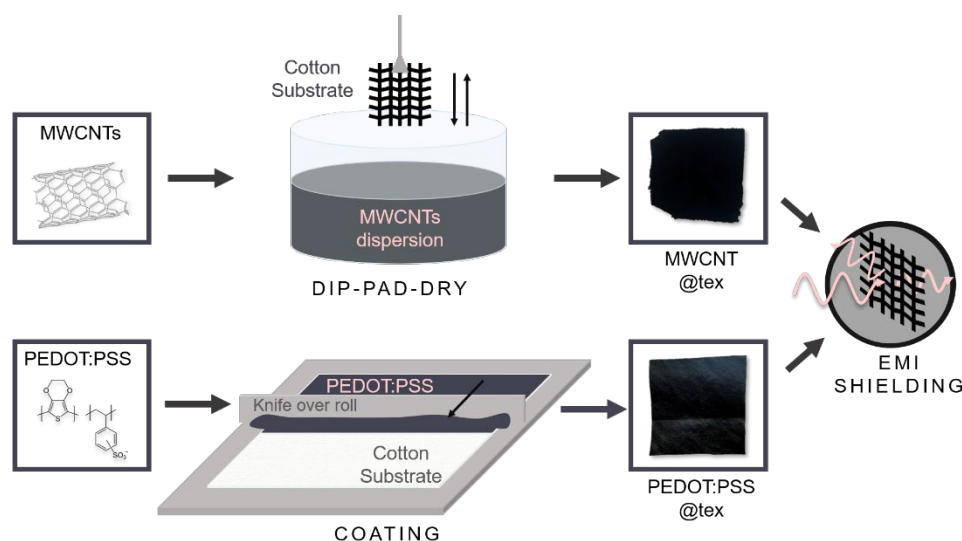


Fig. 1. Dip-pad-dry and coating processes used for the fabrication of the MWCNT- and PEDOT:PSS-coated fabrics, respectively.

Optical microscope images were collected to provide information on the structure of the fabrics before and after their coating with the shielding materials. The thickness of the samples was measured

using a Mitutoyo Digimatic Indicator (accuracy of 1 μm). The electrical resistance was measured using the four-probe method, in which a 2410-C from Ketheley Instruments Inc. was used to apply the current intensity between the external contacts and then measure the voltage between the internal ones. The electrical conductivity (σ) was calculated from the Ohm's Law and using the following equation:

$$\sigma = \frac{d}{RA} \quad (1)$$

where d is the distance between the contacts, R is the electrical resistance and A is the sample area.

EMI shielding properties were measured using the transmission line test with waveguides. In this setup, a transmission line was created using two rectangular waveguides, and the sample under test was placed in the middle junction between them. This transmission line was connected to a vector network analyzer (VNA) 37247D from Anritsu. The VNA emitted the EM radiation and received it after passing through the sample. From these values, the VNA returned the scattering parameters (S_{21} and S_{11}) that are related to the transmission ($T = |S_{21}|^2$) and reflection ($R = |S_{11}|^2$) coefficients, respectively. In this setup, three types of commercial grade straight waveguide sections were used from Altaix Electronica (Spain), for measuring frequencies in the ranges of 5.85–8.2 GHz (WR-137), 8.2–12.4 GHz (WR-90) and 12.4–18 GHz (WR-62), leading to an overall band frequency of 5.85–18 GHz.

SE was calculated through the power loss between the incident and transmitted EM fields after passing through the shield. Since the shielding process is a result of the involved mechanisms, the SE can be calculated by [18]:

$$SE = SE_A + SE_R + SE_{MR} \quad (2)$$

where SE_A is the SE by absorption, SE_R is the SE by reflection and SE_{MR} is the SE by multiple reflections.

These quantities can be calculated by T , R and absorption (A) coefficients, which refer to the fractions of power that are transmitted, reflected and absorbed, respectively. Thus,

$$SE_T = -10 \log(T) \quad (3)$$

$$SE_R = -10 \log(1 - R) \quad (4)$$

$$SE_A = SE_T - SE_R - SE_{MR} \quad (5)$$

Since multiple reflections can be negligible, then:

$$SE_A = -10 \log \frac{T}{1 - R} \quad (6)$$

By using equations 2–6, the values of SE_R , SE_A and SE_T were obtained. These parameters were investigated over the frequency range of 5.85–18 GHz.

Results and Discussion

The attainment of a uniform coating is a main requirement while applying an EMI shielding material on a fabric substrate. The MWCNT@tex, which was prepared by the dip-pad-dry process, presented a black coloration and homogeneous coating; nevertheless, it presented increased stiffness relative to the parent textile. On the other hand, the PEDOT:PSS@tex-based sample prepared by coating displayed blue coloration and a very smooth surface. The described topology of the textiles before and after the coating processes is illustrated in Fig. 2, where it can be observed the change of

coloration of the fabrics, confirming the incorporation of the materials. Additionally, the difference between the topology of the two types of parent textiles is perceptible, since they differ in color, grammage and thickness.

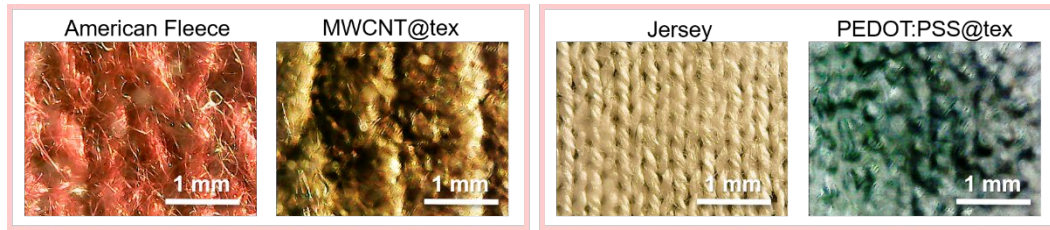


Fig. 2. Images of the textiles before and after the coating process for MWCNT@tex (left) and PEDOT:PSS@tex (right), captured with an optical microscope.

The successful incorporation of the materials was also confirmed by the increase of the samples mass (Table 1). The MWCNT-based sample contained 9.4 wt.% of MWCNT@tex, while the PEDOT:PSS@tex had significantly higher material loading, of 70.7 wt.%. The thickness of the textiles also changed upon the incorporation processes from $\sim 677 \pm 83 \mu\text{m}$ to $995 \pm 10 \mu\text{m}$ for MWCNT@tex, and from $\sim 140 \pm 13 \mu\text{m}$ to $208 \pm 13 \mu\text{m}$ for PEDOT:PSS@tex, corresponding, in both cases, to an increase of 1.5 times relative to the parent substrates. The thickness increase effect is more perceptible for MWCNT@tex ($\Delta t = 318 \pm 11 \mu\text{m}$), which could be a disadvantage for applications where low thickness is a desired property. In contrast, the PEDOT:PSS@tex sample had a very small increase of thickness ($\Delta t = 68 \pm 27 \mu\text{m}$), preserving the textile flexibility features.

After coating processes, there was a significant improvement in the electrical conductivity of the samples, changing from pure electrical insulators to conductors. The electrical conductivity was higher for PEDOT:PSS@tex than for MWCNTs@tex, of 31.02 S m^{-1} and 3.99 S m^{-1} , respectively.

Table 1. Properties of the produced EMI textile shields^a

Sample	Weight [wt.%]	Thickness (t) ± 0.001 [mm]	Electrical Conductivity (σ) [S m^{-1}]	SE_{ave} [dB]	ΔSE [dB]	SE/t [dB mm^{-1}]	$SE/\Delta m$ [dB g^{-1}]
MWCNT@tex	9.4	0.995	3.99	35.6	2.0	36	127
PEDOT:PSS@tex	70.7	0.208	31.02	38.3	0.6	184	70

^a Weight percentage (wt.%), thickness (t , mm), electrical conductivity (σ , S m^{-1}), average shielding effectiveness (SE_{ave} , dB) measured from 5.85 to 18 GHz and the respective standard deviation (ΔSE , dB), average SE normalized by thickness (SE/t , dB mm^{-1}) and average SE normalized by weight variation ($SE/\Delta m$, dB g^{-1}).

The shielding properties (SE_R , SE_A and SE) vs. frequency curves for MWCNT@tex and PEDOT:PSS@tex are presented in Fig. 3. The frequency-dependent SE curves of the parent substrates are also shown in Fig. 3c.

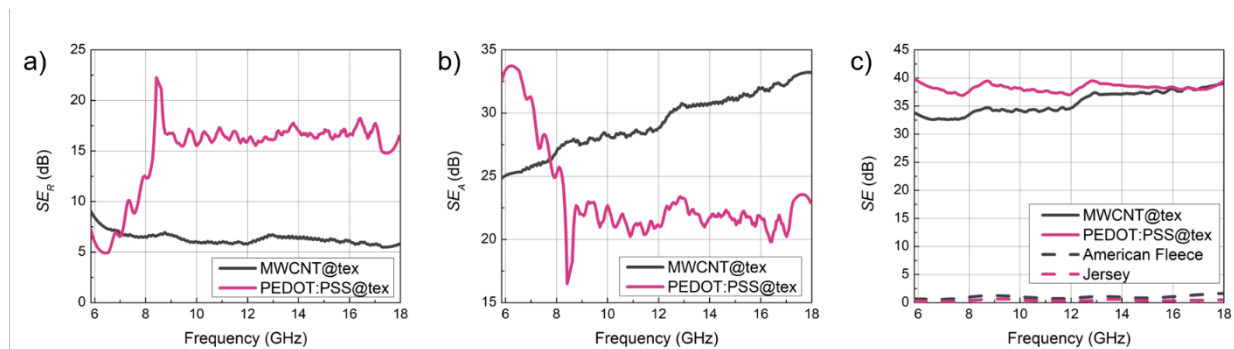


Fig. 3. Frequency-dependent shielding properties of the coated samples from 5.85 GHz to 18 GHz: a) shielding effectiveness by reflection; b) shielding effectiveness by absorption and c) total shielding effectiveness.

The average EMI shielding due to reflection in the measured band frequency was $\sim 6.3 \pm 0.6$ dB for MWCNT@tex and $\sim 14.8 \pm 3.7$ dB for PEDOT:PSS@tex, while the average EMI shielding by absorption was $\sim 29.3 \pm 2.4$ dB for MWCNT@tex and $\sim 23.4 \pm 3.7$ dB for PEDOT:PSS@tex. For both shields, the mechanism of absorption was dominant. Moreover, this feature was more relevant for MWCNT@tex, where the shielding by reflection was smaller, being 2.3 times lower than the value presented by PEDOT:PSS@tex. The PEDOT:PSS@tex presented the best reflectivity when compared with MWCNT@tex, which presented much higher absorption features. The SE_R is mainly affected by σ , which is in accordance with the results obtained herein, in which the highest σ was obtained for PEDOT:PSS@tex. In contrast, the absorption mechanism is affected by ϵ , μ and t . Since MWCNT@tex does not display magnetic properties, the higher value of SE_A relative to the SE_R could be justified by its dielectric properties. Moreover, since the absorption process takes place inside the shield instead of occurring at the surface, like reflection, the thickness of the shield becomes a prominent factor. This fact is corroborated by the smoother and practically constant $SE_R(f)$ curve obtained for MWCNT@tex, while the $SE_A(f)$ curve presented higher values throughout the measured frequency range, and increased as the frequency increased. This EMI rising trend with frequency can be justified by the fact that the wavelength of the EM radiation becomes smaller as the frequency increases, hindering its penetration through the conductive paths that are present within the textile fibres. On the other hand, for PEDOT:PSS@tex, the SE_R values increased as the frequency increased, reaching a maximum value of ~ 22 dB at the frequency of 8.4 GHz, and stabilizing afterwards. Simultaneously, a decrease of the SE_A was observed, reaching a minimum of ~ 16 dB at 8.4 GHz.

Concerning the overall average shielding effectiveness, the values were above 30 dB and comparable for both samples: $\sim 35.6 \pm 2.0$ dB and $\sim 38.3 \pm 0.6$ dB for MWCNT@tex and PEDOT:PSS@tex, respectively (Fig. 4). The parent textiles did not display any shielding properties, having $SE < 1$ dB.

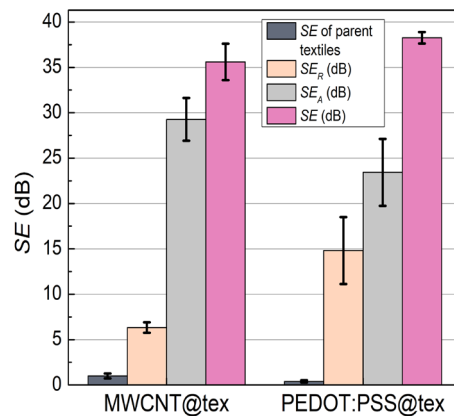


Fig. 4. Average SE (in dB) by reflection, absorption and total SE for MWCNT@tex and PEDOT:PSS@tex and the respective parent textiles.

Although the total SE values were similar for both PEDOT:PSS@tex and MWCNT@tex, from a more practical and comparative point of view, one should compare the shielding properties normalized to the thickness of the shield or to the quantity of material that was used to produce such shield. The authors consider that these normalizations are more realistic and helpful in the selection process of EMI shields for diverse applications, where thickness and lightness could be key properties (e.g., wearables and aerospace applications). Therefore, the SE was normalized to the thickness (SE/t) and weight variation ($SE/\Delta m$) and those results are summarized in Table 1. When the effect of the thickness of the sample was under investigation, the SE/t was higher for PEDOT:PSS@tex (184 dB mm^{-1}) than for MWCNT@tex (36 dB mm^{-1}). Concerning the weight, $SE/\Delta m$ was higher for MWCNT@tex (127 dB g^{-1}) than for PEDOT:PSS@tex (70 dB g^{-1}). Thus, for thinner coatings and consequently flexible textiles, PEDOT:PSS@tex would provide better shielding, while for less material usage (lighter), MWCNT@tex is preferred.

Through the SE values of the shielding materials, it is possible to classify them in 5 different grades, from excellent to fair. This classification, presented in Table 2, comprises professional use (*e.g.*, protective uniforms) and general use (*e.g.*, casual clothing, maternity wear) [19].

Table 2. Classification of the shielding effectiveness for professional and general use. Adapted from [19].

	Grade	SE range
Professional Use	Excellent	$SE > 60$ dB
	Very Good	$60 \text{ dB} \geq SE > 50$ dB
	Good	$50 \text{ dB} \geq SE > 40$ dB
	Moderate	$40 \text{ dB} \geq SE > 30$ dB
	Fair	$30 \text{ dB} \geq SE > 20$ dB
General Use	Excellent	$SE > 30$ dB
	Very Good	$30 \text{ dB} \geq SE > 20$ dB
	Good	$20 \text{ dB} \geq SE > 10$ dB
	Moderate	$10 \text{ dB} \geq SE > 7$ dB
	Fair	$7 \text{ dB} \geq SE > 5$ dB

In terms of classification, both coated textiles can be classified as moderate for professional use and as excellent for general use, according to Table 2. Hence, the developed shields grant the possibility of having high levels of SE , comparable to the reported state-of-the-art [5–10], with the advantage of being produced through facile and scalable processes that can be applied in the textile industry.

Conclusions

In conclusion, it was verified that the use of MWCNTs or the conductive polymer PEDOT:PSS was a promising strategy for EMI shielding textiles. Uniform and smooth coatings were obtained with the application processes used, dip-pad-dry for MWCNT@tex and coating for PEDOT:PSS@tex. The fabricated functional textiles displayed good electrical properties, presenting σ values of 3.99 S m^{-1} for MWCNT@tex and 31.02 S m^{-1} for PEDOT:PSS@tex. It was possible to achieve absolute SE values above 30 dB for both functional textiles: 35.6 dB for MWCNT@tex and 38.25 dB for PEDOT:PSS@tex, which are classified as excellent for general use. Moreover, PEDOT:PSS had the advantage of creating a thinner textile-based shield (184 dB mm^{-1}), while MWCNT was more effective when low material usage was desired (127 dB g^{-1}). The preferred shielding mechanism was absorption, which was more relevant in MWCNT@tex. Hence, the methods and materials used in this work are effective, scalable, suitable to industry and could be applied in a diverse range of EMI shielding applications, such as wearable items, radar protection and aerospace applications.

Acknowledgments

The work was supported by FEDER through COMPETE 2020 under the project RFProTex - POCI-01-0247-FEDER-039833, and by FCT/MCTES through national funds in the framework of the projects UIDB/50006/2020, UIDB/04968/2020, UIDB/50020/2020 and UIDP/50020/2020. AS thanks FEDER through COMPETE 2020 for PhD scholarship (POCI-01-0247-FEDER-039833). OSGPS acknowledges FCT funding under the Scientific Employment Stimulus - Institutional Call CEECINST/00049/2018. CP thanks FCT for the FCT Investigator contract IF/01080/2015.

References

- [1] C. Liu, L. Wang, S. Liu, L. Tong, X. Liu, Fabrication strategies of polymer-based electromagnetic interference shielding materials, *Adv. Ind. Eng. Polym. Res.* 3 (2020) 149–159. <https://doi.org/10.1016/j.aiepr.2020.10.002>.
- [2] F. Batool, S., Bibi, A., Frezza, F., Mangini, Benefits and hazards of electromagnetic waves, telecommunication, physical and biomedical: A review, *Eur. Rev. Med. Pharmacol. Sci.* 23 (2019) 3121–3128. https://doi.org/10.26355/eurrev_201904_17596.
- [3] M. Jaroszewski, S. Thomas, A. V. Rane, *Advanced Materials for Electromagnetic Shielding*, John Wiley & Sons, Inc., Hoboken, NJ, USA, 2018. <https://doi.org/10.1002/9781119128625>.
- [4] D. Jiang, V. Murugadoss, Y. Wang, J. Lin, T. Ding, Z. Wang, Q. Shao, C. Wang, H. Liu, N. Lu, R. Wei, A. Subramania, Z. Guo, Electromagnetic Interference Shielding Polymers and Nanocomposites - A Review, *Polym. Rev.* 59 (2019) 280–337. <https://doi.org/10.1080/15583724.2018.1546737>.
- [5] B.P. Singh, V. Choudhary, P. Saini, R.B. Mathur, Designing of epoxy composites reinforced with carbon nanotubes grown carbon fiber fabric for improved electromagnetic interference shielding, *AIP Adv.* 2 (2012) 022151. <https://doi.org/10.1063/1.4730043>.
- [6] M. Sang, S. Wang, S. Liu, M. Liu, L. Bai, W. Jiang, S. Xuan, X. Gong, A Hydrophobic, Self-Powered, Electromagnetic Shielding PVDF-Based Wearable Device for Human Body Monitoring and Protection, *ACS Appl. Mater. Interfaces.* 11 (2019) 47340–47349. <https://doi.org/10.1021/acsami.9b16120>.
- [7] L. Zou, C. Lan, X. Li, S. Zhang, Y. Qiu, Y. Ma, Superhydrophobization of cotton fabric with multiwalled carbon nanotubes for durable electromagnetic interference shielding, *Fibers Polym.* 16 (2015) 2158–2164. <https://doi.org/10.1007/s12221-015-5436-1>.
- [8] S. Ghosh, S. Ganguly, S. Remanan, N.C. Das, Fabrication and investigation of 3D tuned PEG/PEDOT: PSS treated conductive and durable cotton fabric for superior electrical conductivity and flexible electromagnetic interference shielding, *Compos. Sci. Technol.* 181 (2019) 107682. <https://doi.org/10.1016/j.compscitech.2019.107682>.
- [9] L. Li, B. Sun, W. Li, L. Jiang, Y. Zhou, J. Ma, S. Chen, X. Ning, F. Zhou, Flexible and Highly Conductive AgNWs/PEDOT:PSS Functionalized Aramid Nonwoven Fabric for High-Performance Electromagnetic Interference Shielding and Joule Heating, *Macromol. Mater. Eng.* (2021) 2100365. <https://doi.org/10.1002/mame.202100365>.
- [10] H. Lai, W. Li, L. Xu, X. Wang, H. Jiao, Z. Fan, Z. Lei, Y. Yuan, Scalable fabrication of highly crosslinked conductive nanofibrous films and their applications in energy storage and electromagnetic interference shielding, *Chem. Eng. J.* 400 (2020) 125322. <https://doi.org/10.1016/j.cej.2020.125322>.
- [11] J. Kruželák, A. Kvasničáková, K. Hložeková, I. Hudec, Progress in polymers and polymer composites used as efficient materials for EMI shielding, *Nanoscale Adv.* 3 (2021) 123–172. <https://doi.org/10.1039/D0NA00760A>.
- [12] M. Qiu, Y. Zhang, B. Wen, Facile synthesis of polyaniline nanostructures with effective electromagnetic interference shielding performance, *J. Mater. Sci. Mater. Electron.* 29 (2018) 10437–10444. <https://doi.org/10.1007/s10854-018-9100-6>.
- [13] H.K. Kim, M.S. Kim, S.Y. Chun, Y.H. Park, B.S. Jeon, J.Y. Lee, Y.K. Hong, J. Joo, S.H. Kim, Characteristics of electrically conducting polymer-coated textiles, *Mol. Cryst. Liq. Cryst.* 405 (2003) 161–169. <https://doi.org/10.1080/15421400390263550>.

-
- [14] W.-L. Song, X.-T. Guan, L.-Z. Fan, W.-Q. Cao, C.-Y. Wang, M.-S. Cao, Tuning three-dimensional textures with graphene aerogels for ultra-light flexible graphene/texture composites of effective electromagnetic shielding, *Carbon N. Y.* 93 (2015) 151–160. <https://doi.org/10.1016/j.carbon.2015.05.033>.
- [15] M. Dai, Y. Zhai, Y. Zhang, A green approach to preparing hydrophobic, electrically conductive textiles based on waterborne polyurethane for electromagnetic interference shielding with low reflectivity, *Chem. Eng. J.* 421 (2021) 127749. <https://doi.org/10.1016/j.cej.2020.127749>.
- [16] C. Xu, J. Zhao, Z. Chao, J. Wang, W. Wang, X. Zhang, Q. Li, Developing thermal regulating and electromagnetic shielding textiles using ultra-thin carbon nanotube films, *Compos. Commun.* 21 (2020) 100409. <https://doi.org/10.1016/j.coco.2020.100409>.
- [17] A. Sousa, R. Matos, J. Barbosa, J. Ferreira, G. Santos, A. Silva, J. Morgado, P. Soares, S.A. Bunyaev, G.N. Kakazei, J.A. Moreira, O.S. Soares, M.F. Pereira, C. Freire, C. Pereira, A.M. Pereira, Production of electromagnetic shielding textiles based on industrial-grade multi-walled carbon nanotubes and graphene nanoplatelets by dip-pad-dry process, Under Revision (2021).
- [18] M. González, J. Pozuelo, J. Baselga, Electromagnetic Shielding Materials in GHz Range, *Chem. Rec.* 18 (2018) 1000–1009. <https://doi.org/10.1002/tcr.201700066>.
- [19] S. Palanisamy, V. Tunakova, J. Militky, Fiber-based structures for electromagnetic shielding – comparison of different materials and textile structures, *Text. Res. J.* 88 (2018) 1992–2012. <https://doi.org/10.1177/0040517517715085>.

CHAPTER 2:

Technical Textiles and Fibers for Reinforcing Composite Materials

Tetrahedral Profiled Carbon Rovings for Concrete Reinforcements

Paul Penzel^{1,a*}, Maximilian May^{2,b}, Lars Hahn^{1,c}, Chokri Cherif^{1,d},
Manfred Curbach^{3,e}, Viktor Mechtcherine^{4,f},

¹Technische Universität Dresden, Institute of Textile Machinery and High Performance Material Technology (ITM), Hohe Str. 6, 01069 Dresden, Germany

²CARBOCON GMBH, Ammonstraße 72, 01067 Dresden, Germany

³Technische Universität Dresden, Institute of Concrete Structures, 01062 Dresden, Germany

⁴Technische Universität Dresden, Institute of Construction Materials, 01187 Dresden, Germany

^apaul.penzel@tu-dresden.de, ^bm.may@carbocon-gmbh.de, ^clars.hahn@tu-dresden.de,

^dchokri.cherif@tu-dresden.de, ^emanfred.curbach@tu-dresden.de,

^fviktor.mechtcherine@tu-dresden.de

Keywords: carbon reinforced concrete; bond behavior; bond mechanisms; profiling technology; tensile test; bond test

Abstract. Textile reinforcements have established themselves as a convincing alternative to conventional steel reinforcements in the building industry. Due to their high load-bearing capacities in addition to a smaller concrete cross section required, the bond between textile and concrete is extremely important. In contrast to ribbed steel bars ensuring a stable mechanical interlock with concrete (form fit), the bond force of carbon rovings has so far been transmitted primarily via the coating of the textile, i.e. by an adhesive bond with the concrete matrix (material fit). However, this material fit must be activated over relatively large yarn areas, which does not allow material-efficient utilization of the mechanical load capacity of the textile reinforcement. Solutions involving profiled rovings promise significant improvements in the bonding behavior by creating an additional mechanical interlock with the concrete matrix. In order to achieve a form-fit effect between roving and concrete, a roving geometry inspired by ribbed steel bars has to be created. For this purpose, an innovative profiling process was developed and implemented.

Introduction

In the past two decades the use of textile reinforcements in concrete has been a well researched topic and in recent years [1]-[6] they have established themselves as a worthwhile alternative to reinforcing steel in the building industry. Especially their high tensile properties with up to three times the tensile strength of steel and their high load-bearing capacities in combination with the alkali resistance of the carbon fibers makes them stand out compared to conventional steel reinforcements, that need a comparatively thick concrete overlay of about 60 mm to protect them for outside influences, such as moisture, as an eventual corrosion can lead to a decrease of the material strength [7].

In face of the climate change and considering the high CO₂ emission for concrete production, the reduced material use in carbon reinforced concrete (CRC) proves to be a promising alternative for a new sustainable and lasting building style. One major step for a standardized application of biaxial textile structures was the introduction of the first general building approval for strengthening of steel reinforced constructions under bending with textile reinforced concrete in 2014 [8].

Because of the high load-bearing capacities of the textile structure (e.g. tensile strength ≥ 3000 MPa and tensile stiffness ≥ 200 GPa) in addition to a reduced concrete cover of about 10-20 mm [7], high demands are to be made on the bond between textile and the surrounding concrete matrix. The bond between cementitious matrix and reinforcement can be generally characterized by three different mechanisms: the adhesive bond (material fit), a mechanical interlock (form fit) and friction (Fig. 1), e.g. [9], [10].

Depending on the fiber material, yarn processing, impregnation and profile of the yarn, the proportion of the individual bond mechanisms and most important of all, the total bond resistance, vary. In

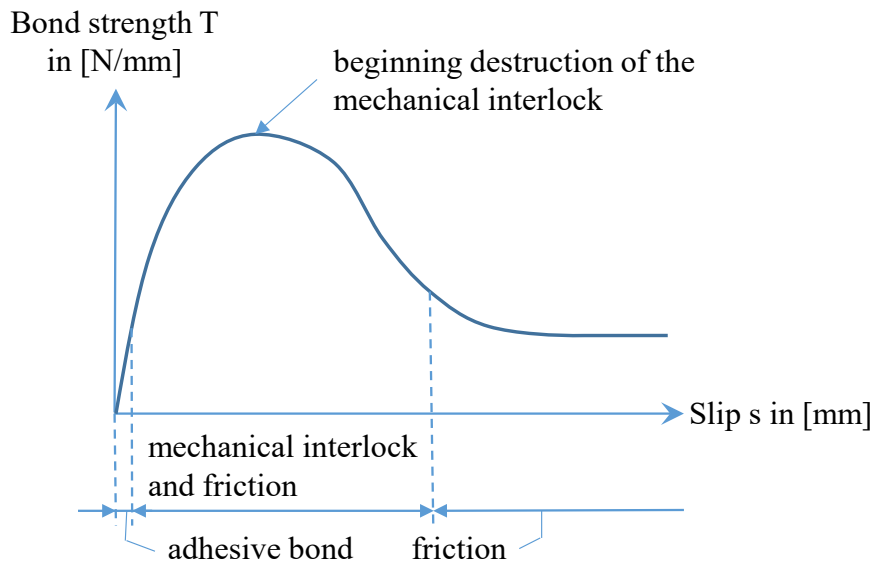


Figure 1. Schematic diagram of the bond mechanism in dependence on the slip (acc. to [10])

contrast to ribbed steel bars, that create a stable mechanical interlock resulting in a high transmittable bond stress through the defined rib geometry, the bond stress of carbon rovings has so far been transmitted primarily through an adhesive bond with the surrounding concrete matrix via the coating of the textile and friction [1], [11], [12]. Compared to the form fit effect of profiled rebars, only relatively small bond stresses can be transmitted via the material fit of unprofiled rovings resulting in an inefficient use of the mechanical load capacity of the textile reinforcement [13]. Therefore solutions involving profiled rovings promise significant improvements in the bonding behavior by creating an additional mechanical interlock with the surrounding concrete matrix [14].

In order to achieve a form-fit effect between a fiber-based reinforcement and concrete, a defined reinforcement geometry has to be created. Hereby various methods for the surface modification have been developed and tested in the past years. For example, surface treatments such as subtractive milling allows strong and defined surface profiles, but also additive methods like over-braiding, sand coating, wrapping and the application of plastic ribs are possible, see e.g. [10], [13], [15]-[24]. All these methods have the fundamental deficit that the applied profile fails or shears off by surpassing higher bond forces because of a failure of the inner bond of the reinforcement (e.g. with milled ribs) or of the bond between yarn resp. bar and additionally applied surface structure. Solutions with a profile implemented in the yarn structure itself allow a permanent and durable roving geometry [25]. Well known methods are for example braiding, twisting, cabling and winding of the yarn [7]. A decisive disadvantage of these yarn profiling methods is the principle-related yarn elongation under stress and the telescopic failure of the yarn because of the newly created core sheath yarn structure [26]. These properties makes those yarn structures unsuitable for concrete reinforcement, because an increased elongation before complete load bearing after the failure of the concrete matrix results in increase crack openings [27]. Therefore, profiling processes are needed, that maintain the high tensile properties of the carbon fibers yet ensuring a permanent and bond-optimized roving geometry [25], [26]. For this purpose, a completely new and innovative yarn shaping process was developed and implemented at the Institute of Textile Machinery and High Performance Material Technology (ITM), where the roving obtains a patented tetrahedral shape through a complete geometrical profiling [28]. Hereby the shaping of the roving distinguishes itself by a uniform reorientation of all filaments, yet ensuring a sectional linear orientation of each filament in the roving for minimizing yarn elongation under load [25].

Materials and Methods

Profiled carbon rovings were produced from 3,200 tex carbon fiber heavy tows (CFHT) with 48 k filaments from Teijin Carbon, Germany (TENAX-E STS40 F13 [29]). As impregnation agent, an aqueous polymer dispersion on acrylate basis with 50 % solid content called TECOSIT R H- 0N from the company CHT Germany GmbH was selected. For the profiling of the carbon rovings, a newly developed profiling unit was used. This unit consists of two profile bars with alternately intersecting pins that interlock when the unit is closed. Within the cavity between the interlocking bars the roving is shaped into the new geometry, whereas the roving is compacted at the touching pins. During the shaping process, the CFHT acquires a new and innovative geometry in the form of a tetrahedral shape (Fig. 2 (a)) with a profile spacing of 20 mm and a defined deviation from the linear course on the roving surface (Fig. 2 (b)) [7]. The properties of the profile can be described by the difference between the maximum and minimum diameter in a cross-sectional taper (Fig. 2 (c)). The special feature of this geometry is the uniform reorientation of all filaments within the roving. Through the consolidation of the polymer matrix under IR radiation, the profiling is permanently stabilized.

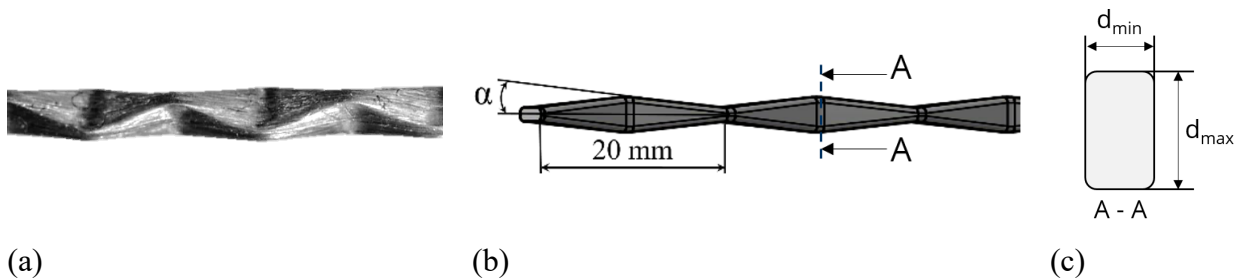


Figure 2. Profiled carbon roving with a tetrahedral geometry; original (a) and schematic (b) illustration and a schematic cross-section (c)

As a reference (Ref) for the tensile properties of the profiled rovings, a un-impregnated roving from a spool (Ref-Spool) (3,200 tex 48 k TENAX-E STS40 F13 [29]) and an impregnated, unprofiled roving from a commercial textile reinforcement (Ref-Textile) called SITgrid 040 from the company Wilhelm Kneitz Solutions in Textile GmbH (Germany) with the same impregnation agent and roving material was used (Fig. 5 (a)). This textile was extensively tested during the Carbon-Concrete-Composite (C³) - project [30] and represents a reliable reference.

Yarn profiling technology

The general profiling process including the impregnation is illustrated in Fig. 3.

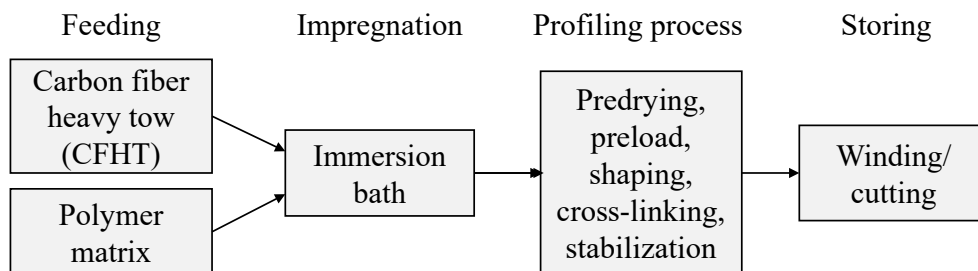


Figure 3. Schematic diagram of the profiling process

The profiling is divided into four separate process sections. First of all, the CFHT and the polymer dispersion are stored separately. Before the shaping, a single CFHT is completely immersed into the impregnation agent with no tension applied. This enables a very good impregnation, because the polymer can penetrate the entire roving cross-section and also embeds the core filaments well, resulting in an improved inner bond, thereby leading to a uniform activation of all filaments under load and thus to a homogeneous stress distribution in the yarn's cross-section. The immersed roving is then placed in the profiling unit with the unique profiling tools, that when closed form a cavity as a negative to the tetrahedral shape. Hereby the roving is uniformly shaped into the new geometry,

which is then stabilized via infrared radiation. During the stabilization the water of the polymer dispersion is evaporated until only the polymer is left. After the cross-linking is completed, the roving is cooled and removed from the unit.

For first test, a prototype unit was used, that allows a static production of defined roving lengths. In order to produce continuously, a laboratory unit (Fig. 4) with the same general process was built at the ITM [31]. In contrast to the prototype unit, two circumferential chains with profiling tools define the shape of the roving geometry. The profile itself can be varied through the vertical distance of the interlocking profiling tools between the upper and lower chain. To ensure a high reproducible quality the impregnated roving is clamped between the interlocking tools during the drying, cross-linking and cooling until the shape is permanently stabilized. Because of the continuous production, quasi-endless rovings can be produced. Due to their flexibility, they can be wound up and stored as a coil which allows universal applications for further textile processing.

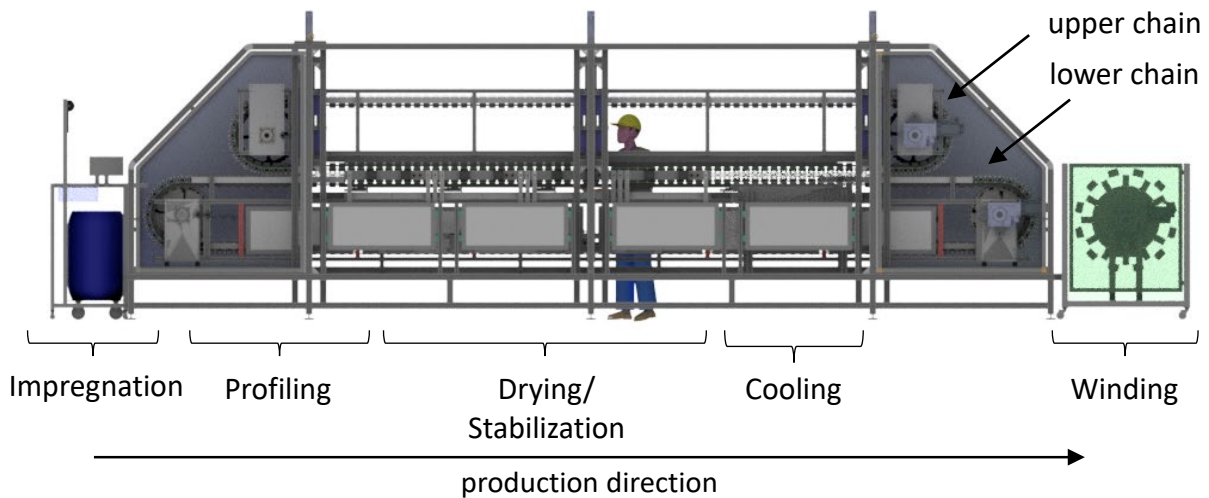


Figure 4. Schematic illustration of the laboratory profiling unit

With the laboratory unit, rovings with different profile characteristics were produced. In Fig. 5 the different roving characteristics and their schematic cross-sections are illustrated.

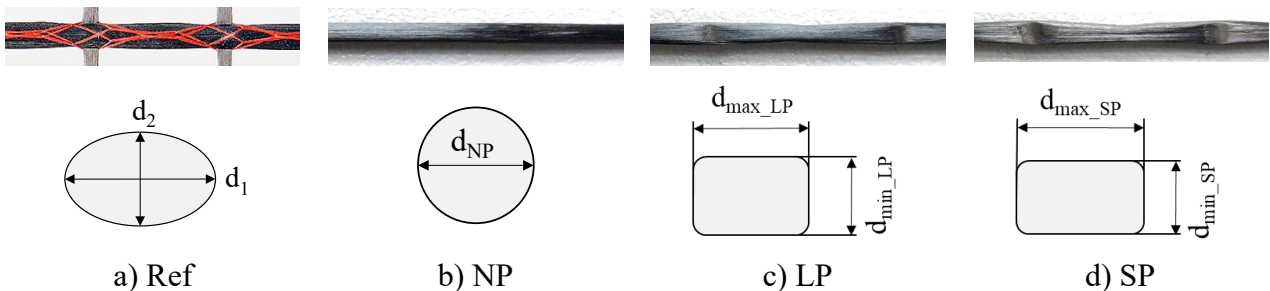


Figure 5: Rovings with different profile characteristics; a) Ref-Textile, b) NP, c) LP, d) SP

For a direct comparison to the reference textile, at first rovings with no profile (NP) (Fig. 5 (b)) were produced by increasing the vertical distance between the profile tools, that no shaping of the CFHT happened. Then, profiled rovings with different profile heights were produced by successively decreasing the vertical distance of the profile chains. So, rovings with a light (LP) and a strong profile (SP) were produced (Fig. 5 (c) and (d)). The difference between the minimum and maximum diameter for defining the profile strenght of the LP-rovings was about 0.6 mm and for the SP-rovings approximately 1.0 mm. The NP-roving had a circular cross-section with a diameter of 2.2 mm. The roving extracted from the reference textile (Fig. 5 (a)) had a relatively undefined oval cross-section due to the warp-knitting process and constriction of the knitting thread. For determination of the tensile strength, the proportion of the impregnation in the cross-section area was not taken into account. It was defined by the smallest packing density of the filaments. With a fiber density of 1.77 g/cm³ and a fineness of 3,200 tex, the resulting cross-sectional area of the yarn is 1.81 mm².

Tensile tests on pure yarns

For the determination of the tensile properties of the different rovings, a yarn from spool (Ref-Spool), a roving from the reference textile SITgrid 040 (Ref-Textile) as well as an unprofiled (NP) and a light profiled (LP) roving, were tested. The yarn from spool was tested according to ISO 3341 [32] with wrap clamps. Due to the stiffness of the impregnated rovings resulting in filament damage when wrapped around the clamps, the ends of the single yarns have been resinated and clamped between metal clamps with a pressure of 35 bar. The tests were conducted acc. to DIN EN ISO 10618 [33]. For comparability of the results between the yarn from spool and the impregnated rovings, examinations of the influence of the clamping method on the determined tensile properties e.g in [34], especially for profiled rovings, are needed.

The free yarn length of the impregnated rovings was 200 mm. During the testing with a test speed of 3 mm/min, the entered force and elongation were recorded using reflex markers on the yarn and optical sensors. All tensile tests on pure yarns were performed with the testing machine Zwick 100. The testing parameters are shown in Tab. 1.

Table 1: Pre-adjustments for the tensile strength testing methods

Testing method	ISO 3341 [32]	DIN EN ISO 10618 [33]
Sample holder	Wrap clamps SPH50, steel smooth	Metal clamps Demgen, steel file cut, 50 x 60 mm, 35 bar
Force tensor	100 kN	100 kN
Position encoder	Optical elongation	Optical elongation
Pre-force	10 N	10 N
Velocity of E-module	500 mm/min	3 mm/min
Velocity of testing	500 mm/min	3 mm/min
Clamping length	500 mm	200 mm
Test specimens	Ref-spool	Ref-Textile, NP, LP, SP
Specimen preparation	Yarn from spool	Impregnated roving with resinated clamping area

Tensile test on the CRC composite

For the tensile test on CRC samples, several yarns were clamped in a plastic framework to ensure a parallel and stretched position in the middle of the sample. Then, the fine grained concrete (Pagel TF10 [8], [35]) was filled in through a lamination process. The production of the specimens is shown in Fig. 6.

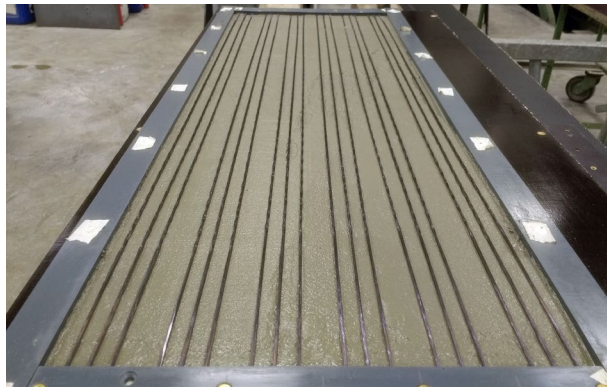


Figure 6. Manufacturing of the specimen for the tensile tests on CRC composite

The 1140 mm long, 10 mm thick and 500 mm wide plate was then covered with damp cloths. After three days, the plate was demoulded and stored for 4 days in a water bath. Then it was stored in a climate chamber until the tensile tests. At an age of circa 28 days, the plate was sawn in 6 cm wide stripes. Every stripe contained three profiled rovings.

The tests were carried out at 20 °C at the Otto-Mohr-Laboratory of the Technische Universität Dresden. Information about the test set-up and the path-controlled test procedure can be found in [36]. During the tests, the machine force and way were recorded as well as the elongation of the middle part of free specimen length with two displacement transducers with a measuring length of 200 mm.

Bond tests

For the analysis of the bonding behavior, this study focused on the pull-out test results. Pull-out specimens for testing purposes were created by embedding the profiled carbon rovings in a fine concrete drymix (binder compound BMK 45-220-2) in a cube formwork at the Institute of Construction Materials of the Technische Universität Dresden. Hereby the specimens consist of two centered concrete blocks at the yarn ends and a free yarn segment of 120 mm in-between the blocks. The embedment length at the upper concrete block was set to 50 mm with a concrete cover of 40 mm and for a defined yarn fixing the lower concrete block has an increased embedment length of 90 mm. The specimens are fixed in an upper and lower specimen holder and the pull-out strength was measured by a single-sided pull-out from the upper concrete block with a controlled quasi static load. The pull-out-length is measured through an optical system consisting of a laser sensor head and aluminium clips, which are fixed to the yarn. To determine the characteristic bond-slip relationship, the specimens were tested at 20 °C exactly 28 days after the embedment. Different specimens (Fig. 5 b, c, d) were tested from rovings with no profile, with a light profile and with a strong profile, all produced on the laboratory unit.

Results and Discussion

The following two diagrams show the mean-values of the tensile strength (Fig. 7 left) and the Young's modulus (Fig. 7 right) with the single standard deviation of the different series of roving configurations. For each series, a minimum of seven single specimens were tested.

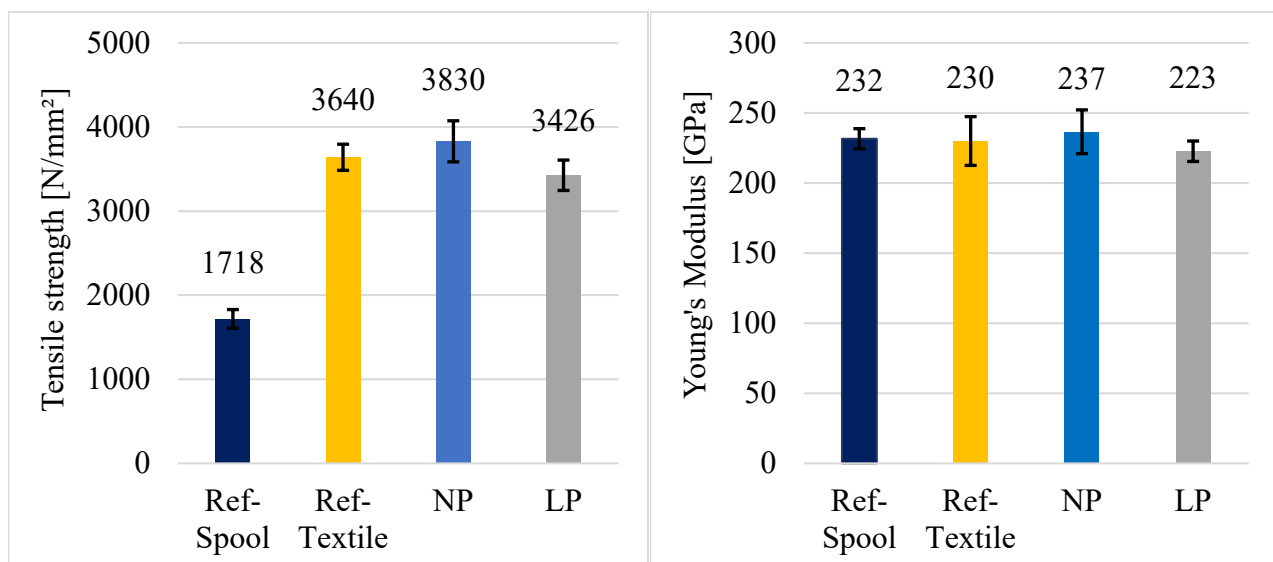


Figure 7. Tensile strength (left) and Young's Modulus (right) of different CFHTs

The tensile tests have shown that the impregnated rovings have at least twice the tensile strength of the roving without impregnation (Fig. 7 left). As described before, the impregnation improves the tensile strength due to a higher inner bond between the filaments and their more uniform activation. With about 3,800 N/mm², the unprofiled roving from the laboratory unit achieves the highest tensile strength of all roving configurations. The thesis is that the impregnation in the immersion bath, with

minimal tension applied to the yarn, results in a more even distribution of impregnation in the roving and reduced air gaps between the fibers compared to warp-knitted rovings with subsequent impregnation, leading in a better material utilization. In order to proof this thesis, microsection analysis are carried out in further examinations. The profiled roving from the laboratory unit with a mean value of about 3,400 N/mm² achieves almost the same tensile strength as the reference textile with 3,600 N/mm².

The Young's modules of the different yarn configurations are illustrated in Fig. 7 (right). All rovings showed approximately the same values of about 230 GPa. Most interesting is the Young's modulus of the profiled yarn with about 220 GPa. This illustrates, that the profiling has only a marginal influence on the tensile properties of the roving and due to the defined deviation of the filament course with a uniform filament length, the profiled roving maintained the high tensile properties. It had comparable properties to the impregnated, unprofiled yarn extracted from the reference textile (Ref-Textile) and is therefore suitable for concrete reinforcements with high tensile stiffness [27]. It is also noticeable, that the profiled roving had a reduced standard deviation compared to the reference textile, which indicates uniform and consistent material properties due to a reproducible process.

In the following diagram (Fig. 8) the mean value curve of tensile tests on the profiled rovings embedded in the concrete matrix are displayed. Hereby, the characteristic crack formation process of the composite starting at about 0.2 % elongation is recognizable. With increasing load, more cracks form until the completed crack pattern is reached. In the following, the complete load is carried by the textile reinforcement until failure. Remarkable is the high tensile strength of the profiled rovings, achieving a mean value of 3,550 N/mm². The strength increase of the composite compared to that of the single rovings resulted from the different load application on the roving. In the yarn tensile test, the entire, single roving is under load until the weakest roving section fails. During the tensile test of the composite only sections of the roving in the cracks are fully stressed, and the load is distributed between the three embedded rovings. Therefore, the weakest section is less likely to be tested, resulting in higher tensile strengths.

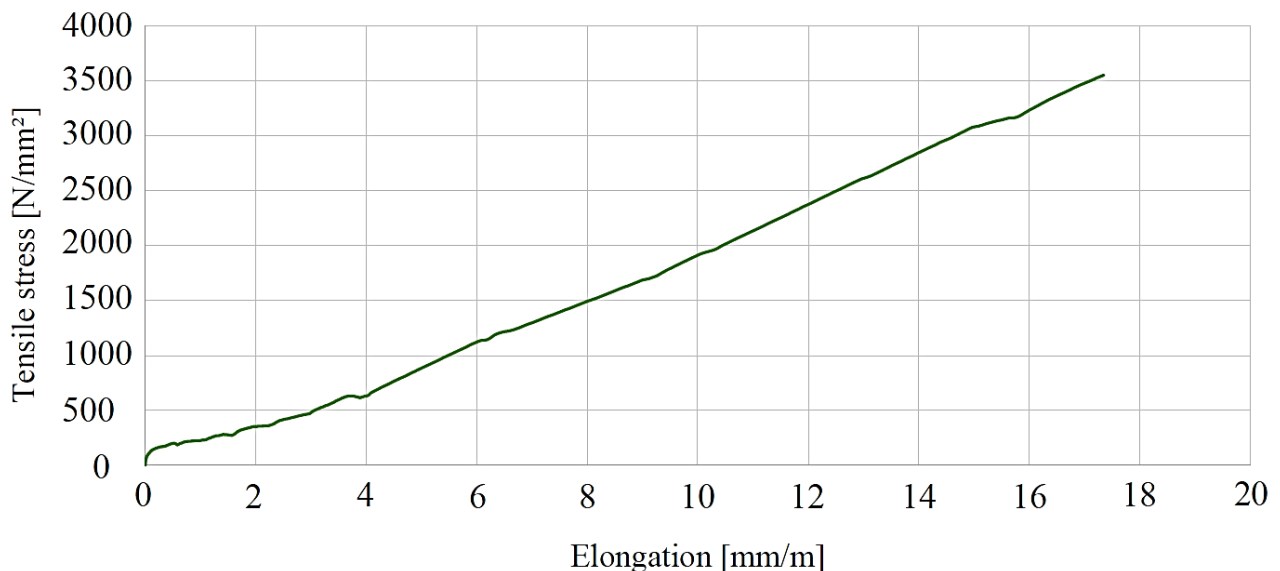


Figure 10. Tensile stress-elongation curve of profiled rovings embedded in fine concrete, mean value curve

The characteristic bond behavior of different profiled carbon rovings (Fig. 5 c, d) in concrete is shown in comparison with an unprofiled roving (Fig. 5 b) in Fig. 9 as mean value curves of five single tests each. Hereby the mean value of the maximum transmitted bond stress is displayed in the diagram.

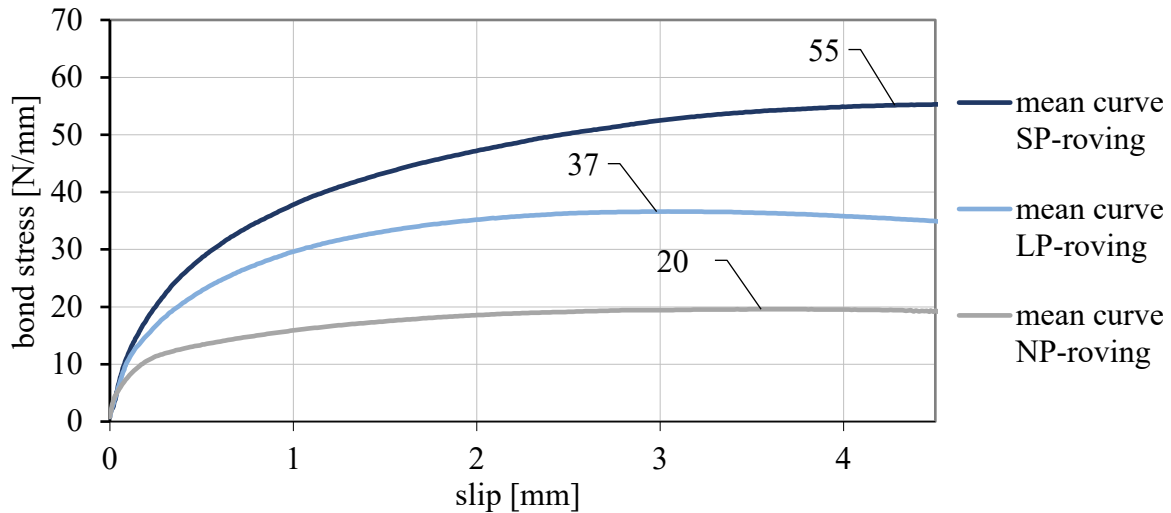


Figure 9. Bond stress-slip relationship of the different profiled rovings, determined on samples with a concrete cover of 40 mm and an embedment length of 50 mm at 20 °C; SP – strong profile, LP – light profile, NP – no profile

Due to the improved mechanical interlock of the profiled rovings, the resulting bond strengths are well above that of rovings with no profile. The diagram shows, that rovings with a strong profile transmit up to 2.5 times the bond force of rovings with no profile. Light profiled rovings achieve almost twice the maximum bond strength of unprofiled ones.

Hence, the defined tetrahedral profiling shows three effects. On the one hand, the rovings offer enhanced bond stiffness, recognisable by the steeper slope of the curve, and on the other hand they provide increased pull-out resistance. The results thus show that it is possible to influence the bond properties through a defined profile geometry. Furthermore, the profiling process does not negatively influence the tensile load-bearing behavior.

Conclusion

Results show that the newly developed profiled carbon rovings are able to transmit higher pull-out loads and demonstrate a significantly improved bond-slip behavior compared to straight fiber strands, yet maintaining their high tensile properties making them particularly suitable as concrete reinforcement. The creation of a form-fit based on a uniform reorientation of all filaments enhances the bonding between carbon rovings and concrete matrix. In conclusion, the newly developed profiled carbon rovings make an important contribution to the production of high performance CRC structures with significantly better bond behavior and enhanced material efficiency. To enable the industrial application, an automated laboratory unit has been developed at the ITM of the TU Dresden.

In order to produce profiled, grid-like textile reinforcement structures for concrete applications (Fig. 10), conventional textile manufacturing processes for the production of textile reinforcement structures, such as the multiaxial warp knitting technology, have to be adapted and further developed. Optimization of the roving geometry through a fundamental analysis of the bonding mechanisms between the concrete matrix and the profiled roving will be the subject of future research. Furthermore an analysis of the uniform reshaping of the filaments through micrographic examinations will be part of further studies.

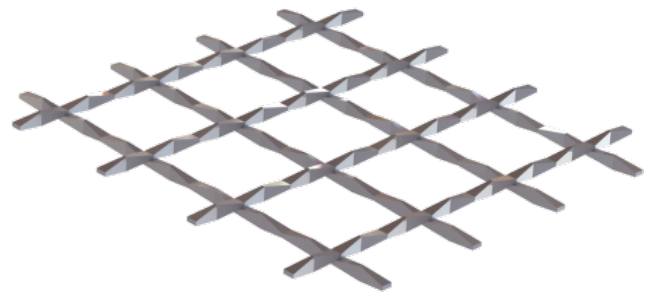


Figure 10. Modell of a grid-like textile structure with tetrahedral profiled CF rovings

Acknowledgement

The IGF research project 21375 BR of the Forschungsvereinigung Forschungskuratorium Textil e. V. is funded through the AiF within the program for supporting the „Industriellen Gemeinschaftsforschung (IGF)“ from funds of the Federal Ministry for Economic Affairs and Climate Action on the basis of a decision by the German Bundestag.

We thank the mentioned institutions for providing the financial means. We would also like to thank all involved companies for their technical support and the provision of test material as well as all other partners who supported us in the research on this topic.

References

- [1] Curbach, M.; Ortlepp, R. (Editor): *Textile Bewehrungen zur bautechnischen Verstärkung und Instandsetzung – Abschlussbericht des SFB 528*. TU Dresden, 2012
- [2] Hegger, J.; Will, N.; Schneider H. N.; Kölzer, P.: *Neue Bauteile aus textilbewehrtem Beton*. In: *Beton- und Stahlbetonbau* 99 (2004), Nr. 6, pp. 68–71
- [3] Curbach, M.: *CUBE - Ergebnishaushaus des C³-Projekts*. In: *Tagungsband der 10. Carbon- und Textilbetontage*, 2018, pp. 102–103
- [4] Triantafillou, T. (Editor): *Textile Fibre Composites in Civil Engineering*. Amsterdam: Elsevier/Woodhead Publishing, 2016
- [5] Bentur, A.; Mobasher, B.; Peled, A.: *Textile Reinforced Concrete*. CRC Press, 2017
- [6] Scheerer, S.; Schladitz, F.; Curbach, M.: *Textile reinforced Concrete - from the idea to a high performance material*. In: *Brameshuber, W. (Editor.): Proceedings of the FERRO-11 and 3rd ICTRC in Aachen*. Bagneux: Rilem Publications S.A.R.L., 2015, pp. 15-33
- [7] Cherif, C. (Editor): *Textile materials for lightweight constructions: Technologies – methods – materials – properties*. Heidelberg: Springer, 2016
- [8] DIBt: *Allgemeine bauaufsichtliche Zulassung Nr. Z-31.10-182: Verfahren zur Verstärkung von Stahlbeton mit TUDALIT (Textilbewehrter Beton)*. 2014
- [9] Eligehausen, R.; Popov, E.; Bertero, V.: *Local Bond stress slip relationship of deformed bars under generalized excitations*. In: *Proceedings of the 7th European Conference on Earthquake Engineering*. Vol. 4: Techn. Chamber of Greece, 1982, pp. 69-80
- [10] Lorenz, E.: *Endverankerung und Übergreifung textiler Bewehrungen in Betonmatrices*. Doctoral thesis, TU Dresden, 2014
- [11] Hahn, L.; Rittner, S.; Nuss, D.; Ashier, M.; Cherif, C.: *Development of Methods to Improve the Mechanical Performance of Coated Grid-Like Non-Crimp Fabrics for Construction Applications*. In: *Fibres and Textiles in Eastern Europe* 27 (2019), pp. 51–58
- [12] Preinstorfer, P.; Kromoser, B.; Kollegger, J.: *Kategorisierung des Verbundverhaltens von Textilbeton*. *Bauingenieur* 94 (2019) 12, pp. 416–424
- [13] Preinstorfer, P.: *Zur Spaltrissbildung von textilbewehrtem Beton*. Doctoral thesis, TU Wien, 2019
- [14] Hengstermann, M.: *Garnstrukturen mit verbesserter Kraftübertragung durch Formschluss*. In: *Proceedings. 10. Carbon- und Textilbetontage 2018, Dresden, 25.-26.09.2018*, pp. 94-95
- [15] Schumann, A.: *Experimentelle Untersuchungen des Verbundverhaltens von Carbonstäben in Betonmatrices*. Doctoral thesis, TU Dresden, 2021
- [16] Preinstorfer, P.; Kromoser, B.; Kollegger, J.: *Einflussparameter auf die Spaltrissbildung in Textilbeton*. *Beton- und Stahlbetonbau* 113 (2018) 12, pp. 784–794

-
- [17] Pritschow, A.: Zum Verbundverhalten von CFK-Bewehrungsstäben in Bauteilen aus ultrahochfestem Beton. Doctoral thesis, Universität Stuttgart, 2016
- [18] Sayed Ahmed, M.; Sennah, K.: Pullout strength of sand-coated gfrp bars embedded in ultra-high performance fiber reinforced concrete. In: Proc. of CSCE 2014 – 4th Int. Structural Specialty Conf., 2014, pp. CST-28-1–CST-28-10
- [19] Fingerloos, F.; Hegger, J.; Zilch, K.: Eurocode 2 für Deutschland. 2. Aufl., Berlin: Ernst & Sohn/Beuth, 2016
- [20] Lin, Z.; Li, V. C.: Crack bridging in fiber reinforced cementitious composites with slip-hardening interfaces. *Journal of Mechanical and Physical Solids* 45 (1999), pp. 763–787
- [21] Schumann, A.; May, M.; Schladitz, F.; Scheerer, S.; Curbach, M.: Carbonstäbe im Bauwesen. In: *Beton- und Stahlbetonbau* 115 (2020), no. 12, pp. 962–971
- [22] Scheerer, S.; Schütze, E.; Curbach, M.: Strengthening and Repair with Carbon Concrete Composites - the First General Building Approval in Germany. RILEM Book series 15, Dordrecht: Springer, 2018, pp. 743-751
- [23] Gries, T.; Kolkmann, A.: Garnentwicklung zur zielgerichteten Beeinflussung der mechanischen Garn-Charakteristik. In: Curbach, M. (Editor): *Textile Reinforced Structures: Proc. of the 2nd Colloquium on Textile Reinforced Structures (CTRS2)*, 2003, pp. 29–40
- [24] Kolkmann, A.; Wulfhorst, B.: Garnstrukturen für den Einsatz in Textilbewehrtem Beton. In: Hegger, J. (Ed.): *Textilbeton – 1. Fachkolloquium der Sonderforschungsbereiche 528 und 532*, Aachen, Germany, 15.2.–16.02.2001, RWTH Aachen, 2001, pp. 35–44
- [25] Cherif, C.: Neuartige Profil-Carbonrovings für die Betonbewehrung. In: *Proceedings. 11. Carbon- und Textilbetontage 2019*, Dresden, 24.-25.09.2019, pp. 18–19
- [26] Hengstermann, M.; Abdkader, A.; Cherif, Ch.: Innovative oberflächenprofilerte Bewehrungsgarnstrukturen mit verbesserter Kraftübertragung im Beton. *TUDALIT-Magazin* (2019) 20, p. 7
- [27] Jesse, F.; Curbach, M.: Verstärken mit Textilbeton. In: Bergmeister, K.; Fingerloos F.; Wörner, J.-D. (Eds.): *BetonKalender 2010*, Kap. VII, Berlin: Ernst & Sohn, 2010, pp. 458–565
- [28] Waldmann, M.; Rittner, S.; Cherif, C.: Bewehrungsstab zum Einbringen in eine Betonmatrix sowie dessen Herstellungsverfahren, ein Bewehrungssystem aus mehreren Bewehrungsstäben sowie ein Betonbauteil. Technische Universität Dresden. DE 10 2017 107 948 A1. 12.04.17
- [29] Teijin Carbon Europe: Produktdatenblatt - Tenax® Filament yarn.
- [30] C³ - Carbon Concrete Composite e. V.: Homepage. www.bauen-neu-denken.de (22.09.21)
- [31] Hahn, L.; Cherif, C.: Fortschritte bei Fertigung von profilierten Carbonpolymergarnen mit höchsten Verbundeigenschaften. In: *TUDALIT-Magazin* (2020), 22, p. 1
- [32] ISO 3341:2000-05: Textilglas – Garne – Bestimmung der Reißkraft und Bruchdehnung. 2000
- [33] DIN EN ISO 10618:2004-11: Kohlenstofffasern – Bestimmung des Zugverhaltens von harzimprägnierten Garnen. 2004
- [34] Wendler, J.; Hahn, L.; Farwig, K.; Nocke, A.; Scheerer, S.; Curbach, M.; Cherif, C.: Entwicklung eines neuartigen Prüfverfahrens zur Untersuchung der Zugfestigkeit von Fasersträngen für textile Bewehrungsstrukturen. *Bauingenieur* 95 (2020) 9, pp. 325–334
- [35] PAGEL® Spezial-Beton GmbH & Co. KG: Technisches Merkblatt PAGEL®/TUDALIT®-Feinbeton. 2016
- [36] Schütze, E.; Bielak, J.; Scheerer, S.; Hegger, J.; Curbach, M.: Einaxialer Zugversuch für Carbonbeton mit textiler Bewehrung. *Beton- und Stahlbetonbau* 113 (2018) 1, pp. 33-47

Spherically Curved Woven Fabrics - Shaping on the Loom

Nuss Dominik^{1,a*}, Pham Minh Quang^{1,b}, Sennewald Cornelia^{1,c},
Hoffmann Gerald^{1,d}, Cherif Chokri^{1,e}

¹TU Dresden, Institute of Textile Machinery and High Performance Material Technology, Dresden
(Germany)

^{a*}dominik.nuss@tu-dresden.de, ^bminh_quang.pham@tu-dresden.de,
^ccornelia.sennewald@tu-dresden.de, ^dgerald.hoffmann@tu-dresden.de,
^echokri.cherif@tu-dresden.de

Keywords: Spherically curved woven fabrics, 3D net shape fabrics, woven fabrics.

Abstract. Fiber-reinforced plastic (FRP) structures are established in numerous lightweight solutions. Among textile products available for technical applications, flat woven fabrics are commonly used to produce 3D components. In order to convert the flat woven structures into 3D geometries, draping and cutting processes are applied primarily. This leads to structural distortions, yarn interruption and overlaps of the layers. Beside the resulting reduction of mechanical properties, manual work steps are necessary. 3D woven fabrics offer outstanding possibilities for realizing net-shape FRP lightweight structures while avoiding these disadvantages. A current challenge in the manufacture of 3D net-shape structures is the direct generation of desired geometry during the weaving process. The aim of the presented work is the development of a novel weaving technology that enables the creation of spherically curved woven fabrics. Constructive-technological solutions are presented and the required mathematical as well as weaving modelling is shown.

Introduction.

Textile woven fabrics are primarily produced as 2D structures on classic weaving machines and made available as rolls for further processing steps. However, three-dimensional structures are required for numerous applications. In Particular, technical textiles made of high-performance fibres for the use in composite sector must meet special requirements of complex 3D structures. In general, there are two basic processes for converting conventional 2D textiles into a three-dimensional shell-like structure. Firstly, using the fabrication process, almost any geometry can be created by cutting individual parts and then joining them by sewing or gluing. However, composite components produced in this way show overlaps of the individual cut parts at the joints, leading to thick spots in the final product. The force flow along the reinforcement yarns is interrupted at these points and the component becomes more sensitive to shear forces. This prevents an optimal exploitation of the outstanding properties of high-performance materials [1]. In addition, the individual manufacturing steps are usually associate with manual work that makes the process cost-intensive [2]. Secondly, shell-shaped preforms for fibre reinforced plastic components can be obtained from 2D textiles through draping processes. However, this process is limited in terms of producing a wrinkle-free shape. In addition, the draping capacity of the textile is significantly reduced by the use of almost stiff high-performance fibres such as carbon or glass.

As an alternative to these methods, spherically curved textile surfaces can be produced directly during the manufacturing process. The focus of numerous research activities is to reduce the process costs during preform production through concepts for the production of near-net-shape semi-finished products [3–5]. In particular, developments were made in the field of textile fabrication technology for the direct production of three-dimensional structures. In the field of knitting technology, solutions were developed for flat knitting machines as well as for multiaxial knitting machines [6–9]. In addition, there are numerous developments in the field of weaving technology [9–15].

The "Shape 3 weaving process" developed by Büsgen is particularly suitable for the fabrication of spherically curved woven fabrics [16]. In the process, a special fabric take-up is combined with a V-shaped reed that can be moved vertically up and down. Both the distance between the warp yarns and

the length of the individual warp yarns can be varied to create a 3D textile structure. The 3D fabric produced via a programmable take-up mechanism. The fabric is then cut out of the weaving plane using a frame with cutting edges. The fabric has a lower yarn density in the area of the curvature than in the surrounding area. This difference can be compensated by varying the fabric weave pattern. The Shape-3 process is limited in terms of the width of the fabric, as the use of the V-shaped reed cannot be carried out on weaving machines with width over 100 cm. In addition, no variation of the target geometry is possible without changing the fabric take-up.

Since a weaving processes is missing which combines high productivity with simultaneous variability, a new weaving process for the production of three-dimensional structures was developed in the present work. The aim is to use conventional wide weaving machines without the need for costly modification.

Description and Development of Noval Take-up-Free-Weaving-Technology.

In conventional weaving, 2D fabrics are created with constant spacings between weft and warp yarns over the entire length and width of the fabric, respectively. Within classical woven structures, the warp spacing can only be varied over the entire fabric width and the parallelism between the yarns is not cancelled. Thus, the local warp yarn distances are independent of the respective crossing weft yarns. If, on the other hand, yarn spacing of a warp yarns is changed locally with the weft yarn crossing in each case, the parallel alignment is cancelled. If these yarn spacings are now inserted in such a way that a widened area of the warp yarns is enclosed by a targeted tapering of the warp yarns or correspondingly vice versa, the fabric curves up into a spherical curvature at this point (Figure 1).

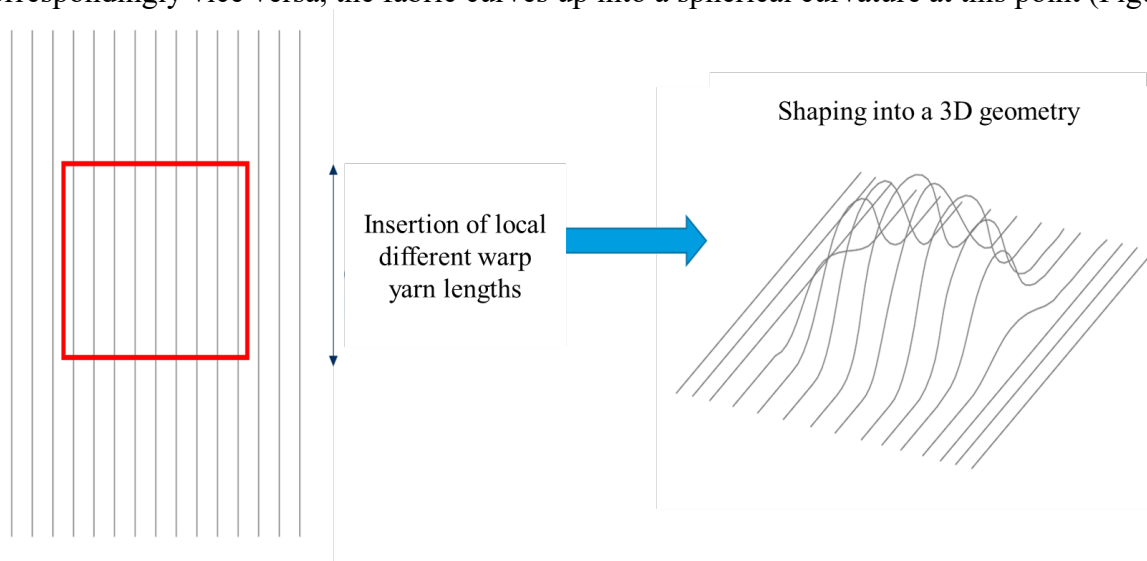


Figure 1: Creation of spherically curved structure via different warp lengths

The basic idea of the presented work is to realize these different warp lengths across the fabric width by implementing different weave patterns for the interlacing between weft and warp yarns. In fact, short weft yarns can be inserted when the number of crossing points with warp yarns reduces (Figure 2). To insert warp yarns with different lengths into certain fabric areas, it is necessary to push the corresponding weft yarns together. This is not possible by using the common take-up of a loom because all warp yarns are pulled in the same way. Therefore the take-up free weaving technology has been developed, which in combination with creel feeding system allows the maximum flexibility of inserting different warp lengths.

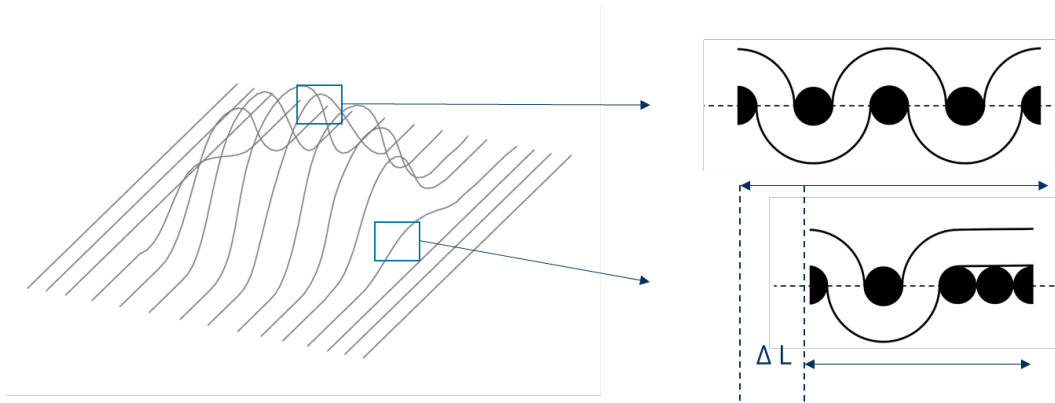


Figure 2: Insertion of different warp length via weave pattern interlacing

To insert different warp yarn lengths into the fabric by using a conventional loom it is possible not to pull on all warp yarns in the same way. The development of take-up-free weaving can avoid the need

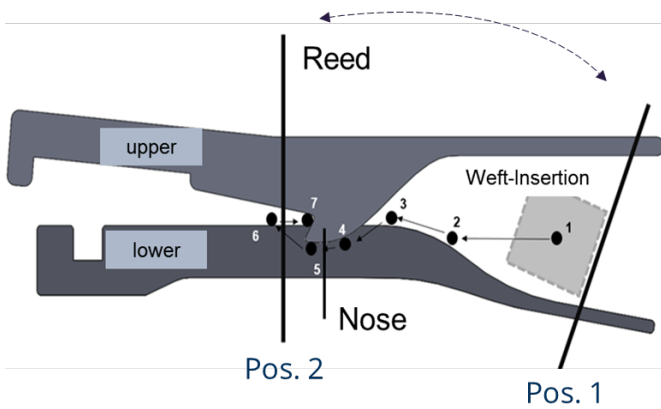


Figure 3: Hook system for take-up-free weaving

Figure 3 shows the developed construction principle. A two-part hook system is used so that the weft yarns can be entered between these hooks. Both hooks have long “tips”, which are engaged between the reed bars so that the reed will not crash the hooks. To insert the weft yarns into the fabric, the reed pushes the weft yarns over the lower hook into the nose of the upper hook when moving from position 1 to position 2 (Figure 3, steps 1-7). This ensures a smooth insertion of weft yarn and a high process reliability.



Figure 4: Installation of the weft yarn retention system

for a costly special take-up which should be able to pull on each warp separately. Therefore, a weft retention system was developed to enable take-up-free weaving. The solution involves a hook-based system, which can be installed in the fabric formation zone and locks the weft yarns during the weaving process. Additionally the slipping back into the weave formation zone and the collision with the weft insertion elements can be avoided. The movement of the fabric itself is done by beating up process of the reed.

Through the fixation of the weft yarns, the entire fabric is prevented from sliding back into the weft insertion zone. In addition, the warp tension required in the weaving process is maintained. The movement of the reed initiates the transport of the fabric itself. The developed system can be installed in a common loom. To carry out the test series, the developed weft retention system was installed and tested at a Dornier PTSJ rapier weaving machine with a Jacquard device (Figure 4). The system was assisted with a selvage bracket to improve the safety of the weft yarn insertion process.

Description of The Basics in Take-up-Free Weaving.

Without using the conventional take-up, the fabric is taken up only via the weft stop motion and warp yarns are incorporated with different lengths depending on the weave pattern. In order to create a spherically curved structure, the yarn distances must either be locally extended or reduced according to the existing curvature. By using the Jacquard technique, it is possible to control each individual warp yarn so that it performs a shed change or remains in the previous position. This makes it possible to insert different warp yarn lengths into the structure according to the number of intersections between weft and warp yarns. To calculate the different incorporation of the warp lengths by using different weaves a density factor of the weave pattern can be determined. This is calculated on the basis of the number of yarn cross-sections resulting from the intersections within a weave unit. The cross-sections are calculated for each column and row summed up and divided by the maximum possible intersection (plain weave) (Eq. 1). For example, the density factor of the weave pattern twill weave shown in Figure 5 is 0.563.

$$p = \frac{\sum_1^i b_i * \sum_1^j b_j}{R^2} \tag{1}$$

p	theoretical density factor
b _i	cross-sections along warp direction
b _j	cross-sections along weft direction
R	maximal cross-sections within the repeat size

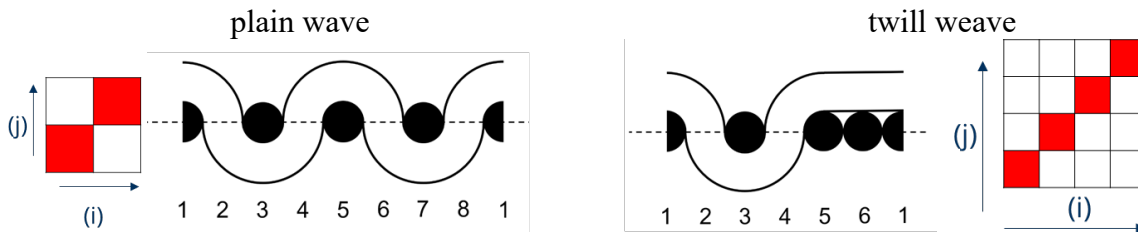


Figure 5: Calculation of theoretical density factor of twill weave

To crosslink the needed length of the warp yarns with the calculated density factor of the weave pattern, it is necessary to determine the resulting weft density. The weft density can be associated directly with the warp length to be realized by creating the ratio between the length of the curvature and the surrounded flat length (Eq. 2 and Figure 6). With this correlation, it is possible to assign the needed weave pattern to the resulting warp length.

$$\frac{\text{weft density I}}{\text{weft density II}} = \frac{\text{warp length II}}{\text{warp length I}} \tag{2}$$

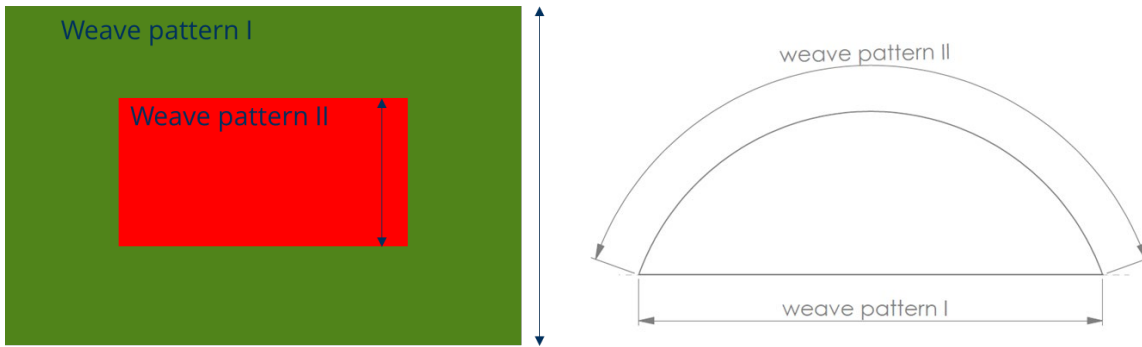
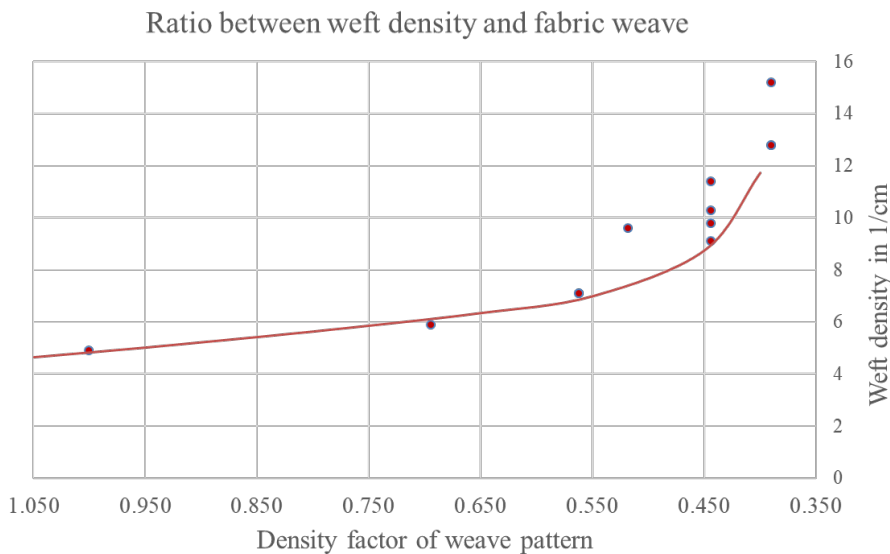


Figure 6: Calculation model of different warp lengths

Practical Investigations and Results

Developed calculation model:

To carry out the experimental work, the weft retention system was implemented in a Dornier PTSJ rapier weaving machine with a nominal width of 1400 mm. The shedding is done with a Jacquard shedding device from Stäubli with single yarn control. Glass fibre rovings with a titre of 1200 tex were used as warp and weft yarn material. A warp yarn density of 5 yarns per cm was drawn in. The warp was drawn off tangentially from a creel equipped with disc bobbins. The creel was equipped with a passive compensation so that the warp yarn tension forces are maintained accordingly during weaving.



To determine the basic relationships between the resulting weft density for corresponding weaves and the associated density factors, selected weaves were produced and evaluated within an experimental plan. For this purpose, plain weave (maximum density factor), variations of twill weaves as well as satin weaves were woven without take-up and their resulting weft density was evaluated.

Figure 7: Ratio between weft density and density factor of the weave pattern

The relationship between weft density and density factor of the present weave type is shown in Figure 7. The weft density decreases with increasing density factor. Using numerical methods, the function according to equation (3) was developed from the measuring points. Taking into account the retention of the yarn material as well as the present machine settings, this enables the determination of weft density of any weave pattern. Using the equation, the weft density of the density factor present in the target area can be determined in advance, which in turn results in an optimally screened allocation of the weave for insertion of the defined warp yarn length.

$$weft_{density} = a * e^{bp} + c * e^{dp}; 0 < p < 1 \tag{3}$$

p	theoretical density factor (with Eq. 1)	
Equation constants	a =	2.458e ⁺⁰⁴
	b =	-21.77
	c =	10.46
	d =	-0.7742

The developed equation (3) has been implemented in a program routine to assign the required weave pattern to the yarn length necessary to achieve the target geometry of the textile. The geometry is covered with points using Matlab script and the distances between these points are calculated. The distances between the points correlate to the weave rapport. The calculated lengths are set in relation to the basic length around them. The ratio is assigned to a proper weft density ratio, which in turn allows the corresponding weaves to be determined according to equation (3). The control file for the Jacquard machine is created using the EAT-Design-Scope software. For this purpose, the developed programme outputs a colour file to which the corresponding weave is assigned.

Table 1: Description of previous calculation (example of one warp yarn length)

Warp yarn length on the spherical geometry	240.35 mm
Base length	179.59 mm
Length ratio	0.75
Calculated density factor weave pattern I (for base length)	0.56 (twill 1-3)
Calculated density factor weave pattern II (for warp length)	1.0 (plain)
Weft density weave pattern I (with Eq. 3)	6.90
Weft density weave pattern II (with Eq. 3)	4.83
Weft density ratio	0.70

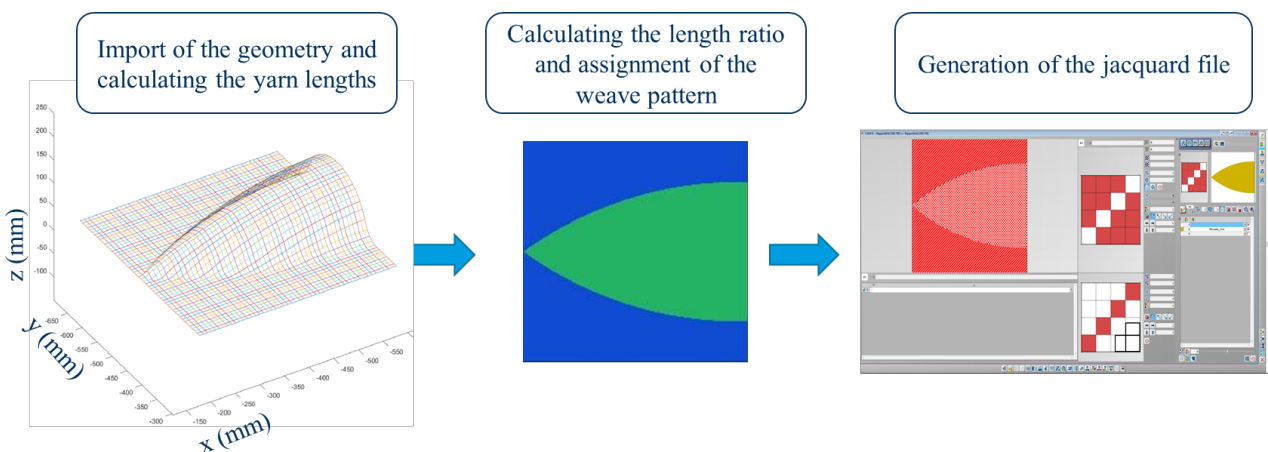
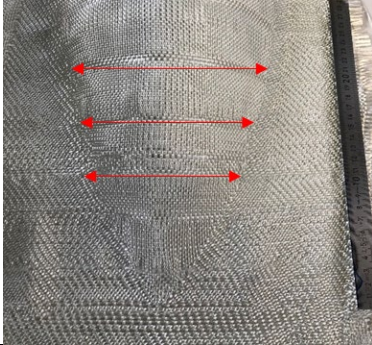


Figure 8: Developed process to determine the weave pattern arrangement

To validate the developed theory and calculation, a spherically curved functional pattern with increasing warp length was woven and analysed. Using the developed program routine the warp yarn length are calculated and the ratio has been formed. In order to check the inserted lengths, the arc lengths were measured at different points, put into the ratio and compared with the previously

calculated weft density ratio. As a result, the averaged measured warp yarn length ratio is 0.76 and thus within the previously calculated range of the weft density ratio.

Table 2: Checking the warp yarn lengths for take-up-free weaving

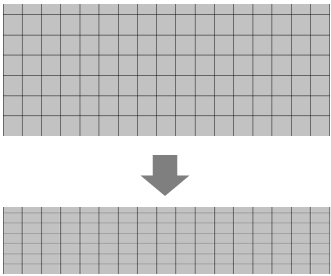
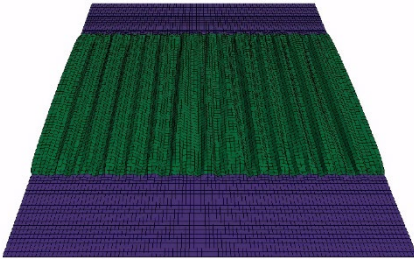

Measurement		Warp length	Basic length	Ratio
a		230 mm	170 mm	0.74
b		190 mm	148 mm	0.78
c		150 mm	115 mm	0.77

Developed simulation model:

In order to simulate the forming process of the curved fabrics, an orthotropic material model was developed using LS-DYNA. This is based on the fact that locally different changes in length are a result of the different weft densities in the fabric structure. By introducing different expansion coefficients corresponding to the calculated weft density ratios, these changes in length can be specifically simulated. The correlation between the weft density ratio and the resulting change in length was checked using the weave pattern combination shown in Table 3.

For the shaping simulation of the structure to be woven, the calculated partial surface pieces with the respective weave pattern areas were read into the LS-DYNA script in the form of the obtained pixel code output and the corresponding expansion coefficients were inserted.

Table 3: Developed process simulation

		
Input of different expansion coefficients into LS-DYNA	Simulation of different local weaving Green: plain Blue: 4/4 twill S direction	Checking the length change of the weave combination

Validation of the developed processes using a demonstrator component:

With the development and production of a spring dome demonstrator, the developed technology of take-up-free weaving was validated for the provision of directly woven three-dimensional fabric semi-finished products. For this purpose, the geometry of the CAD model (Figure 9) was imported into the developed programme and the necessary warp yarn distances were calculated. The corresponding weaves were assigned to the ratio formed and the image file was created (Table 4).

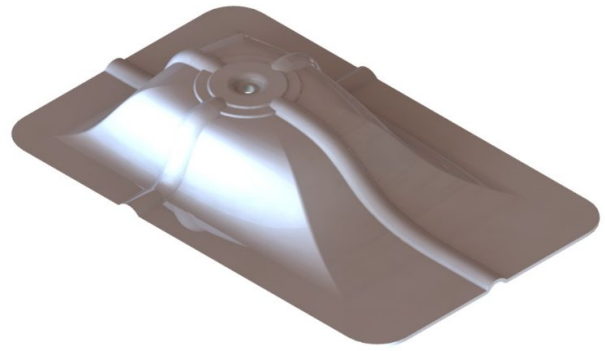


Figure 9: Demonstrator component of a spring dome

Table 4: Calculation of the different weave pattern areas of the component

Area	Weave pattern	
Red	Twill 3-3	
Blue	Twill 1-4	
Green	Twill 1-3	
Brown	Twill 1-2	
Yellow	5 end stitched twill	

Before the structure was manufactured, the mouldability was examined by using a developed simulation model. For this purpose, the strain coefficients equivalent to the weft density ratios were assigned to the corresponding weave areas. Afterwards, the moulding of the dry fabric was calculated (Figure 10).

The control file for the Jacquard machine was then created. For this purpose, the necessary weaves were created in EAT DesignScope, the image file was read in and the corresponding weaves were assigned to the subareas. The control file was read into the existing Jacquard machine and the necessary settings for the selvage bracket were made in the control system of the Dornier PTSJ weave machine. The weaving pattern was then produced and cut out of the weaving plane. The semi-finished product was finished using the existing tool, consisting of an upper and lower tool.

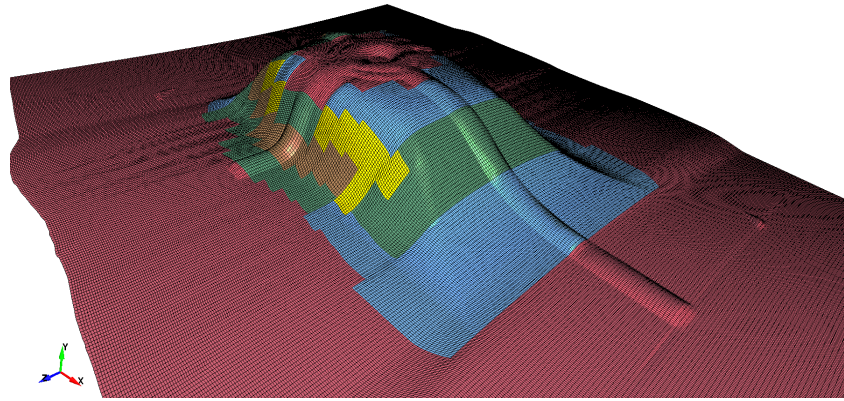


Figure 10: Simulation of the moulding process

Analyse of the preform geometry:

To analyse the dry woven preform of demonstrator (Figure 11) and to validate the developed process chain, the manufactured dry textile preform product was examined with regard to geometric accuracy. For this purpose, the textile semi-finished product was recorded by means of a laser triangulation process. The result of the scan was implemented in MatLab and compared with the CAD output geometry. For this purpose, the geometry of the CAD output model was placed in the result of the scan in such a way that the output model intersects it centrally. The result shows the deviation below (blue) and above (yellow) zero position. Taking into consideration the fabric thickness and different fabric weaves, there is a maximum deviation of ± 3 mm in the geometry of the manufactured textile semi-finished product compared to the initial model (Figure 12).



Figure 11: Moulded dry preform

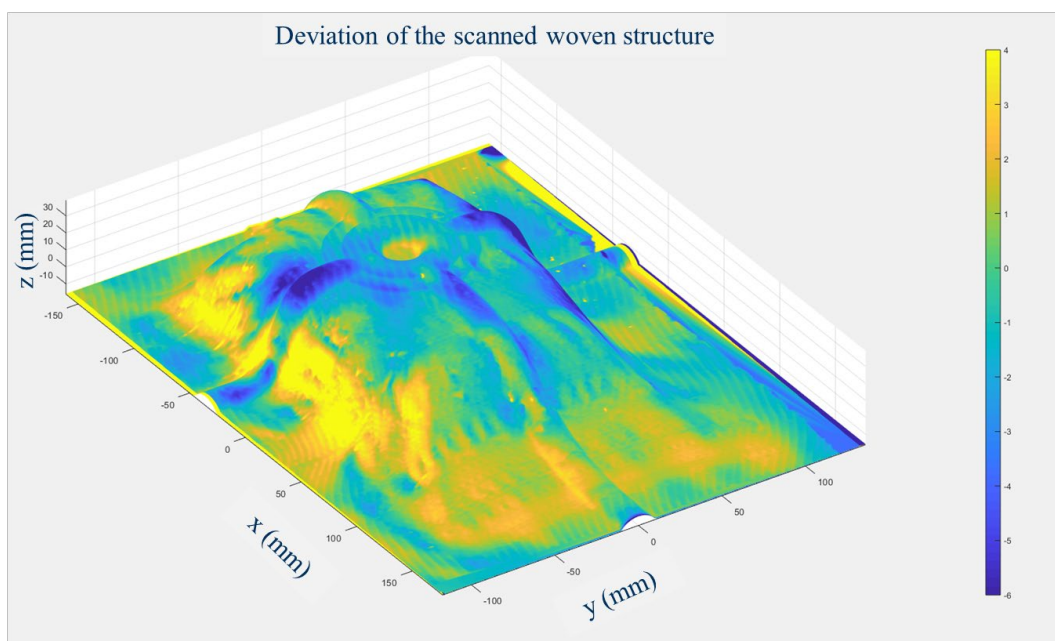


Figure 12: Deviation of the woven preform

Finishing the demonstrator:

After the investigation of the geometry of the preform, the component was finished using the vacuum infusion process, whereby the woven structure was infiltrated with epoxy resin, cured at room temperature and finally demoulded. A resin system with a mixing ratio of resin to hardener of 100 to 30, a dripping time of 100 g per 4 hours was used. After demoulding, the components were annealed at 80 °C for 24 hours to ensure complete curing of the resin.



Figure 13: Finished component

Results of the demonstrator:

To evaluate the mechanical performance of the consolidated FRP component, a reference component was manufactured using a classically assembled preform. A single-layer plain fabric with the same yarn count was chosen as the textile reinforcement of the reference component for the demonstrator. The demonstrator and the manufactured reference component were examined with regard to an initial assessment of the impact behaviour by means of compression testing. The test was carried out on a Zwick Z100 testing machine. The FRP specimens were placed between two steel compression plates at a preload of 20 N and the resistance to deformation was tested at a test speed of 1 mm/min up to a maximum deflection of 20 mm. For an accurate assessment of the lightweight design, the performance was related to the weight per unit area. To compare the properties of the components deformations stiffness until the first fracture and resulting force after the maximum deflection was calculated. As a result, the demonstrator shows a 34 % higher deformation stiffness and fails at a 19.5 % higher compressive force compared to the reference component (Figure 14).

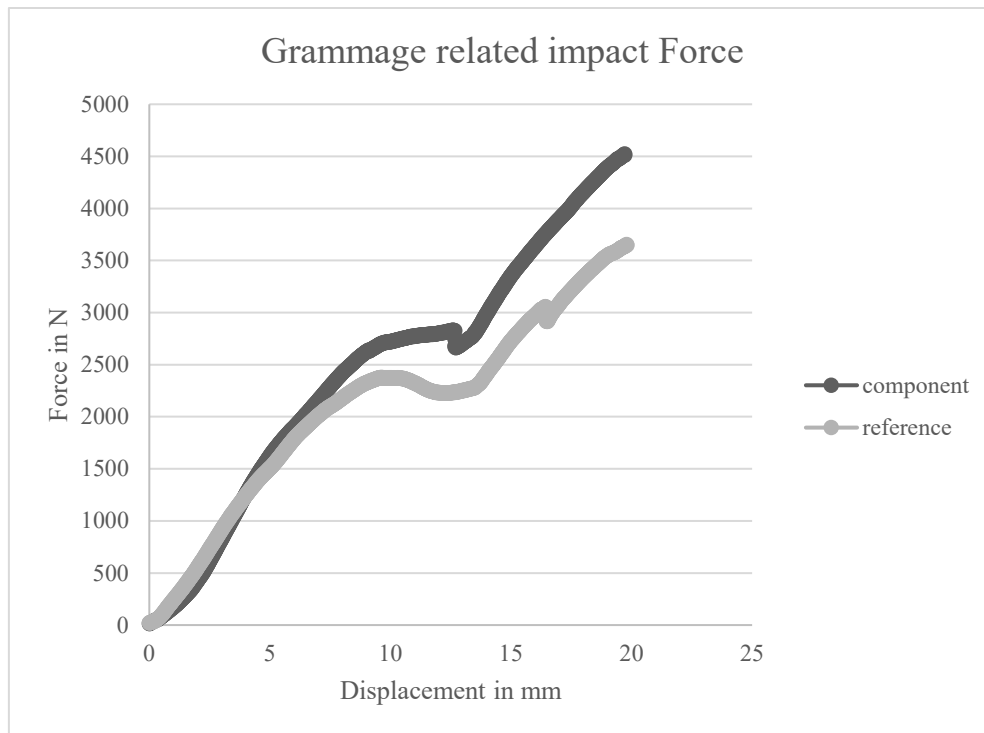


Figure 14: Result of the impact behaviour

Summary.

To sum up, the developed technology for take-up-free weaving enables the manufacturing of spherically curved woven fabrics directly on the loom. During the weaving process, this production technology enables the introduction of different warp yarn lengths into the fabric structure by means of different weave patterns. The systematic arrangement of the different weave areas results in a purposeful adjustment of warp yarn length, based on which a three-dimensional fabric structure is formed. With the assistance of the developed calculation model, it is possible to investigate the warp yarn length needed to generate the final geometry of the structure. Thereby warp yarn length ratios are formed and related to a suitable weft density ratio to generate different warp yarn lengths. The developed theory has been validated with selected geometry. To determine the weaving feasibility of the target structure before manufacturing a simulation model was developed. This can be used to check the moulding of the fabric in advance by calculating the different inserted warp lengths of the weave pattern arrangement.

The completely developed technology has been validated with by producing a demonstrator component. The developed tools has been used to calculate the needed warp yarn lengths and to generate the weave pattern that is later woven by using weft yarn retention system instead of conventional take-up. To evaluate the geometric accuracy of the final component, the dry preform has been scanned to determine the deviation compared to the initial geometry. The impact force has been measured and compared to a reference component which has been manufactured via sequential preforming. Finally, the component produced with the newly developed technology shows the advantages of weaving spherically curved fabric with continuous yarns through the composite.

At the end the developed technology for weaving without take-up provides completely new textile structures of which the potential needs to be explored in further researches.

Funding

The research project was carried out in the framework of the industrial collective research programme (IGF no. 19805 BR). It was supported by the Federal Ministry for Economic Affairs and Energy (BMWi) through the AiF (German Federation of Industrial Research Associations eV) based on a decision taken by the German Bundestag.

Acknowledgements

The authors express their gratitude to the “Arbeitsgemeinschaft industrieller Forschungsvereinigungen” for the financial support of the project IGF 19805 BR.

References

- [1] HÜBNER, Matthias ; STAIGER, Elias ; KÜCHLER, Kristin ; GEREKE, Thomas ; CHERIF, Chokri: *Simulation of Patched Woven Fabric Composite Structures Under Tensile Load*. In: *Tekstilec 59* (2016), Nr. 2, S. 175–181
- [2] KASHIF, Muhammad ; HAMDANI, Syed Talha Ali ; NAWAB, Yasir ; ASGHAR, Muhammad Ayub ; UMAIR, Muhammad ; SHAKER, Khubab: *Optimization of 3D woven preform for improved mechanical performance*. In: *Journal of Industrial Textiles* 48 (2019), Nr. 7, S. 1206–1227
- [3] FAZELI, Monireh ; HÜBNER, Matthias ; LEHMANN, Theo ; GEBHARDT, Ulrike ; HOFFMANN, Gerald ; CHERIF, Chokri: *Development of seamless woven node element structures for application in integral constructions*. In: *Textile Research Journal* 86 (2016), Nr. 11, S. 1220–1227
- [4] CHERIF, Chokri: *Textile Werkstoffe für den Leichtbau : Techniken - Verfahren - Materialien - Eigenschaften*. Berlin, Heidelberg : Springer-Verlag Berlin Heidelberg, 2011
- [5] MOUNTASIR, Adil ; LÖSER, Michael ; HOFFMANN, Gerald ; CHERIF, Chokri ; GROßMANN, Knut: *3D Woven Near-Net-Shape Preforms for Composite Structures*. In: *Advanced Engineering Materials* 18 (2016), Nr. 3, S. 391–396
- [6] SANKARAN, Vignaesh ; RUDER, Tristan ; RITTNER, Steffen ; HUFNAGL, Evelin ; CHERIF, Chokri: *A multiaxial warp knitting based yarn path manipulation technology for the production of bionic-inspired multifunctional textile reinforcements in lightweight composites*. In: *Journal of Industrial Textiles* 45 (2016), Nr. 6, S. 1188–1203
- [7] BOLLENGIER, Quentin ; WIECZOREK, Florian ; HELLMANN, Sven ; TRÜMPER, Wolfgang ; CHERIF, Chokri: *One-step manufacturing of innovative flat-knitted 3D net-shape preforms for composite applications*. In: *IOP Conference Series: Materials Science and Engineering* 254 (2017), S. 42007
- [8] TRÜMPER, W. ; LIN, H. ; CALLIN, T. ; BOLLENGIER, Q. ; CHERIF, C. ; KRZYWINSKI, S.: *Recent developments in multi-layer flat knitting technology for waste free production of complex shaped 3D-reinforcing structures for composites*. In: *IOP Conference Series: Materials Science and Engineering* 141 (2016), S. 12015
- [9] SANKARAN, Vignaesh ; RITTNER, Steffen ; HAHN, Lars ; CHERIF, Chokri: *Development of multiaxial warp knitting technology for production of three-dimensional near net shape shell preforms*. In: *Textile Research Journal* 87 (2016), Nr. 10, S. 1226–1241
- [10] PERERA, Yasith Sanura ; MUWANWELLA, Rajapaksha Mudiyansele Himal Wido ; FERNANDO, Philip Roshan ; FERNANDO, Sandun Keerthichandra ; JAYAWARDANA, Thantirige Sanath Siroshana: *Evolution of 3D weaving and 3D woven fabric structures*. In: *Fashion and Textiles* 8 (2021), Nr. 1, S. 331
- [11] ANSAR, Mahmood ; XINWEI, Wang ; CHOUWEI, Zhou: *Modeling strategies of 3D woven composites : A review*. In: *Composite Structures* 93 (2011), Nr. 8, S. 1947–1963
- [12] CHEN, Xiaogang ; TAYLOR, Lindsay Waterton ; TSAI, Li-Ju: *An overview on fabrication of three-dimensional woven textile preforms for composites*. In: *Textile Research Journal* 81 (2011), Nr. 9, S. 932–944
- [13] SCHMOLDT, A. ; BENTHE, H. F. ; HABERLAND, G.: *Digitoxin metabolism by rat liver microsomes*. In: *Biochemical pharmacology* 24 (1975), Nr. 17, S. 1639–1641

-
- [14] MOUNTASIR, A. ; HOFFMANN, G. ; CHERIF, Ch. ; LÖSER, M. ; GROßMANN, K.: *Competitive manufacturing of 3D thermoplastic composite panels based on multi-layered woven structures for lightweight engineering*. In: *Composite Structures* 133 (2015), 1–4, S. 415–424
- [15] CHEN, Xiaogang (Hrsg.): *Advances in 3D textiles*. First edition. Cambridge, UK : Woodhead Publishing Limited in association with The Textile Institute, 2015 (Woodhead publishing series in textiles number 167)
- [16] BUESGEN, A.: Shell three-dimensional woven textiles. In: CHEN, Xiaogang (Hrsg.): *Advances in 3D textiles*. First edition. Cambridge, UK : Woodhead Publishing Limited in association with The Textile Institute, 2015 (Woodhead publishing series in textiles, number 167), S. 79–98

The Evaluation of Thermal Insulation Performances of 100% Recycled Thermoplastic Composites

Merve Kucukali-Ozturk^{1,a*}, Ipek Yalcin-Enis^{2,b}, Hande Sezgin^{2,c}

¹Istanbul Bilgi University, School of Applied Sciences, Fashion and Textile Design, Istanbul, Turkey

²Istanbul Technical University, Textile Technologies and Design Faculty, Istanbul, Turkey

^amerve.kucukali@bilgi.edu.tr, ^bipekyalcin@itu.edu.tr, ^csezginh@itu.edu.tr

Keywords: Denim waste, packaging waste, recycling, composite, thermal conductivity

Abstract. Considering the risks facing nature today, the search for sustainable materials has become a necessity. The polyethylene, which is the main waste of the packaging sector, and the cotton fibers, which are among the leading wastes of the textile industry, are increasing day by day and the recycling these wastes by using them as reinforcement materials in composites emerges as a sustainable solution. The main purpose of this study is to develop a thermal insulation panel by combining the wastes from two different sectors. Therefore, 100% recycled composite materials are designed according to the different numbers and sequences of recycled cotton fiber layers and recycled polyethylene matrix plates and produced by hot press method. The physical and thermal properties of the samples are tested to evaluate their usability as a sustainable insulation panel.

Introduction

The consumption is continuously increasing due to the easiness of reaching raw materials and frequently changing requirements of the humanity. Plastics and textile materials are two major consumer goods leading the consumption economy [1, 2].

The rate of textile waste per capita is increasing day by day with a great acceleration. In the light of the researches, it is predicted that the amount of textile waste per capita in the world in 2030 will be 17.5 kg [3]. The share allocated to cotton products in the textile sector is substantial and the cotton generates a large amount of solid waste both during its cultivation and through the textile industry (eg the process of combing cotton) [4]. There are several methods like disposal or energy recovery to handle these textile wastes. However, the most preferred options are recycling and reuse when the environmental issues are considered [5].

Plastics, which have become indispensable for our daily life, are accepted as extremely important materials of modern life with their superior properties such as low price, stability and flexibility [6]. However, one of the most critical environmental problems affecting all living things, ecosystems and even the economy around the world in recent years is the problem of the ever-increasing accumulation of plastic waste. On the other hand, the production of plastics also causes harmful gases such as carbon monoxide, dioxins, nitrogen oxides and hydrogen cyanide to be released into the air, which pose a serious threat to both the environment and human health [7]. Although there are many recycling methods, mechanical separation and recycling is known as the preferred method for the reuse of thermoplastic wastes [6]. Polyethylene, which has a large share among plastics, stands out with its advantages such as high chemical resistance, non-toxicity, excellent electrical properties and lightness. This high demand leads to high production volumes, resulting in high consumption rates, which highlights the importance of polyethylene collection and disposal [8].

Today, there is a tendency towards environmentally friendly alternatives in material selection for many application areas, and this trend ensures the widespread use of natural or recycled materials in insulation panels, as in other areas [9]. Examining previous studies, it has been proven that textile-reinforced polymeric-based composite materials can be used in construction and building applications [3, 10]. These studies mainly focus on the use of recycled textile wastes of synthetic fibers such as polyester [11, 12] and natural fibers like wool, cotton, and flax [13-15] as a reinforcement/filling

material in composite structures. On the other hand, thermal insulation property of composite materials consisting of both recycled textile material and thermoplastic resin was rarely studied [16].

In this study, 100% recycled composite materials are designed according to the different numbers and sequences of recycled cotton fiber layers and recycled polyethylene matrix plates. The physical and thermal properties of the samples are tested to evaluate their usability as a sustainable insulation panel.

Materials and Methods

Materials. In this study, HDPE water bottle caps are used as matrix material, whereas cotton fibers (supplied by Realkom Company, Turkey) utilized from waste denim fabrics are used as reinforcement materials (Fig. 1).



Figure 1. Matrix and reinforcement materials

Methods.

The production of composite materials. The production stages of composite materials are categorized into three parts. In the first part, reinforcement material is prepared. For this process, the waste denim fabrics are opened into their fibers using a rag pulling machine (Balkan Machinery). This process is repeated twice in order to achieve smooth fibers. Then, these fibers are transferred to the carding machine (Mesdan Machinery) to obtain enhanced fiber alignment and to eliminate the undesired fiber bundles. Lastly, fibers are wound on the drum 10 times to achieve required web density and then cut in linear form (Fig. 2).



Figure 2. Preparation process of reinforcement material

Secondly, the matrix plates are produced. HDPE bottle caps that are collected and cleaned are placed between Teflon sheets in 9x13 form for the production of 50x50 cm matrix plate by using a hot press machine (MKA Machine, Fig. 3). The caps are exposed to an increasing temperature for 30 min and left to be soften before pressing. Production temperature is adjusted to 140°C and the matrix plates are hold under 18 tons pressure for 1 h. Then these plates are cooled under pressure for 24 h in order to get homogenous and smooth surfaces.



Figure 3. Hot press machine and the produced matrix plate

Lastly, the composite panels are designed and produced. At this stage, the pre-produced matrix plates and carded fiber webs are arranged in different sequences to create different composite designs and each of them is covered with Teflon paper before placing into the hot press machine. Production temperature is adjusted to 140°C and 8 tons of pressure is applied. Five different composite designs (PFP, PFFP, PFFFFP, PFPFP and PFPFPFP) are prepared. In sample codes, P and F refer to polyethylene plate and fiber web, respectively. In Fig. 4, polyethylene plates (P) are shown in blue color while fiber webs are in orange.

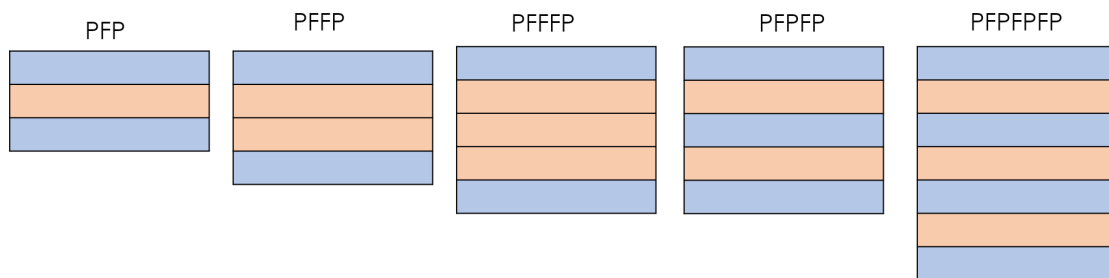


Figure 4. Composite structure designs

Test methods. Composite samples that are designed and produced are prepared for physical and thermal analyses. Thickness of the samples are measured by standard gage micrometer. In order to calculate fiber weight ratio, the weights of fiber webs are measured for specified unit area and proportioned to the total weight of the composite sample. For areal density, the ratio of total weight of composite to the total area of composite (g/m^2) is calculated using the experimental data. All data is given as an average of at least 5 measurements.

Heat transfer measurement test is performed for at least 5 samples according to ASTM E1225 standard. Each sample was cut into circular forms with 112 mm of diameters (Fig. 5).



Figure 5. Composite samples and the experimental setup for thermal analysis

Results and Discussion

The average thickness, areal density and the fiber weight ratio values of the composite samples are given in Table 1.

Table 1. Physical properties of composite materials

Sample Code	Avg. Areal Density [g/m ²] \pm SD	Avg. Thickness [mm] \pm SD	Avg. Fiber Weight Ratio [%] \pm SD
PFP	867 \pm 14	0.86 \pm 0.03	12.9 \pm 2.2
PFFP	1183 \pm 17	1.26 \pm 0.04	23.9 \pm 3.6
PFFFP	1573 \pm 17	3.50 \pm 0.09	36.0 \pm 3.9
PFPPF	1543 \pm 19	1.52 \pm 0.01	17.5 \pm 2.8
PFPPFPF	2170 \pm 23	2.10 \pm 0.03	18.4 \pm 2.6

The results show that the thicknesses of the samples increased with increasing fiber web layers for the PFP, PFFP and PFFFP samples. However, the use of a matrix plate instead of a fiber web layer reduces the overall thickness, as can be seen from the PFFFP and PFPPF samples. This is due to the fact that inserting a matrix plate between the fibrous layers results in more compact structures under applied heat and pressure. On the other hand, when the PFPPFP and PFFFP samples, in which the same number of fibrous layers used are compared, it is observed that the thickness value again decreased from 3.5mm to 2.1mm for the PFPPFP sample with extra matrix plates placed between the fiber web layers. The reason for this is similarly, the matrix plates located between the fibrous layers melt, preventing the bulky structure and thus leading to the production of more compact and thinner samples.

On the other hand, there is an increase in areal density values in direct proportion to the increasing number of layers, while PFFFP and PFPPF samples with the same layer number have similar areal density values. In composites from PFP to PFFFP, fiber weight ratios increase from 12.9% to 36%, respectively, with the increase of fiber layers. On the other hand, when the PFFP and PFPPF samples are compared, it is observed that the fiber weight ratio decreases from 23.9% to 17.5% with the extra matrix plate added in the PFPPF. As a result, the type of components, the number of their layers and their placement relative to each other in the structure affect the fiber weight ratio of the composites.

Thermal conductivity coefficients of composite structures are given in Table 2.

Table 2. Thermal conductivity coefficients of composite materials

Sample Code	Calculated λ [W/(m.K)] \pm SD
PFP	0.360 \pm 0.021
PFFP	0.279 \pm 0.016
PFFFP	0.106 \pm 0.001
PFPPF	0.436 \pm 0.026
PFPPFPF	0.471 \pm 0.029

When the first three samples (PFP, PFFP and PFFFP) are compared with each other, it is seen that the thermal conductivity coefficients of the samples decrease with increasing fiber content. This is due to the airy structure created by the increased fiber content in the composite structure. Air accumulates in the gaps formed by the fibrous content and this structure allows the material to exhibit insulation properties [17].

If the PFFP and PFPPF composite samples which have same amount of fibrous layer are compared, it is noticed that there is a distinct difference between each other. According to the results, the thermal coefficient of the PFFP is 0.279 W/(m.K), whereas the thermal coefficient of PFPPF is 0.436 W/(m.K). This difference is resulted from the extra matrix plate introduced to the composite structure. With the presence of this matrix plate placed between fiber webs, compactness increases which results in elimination of structural air gaps thus poor thermal insulation features [18]. These findings also

support the physical attest results given in Table 1. Accordingly, PFFFP and PFFFPFP samples show similar characteristics too. However, when PFFFP and PFFFPFP samples are compared, no distinct difference in thermal conductivity coefficients are noticed since there are several matrix layers that compress fibers and reduce the insulation features.

It is concluded that the thermal conductivity values of composite structures designed and produced from waste materials cannot compete with commercial insulation materials such as polyurethane foam (0.024 W/(m.K)) and glass wool (0.043 W/(m.K)). However, when the results of PFFFP and PFFFPFP samples are examined, it is understood that the thermal conductivity values of these samples are comparable with those of supporting materials such as oak wood, pine wood, siporex board, thermolite board, light plaster and insulation brick (thermal conductivity values: 0.10-0.20 W/(m.K)), and can be an alternative to these products. In addition to the contribution of the produced materials to waste management, their low weight also provides an advantage for use in the construction industry [19].

Conclusion

In this study, 100% recycled composite panels including recycled denim wastes and recycled HDPE bottle caps are successfully produced. Both physical measurements and thermal analyzes of composite samples with different layer numbers and sequences were carried out. In the findings that the physical results support the thermal results, it is observed that the increased number of fiber layers increased the overall thickness of the composite samples, but the matrix plates added together melted to reduce the bulky structure of these fibers, resulting in a more compact and thinner material. Thermal test results indicate that increasing fiber content leads in reduced thermal conductivity coefficients due to the air gaps trapped in the structure. Among samples, PFFFP, which has the thickest fiber web layer between two matrix plates, has the minimum thermal conductivity coefficient of 0.106W/(m.K) which can be the best promising one for the isolation purposes.

Acknowledgment

This study is supported by the Istanbul Technical University, Scientific Research Projects Fund under grant no: 41926. The authors would like to thank to Aybike Busra Sivrice and Sinem Hazal Akyildiz, for their contribution to this study.

References

- [1] B. Utebay, P. Celik, A. Cay, Effects of cotton textile waste properties on recycled fibre quality, *J. Clean. Prod.* 222 (2019) 29-35.
- [2] R. Geyer, J.R. Jambeck, K.L. Law, Production, use, and fate of all plastics ever made, *Sci. Adv.* 3(7) (2017) e1700782.
- [3] Z. Kamble, B.K. Behera, Sustainable hybrid composites reinforced with textile waste for construction and building applications, *Constr. Build. Mater.* 284 (2021) 122800.
- [4] N.H.N. Do, V.T. Tran, Q.B.M. Tran, K.A. Le, Q.B. Thai, P.T.T. Nguyen, H.M. Duong, P.K. Le, Recycling of pineapple leaf and cotton waste fibers into heat-insulating and flexible cellulose aerogel composites, *J. Polym. Environ.* 29 (2021) 1112–1121.
- [5] I. Yalcin-Enis, M. Kucukali-Ozturk, H. Sezgin, Risks and management of textile waste, in: K.M. Gothandam, S. Ranjan, N. Dasgupta, E. Lichtfouse (Eds.), *Nanoscience and Biotechnology for Environmental Applications*, Springer, Cham, 2019, pp. 29–53.
- [6] S.S. Ali, T. Elsamahy, R. Al-Tohamy, D. Zhu, Y.A.G. Mahmoud, E. Koutra, D. Zhu, J. Sun, Plastic wastes biodegradation: Mechanisms, challenges and future prospects, *Sci. Total Environ.* 780 (2021) 146590.

-
- [7] S.S. Ali, T. Elsamahy, E. Koutra, M. Kornaros, M. El-Sheekh, E.A. Abdelkarim, D. Zhu, J. Sun, Degradation of conventional plastic wastes in the environment: A review on current status of knowledge and future perspectives of disposal, *Sci. Total Environ.* 771 (2021) 144719.
- [8] M. Martínez-López, G. Martínez-Barrera, R. Salgado-Delgado, O. Gencel, Recycling polypropylene and polyethylene wastes in production of polyester based polymer mortars. *Constr. Build. Mater.* 274 (2021) 121487.
- [9] S. Islam, G. Bhat, Environmentally-friendly thermal and acoustic insulation materials from recycled textiles, *J. Environ. Manag.* 251 (2019) 109536.
- [10] D.G.K. Dissanayake, D.U. Weerasinghe, L.M. Thebuwanage, U.A.A.N. Bandara, An environmentally friendly sound insulation material from post-industrial textile waste and natural rubber, *J. Build. Eng.* 33 (2021) 101606.
- [11] I. Yalcin, T.Gok Sadikoglu, O.B. Berkalp, M. Bakkal, Utilization of various non-woven waste forms as reinforcement in polymeric composites, *Textil. Res. J.* 83(15) (2013) 1551-1562.
- [12] W. Baccouch, A. Ghith, I. Yalcin-Enis, H. Sezgin, W. Miled, X. Legrand, F. Faten, Investigation of the mechanical, thermal, and acoustical behaviors of cotton, polyester, and cotton/polyester nonwoven wastes reinforced epoxy composites, *J. Ind. Text* <https://doi.org/10.1177/1528083720901864>
- [13] A.H. Hassanin, Z. Candan, C. Demirkir, T. Hamouda, Thermal insulation properties of hybrid textile reinforced biocomposites from food packaging waste, *J. Ind. Text.* 47(6) (2018) 1024-1037.
- [14] I. Susoeva, T. Vakhnina, A. Titunin, Y. Grunin, Water resistance of thermal insulation composites with cellulose-containing filler, *E3S Web of Conferences* 263 (2021) 01002.
- [15] T.N. Vahnina, I.V. Susoeva, A.A. Titunin, Thermal-insulation boards from fibrous plant wastes and urea-formaldehyde binder, *Mag. Civ. Eng.* 7 (2018) 136-147.
- [16] H. Sezgin, M. Kucukali-Ozturk, O.B. Berkalp, I. Yalcin-Enis, Design of composite insulation panels containing 100% recycled cotton fibers and polyethylene/polypropylene packaging wastes., *J. Clean. Prod.* 304 (2021) 127132.
- [17] D. Duran, A research on thermal insulation properties of nonwovens produced with recycled jute and wool fibres. *Tekst.ve Konfeksiyon* 26(1) (2016) 22-30.
- [18] S. Yukseloglu, M. Caliskan, Mechanical and thermal properties of wool waste fabric reinforced composites, *Tekst. ve Muhendis* 22(97) (2015) 14-20.
- [19] C. Yertutan and M. C. Bulbul, 2020, Dissertation Thesis, Istanbul Technical University, Istanbul, Turkey.

CHAPTER 3:

Modelling of Yarn Interaction and Textile Mechanical Behaviour

Mechanical Properties of Carbon Fiber Reinforced Composites Filled with Carbon Microparticles

NOVOTNÁ Jana^{1,a*}, Blanka Tomková^{1,b} and Lukáš Výborný^{1,c}

¹Technical University of Liberec, Dep. Of Material Engineering, Studentská 2, 46117 Liberec, Czech Republic

^ajana.novotna3@tul.cz, ^bblanka.tomkova@tul.cz, ^clukas.vyborny@tul.cz

*Email: jana.novotna3@tul.cz

Keywords: carbon fibers (CFs), carbon fiber reinforced epoxy (CFRE) composites, carbon microparticles, mechanical properties.

Abstract. The aim of this work is to investigate the effect of carbon micro particles used as epoxy resin fillers, for the mechanical properties of reinforced composites unidirectionally oriented carbon fibers. The motivation for this work was expansion knowledge of the possibilities of improving the user properties of these materials at maintaining their weight, thus finding new areas for application recycled carbon fibers from composite waste, which would also contribute to the solution issues of recycling and subsequent use of today's mostly landfilled composites. This work deals with the influence of carbon fillers embedded in epoxy resin on tensile and flexural properties of carbon fiber reinforced epoxy (CFRE) composites. Samples were made from unidirectional carbon multifilaments, and epoxy resin modified with selected carbon fillers in 2.5weight% concentrations. Composites were subsequently examined using flexural and tensile tests. All specimen filled with carbon particles showed increase of both, flexural and tensile properties, if compared to neat epoxy composites.

Introduction

Theoretically, we can improve the mechanical properties of fiber composites by increasing volume fractions of fiber reinforcement [1]. Unfortunately, this adjustment leads to an increase in weight (and prices) construction, where, for example, a standard glass-epoxy fiber composite, which has at volume fraction of 50% glass fibers density about 1650 kg.m⁻³, at volume 60% share already has a density of 1800 kg.m⁻³, which is about 150 kg of material per m³ more.

Another problem is the current technology of production of these composites (lamination to negative forms or winding rovings to a positive form), where real products reach volume filling with reinforcing fibers between 45-55%. At present, therefore the developers of these materials focus on the possibility of improving the mechanical properties composite matrices, which are a binder of fiber reinforcement, and one of the investigated the possibility is to use particulate fillers in the matrix structure [3].

This work investigates the effect of carbon microparticles used as epoxy resin fillers for the mechanical properties of reinforced composites unidirectionally oriented carbon fibers. The motivation for this work was both expansion knowledge of the possibility of improving the user properties of these materials at maintaining / reducing their weight, thus finding new areas for application recycled carbon fibers from composite waste, which would also contribute to the solution issues of recycling and subsequent use of today's mostly landfilled CFRE.

Materials and Methods

Material preparation. Carbon fiber reinforced composites is formed with unidirectional carbon fibers Tenax (1600 Tex, 1770kg/m³, 24000 filaments). Resin matrix system is based on green epoxy 520/492 from company Spolchemie. This epoxy is certified EPD for significant CO₂ savings in production, low oil content and high content of renewable resources [4]. As fillers were used the following materials: (1) recycled Carbisio Milled Carbon Fibers (CMF)[5], (2) Graphite platelets [6],

(3) 5x milled Carbonized Acrylic Fibrous Wastes (CAFW) [7], (4) 1x milled recycled CMF, (5) 5x milled recycled CMF.

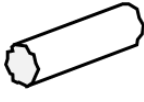





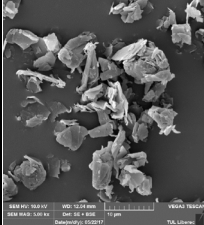
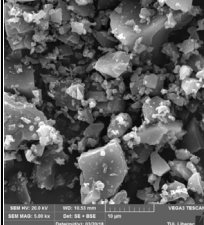
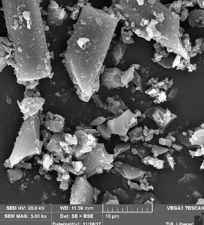
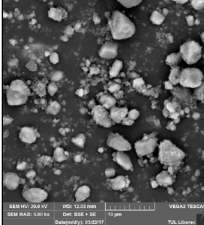
Types	1. CMF	2. Graphit	3. CAFW 5x milled	4. CMF 1x mill.	5. CMF 5x mill.
average area [μm ²]	500	6,4	6,5	121,8	53,5
Particle geometry	 cylindrical	 sheet	 acicular	 combined	 aggregate
SEM pictures					

Figure 1. Types of used fillers

Preparation of carbon particles from type (3) to type (5) using dry pulverization was carried out using high energy planetary ball milling (Fritsch). The sintered corundum container and zirconium balls were chosen for both 5 min. (1 cycle) and 30 min. (5 cycles) runs of dry milling. Samples (1) and (2) (Carbisio CMF and Graphite) were not milled.

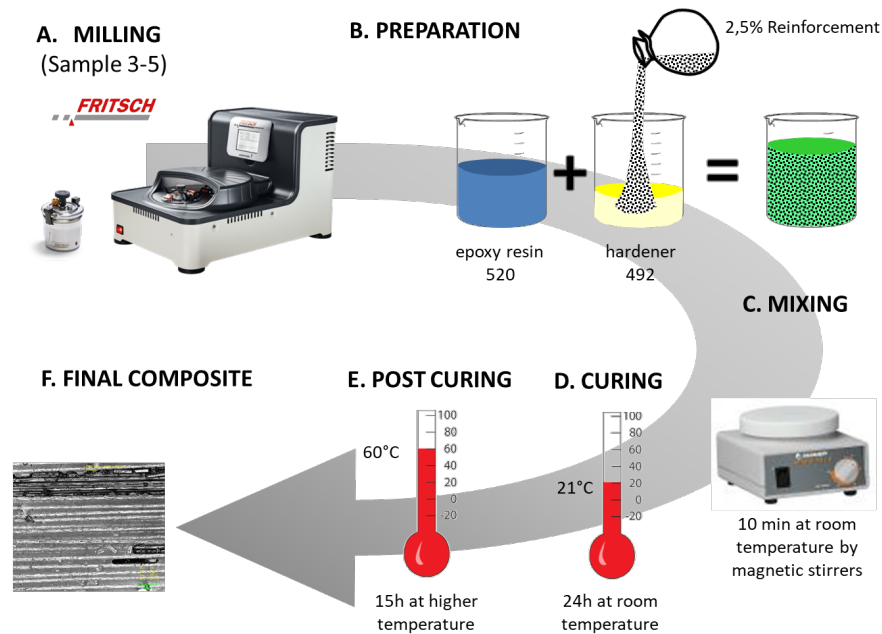


Figure 2. Scheme of preparations

Test Methods. To evaluate the effect of carbon fillers on CFRE composites, two testing methods were selected as described below. For testing of flexural properties – 3PB test EN ISO 14125, and for testing of tensile properties - tensile test EN ISO 527-4 were used. Both tests were run on a tensile device TIRA TEST 2300 (Labortech), see Fig. 3, having adjustable measurement modules and corresponding tensile and 3PB jaws for both types of tests. Comparison of resultant flexural and tensile properties (strengths and moduli) are shown in Figures 4, and 5. All samples were tested in the longitudinal direction of the fibers.

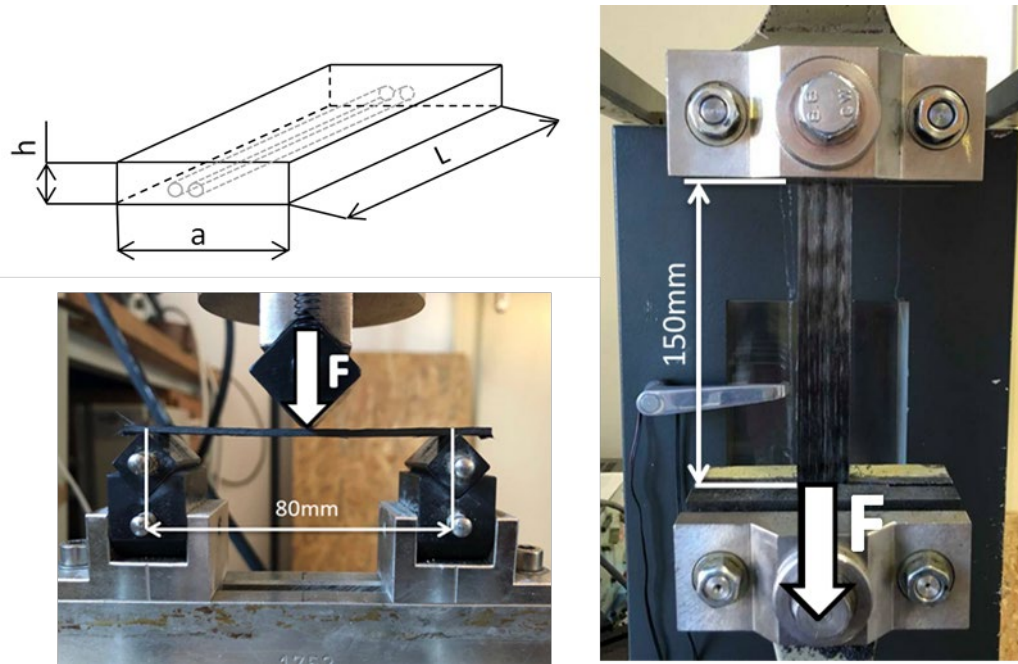


Figure 3. Test samples –scheme, TIRA TEST: 3PB, tensile properties.

Results and Discussion

3PB. The modulus of elasticity can be defined as the internal resistance of a material to elastic deformation. As the modulus of elasticity increases, the stress required to achieve it increases specified deformations [8].

During the bending test, the flexural modulus, which is defined as the ratio of the stress differences of the outer surface of the samples to the difference in deformations bending determined by ISO. The values of bending stress must be based on the values of forces used for specified deformations.

The obtained results show that the samples showed the highest dispersion of flexural strength with 5x milled CMF in an epoxy matrix, which thus reached the maximum and minimum flexural strength compared to other samples. High coefficient of variation and the highest range of values when measuring three-point bending in a sample of 5x milled CMF may be caused by sedimentation of the ground particles in the composite matrix when impregnating the reinforcement, or by mixing the ground particles into lower ones layers of the composite, which can then form places in the fiber reinforcement through which it is not possible fibers impregnate with the matrix.

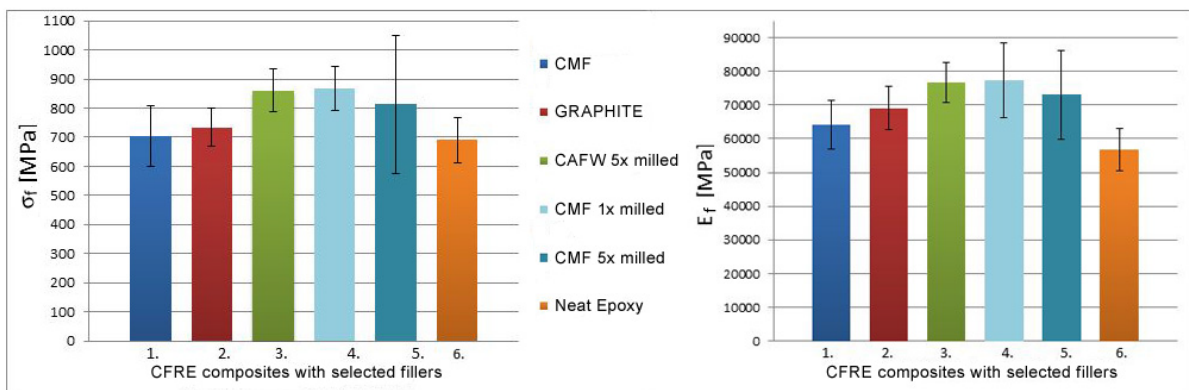


Figure 4. Flexural strength σ_f [MPa] and modulus E_f [MPa] of filled and neat CFRE composites

Tensile properties. The princip of the test is the clamping of the samples of rectangular cross-section into the tearing jaws device and subsequent stressing of the clamped samples by uniaxial

tension. The jaws are anchored on the cross-members of the tearing device, whereby the tensile stress in the material is created constant by moving one of the crossbars [9]. The direction of the applied force during the tensile test is marked on Figure 4. The stress on the test specimen lasts in most tests until damage or rupture of the material when it reaches its ultimate strength.

From the graphic representation in Figure 5 it can be stated that the highest tensile strengths reached composite samples with 1times milled Carbisio fibers in epoxy resin. Samples containing 5x milled particles had the second highest values of tensile strength times milled Carbonized Acrylic Fibrous Wastes, which again achieved better strength values than particles graphite, but with a much smaller difference than the flexural strength values in the test three-point bend.

The lowest tensile strength was achieved by a sample with pure epoxy resin. Thus low values of tensile strength and modulus of elasticity may indicate that in the absence fillers in the resin, the composite material becomes far more brittle and less tough when uniaxial bending stress.

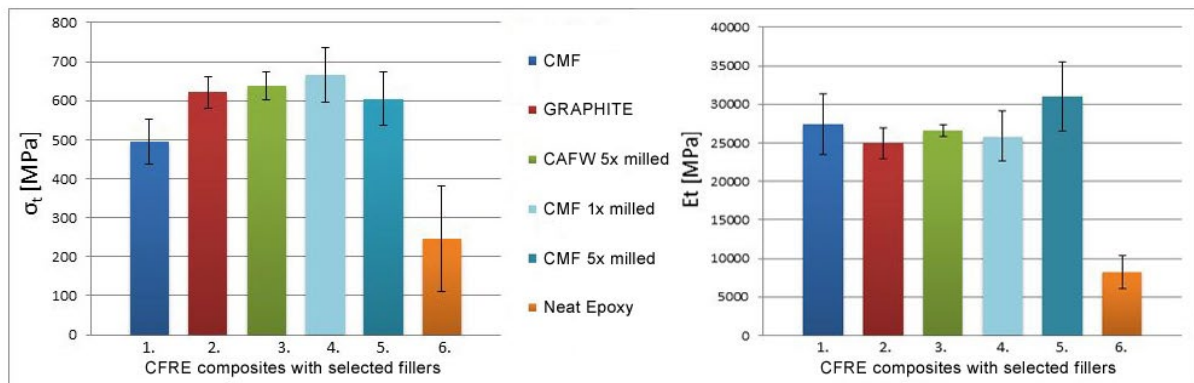


Figure 5. Tensile strength σ_t [MPa] and modulus E_t [MPa] of filled and neat CFRE composites

It is obvious that carbon filling improved both, flexural and tensile properties of CFRE composites, in addition with minimal increase of volume density [2]. The highest flexural and tensile strengths obtained samples with 1x milled CMF, the neat epoxy systems are the weakest.

In terms of carbon fillers used, the fillers achieved better results from recycled carbon fibers than graphite, which is the appearance to the purchase price and the origin of graphite is a very important finding. Especially composite samples from recycled ones achieved good mechanical properties ground CMF fibers, where the properties of the commercially available form have been improved ground fibers. If the Carbisio fibers were ground once more and 5x, it happened for composites to intensify mechanical properties.

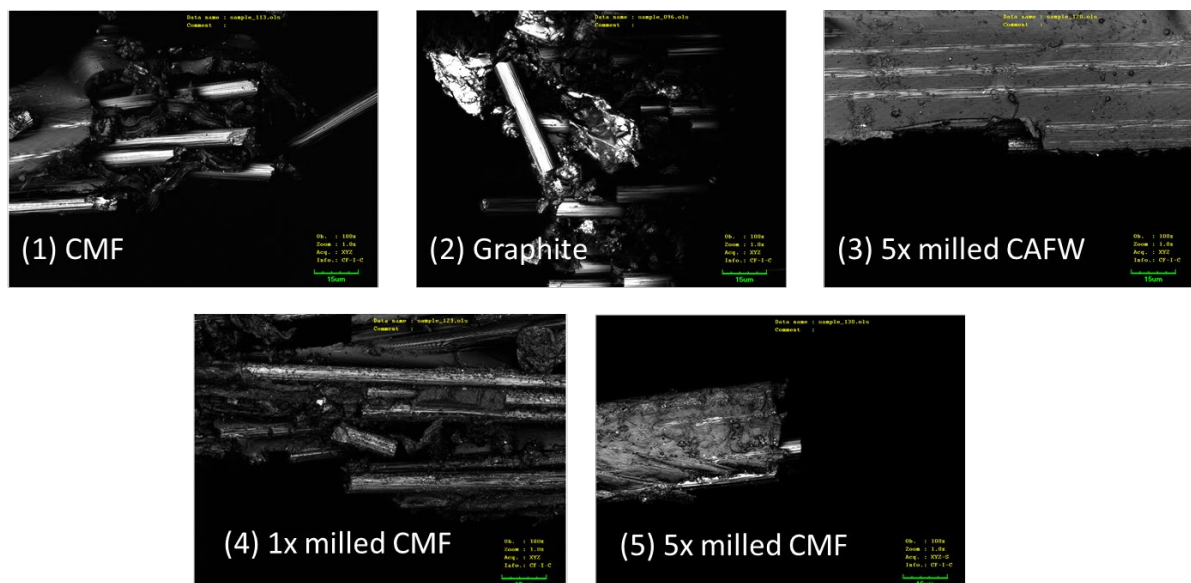


Figure 6. SEM image composite damage - 100x magnified

Conclusion

This work was focused on the study of the influence of different types of carbon particles that were used as a filler in epoxy resin, for the mechanical properties of composites reinforced with unidirectionally oriented carbon fibers.

Suitable carbon fillers were selected and designed optimal concentration in epoxy resin. Recycled types of carbon fillers were milled. From a matrix of composite with carbon particles and fiber reinforcement, composites were made on which they were made mechanical tests for resistance to bending and tensile. From the results of these tests and after analysis of the obtained data showed that they have carbon fillers in the resin positive effect on the resulting mechanical properties of the cured composite at the selected concentration 2.5 weight %. After comparing the results with composites with pure epoxy resin, so we can say that carbon fillers are suitable for improvement mechanical properties of composites with fiber reinforcement.

When summarizing the results of all mechanical tests, it can be stated that carbon filled epoxy composites performed better than those with neat epoxy. It indicates carbon fillers have great potential for improving the mechanical properties of CFRE. It is also remarkable that the best results were achieved for particles from recycled carbon fiber sources.

With today's growing production of carbon composites, it is important to raise the issue possible use and recycling of composites that can no longer serve their purpose and be avoided thus their landfilling. From this point of view, the work brought new knowledge about the possible use of recycled particles to improve the mechanical properties of fiber composites reinforcement, which may bring further ideas to address the issue of recycling and subsequent use of today's mainly landfilled CFRE.

Acknowledgment

Authors are grateful for the financial support from the Student research project 2020 No. 21409 supported by Czech Ministry of Education, and by Faculty of Textile, Technical University of Liberec.

References

- [1] KIRAN, M. D., H. K. GOVINDARAJU, T. JAYARAJU a Nithin KUMAR. Review-Effect of Fillers on Mechanical Properties of Polymer Matrix Composites. *Materials Today: Proceedings* [online]. 2018, **5**(10), 22421–22424. ISSN 22147853. Dostupné z: doi:10.1016/j.matpr.2018.06.611
- [2] LAM, Chun Ki, Hoi Yan CHEUNG, Kin Tak LAU, Li Min ZHOU, Man Wai HO a David HUI. Cluster size effect in hardness of nanoclay/epoxy composites. *Composites Part B: Engineering* [online]. 2005, **36**(3), 263–269. ISSN 13598368. Dostupné z: doi:10.1016/j.compositesb.2004.09.006
- [3] THOPPUL, S. D., A.J. FINEGAN a R. F. GIBSON. Mechanics of mechanically fastened joints in polymer-matrix composite structures - A review [online]. 2009, **69**, 301–329. Dostupné z: doi:DOI:10.1016/j.compscitech.2008.09.037
- [4] *Chemex* [online]. 2018. Dostupné z: <http://www.chemex.cz/>
- [5] *Technical Information for Carbisol Mil 10 µ Milled Carbon Fibre* [online]. 2018. Dostupné z: <http://www.easycomposites.co.uk>
- [6] *Graphit 282863* [online]. Dostupné z: <https://www.sigmaaldrich.com/MSDS/MSDS/DisplayMSDSPage.do?country=CZ&language=cs&productNumber=282863&brand=ALDRICH&PageToGoToURL=https%3A%2F%2Fwww.sigmaaldrich.com%2Fcatalog%2Fsearch%3Fterm%3D282863%26interface%3DAll%26N%3D0%26mode%3Dmatch%2520partialmax>

- [7] BAHETI, Vijay, Salman NAEEM, Jiri MILITKY, Malgorzata OKRASA a Blanka TOMKOVA. Optimized Preparation of Activated Carbon Nanoparticles from Acrylic Fibrous Wastes. *Fibers and Polymers* 16 [online]. 2015, 10. Dostupné z: doi:10.1007/s12221-015-5364-0
- [8] VRBKA, Jan. Mechanika kompozitů. *Ústav mechaniky těles, mechatroniky a biomechaniky Fakulta strojního inženýrství VUT v Brně Brno*. 2008.
- [9] QIN, Wenzhen, Frederic VAUTARD, Lawrence T. DRZAL a Junrong YU. Mechanical and electrical properties of carbon fiber composites with incorporation of graphene nanoplatelets at the fiber-matrix interphase. *Composites Part B: Engineering* [online]. 2015. ISSN 13598368. Dostupné z: doi:10.1016/j.compositesb.2014.10.014

An Alpha Finite Element Method for Linear Static and Buckling Analysis of Textile-Like Sheet Materials

Nguyễn T. Quyên^{1,a*}, Nguyễn T. Quốc^{2,3}, Nguyễn Đ. Tru⁴,
Abel J.P. Gomes^{2,3} and Fernando B.N. Ferreira¹

¹2C2T - Centro de Ciência e Tecnologia Têxtil, Departamento de Engenharia Têxtil, Universidade do Minho, Campus de Azurém, 4804-533 Guimarães, Portugal

²Departamento de Informática, Universidade da Beira Interior, Convento de Sto. António, 6201-001 Covilhã, Portugal

³Instituto de Telecomunicações, Rua Marquês d'Ávila e Bolama, 6201-001 Covilhã, Portugal

⁴Faculty of Textile and Garment Technology, Ho Chi Minh City Industry and Trade College, 20 Tang Nhon Phu, Phuoc Long B Ward, District 9, Ho Chi Minh, Vietnam

^aquyen@2c2t.uminho.pt, ^bquoc.nguyen@ubi.pt, ^cdinhtru1509@gmail.com, ^dagomes@di.ubi.pt, ^efnunes@det.uminho.pt

Keywords: Textile-like sheet material; Mindlin–Reissner plate theory; Buckling analysis; Finite element method; Alpha finite element method

Abstract. A four node isoparametric shell element (Q4) based on Mindlin/Reissner plate theory and the alpha finite element method (α FEM) was formulated for obtaining a nearly exact solution of linear static and buckling analysis of textile-like sheet material. The novel idea of α FEM-Q4 is assumed to be similar to the framework of conventional finite element approaches for Q4, but the gradient of strains is scaled by a factor $\alpha \in [0, 1]$. The numerical examples demonstrate that the α FEM-Q4 can improve the accuracy of FEM solution in static and buckling analysis shell structures of non-woven fabric. However, the α FEM-Q4 cannot provide the nearly exact solution to all elasticity problems. In addition, it also requires a quadrilateral mesh that cannot be fully generated by common geometric algorithms for complicated problem domains.

Introduction

A textile-like sheet materials in terms of plate and shell are one of the attractive lightweight structures that are extensively used by engineers in numerous industries [1-5]. Thin-shell structures (also called plate and shell structures) are thin in thickness and have significant length in other two directions [6, 7], e.g., woven and nonwoven fabrics, being denoted as thickness-to-length ratio $\left(\frac{t}{L}\right)$. The applied loads on the shell surface commonly transmit through bending, tensile, shear and compressive stresses [4, 8-10]. Because of the complex form and load conditions of plate and shell structures their governing differential equation are complicated [11-13]. In plate and shell structural analysis, the finite element method is one of the most appropriate solution meeting the engineer. For instance, finite element method is applied for linear, nonlinear, static and dynamic analysis in design, development and manufacture of engineered fabric and composite structures [7-9, 14].

Generally, there are four types of shell elements being used in analysis of plate and shell structures: flat shell finite elements, curved shell finite elements, axisymmetric shell finite elements and degenerated solid finite elements. Due to the simple theoretical formulation and efficient computation of flat shell element, this type of finite element is more employed than the other ones in finite element analysis of plate and shell structures. However, there are still a number of difficulties and a numerous number of solutions regarding to the theoretical development and practical improvement of shell elements based on Mindlin/Reissner plate theory can be found in recent literatures [1, 12, 15-17]. Recently, an alpha finite element method (α FEM) has proposed by Liu et. al. [18-20] for obtaining nearly exact solution in energy norm for computational mechanics' problems using meshes that can be generated automatically for subjectively complicated domains. Thus, the main purpose of this

paper is to present a formulation of a four node isoparametric shell element based on Mindlin/Reissner plate theory and the alpha finite element method (α FEM), briefly illustrating the improvement of numerical precision and computational efficiency in finite element analysis of plate/shell structures and applying to the linear static and buckling analysis of textile-like sheet materials.

Formulations for Linear Static and Buckling Analysis

An arbitrary fabric sample can be assumed as a three dimensional solid that is described as an elastic domain $\Omega \in \mathbb{R}^3$ with a Lipschitz-continuous boundary Γ and a body force \mathbf{b} acting within the domain Ω . The boundary Γ comprises of two parts, namely Γ_u where Dirichlet conditions $\bar{\mathbf{u}}$ are prescribed, and Γ_t where Neumann conditions $\bar{\mathbf{t}} = \bar{\mathbf{t}}$ are prescribed. Γ_u and Γ_t form a partition of the boundary Γ such as $\Gamma = \Gamma_u \cup \Gamma_t$. The static equilibrium equation governing the solid can be written in term of the stress field

$$\frac{\partial \sigma_{ij}}{\partial x_j} + b_i = 0 \text{ with } i, j = 1, \dots, 3 \text{ in } \Omega. \quad (1)$$

Let $C_{ijkl}\varepsilon_{kl}$ be the elasticity tensor being the material constants of the solid. The stresses relate to the strains ε_{ij} via the constitutive equation (also known as the generalized Hook's law)

$$\sigma_{ij} = C_{ijkl}\varepsilon_{kl} \text{ with } i, j, k, l = 1, \dots, 3 \text{ in } \Omega. \quad (2)$$

For isotropic Saint-Venant Kirchhoff elastic materials, let λ and μ stand for the Lamé's elastic constants, C_{ijkl} can be rewritten in the form of

$$C_{ijkl} = \lambda \delta_{ji} \delta_{kl} + \mu (\delta_{ik} \delta_{jl} + \delta_{il} \delta_{jk}). \quad (3)$$

The strain tensor ε_{kl} relates to the displacements in the form of compatibility equations (or the kinematic equations)

$$\varepsilon_{ij} = \frac{1}{2} \left(\frac{\partial u_i}{\partial x_j} + \frac{\partial u_j}{\partial x_i} \right), \quad (4)$$

with u_i ($i = 1, \dots, 3$) is the displacement component corresponding to the x_i -direction at a point in Ω . Substituting Eq. 2 and Eq. 4 into Eq. 1, the equilibrium equations can be expressed in terms of displacements

$$\frac{\partial}{\partial x_j} \left(C_{ijkl} \frac{\partial u_k}{\partial x_l} \right) + b_i = 0 \text{ with } i, j, k, l = 1, \dots, 3 \text{ in } \Omega. \quad (5)$$

For concise expressions, the Eq. 1, Eq. 2 and Eq. 5, respectively, can be rewritten in the matrix forms such as

$$\mathbf{L}^T \boldsymbol{\sigma} + \mathbf{b} = \mathbf{0}, \quad (6)$$

$$\boldsymbol{\sigma} = \mathbf{D} \boldsymbol{\varepsilon}, \quad (7)$$

$$\boldsymbol{\varepsilon} = \mathbf{L} \mathbf{u}, \quad (8)$$

where constants \mathbf{D} is the elasticity tensor can be found in literatures [7, 13] and can refer to [21, 22] for plane stress analysis. Substituting Eq. 8 into Eq. 7 which gives the equilibrium equation written in matrix form having the displacements as the main field variables. Thus, the Dirichlet and the Neumann boundary conditions are also specified as

$$\mathbf{u} = \mathbf{u}_\Gamma, \quad (9)$$

$$\mathbf{L}_n^T \boldsymbol{\sigma} = \mathbf{t}_\Gamma, \quad (10)$$

in which \mathbf{L}_n is the matrix of the unit outward normal components. Hence, the strain energy (or potential energy) for elastic solid can be quantified via

$$\mathbf{U} = \frac{1}{2} \int_\Omega \boldsymbol{\varepsilon}^T(\mathbf{x}) \boldsymbol{\sigma}(\mathbf{x}) d\Omega = \frac{1}{2} \int_\Omega \boldsymbol{\varepsilon}^T(\mathbf{x}) \mathbf{c} \boldsymbol{\varepsilon}(\mathbf{x}) d\Omega, \quad (11)$$

Consider Eq. 6 to Eq. 11 and apply the typical Mindlin-Reissner plate theory [16, 23], as shows in Fig. 1, for which the analysis of the membrane deformations, the uncoupling of bending and shear deformations are feasible. Thus, the displacement assumption gives

$$\begin{aligned} u(x, y, z) &= u_0(x, y) + z\beta_x(x, y) \\ v(x, y, z) &= v_0(x, y) + z\beta_y(x, y). \\ w(x, y, z) &= w_0(x, y) \end{aligned} \tag{12}$$

with u_0 , v_0 and w_0 standing, correspondingly, for the displacement components along x , y and z directions. $\beta_x = \frac{\partial w}{\partial x}$ and $\beta_y = \frac{\partial w}{\partial y}$ are, respectively, the rotations of the normal to the undeformed mid-surface in the x - z and y - z planes.

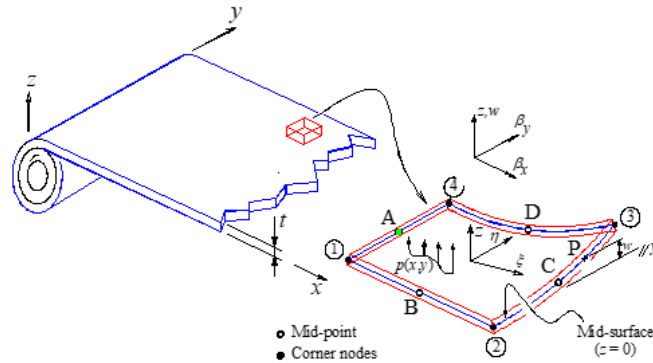


Figure 1. A four-node isoparametric quadrilateral shell element.

The matrices of membrane strain $\boldsymbol{\epsilon}^m$, curvature strain $\boldsymbol{\epsilon}^b$ and the transverse shear strain $\boldsymbol{\epsilon}^s$ are calculated from the corresponding differential operators \mathbf{L} as formulated in Eq. 8,

$$\boldsymbol{\epsilon}^m = \begin{Bmatrix} \frac{\partial u}{\partial x} \\ \frac{\partial v}{\partial y} \\ \frac{\partial u}{\partial y} + \frac{\partial v}{\partial x} \end{Bmatrix}, \boldsymbol{\epsilon}^b = \begin{Bmatrix} \frac{\partial \theta_x}{\partial x} \\ \frac{\partial \theta_y}{\partial y} \\ \frac{\partial \theta_y}{\partial x} - \frac{\partial \theta_x}{\partial y} \end{Bmatrix} \text{ and } \boldsymbol{\epsilon}^s = \begin{Bmatrix} \frac{\partial w}{\partial x} + \theta_y \\ \frac{\partial w}{\partial y} - \theta_x \end{Bmatrix}. \tag{13}$$

In the buckling analysis, as the shell being enforced by in-plane pre-buckling stresses σ_x^0 , σ_y^0 and σ_{xy}^0 , the geometric elastic strain energy gives

$$\mathbf{U}_\sigma = \frac{1}{2} \int_V (\boldsymbol{\epsilon}^g)^T(\mathbf{x}) \boldsymbol{\tau} \boldsymbol{\epsilon}^g(\mathbf{x}) dV, \tag{14}$$

with

$$\boldsymbol{\epsilon}^g = \left[\frac{\partial u}{\partial x} \quad \frac{\partial v}{\partial y} \quad \frac{\partial w}{\partial z} \quad \frac{\partial u}{\partial y} + \frac{\partial v}{\partial x} \quad \frac{\partial v}{\partial z} + \frac{\partial w}{\partial y} \quad \frac{\partial u}{\partial z} + \frac{\partial w}{\partial x} \right]^T, \boldsymbol{\tau} = \begin{bmatrix} \bar{\tau} & \mathbf{0} & \mathbf{0} \\ \mathbf{0} & \bar{\tau} & \mathbf{0} \\ \mathbf{0} & \mathbf{0} & \bar{\tau} \end{bmatrix} \text{ and } \bar{\tau} = \begin{bmatrix} \sigma_x^0 & \sigma_{xy}^0 \\ \sigma_{xy}^0 & \sigma_y^0 \end{bmatrix}. \tag{15}$$

The assumed problem domain $\Omega \in \mathbb{R}^3$ is now discretized into a set of N_e four-node isoparametric quadrilateral shell elements Ω^e , namely Q4, with boundary Γ^e and the total number of nodes N_I . Let $h_I(\mathbf{x})$ and $\mathbf{u}_I = [u_I \quad v_I \quad w_I \quad \theta_{xI} \quad \theta_{yI}]^T$ denote, correspondingly, the bilinear shape functions and the vector of nodal degrees of freedom associated with node I . The displacement assumption [24] and strains in Eq. 13 and Eq. 15 within any element Ω^e can be written as

$$\mathbf{u}^h = \sum_{I=1}^{n_I} \begin{bmatrix} h_I(\mathbf{x}) & 0 & 0 & 0 & 0 \\ 0 & h_I(\mathbf{x}) & 0 & 0 & 0 \\ 0 & 0 & h_I(\mathbf{x}) & 0 & 0 \\ 0 & 0 & 0 & 0 & h_I(\mathbf{x}) \\ 0 & 0 & 0 & h_I(\mathbf{x}) & 0 \end{bmatrix} \mathbf{u}_I, \tag{16}$$

$$\boldsymbol{\varepsilon}^m = \sum_I \mathbf{B}_I^m \mathbf{u}_I, \boldsymbol{\varepsilon}^b = \sum_I \mathbf{B}_I^b \mathbf{u}_I, \boldsymbol{\varepsilon}^s = \sum_I \mathbf{B}_I^s \mathbf{u}_I, \boldsymbol{\varepsilon}^g = \sum_I \mathbf{B}_I^g \mathbf{u}_I, \quad (17)$$

$$\mathbf{B}_I^m = \begin{bmatrix} h_{I,x} & 0 & 0 & 0 & 0 \\ 0 & h_{I,y} & 0 & 0 & 0 \\ h_{I,y} & h_{I,x} & 0 & 0 & 0 \end{bmatrix}, \mathbf{B}_I^b = \begin{bmatrix} 0 & 0 & 0 & h_{I,x} & 0 \\ 0 & 0 & -h_{I,y} & 0 & 0 \\ 0 & 0 & -h_{I,x} & h_{I,y} & 0 \end{bmatrix}, \quad (18)$$

$$\mathbf{B}_I^s = \begin{bmatrix} 0 & 0 & h_{I,x} & 0 & h_I \\ 0 & 0 & h_{I,y} & -h_I & 0 \end{bmatrix}, \mathbf{B}_I^g = \begin{bmatrix} h_{I,x} & 0 & 0 & 0 & 0 \\ 0 & 0 & 0 & 0 & 0 \\ h_{I,y} & h_{I,x} & 0 & 0 & 0 \\ 0 & h_{I,y} & 0 & 0 & 0 \\ 0 & 0 & h_{I,x} & 0 & 0 \\ 0 & 0 & h_{I,y} & 0 & 0 \end{bmatrix}. \quad (19)$$

The formulation for the buckling analysis of a Mindlin-Reissner shell can be expressed in matrix form,

$$\mathbf{k}_G^e \ddot{\mathbf{u}} + \mathbf{k}^e \mathbf{u} = \mathbf{0} \quad (20)$$

where the geometrical element stiffness matrix \mathbf{k}_G^e and the element stiffness matrix \mathbf{k}^e can be defined by

$$\mathbf{k}_G^e = t \int_{\Omega^e} (\mathbf{B}^g)^T \boldsymbol{\tau} \mathbf{B}^g d\Omega, \quad (21)$$

$$\mathbf{k}^e = \int_{\Omega^e} (\mathbf{B}^m)^T \mathbf{D}^m \mathbf{B}^m d\Omega + \int_{\Omega^e} (\mathbf{B}^b)^T \mathbf{D}^b \mathbf{B}^b d\Omega + \int_{\Omega^e} (\mathbf{B}^s)^T \mathbf{D}^s \mathbf{B}^s d\Omega. \quad (22)$$

To overcome the shear locking phenomenon [25-28] that may exhibit in thick shell models, the mixed interpolation of tensorial components method for a four-node isoparametric quadrilateral element, namely MITC4, is directly adopted into the present formulation via the formulation of Bathe et al. [23, 28]. and the configuration in Fig. 1. The performance of drilling degrees of freedom θ_{zI} associated with each node $I \in \Omega^e$ is needed to be improved as published in the literatures [25, 26]. Thus, the arbitrary stiffness co-efficient θ_z is set to be

$$\theta_{zI} = 10^{-3} \times \max\{\text{diag}(\mathbf{k}_I^e)\}. \quad (23)$$

To analyze the buckling effect, the discretized governing equation in terms of the global stiffness matrices \mathbf{K} and \mathbf{K}_g regarding to Eq. 21 and Eq 22, which given

$$(\mathbf{K} - \lambda_c \mathbf{K}_g) \mathbf{u} = \mathbf{0}, \quad (24)$$

with λ_c representing the critical buckling load.

α FEM Formulation

The α FEM-Q4 [29] is similar to the conventional finite element formulation for Q4 elements in literatures [30]. In the α FEM, each assumed strain field can be formulated by adding the averaged nodal strains with an adjustable factor α to the compatible strains. The strain vector $\boldsymbol{\varepsilon}^*$ in Eq. 17 can be rewritten into the form of constants $\boldsymbol{\varepsilon}_c^h$ and $\boldsymbol{\varepsilon}_v^h(\xi, \eta)$ as,

$$\boldsymbol{\varepsilon}^h(\mathbf{x}(\xi, \eta)) = \nabla_s \mathbf{u}^h = \sum_{I=1} \mathbf{B}_I(\mathbf{x}(\xi, \eta)) \mathbf{u}_I = \boldsymbol{\varepsilon}_c^h + \boldsymbol{\varepsilon}_v^h(\xi, \eta), \quad (25)$$

in which $\boldsymbol{\varepsilon}_c^h = \{\varepsilon_{c1} \ \varepsilon_{c2} \ \varepsilon_{c3}\}^T$ and $\boldsymbol{\varepsilon}_v^h = \{\eta \varepsilon_{v1} \ \xi \varepsilon_{v2} \ \xi \varepsilon_{v1} + \eta \varepsilon_{v2}\}^T$. The scalars ε_{c1} , ε_{c2} , ε_{c3} , ε_{v1} and ε_{v2} are depending on the displacement of nodes of the element. The Jacobian matrix $\mathbf{J}(\xi, \eta)$ is also rewritten in the form of constants \mathbf{J}_c and $\mathbf{J}_v(\xi, \eta)$ as

$$\mathbf{J}(\xi, \eta) = \mathbf{J}_c + \mathbf{J}_v(\xi, \eta) \quad (26)$$

The strain vector $\boldsymbol{\varepsilon}^h$ “being scaled” in the α FEM can be expressed with

$$\tilde{\boldsymbol{\varepsilon}}^h(\alpha, \xi, \eta) = \tilde{\mathbf{B}} \mathbf{d} = \sum_{I=1} \tilde{\mathbf{B}}_I(\mathbf{x}(\alpha, \xi, \eta)) \mathbf{u}_I = \boldsymbol{\varepsilon}_c^h + \alpha \boldsymbol{\varepsilon}_v^h(\xi, \eta) \quad (27)$$

with $\alpha \in [0,1]$ is a scaling factor. The scaled strain matrix $\tilde{\mathbf{B}}$ in Eq. 25 of which $\tilde{\mathbf{B}}_I$ associated with node I of element, can be written into the summation form of constant parts \mathbf{B}_c and $\mathbf{B}_v(\xi, \eta)$ as

$$\tilde{\mathbf{B}} = \mathbf{B}_c + \alpha \mathbf{B}_v(\xi, \eta) \quad (28)$$

The Jacobian matrix $\mathbf{J}(\xi, \eta)$ in Eq. 26 is also “scaled” as

$$\tilde{\mathbf{J}} = \mathbf{J}_c + \alpha \mathbf{J}_v(\xi, \eta) \quad (29)$$

where \mathbf{J}_c and $\mathbf{J}_v(\xi, \eta)$ are components of the Jacobian matrix.

Numerical Example and Results

Fig. 2 shows the numerical results of a linear static and buckling analysis of a rectangular non-woven fabric sheet [14] that regards to the thickness-to-length ratio $\frac{t}{L}$, shear factor corrections k and Poisson's ratio ν (referring to Eq. 3 and Eq. 7).

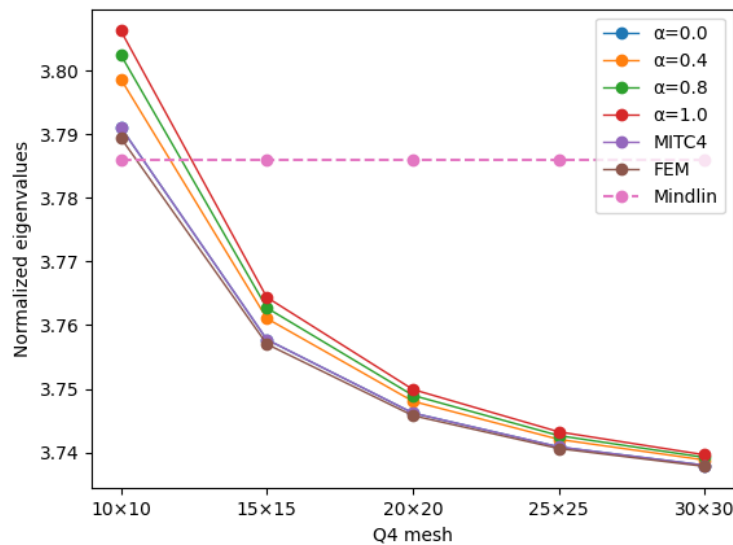


Figure 2. Normalized eigenvalues for buckling ($k_b = \frac{L^2 \lambda_{cr}}{\pi^2} \mathbf{D}_{11}^b$) of a square simply supported multi-layer nonwoven fabric sheet on all edges with $\frac{t}{L} = 0.1$, $k = 0.8333$, $\nu = 0.3$.

The well-known shear locking phenomenon has been resolved using the assumed MITC [31]. The normalized eigenvalues approximated by α FEM-Q4 show a good agreement to the analytical solution implemented with Mindlin's theory [32], and also numerical solutions based on MITC4 and FEM formulations under the simply supported boundary conditions.

Conclusion

The α FEM-Q4 shows that the numerical results from the solution can improve the numerical accuracy in linear static and buckling analysis of textile-like sheet materials without decreasing the computational efficiency. The solution also indicates a good agreement with the analytical solution and numerical reference solutions regarding complex mathematical models in terms of thin shell structures in textile engineering.

Acknowledgment

The first and fourth author acknowledge FCT for the conceded financial support through Project UID/CTM/00264/2019 of 2C2T – Centro de Ciência e Tecnologia Têxtil, hold by National Funds of FCT/MCTES. The second and third author acknowledge support by FCT/MCTES through national funds and when applicable co-funded EU funds under the project SFRH/BD/136554/2018.

References

- [1] Zeng, W. and G.R. Liu, Smoothed Finite Element Methods (S-FEM): An Overview and Recent Developments, *Archives of Computational Methods in Engineering*, 25 (2018) 397-435, doi:10.1007/s11831-016-9202-3
- [2] Yue, J., G.-R. Liu, M. Li, and R. Niu, A cell-based smoothed finite element method for multi-body contact analysis using linear complementarity formulation, *International Journal of Solids and Structures* (2018), doi:https://doi.org/10.1016/j.ijsolstr.2018.02.016
- [3] Zhang, Q. and C.-W. Kan, A Review of Fusible Interlinings Usage in Garment Manufacture, *Polymers*, 10 (2018), doi:10.3390/polym10111230
- [4] Kyosev, Y., *Topology-Based Modeling of Textile Structures and Their Joint Assemblies: Principles, Algorithms and Limitations*, Springer International Publishing, 2018.
- [5] Shishoo, R., *Textile Advances in the Automotive Industry*, Woodhead Publishing Ltd., 2008.
- [6] Zulifqar, A., Z. Khaliq, and H. Hu, Textile Mechanics, in: *In Handbook of Fibrous Materials*, 2020, pp. 455-476)
- [7] Hu, J., *Structure and mechanics of woven fabrics*, Woodhead Publishing Ltd., Cambridge, 2004.
- [8] Hu, J., B. Kumar, and J. Lu, *Handbook of Fibrous Materials*, 2 Volumes: Volume 1: Production and Characterization / Volume 2: Applications in Energy, Environmental Science and Healthcare, Wiley, 2020.
- [9] Akankwasa, N. and D. Veit, *Advances in Modeling and Simulation in Textile Engineering*, Woodhead Publishing, 2021.
- [10] Ahmad, S., A. Rasheed, A. Afzal, and F. Ahmad, *Advanced Textile Testing Techniques*, CRC Press, 2017.
- [11] Pinder, G.F., *Numerical Methods for Solving Partial Differential Equations: A Comprehensive Introduction for Scientists and Engineers*, Wiley, 2018.
- [12] Liu, G.R., An Overview on Meshfree Methods: For Computational Solid Mechanics, *International Journal of Computational Methods*, 13 (2016) 1630001, doi:10.1142/S0219876216300014
- [13] Veit, D., *Simulation in textile technology: Theory and applications* (1 ed.), Woodhead Publishing, 2012.
- [14] Hu, J., M.A. Jahid, N. Harish Kumar, and V. Harun, Fundamentals of the Fibrous Materials, in: *In Handbook of Fibrous Materials*, 2020, pp. 1-36)
- [15] Liu, G.-R., The smoothed finite element method (S-FEM): A framework for the design of numerical models for desired solutions, *Frontiers of Structural and Civil Engineering*, 13 (2019) 456-477, doi:10.1007/s11709-019-0519-5
- [16] Radwańska, M., A. Stankiewicz, A. Wosatko, and J. Pamin, *Plate and Shell Structures: Selected Analytical and Finite Element Solutions*, Wiley, 2016.
- [17] Nguyen-Hoang, S., P. Phung-Van, S. Natarajan, and H.-G. Kim, A combined scheme of edge-based and node-based smoothed finite element methods for Reissner–Mindlin flat shells, *Engineering with Computers*, 32 (2016) 267-284, doi:10.1007/s00366-015-0416-z
- [18] Thai-Hoang, C., N. Nguyen-Thanh, H. Nguyen-Xuan, and T. Rabczuk, An alternative alpha finite element method with discrete shear gap technique for analysis of laminated composite plates, *Applied Mathematics and Computation*, 217 (2011) 7324-7348, doi:http://dx.doi.org/10.1016/j.amc.2011.02.024
- [19] Nguyen-Thanh, N., T. Rabczuk, H. Nguyen-Xuan, and S. Bordas, An alternative alpha finite element method with discrete shear gap technique for analysis of isotropic Mindlin–Reissner plates, *Finite Elements in Analysis and Design*, 47 (2011) 519-535, doi:http://dx.doi.org/10.1016/j.finel.2011.01.004
- [20] Liu, G.R., T. Nguyen-Thoi, and K.Y. Lam, A novel alpha finite element method (α FEM) for exact solution to mechanics problems using triangular and tetrahedral elements, *Computer Methods in Applied Mechanics and Engineering*, 197 (2008) 3883-3897, doi:http://dx.doi.org/10.1016/j.cma.2008.03.011

-
- [21] Gigli, N. and B. Han, Sobolev Spaces on Warped Products, *Journal of Functional Analysis* (2015), doi:10.1016/j.jfa.2018.03.021
- [22] Thai-Hoang, C., N. Nguyen-Thanh, H. Nguyen-Xuan, T. Rabczuk, and S. Bordas, A cell — based smoothed finite element method for free vibration and buckling analysis of shells, *KSCE Journal of Civil Engineering*, 15 (2011) 347-361, doi:10.1007/s12205-011-1092-1
- [23] Ventsel, E. and T. Krauthammer, *Thin Plates and Shells: Theory: Analysis, and Applications*, CRC Press, 2001.
- [24] Hinton, E., *Numerical methods and software for dynamic analysis of plates and shells*, Pineridge Press, Swansea, U.K., 1988.
- [25] Zienkiewicz, O.C. and R.L. Taylor, *The Finite Element Method for Solid and Structural Mechanics* (6 ed. Vol. 2), Butterworth-Heinemann Ltd, 2005.
- [26] Zienkiewicz, O.C., R.L. Taylor, and J.Z. Zhu, Shells as an assembly of flat elements, in: *In The Finite Element Method Set (Sixth Edition)*, Oxford, Butterworth-Heinemann, 2005, pp. 426-453)
- [27] Hughes, T.J.R., M. Cohen, and M. Haroun, Reduced and selective integration techniques in the finite element analysis of plates, *Nuclear Engineering and Design*, 46 (1978) 203-222, doi:10.1016/0029-5493(78)90184-x
- [28] Malkus, D.S. and T.J.R. Hughes, Mixed finite element methods reduced and selective integration techniques: a unification of concepts, *Computer Methods in Applied Mechanics and Engineering*, 15 (1978) 63-81,
- [29] Liu, G.-R. and T. Nguyen-Thoi, *Smoothed finite element methods*, Taylor and Francis Group, LLC, 2010.
- [30] Liu, G.R., T. Nguyen-Thoi, and K.Y. Lam, A novel FEM by scaling the gradient of strains with factor α (α FEM), *Computational Mechanics*, 43 (2008) 369, doi:10.1007/s00466-008-0311-1
- [31] Bathe, K.-J. and E.N. Dvorkin, A formulation of general shell elements—the use of mixed interpolation of tensorial components, *International Journal for Numerical Methods in Engineering*, 22 (1986) 697-722, doi:10.1002/nme.1620220312
- [32] Liew, K.M., J. Wang, T.Y. Ng, and M.J. Tan, Free vibration and buckling analyses of shear-deformable plates based on FSDT meshfree method, *Journal of Sound and Vibration*, 276 (2004) 997-1017, doi:https://doi.org/10.1016/j.jsv.2003.08.026

A Node-Based Strain Smoothing Technique for Free Vibration Analysis of Textile-Like Sheet Materials

Nguyễn T. Quyên^{1,a*}, Nguyễn T. Quốc^{2,3,b}, Nguyễn Đ. Tru^{4,c},
Abel J.P. Gomes^{2,3,d} and Fernando B.N. Ferreira^{1,e}

¹2C2T - Centro de Ciência e Tecnologia Têxtil, Departamento de Engenharia Têxtil, Universidade do Minho, Campus de Azurém, 4804-533 Guimarães, Portugal

²Departamento de Informática, Universidade da Beira Interior, Convento de Sto. António, 6201-001 Covilhã, Portugal

³Instituto de Telecomunicações, Rua Marquês d'Ávila e Bolama, 6201-001 Covilhã, Portugal

⁴Faculty of Textile and Garment Technology, Ho Chi Minh City Industry and Trade College, 20 Tang Nhon Phu, Phuoc Long B Ward, District 9, Ho Chi Minh, Vietnam

^aquyen@2c2t.uminho.pt, ^bquochcmvn@gmail.com, ^cdinhtru1509@gmail.com, ^dagomes@di.ubi.pt, ^efnunes@det.uminho.pt,

Keywords: Textile-like sheet material; Mindlin–Reissner plate theory; Free vibration analysis; Finite element method; Strain smoothing technique; Node-based smoothed finite element

Abstract. This paper presents an implementation of the node-based smoothed finite element method and Reissner-Mindlin plate theory for a four node isoparametric shell element to improve the numerical precision and computational efficiency subjected to free vibration analysis of textile-like sheet materials. A one smoothing cell integration scheme in the strain smoothing technique is implemented to contrast the shear locking phenomenon that may exists in the analysis for moderately-thick and thick shell models. Various numerical results of free vibration analysis for a multi-layer nonwoven fabric sample are compared with other existing analytical solutions and numerical solutions in literatures to demonstrate the effectiveness of the present method. An advantage of the present formulation is that it can improve the numerical precision without decreasing the computational efficiency.

Introduction

The finite element method (FEM) is an efficient tool for analyses of shell/plate structures to help understanding of vibration and buckling behavior of textile-like sheet materials, e.g., the basic practical problem of residual curvature in the fusible interlinings [1-3], through garment manufacturing and also during its use as a garment, as detailed in references [4-6]. However, FEM has some limitations or drawbacks being found during its intensive applications, including in references [7-10]. The node-based smoothed finite element method (NS-FEM), presented by Liu and his coworkers [11-14], is a method formulated through the combinations of the conventional FEM and some techniques from the meshfree methods, and have partly resolved some known issues existing in standard FEM. The strain smoothing stabilization technique evaluates the nodal strain as the divergence of a spatial average of the compatible strain field avoiding the derivative evaluations of mesh-free shape functions at nodes and hence eliminates defective modes [10, 15, 16]. This technique avoids evaluating derivatives of mesh-free shape functions at nodes and therefore eliminates defective modes. This paper is to present a finite element formulation of plate/shell structures based on the node-based strain smoothing technique in finite elements and Mindlin-Reissner plate theory. The present method illustrates that the numerical solution can help increasing the numerical accuracy and the computational efficiency for free vibration analysis of textile-like sheet materials.

Finite Element Formulation

Assume that a fabric sheet is a three-dimensional elastic domain $\Omega \in \mathbb{R}^3$ as a solid body being thin in thickness but having significant length in other two directions [17, 18]. The domain Ω has a Lipschitz-continuous boundary Γ and a body force \mathbf{b} . The first parts of boundary Γ , namely Γ_u where Dirichlet conditions $\bar{\mathbf{u}}$ are prescribed, and the second part denoted with Γ_t where Neumann conditions $\bar{\mathbf{t}} = \bar{\mathbf{t}}$ are also prescribed. Γ_u and Γ_t construct a partition of the boundary Γ for instance $\Gamma = \Gamma_u \cup \Gamma_t$.

The static equilibrium equation governing the solid can be written in term of the stress field as

$$\mathbf{L}^T \boldsymbol{\sigma} + \mathbf{b} = \mathbf{0} \text{ in } \Omega. \quad (1)$$

Let \mathbf{D} be the elasticity matrix [18, 19] that governs the material constants of the solid for plane stress analysis [13, 18, 20, 21] in the present formulation. The stresses $\boldsymbol{\sigma}$ relate to the strains $\boldsymbol{\varepsilon}$ via the generalized Hook's law (also known as the constitutive equations), which gives

$$\boldsymbol{\sigma} = \mathbf{D}\boldsymbol{\varepsilon}. \quad (2)$$

The strain matrix $\boldsymbol{\varepsilon}$ relates to the displacements in the form of compatibility equations (or the kinematic equations)

$$\boldsymbol{\varepsilon} = \mathbf{L}\mathbf{u}, \quad (3)$$

with \mathbf{u} is the displacement component at a point in Ω . Substituting Eq. 8 into Eq. 7 which gives the equilibrium equation in terms of the displacements.

The conditions of Dirichlet boundary Γ_u and the Neumann boundary Γ_t are also defined as

$$\mathbf{u} = \mathbf{u}_\Gamma, \quad (4)$$

$$\mathbf{L}_n^T \boldsymbol{\sigma} = \mathbf{t}_\Gamma, \quad (5)$$

in which \mathbf{L}_n is the matrix of unit outward normal components. Hence, the strain energy (or potential energy) for elastic solid can be quantified via

$$\mathbf{U} = \frac{1}{2} \int_{\Omega} \boldsymbol{\varepsilon}^T(\mathbf{x}) \boldsymbol{\sigma}(\mathbf{x}) \, d\Omega = \frac{1}{2} \int_{\Omega} \boldsymbol{\varepsilon}^T(\mathbf{x}) \mathbf{c} \boldsymbol{\varepsilon}(\mathbf{x}) \, d\Omega. \quad (6)$$

The configuration domain $\Omega \in \mathbb{R}^3$ that forms the shell mid-surface based on the Mindlin-Reissner plate theory being defined by

$$V = \left\{ (x, y, z) \in \mathbb{R}^3 \mid (x, y) \in \Omega \subset \mathbb{R}^2, z \in \left[-\frac{t}{2}, \frac{t}{2} \right] \right\}. \quad (7)$$

For approximation of the stress state in a moderately thick shell, to which the analysis of the membrane deformations can be performed, the displacement assumption gives

$$\begin{aligned} u(x, y, z) &= u_0(x, y) + z\beta_x(x, y) \\ v(x, y, z) &= v_0(x, y) + z\beta_y(x, y). \\ w(x, y, z) &= w_0(x, y) \end{aligned} \quad (8)$$

in which u_0 , v_0 and w_0 denote the displacement components along x -, y - and z -directions, respectively. β_x and β_y stand for the normal rotations to the undeformed mid-surface corresponding to the x - z and y - z planes having $\beta_x = \frac{\partial w}{\partial x}$ and $\beta_y = \frac{\partial w}{\partial y}$.

The membrane strain $\boldsymbol{\varepsilon}^m$, curvature strain $\boldsymbol{\varepsilon}^b$ are calculated from the corresponding 2D differential operators \mathbf{L} , as presented in Eq. 8, which are

$$\mathbf{L}_{2D}^m = \begin{bmatrix} \frac{\partial}{\partial x} & 0 \\ 0 & \frac{\partial}{\partial y} \\ \frac{\partial}{\partial y} & \frac{\partial}{\partial x} \end{bmatrix} \text{ and } \mathbf{L}_{2D}^b = \begin{bmatrix} 0 & \frac{\partial}{\partial x} \\ -\frac{\partial}{\partial y} & 0 \\ -\frac{\partial}{\partial x} & \frac{\partial}{\partial y} \end{bmatrix}. \quad (9)$$

From the displacement components in Eq. 8 with $\mathbf{u} = [u_0 \quad v_0 \quad w_0]^T$ and $\boldsymbol{\beta} = [\beta_x \quad \beta_y]^T$, Eq. 9 can be rewritten as

$$\boldsymbol{\varepsilon}^m = \mathbf{L}_{2D}^m \mathbf{u} = \begin{bmatrix} u_{0,x} \\ v_{0,y} \\ u_{0,y} + v_{0,x} \end{bmatrix}, \boldsymbol{\varepsilon}^b = \mathbf{L}_{2D}^b \boldsymbol{\beta} = \begin{bmatrix} \beta_{x,x} \\ -\beta_{y,y} \\ \beta_{x,y} - \beta_{y,x} \end{bmatrix}, \quad (10)$$

while the transverse shear strain $\boldsymbol{\varepsilon}^s$ can be quantified using

$$\boldsymbol{\varepsilon}^s = \begin{Bmatrix} \gamma_{xy} \\ \gamma_{yz} \end{Bmatrix} = \begin{bmatrix} w_{,x} + \beta_x \\ w_{,y} - \beta_y \end{bmatrix}. \quad (11)$$

Let the problem domain $\Omega \in \mathbb{R}^3$ be discretized into a set of N_e four-node isoparametric quadrilateral shell elements Ω^e referred to as Q4 with boundary Γ^e and the total number of nodes N_I . Let $N_I(\mathbf{x})$ and $\mathbf{d}_I = [u_I \quad v_I \quad w_I \quad \theta_{xI} \quad \theta_{yI}]^T$, respectively, indicate the bilinear shape functions and the vector of nodal degrees of freedom associated with node I . The displacement assumption [22] and strains in Eq. 13 and Eq. 15 within any element Ω^e can be written as

$$\mathbf{u}^h = \sum_{I=1}^{n_I} \begin{bmatrix} N_I(\mathbf{x}) & 0 & 0 & 0 & 0 \\ 0 & N_I(\mathbf{x}) & 0 & 0 & 0 \\ 0 & 0 & N_I(\mathbf{x}) & 0 & 0 \\ 0 & 0 & 0 & 0 & N_I(\mathbf{x}) \\ 0 & 0 & 0 & N_I(\mathbf{x}) & 0 \end{bmatrix} \mathbf{d}_I, \quad (12)$$

$$\boldsymbol{\varepsilon}^m = \sum_I \mathbf{B}_I^m \mathbf{d}_I, \boldsymbol{\varepsilon}^b = \sum_I \mathbf{B}_I^b \mathbf{d}_I, \boldsymbol{\varepsilon}^s = \sum_I \mathbf{B}_I^s \mathbf{d}_I, \quad (13)$$

$$\mathbf{B}_I^m = \begin{bmatrix} N_{I,x} & 0 & 0 & 0 & 0 \\ 0 & N_{I,y} & 0 & 0 & 0 \\ N_{I,y} & N_{I,x} & 0 & 0 & 0 \end{bmatrix}, \quad (14)$$

$$\mathbf{B}_I^b = \begin{bmatrix} 0 & 0 & 0 & N_{I,x} & 0 \\ 0 & 0 & -N_{I,y} & 0 & 0 \\ 0 & 0 & -N_{I,x} & N_{I,y} & 0 \end{bmatrix}, \quad (15)$$

$$\mathbf{B}_I^s = \begin{bmatrix} 0 & 0 & N_{I,x} & 0 & N_I \\ 0 & 0 & N_{I,y} & -N_I & 0 \end{bmatrix}. \quad (16)$$

In the free analysis, the formulation of a Mindlin-Reissner shell can be written in the matrix form,

$$\mathbf{m}^e \ddot{\mathbf{d}} + \mathbf{k}^e \mathbf{d} = \mathbf{0}, \quad (17)$$

where the element stiffness matrix \mathbf{k}^e and element mass matrix \mathbf{m}^e are given as

$$\mathbf{k}^e = \int_{\Omega^e} (\mathbf{B}^m)^T \mathbf{D}^m \mathbf{B}^m d\Omega + \int_{\Omega^e} (\mathbf{B}^b)^T \mathbf{D}^b \mathbf{B}^b d\Omega + \int_{\Omega^e} (\mathbf{B}^s)^T \mathbf{D}^s \mathbf{B}^s d\Omega, \quad (18)$$

$$\mathbf{m}^e = \int_{\Omega^e} \mathbf{N}^T \mathbf{m} \mathbf{N} d\Omega, \mathbf{m} = \rho \begin{bmatrix} t & 0 & 0 & 0 & 0 & 0 \\ 0 & t & 0 & 0 & 0 & 0 \\ 0 & 0 & t & 0 & 0 & 0 \\ 0 & 0 & 0 & 0 & \frac{t^3}{12} & 0 \\ 0 & 0 & 0 & \frac{t^3}{12} & 0 & 0 \\ 0 & 0 & 0 & 0 & 0 & 0 \end{bmatrix}, \quad (19)$$

with ρ being the density of the fabric sheet.

The stiffness co-efficient of the drilling degrees of freedom θ_{zI} associated with each node $I \in \Omega^e$, as figured out in the literatures [21, 23], is set to be

$$\theta_{zI} = 10^{-3} \times \max\{\text{diag}(\mathbf{k}_I^e)\}, \quad (20)$$

the element stiffness matrix related to node I is, therefore, written as

$$\mathbf{k}_I^e = \begin{bmatrix} \mathbf{k}_I^m & \mathbf{0}_{2 \times 3} & 0 \\ \mathbf{0}_{3 \times 2} & \mathbf{k}_I^b + \mathbf{k}_I^s & 0 \\ \mathbf{0}_{1 \times 2} & \mathbf{0}_{1 \times 3} & \theta_{zI} \end{bmatrix}. \quad (21)$$

The shear locking phenomenon may exist in moderately thick shell models as figured out in works [21, 23-26]. In the present formulation, the shear strain term is evaluated using one smoothing cell integration scheme (see Eq. 24) in the strain smoothing technique to overcome the shear locking problem.

Consider the node-based strain smoothing technique, each of element $\Omega^e \in \Omega$ is further subdivided into 4 triangular elements, in which the centroid node of Ω^e is the first node of each sub triangular element, with $\Omega^e = \cup_{k=1}^4 \Omega_k^s$, $\Omega_i^s \cap \Omega_j^s = \emptyset$, $i \neq j$ ($i = 1, \dots, 4; j = 1, \dots, 4$), and Ω_k^s indicates the k th smoothing domain of the element Ω^e . Each smoothing domain has the total number n_b^s of boundary segments that $\Gamma_k^s = \cup_{b=1}^{n_b^s} \Gamma_{kb}^e$ with $\Gamma_i^s \cap \Gamma_j^s = \emptyset$, $i \neq j$ ($i = 1, \dots, n_b^s; j = 1, \dots, n_b^s$). The total number of smoothing domains within each discretized element Ω^e can be equal to the total number of discretized elements Ω^e within the system domain Ω . This means that one discretized element Ω^e can be used as one smoothing domain Ω_k^s . Now, direct apply strain smoothing technique with linear strain fields for static as in works [9, 27, 28] to Eq. 13 which can be approximated as

$$\boldsymbol{\varepsilon}^m(\mathbf{x}_k) = \frac{1}{A_k^s} \int_{\Gamma_k^s} \mathbf{n} \cdot \mathbf{u}(\mathbf{x}_k) d\Gamma = \frac{1}{A_k^s} \sum_{l=1}^3 \begin{bmatrix} \bar{b}_{kIx} & 0 & 0 & 0 & 0 & 0 \\ 0 & \bar{b}_{kIy} & 0 & 0 & 0 & 0 \\ \bar{b}_{kIy} & \bar{b}_{kIx} & 0 & 0 & 0 & 0 \end{bmatrix} \cdot \mathbf{d}_I, \quad (22)$$

$$\boldsymbol{\varepsilon}^b(\mathbf{x}_k) = \frac{1}{A_k^s} \int_{\Gamma_k^s} \mathbf{n} \cdot \mathbf{u}(\mathbf{x}_k) d\Gamma = \frac{1}{A_k^s} \sum_{l=1}^3 \begin{bmatrix} 0 & 0 & \bar{b}_{kIx} & 0 & 0 & 0 \\ 0 & -\bar{b}_{kIy} & 0 & 0 & 0 & 0 \\ 0 & -\bar{b}_{kIx} & \bar{b}_{kIy} & 0 & 0 & 0 \end{bmatrix} \cdot \mathbf{d}_I, \quad (23)$$

$$\boldsymbol{\varepsilon}^s(\mathbf{x}) = \frac{1}{A^e} \int_{\Omega^e} \mathbf{n} \cdot \mathbf{u}(\mathbf{x}) d\Gamma = \frac{1}{A^e} \sum_{l=1}^4 \begin{bmatrix} 0 & 0 & \bar{b}_{kIx} & 0 & \bar{b}_{kI} \\ 0 & 0 & \bar{b}_{kIy} & -\bar{b}_{kI} & 0 \end{bmatrix} \cdot \mathbf{d}_I, \quad (24)$$

with

$$\bar{b}_{kIx} = \frac{1}{A_k^s} \int_{\Gamma_k^s} n_x N_I d\Gamma = \frac{1}{A_k^s} \sum_{b=1}^{n_b^s} n_{xb} \cdot N_I(\mathbf{x}_b^G) \cdot l_b, \quad (25)$$

$$\bar{b}_{kIy} = \frac{1}{A_k^s} \int_{\Gamma_k^s} n_y N_I d\Gamma = \frac{1}{A_k^s} \sum_{b=1}^{n_b^s} n_{yb} \cdot N_I(\mathbf{x}_b^G) \cdot l_b. \quad (26)$$

In Eqs. 22, 23 and 24, $A^e = \int_{\Omega^e} d\Omega$ is the area of Ω^e , while $A_k^s = \int_{\Omega_k^s} d\Omega$ is the area of the k th smoothing domain $\Omega_k^s \subset \Omega^e$. In Eq. 25 and Eq. 26, n_{xb} and n_{yb} indicate the components of the outward unit normal to the b th boundary segment and \mathbf{x}_b^G is the coordinate value of Gauss point of the b th boundary segment.

For analyzing the free vibration effect, the discretized governing equation in terms of the global stiffness matrices \mathbf{K} and the global mass matrix \mathbf{M} regarding to Eq. 18 and Eq 19, which given

$$\mathbf{M}\ddot{\mathbf{d}} - \mathbf{K}\mathbf{d} = \mathbf{0}. \quad (27)$$

Substitute the general solution $\mathbf{d} = \bar{\mathbf{d}}\exp(i\omega t)$ into Eq. 27, the natural frequency ω can be quantified by solving

$$(\mathbf{K} - \omega^2 \mathbf{M})\bar{\mathbf{d}} = \mathbf{0}. \quad (28)$$

Numerical Example and Results

In present study, a numerical example for a linear static free vibration analysis of multi-layer nonwoven fabric sheet, a wide range of the sub-cell $\Omega_c^s \subset \Omega^e$ is considered, together with the simply supported boundary conditions. The non-dimensional natural frequencies $\bar{\omega}$ for a non-woven fabric sheet having the thickness-to-length ratio $\frac{t}{L}$, the shear factor corrections k and the Poisson's ratio ν are shown in Fig. 1.

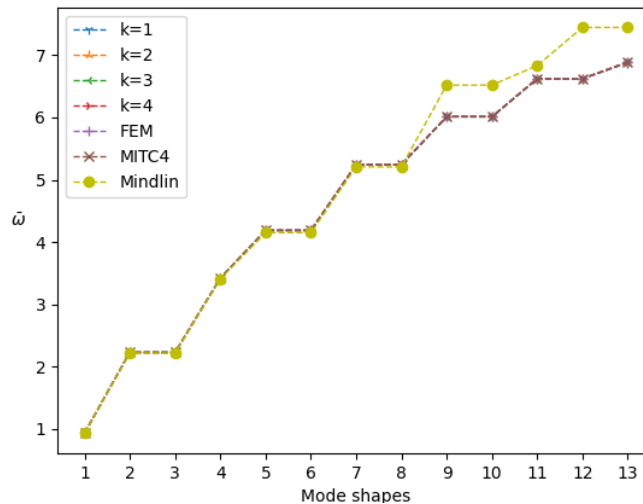


Figure 1. Mode shapes of non-dimensional natural frequency $\bar{\omega}$ for a square simply supported non-woven fabric sheet with $\frac{t}{L} = 0.1$, $k = 0.8333$, $\nu = 0.3$ and $35 \times 35 \Omega^e$.

The numerical results of linear static and free vibration analysis, as illustrated in Fig. 1, indicate a good agreement to the analytical solution (Mindlin's theory) [29], and numerical solutions based on MITC4 and conventional FEM under the simply supported boundary conditions.

Conclusion

The present method can reduce the practical implementation effort and computational cost in comparison to the standard FEM approaches. The shear locking problem has been resolved via the implementation using one smoothing cell integration in the strain smoothing technique. The numerical results show that the solutions can improve numerical accuracy and computational efficiency subjected to free vibration analysis of textile-like sheet materials.

Acknowledgment

The first and fourth author acknowledge FCT for the conceded financial support through Project UID/CTM/00264/2019 of 2C2T – Centro de Ciência e Tecnologia Têxtil, hold by National Funds of FCT/MCTES. The second and third author acknowledge support by FCT/MCTES through national funds and when applicable co-funded EU funds under the project SFRH/BD/136554/2018.

References

- [1] Zhang, Q. and C.-W. Kan, A Review of Fusible Interlinings Usage in Garment Manufacture, *Polymers*, 10 (2018), doi:10.3390/polym10111230
- [2] Phebe, K., K. Kaliappa, and B. Chandrasekaran, Evaluating performance characteristics of different fusible interlinings, *Indian Journal of Fibre and Textile Research*, 39 (2014) 380-385,
- [3] Lai, S.S., Optimal combinations of face and fusible interlining fabrics, *International Journal of Clothing Science and Technology*, 13 (2001) 322-338, doi:10.1108/09556220110405073

-
- [4] Behera, B.K. and P.K. Hari, *Woven Textile Structure: Theory And Applications*, Elsevier Science, 2010.
- [5] Namdar, Ö. and H. Darendeliler, Buckling, postbuckling and progressive failure analyses of composite laminated plates under compressive loading, *Composites Part B: Engineering*, 120 (2017) 143-151, doi:<https://doi.org/10.1016/j.compositesb.2017.03.066>
- [6] Rajesh, M. and J. Pitchaimani, Experimental investigation on buckling and free vibration behavior of woven natural fiber fabric composite under axial compression, *Composite Structures*, 163 (2017) 302-311, doi:<https://doi.org/10.1016/j.compstruct.2016.12.046>
- [7] Hughes, T.J.R., *The Finite Element Method: Linear Static and Dynamic Finite Element Analysis*, Dover Publications, 2012.
- [8] Belytschko, T., W.K. Liu, B. Moran, and K. Elkhodary, *Nonlinear Finite Elements for Continua and Structures*, Wiley, 2013.
- [9] Zeng, W. and G.R. Liu, Smoothed Finite Element Methods (S-FEM): An Overview and Recent Developments, *Archives of Computational Methods in Engineering*, 25 (2018) 397-435, doi:[10.1007/s11831-016-9202-3](https://doi.org/10.1007/s11831-016-9202-3)
- [10] Liu, G.R., An Overview on Meshfree Methods: For Computational Solid Mechanics, *International Journal of Computational Methods*, 13 (2016) 1630001, doi:[10.1142/S0219876216300014](https://doi.org/10.1142/S0219876216300014)
- [11] Liu, G.R., K.Y. Dai, and T.T. Nguyen, A Smoothed Finite Element Method for Mechanics Problems, *Computational Mechanics*, 39 (2007) 859-877, doi:[10.1007/s00466-006-0075-4](https://doi.org/10.1007/s00466-006-0075-4)
- [12] Nguyen-Xuan, H., T. Rabczuk, N. Nguyen-Thanh, T. Nguyen-Thoi, and S. Bordas, A node-based smoothed finite element method with stabilized discrete shear gap technique for analysis of Reissner–Mindlin plates, *Computational Mechanics*, 46 (2010) 679-701, doi:[10.1007/s00466-010-0509-x](https://doi.org/10.1007/s00466-010-0509-x)
- [13] Thai-Hoang, C., N. Nguyen-Thanh, H. Nguyen-Xuan, T. Rabczuk, and S. Bordas, A cell — based smoothed finite element method for free vibration and buckling analysis of shells, *KSCE Journal of Civil Engineering*, 15 (2011) 347-361, doi:[10.1007/s12205-011-1092-1](https://doi.org/10.1007/s12205-011-1092-1)
- [14] Liu, G.-R. and T. Nguyen-Thoi, *Smoothed finite element methods*, Taylor and Francis Group, LLC, 2010.
- [15] Liu, G., K. Dai, and T. Nguyen, A Smoothed Finite Element Method for Mechanics Problems, *Computational Mechanics*, 39 (2007) 859-877, doi:[10.1007/s00466-006-0075-4](https://doi.org/10.1007/s00466-006-0075-4)
- [16] Liu, G.R., T.T. Nguyen, K.Y. Dai, and K.Y. Lam, Theoretical aspects of the smoothed finite element method (SFEM), *International Journal for Numerical Methods in Engineering*, 71 (2007) 902-930, doi:[10.1002/nme.1968](https://doi.org/10.1002/nme.1968)
- [17] Zulifqar, A., Z. Khaliq, and H. Hu, Textile Mechanics, in: *In Handbook of Fibrous Materials*, 2020, pp. 455-476)
- [18] Hu, J., *Structure and mechanics of woven fabrics*, Woodhead Publishing Ltd., Cambridge, 2004.
- [19] Veit, D., *Simulation in textile technology: Theory and applications (1 ed.)*, Woodhead Publishing, 2012.
- [20] Gigli, N. and B. Han, Sobolev Spaces on Warped Products, *Journal of Functional Analysis* (2015), doi:[10.1016/j.jfa.2018.03.021](https://doi.org/10.1016/j.jfa.2018.03.021)
- [21] Zienkiewicz, O.C. and R.L. Taylor, *The Finite Element Method for Solid and Structural Mechanics (6 ed. Vol. 2)*, Butterworth-Heinemann Ltd, 2005.

-
- [22] Hinton, E., Numerical methods and software for dynamic analysis of plates and shells, Pineridge Press, Swansea, U.K., 1988.
- [23] Zienkiewicz, O.C., R.L. Taylor, and J.Z. Zhu, Shells as an assembly of flat elements, in: In The Finite Element Method Set (Sixth Edition), Oxford, Butterworth-Heinemann, 2005, pp. 426-453)
- [24] Hughes, T.J.R., M. Cohen, and M. Haroun, Reduced and selective integration techniques in the finite element analysis of plates, Nuclear Engineering and Design, 46 (1978) 203-222, doi:10.1016/0029-5493(78)90184-x
- [25] Malkus, D.S. and T.J.R. Hughes, Mixed finite element methods reduced and selective integration techniques: a unification of concepts, Computer Methods in Applied Mechanics and Engineering, 15 (1978) 63-81,
- [26] Bathe, K.-J. and E.N. Dvorkin, A formulation of general shell elements—the use of mixed interpolation of tensorial components, International Journal for Numerical Methods in Engineering, 22 (1986) 697-722, doi:10.1002/nme.1620220312
- [27] Liu, G.-R., The smoothed finite element method (S-FEM): A framework for the design of numerical models for desired solutions, Frontiers of Structural and Civil Engineering, 13 (2019) 456-477, doi:10.1007/s11709-019-0519-5
- [28] Yue, J., G.-R. Liu, M. Li, and R. Niu, A cell-based smoothed finite element method for multi-body contact analysis using linear complementarity formulation, International Journal of Solids and Structures (2018), doi:https://doi.org/10.1016/j.ijsolstr.2018.02.016
- [29] Liew, K.M., J. Wang, T.Y. Ng, and M.J. Tan, Free vibration and buckling analyses of shear-deformable plates based on FSDT meshfree method, Journal of Sound and Vibration, 276 (2004) 997-1017, doi:https://doi.org/10.1016/j.jsv.2003.08.026

Simulation of Mechanical Behaviour of Woven Fabrics at the Scale of Yarns under Multi-Loading

OGRENI Nertila^{1,2,3,a*}, ZAVALANI Gentian^{3,b}, NIKOLLA Ligor^{3,c},
SINOIMERI Artan^{1,2,d}

¹Université de Haute-Alsace, LPMT, 11 rue A. Werner, 68200 Mulhouse, France

²Université de Strasbourg, France

³Polytechnic University of Tirana FIMIF, Sheshi "Nene Tereza" n°1, Tirana, Albania

nertila.ogreni@uha.fr, g.zavalani@fimif.edu.al, ligor.nikolla@umt.edu.al, artan.sinoimeri@uha.fr

Keywords: simulation, fibres, yarns, fabrics, mechanics.

Abstract. The mechanical behaviour of textile structures is one of their most important characteristics as far as their end use is concerned. Textile structures, fabrics, or yarns are often considered as continuous mediums apart from the fact that they are composed by some discrete elements, individual fibres composing yarns and yarns composing fabrics. This is known as the transition scale, a very important lock to be considered, to evaluate the real structure behaviour. In this context, this work presents some simulations of the mechanical behaviour of a fabric where the yarn is a continuum material. Particular attention was paid to simultaneous loading in uniaxial or biaxial extension and shear loadings. The results of numerical simulations, which show the deformed fabric unit cell under multiload conditions, are coherent with experimental observations and encourage the authors to continue the present work with parametrical and inverse case studies.

Introduction

A general mechanical model of a single fibre, considered as a thin rod, was developed by De Jong and Postle [1] based on the previous work of Kirchhoff [2]. This approach consists on the minimisation of the potential energy accumulated on the fiber during its deformation. It is necessary to consider some assumptions before analysing different potential energy terms of the fiber.

First, the fibres are considered to have a circular cross section which can change only due to fiber-to-fiber contact and compression. Second, the textile fibers have been considered as thin rods with a linear elastic behaviour. The third assumption is related to the twist energy; this term is assumed to be negligible by respect to the other energy terms. Furthermore, the elongation energy has been taken into account.

As it has been shown [3], the total potential energy accumulated on a fiber i of length L_i composing the unit cell of a fabric can be calculated as the sum of independents energy terms such as:

$$E = \int_0^{L_i} (E_B + E_{TR} + E_S) ds \quad (1)$$

where E_B , E_{TR} , E_S are respectively the terms of the energy density per unit length due to fiber bending, traction and shearing.

Each one of these energy density terms can be expressed as follows:

$$E_B = \frac{B}{2} k^2 ; \quad E_{TR} = \frac{Y}{2} \varepsilon^2 ; \quad E_S = \frac{S_L}{2} \gamma^2 \quad (2)$$

In these relations the parameters related with the material of the fibers are respectively the bending rigidity B , the elongation rigidity Y and the transversal shear rigidity S_L , whereas the parameters related with the geometry, i.e. fiber deformations, are respectively: the total curvature k , the axial elongation ε and the transversal shearing angle γ .

The term of transversal rod shearing energy have also been neglected, compared to the other terms as shown in a previous work [3].

The purpose is to find out the fibre's paths or trajectories that minimize the total energy of the fabric unit cell, which is the equivalent condition of the mechanical equilibrium.

The position of the fibres is given by the coordinative system (Z_1, Z_2, Z_3) , firstly given by Love [4] and after adopted by De Jong and Postle [1].

Let's introduce the Lagrangian for a mechanical system:

$$L(Z_i, \dot{Z}_i, t) = T - W \quad (3)$$

where T and W are respectively kinetic and potential energy.

If a space geometric variable s is used instead of the time t , and the body is deformed under external stresses without moving, i.e. if only static deformation is concerned, the Lagrangian represent the total negative potential energy accumulated in the deformed body.

Let's now introduce Hamiltonian function.

$$H = \sum_{l=1}^g \lambda_l Z'_l - L(Z_k, Z'_k, s) \quad (4)$$

where g is the number of independent variables.

The goal is to find out the evolution of the independent variables along the fiber which minimize the energy accumulated in the fiber when external forces λ_i are applied on it.

The solution is given by the canonical equations of Hamilton:

$$\begin{aligned} \dot{Z}_i &= \frac{\partial H}{\partial \lambda_i} \\ \dot{\lambda}_i &= -\frac{\partial H}{\partial Z_i} \end{aligned} \quad (5)$$

By using the canonical equations of Hamilton (Eq. 5) and the explicit form of Hamilton function (Eq. 4), the coordinates variations and the distributed external forces may be integrated at each iteration path. If the equilibrium is not achieved, it is necessary to calculate the deformation state, represented by the so-called control vector, which is updated by the same Newton-Raphson method as De Jong & Postle [1] as follows:

$$\mathbf{m}_j^i = \mathbf{m}_j^{i-1} + \left[\frac{\partial^2 H}{\partial m_j \partial m_l} \right]^{-1} \frac{\partial H}{\partial m_j} \quad j=1:3 \quad (6)$$

Here, α is a 'dumping factor'. It effects the simulation convergence speed.

Fabrics Modelling

The fabrics considered in the present study are plain weave ones, which are very used in textile industry due to their geometric and mechanical properties.

The yarns composing the fabric are supposed to be continuous and obeying to thin rod mechanics.

Figure 1b shows the symbolic representation of the elementary cell of a plain weave fabric with warp yarns in red and weft ones in blue. To simplify the study of this structure, it is necessary to analyse its geometry, which means to determine different yarn symmetries within the fabric even where the latter is subjected to different loading types.

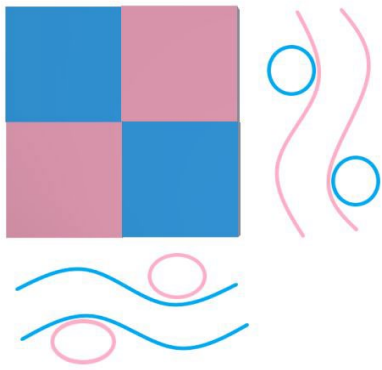


Figure 1a. Symbolic representation of the plain weave fabric.

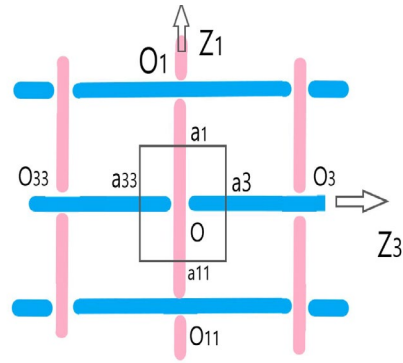


Figure 1b. Schematic representation of the plain weave unit cell.

Table 1. Fabric Symmetry analysis [5].

Segment given:	Symmetric related with:	Symmetric segment:
[Owp a1]	a1	[a1 O1]
[Owp a11]	a11	[a11 O1]
[Owt a3]	a3	[a3 O3]
[Owt a33]	a33	[a33 O3]

OZ_2 is the thickness axis, perpendicular to the fabric plane

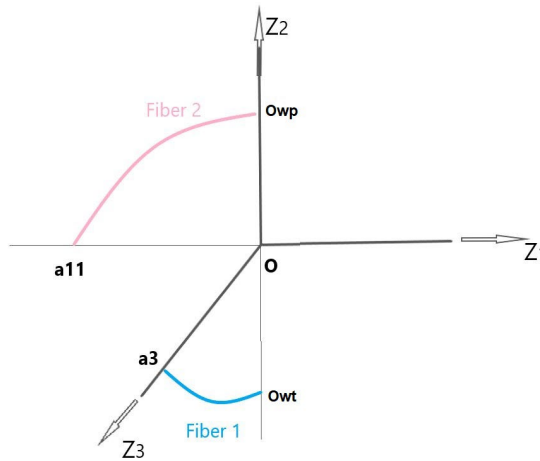


Figure 2. Schematic representation in 3 dimensions of the yarn axes of the fabric representative portion.

Only 1/8th (Fig. 2) of the entire plain weave unit cell (Fig. 1) is necessary to represent the whole structure because of trivial and evident symmetries shown in Table 1. Let's precise that these symmetries are always respected in the case of fabric in-plane deformation.

At the first simulation step, both yarns are placed as straight lines following respectively Z_3 and Z_1 axes with a maximum interpenetration. They are bended during the simulations due yarn-to-yarn contact forces until the mechanical equilibrium of 1/8th of the unit cell is achieved. Then the whole unit cell of the fabric can be built by symmetry considerations.

Equilibrium Under External Forces

After computing the equilibrium geometry without any external constraint, some external forces can be applied in order to find the new equilibrium yarn trajectories and fabric deformations. Based on the most common deformation tests for fabrics, three typical constraints have been applied:

- Traction, uniaxial and biaxial without shear.
- Pure shear.
- Multiload. (Simultaneous shear, uniaxial and biaxial traction)

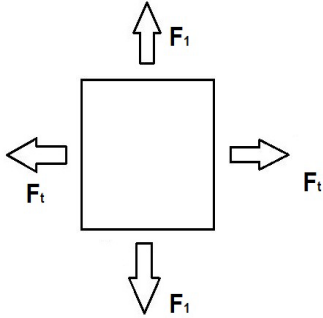


Figure 3a. Schematic representation of the structure under traction in both directions.

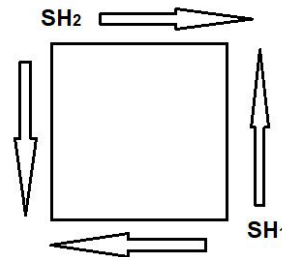


Figure 3b. Schematic representation of pure shear.

Uniaxial / Biaxial Traction. The length of both warp and weft yarns are fixed at 1mm and their diameter is 0.5 mm. The yarn Young’s modulus Y has been varied from 1 to 4 GPa; yarn bending rigidity B from $1 \cdot 10^{-6}$ to $4 \cdot 10^{-6}$ Nm^2 . The same tests for extensible and inextensible fibers have been carried out for both uniaxial and biaxial traction (Fig. 3).

During uniaxial traction tests, the traction force is applied only on the first yarn, whereas for the biaxial tests, transversal traction forces have been applied on the second yarn also.

The fabric strains have been calculated with respect to the fabric dimensions where no external force has been applied, i.e. as Lagrangian ones, as follows: ϵ_1 is the deformation in the traction direction, ϵ_2 is the deformation of the distance $O_{wt}O_{wp}$ in Fig. 2, and ϵ_3 is the width deformation.

Some results for inextensible and extensible yarns are shown below:

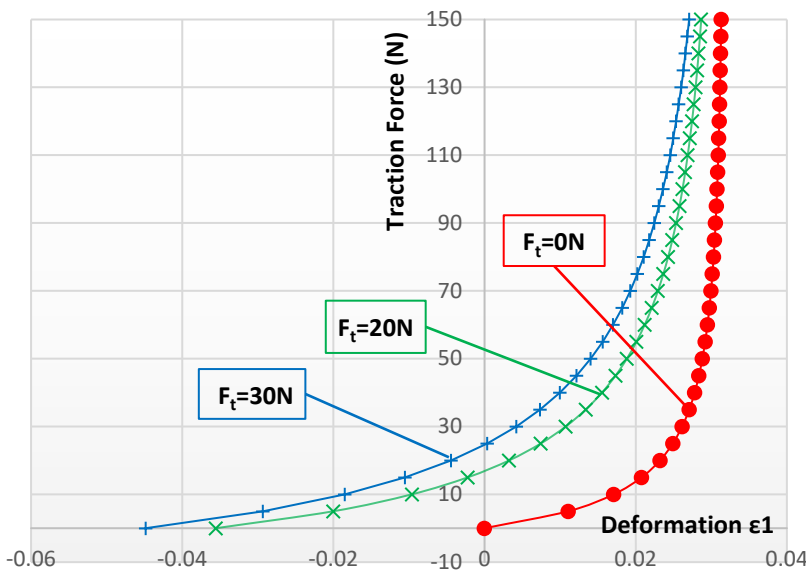


Figure 4a. Uniaxial and biaxial force-deformation curves for *inextensible* yarns.

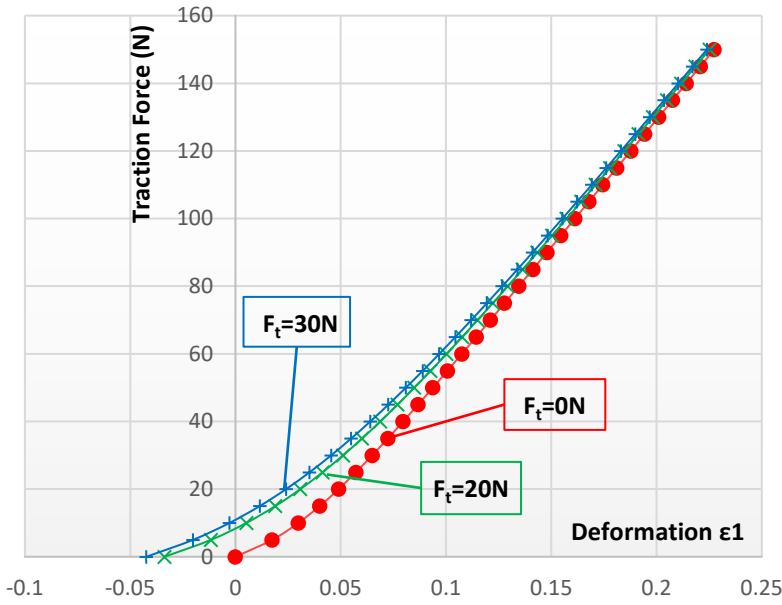


Figure 4b. Uniaxial and biaxial force-deformation curves for *extensible* yarns.

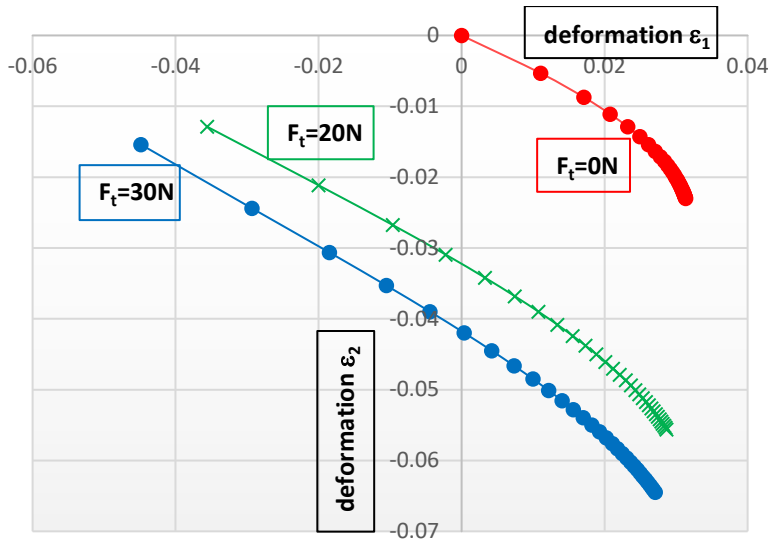


Figure 5a. Deformation ϵ_1 versus deformation ϵ_2 for *inextensible* yarns in both cases: uniaxial traction and biaxial traction for two levels of transversal force F_t 30 N and 20N.

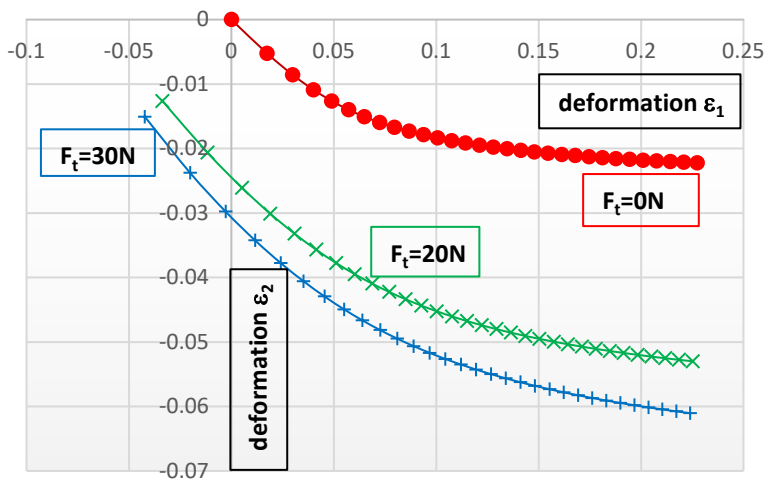


Figure 5b. Deformation ϵ_1 versus deformation ϵ_2 for *extensible* yarns in both cases: uniaxial traction and biaxial traction for two levels of transversal force F_t : 30 N and 20N.

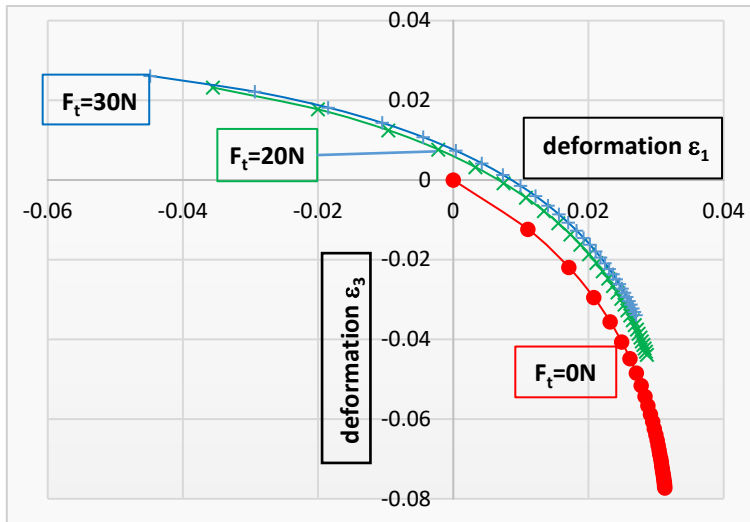


Figure 6a. Deformation ϵ_1 versus deformation ϵ_3 for *inextensible* yarns in both cases: uniaxial traction and biaxial traction for two levels of transversal force F_t 30 N and 20N.

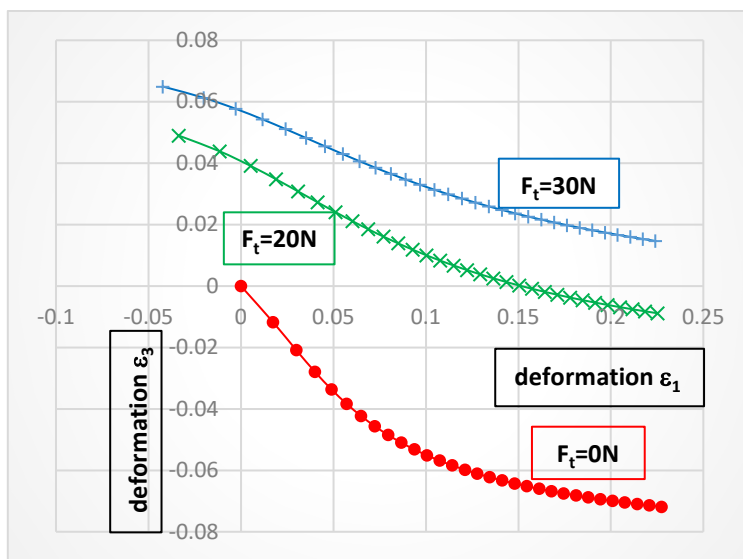


Figure 6b. Deformation ϵ_1 versus deformation ϵ_3 for *extensible* yarns in both cases: uniaxial traction and biaxial traction for two levels of transversal force F_t 30 N and 20N.

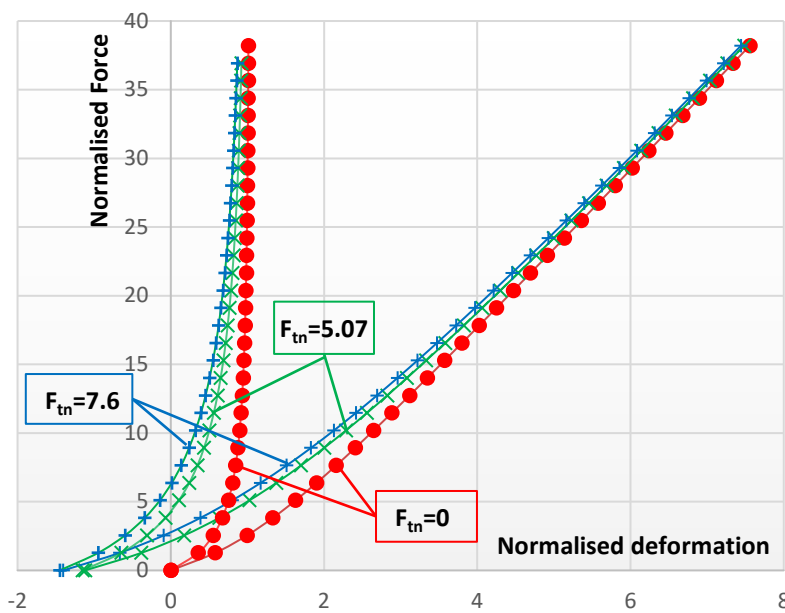


Figure 7. Normalized deformation (deformation divided with the *crimp*) versus normalized force $(F \cdot L^2) / B$ for uniaxial and biaxial extension; extensible yarns (right) and inextensible yarns (left).

Shear Load. When shear forces are applied on the fabric, the mechanical equilibrium (see Fig. 2 and Fig. 3b) of the force moments requires that:

$$SH_1 * Z_3 = SH_2 * Z_1 \tag{7}$$

where Z_3 and Z_1 are the dimensions of the fabric representative portion as shown on Fig. 2.

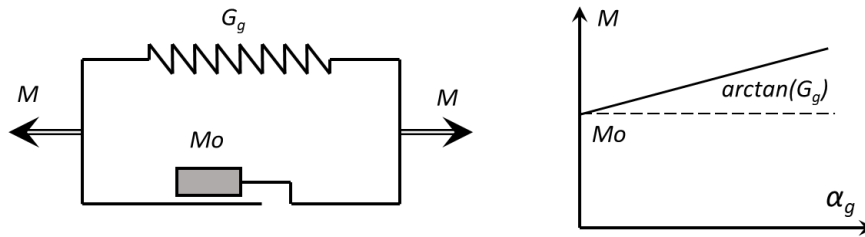


Figure 8. Rheologic Model of slipping between yarns.

In order to introduce a progressive slippage in rotation between warp and weft yarns after a certain threshold M_o of the force moment, as it can be observed experimentally, a rheological model as shown on Fig. 8, has been introduced [5].

As far as the force moment do not exceed a threshold M_o , the tangent of both yarns in Z_1 - Z_3 plane remain orthogonal; the fabric deformations are elastic. Where the shearing forces increase and the threshold M_o is exceeded, the slippage angle α_g between both yarns can be introduced as follows:

$$\alpha_g = \frac{M - M_o}{G_g} \tag{8}$$

where: M is the moment of forces on Z_2 axis (Eq. 7), M_o is the slipping threshold in rotation, G_g is the rigidity in slipping. The angle Z_4 of the tangents of both yarns in Z_1 - Z_3 plane, will be given by:

$$Z_4 = \frac{\pi}{2} - \alpha_g \tag{9}$$

A typical example of shear with no yarn slippage, which means that the tangents of both yarns in Z_1 - Z_3 plane remains $\frac{\pi}{2}$ is given below, on Fig. 9, whereas Fig. 10 shows some simulation results in shear with yarn slippage for different yarn bending rigidity and slippage rigidity.

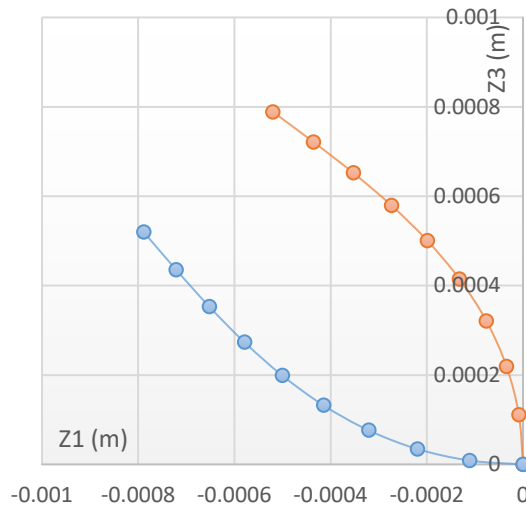


Figure 9. Graphical representation of yarn axes after applying shear forces.

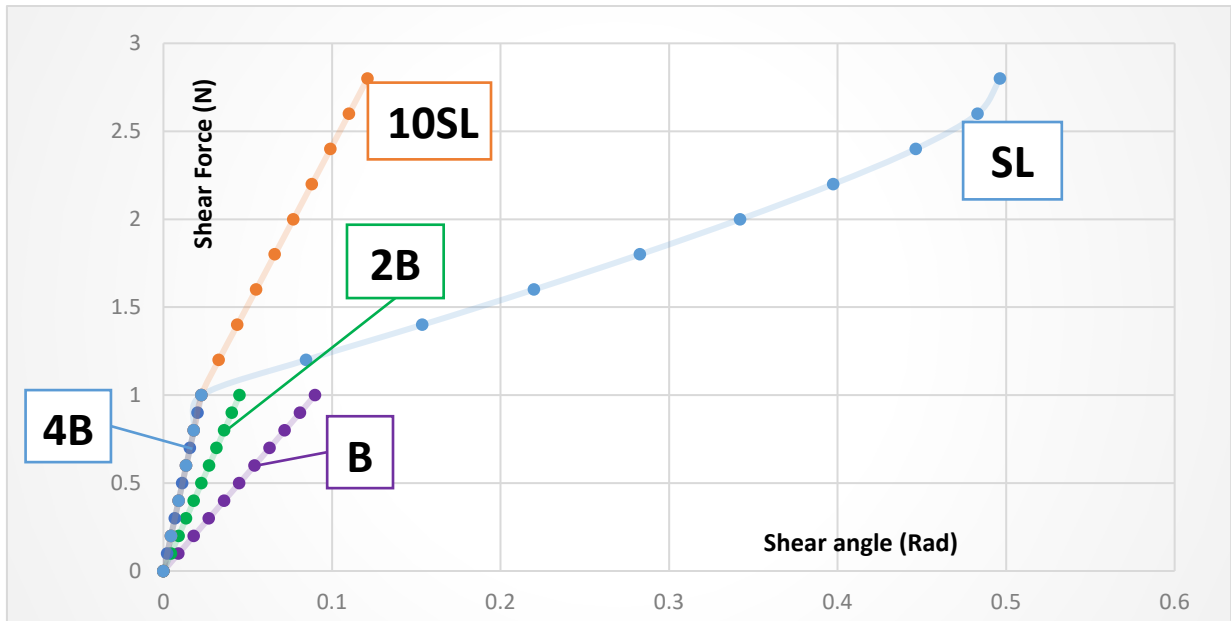


Figure 10. Force-Deformation graph for different values of rigidity in bending (B) and in slipping (SL).

Simultaneous Fabric Multiloading. If yarn slippage has to be considered, the final geometry of the fabric, and consequently the fabric deformation state, will depend on the fabric loading history, due to the existence of the non-conservative effects of slipping phenomenon. Nevertheless, if the loading history is known, the final fabric geometry and deformations can be calculated by the same procedure of progressive fabric loading.

On the other hand, if the slippage is to be neglected, in this case, the simulations of the fabric deformations in the whole domain of acceptable loads can be carried out in order to calculate by interpolation technics the fabric deformation state at any loading state ($F_1, F_{transv}, Shear$)

Some typical multiloading results are shown on Figure 11.

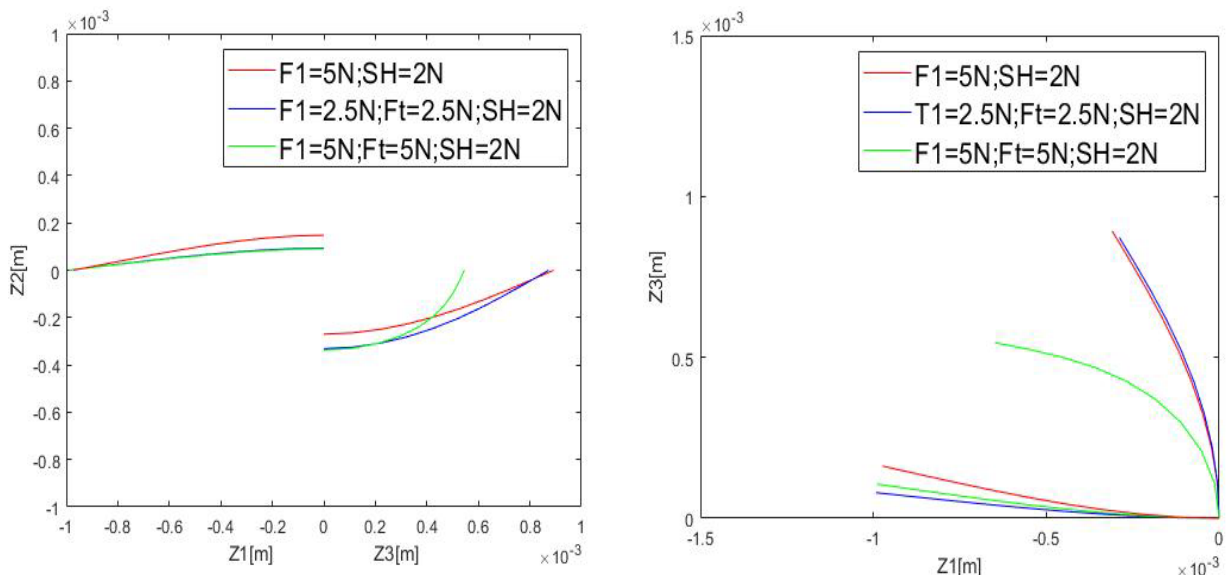


Figure 11. Some typical multiloading results.

Conclusion and Perspectives

As proposed in the present work, it is possible to calculate the geometry of the fabric unit cell submitted to some force condition or state and also to calculate the strain state or tensor associated to this force tensor. Later, it is also possible to calculate by interpolation technics the strain tensor at any

force tensor. The rigidity tensor can also be calculated and analysed in terms of constant and linear or non-linear coefficients in order to construct and predict the behaviour of real samples - made up of thousands of unit cells, each one loaded differently - under typical loading, for example longitudinal traction or bias test.

References

- [1] S. De Jong and R. Postle, A General Energy Analysis of Fabric Mechanics Using Optimal Control Theory, *Textile Res. J.*, 48(3), (1978) 127-135.
- [2] G. Kirchhoff, Über des gleichgewicht und die Bewegung eines unendlich dünnen elastischen Stabes. *Crelles Journal für die reine und angewandte Mathematik*, 56 (1859) 285–313.
- [3] N. Ogreni, A. Sinoimeri, L. Nikolla, Simulation of Mechanical Behaviour of Textile Fibers, 8th International Textile Conference, October 2018, Tirana, ALBANIA, Book of Proceedings 144-158
- [4] A.E.H. Love, *A Treatise on the Mathematical Theory of Elasticity*, fourth edition. Cambridge University Press, Cambridge, 1927.
- [5] A. Sinoimeri, Contribution à l'Étude du Comportement Mécanique des Etoffes par Méthodes Energétiques-Cas de l'Armure Toile, Thèse de Doctorat (PhD), Université de Haute Alsace, (1993).

Keyword Index

3D Net Shape Fabrics	183	Electromagnetic Shielding	161
3D Printing	31	Electronic Textiles	3
A		Embroidered Antenna	55
Abrasion Effects	39	Embroidery	11
Adaptive Fiber-Reinforced Plastics	47	Energy	227
Adhesives	129	Equilibrium	227
Alpha Finite Element Method	211	F	
B		Fibres	227
Bond Behavior	173	Filler Particles	31
Bond Mechanisms	173	Finite Element Method	211, 219
Bond Test	173	Flexible Sensors	143
Buckling Analysis	211	Free Vibration Analysis	219
C		Functional Textiles	161
Carbon Fiber Reinforced Epoxy (CFRE) Composites	205	G	
Carbon Fibers (CFs)	205	Graphene Nanoplatelets	117
Carbon Materials	161	H	
Carbon Microparticles	205	Heat Transfer	153
Carbon Nanotubes	69, 81, 91, 161	Heating Textile	69
Carbon Reinforced Concrete	173	Hydrochromics	97
Coating Process	161	I	
Composite	91, 197	Immiscible Thermoplastic/Elastomer Blend	21
Conductive Polymer Composite	21, 69	M	
Conductive Polymers	161	Mass Transfer	153
Conductive Textiles	31	Mechanical Impact	11
Conductive Yarn	39, 55	Mechanical Properties	205
Copper/Nickel Coating	137	Melt Coating	69
D		Melt Mixing	91
Deformation	227	Melt Spinning	81
Denim Waste	197	Mindlin-Reissner Plate Theory	211, 219
Dip-Pad-Dry Process	161	Monofilament	21
Dispenser Printing	31	N	
E		Node-Based Smoothed Finite Element	219
E-Textiles	3, 39, 153	P	
Electrical Conductivity	91	Packaging Waste	197
Electrical Resistance Values	117		
Electrically Conductive Filament	81		
Electromagnetic Radiation	137		

Percolation Threshold	31	Textile-Like Sheet Material	211, 219
Photocatalytic Activity	63	Textile Sensor	11
Photochromics	97	Thermal Conductivity	197
Photocuring	129	Thermochromics	97
Piezoresistive	143	Thermoplastic Polyurethane	81
Plasma Treatment	117	Thread Tension	55
POF	129	Titanium Dioxide (TiO ₂)	63
Polyamide 6	91		
Polyamide Yarn	11	U	
Polyethylene	91	Ultrathin Nonwoven	137
Pressure Sensors	143		
Profiling Technology	173	V	
		Volatile Organic Compounds (VOCs)	63
R			
Read Range	55	W	
Recycling	197	Wash Testing	3
Resistance	11	Water Leak Detection	21
RFID Tag	55	Weaving	47
		Weft Knitting	39
S		Woven Fabrics	129, 183
Self-Powered Wetness Sensor	107		
Self-Regulating Temperature	69	Y	
Sensors	143	Yarns	227
Shape Memory Alloys	47		
Shielding Effectiveness	137		
Silver Plated	11		
Simulation	227		
Smart Diapers	107		
Smart Safety Bracelet	107		
Smart Textile	39, 69		
Smart Textiles	91, 97, 117, 143		
Spherically Curved Woven Fabrics	183		
Standardization	3		
Stitch Density	55		
Strain Sensor	81		
Strain Smoothing Technique	219		
Stress	153		
Strips	137		
T			
Tactile Internet	39		
Tensile Test	173		
Test Methods	3		
Textile Battery	107		
Textile Design	97		
Textile Fabric	63		
Textile Heat Fluxmeter	153		

Author Index

A

Arruda, L.M. 117
Ashir, M. 47

B

Barbosa, J.R.M. 161
Bessa, J. 117
Böhnke, P.R.C. 11, 39
Boticas, I. 117
Briedis, U. 107
Bunyaev, S.A. 161

C

Cabral, I. 97, 143
Campagne, C. 21, 69
Carvalho, H. 143
Carvalho, M.A. 107
Cayla, A. 21, 69
Cherif, C. 11, 39, 47, 81, 173, 183
Cunha, A. 143
Curbach, M. 173

D

Devaux, É. 21, 69
Duman, M.N. 55
Dupont, D. 63, 153

E

Esmer, G.B. 55

F

Fangueiro, R. 117
Ferreira, F.B.N. 211, 219
Ferreira, J. 161
Freire, C. 161

G

Gidik, H. 63, 153
Gomes, A.J.P. 211, 219
Gries, T. 129

H

Hahn, L. 173
Häntzsche, E. 11, 39
Hemberg, A. 63
Hoffmann, G. 183

K

Kakazei, G.N. 161
Kallweit, J. 129
Kaplan, M. 91
Karthik, D. 137
Krause, B. 91
Kruppke, I. 11, 39
Kucukali-Ozturk, M. 197

L

Lahem, D. 63
Laurent, V. 69
Lemort, G. 69
Lempa, E. 31
Lüneburg, L.M. 11

M

Marischal, L. 69
Matos, R. 161
May, M. 173
Mechtcherine, V. 173
Mersch, J. 81
Militký, J. 137
Mohsenzadeh, E. 63, 153
Moreira, I.P. 117
Morgado, J. 161

N

Nikolla, L. 227
Nocke, A. 11, 39, 47, 81
Novotná, J. 205
Nuss, D. 183

O

Ogreni, N. 227
Osswald, E. 143

		Van Langenhove, L.	31
		Výborný, L.	205
P			
Palanisamy, S.	137		
Pätzel, M.	129		
Penzel, P.	173		
Pereira, A.M.	161		
Pereira, C.	161		
Pereira, M.F.R.	161		
Pham, M.Q.	183		
Pötschke, P.	91		
Probst, H.	81		
Q			
Quoc, N.T.	211, 219		
Quyen, N.T.	211, 219		
R			
Rabe, M.	31		
Regnier, J.	21		
Reisgen, U.	129		
Rotzler, S.	3		
S			
Santos, G.	161		
Schiebahn, A.	129		
Schneider-Ramelow, M.	3		
Seewald, R.	129		
Sennewald, C.	183		
Sezgin, H.	197		
Silva, A.	161		
Sinoimeri, A.	227		
Soares, O.S.G.P.	161		
Soares, P.	161		
Sousa, A.R.	161		
Souto, A.P.	97, 143		
T			
Tlemsani, F.Z.	153		
Tomková, B.	205		
Tru, N.D.	211, 219		
Tunakova, V.	137		
U			
Usta, I.	55		
V			
Vališevskis, A.	107		
		W	
		Wagner, J.	39
		Wang, Y.F.	137
		Warncke, M.	11
		Wieczorek, F.	11, 39
		Winger, H.	11, 39
		Wollmann, J.	81
		Y	
		Yalcin-Enis, I.	197
		Z	
		Zavalani, G.	227